



Technisch-Naturwissenschaftliche  
Fakultät

# **Phase-sensitive Imaging and Image Processing for Optical Coherence Tomography Applications**

DISSERTATION

zur Erlangung des akademischen Grades

**Doktorin**

im Doktoratsstudium der

**TECHNISCHEN WISSENSCHAFTEN**

Eingereicht von:  
Dipl. Phys. Bettina Heise

Angefertigt am:  
Institut für Wissensbasierte Mathematische Systeme (FLLL)  
Zentrum für Oberflächen- und Nanoanalytik (ZONA)

Beurteilung:  
Prof. Dr. Erich Peter Klement  
PD Dr. David Stifter

Linz, Mai 2010



## **Eidesstattliche Erklärung**

Ich erkläre an Eides statt, dass ich die vorliegende Dissertation selbstständig und ohne fremde Hilfe verfasst, andere als die angegebenen Quellen und Hilfsmittel nicht benutzt bzw. die wörtlich oder sinngemäß entnommenen Stellen als solche kenntlich gemacht habe.

Linz, Mai 2010



## Abstract

This work is concerned with the topic of phase-sensitive imaging techniques suitable for the investigation of structures in the micron range, and shows the potential for quantitative analysis resulting from an appropriate image processing for the investigated specimens. The probed samples are mostly of technical nature, but the methods are in general not restricted to technical applications. Moreover, several imaging aspects have originated from biological applications, being recently transferred to technical material sciences.

Concerning imaging technique, we focus on optical coherence tomography (OCT) and in particular on its phase-sensitive modifications: Polarization-sensitive OCT (PS-OCT) and differential phase contrast OCT (DPC-OCT). The comparison to quantitative imaging in phase contrast microscopy techniques (classical phase contrast microscopy, differential interference contrast microscopy, and advanced versions of phase microscopy) has been done to illustrate the similarities, differences, and limitations of both techniques.

We propose two procedures comprehending the measurement, the enhancement and the quantitative analysis of phase-related quantities: In case of PS-OCT we consider the reconstruction of retardation and birefringence distributions, and in case of DPC-OCT imaging, the extraction of the phase gradient fields and the reconstruction of the optical path length maps therefrom.

- From the point of view of physics we demonstrate how existing phase-sensitive OCT techniques can be modified in their imaging setup to allow an advanced data acquisition. Especially, we consider how one-dimensional measurement schemes in DPC-OCT can be extended to allow a two-dimensional solution of the phase reconstruction problem.
- From the point of view of signal processing we illustrate the potential given by extending also the analysis of PS-OCT retardation images from one-dimensional signal processing to two-dimensional image analysis. We include demodulation schemes, based on generalized analytic signal theory and originally developed for two-dimensional fringe pattern analysis of conventional interferometry, in PS-OCT imaging applications.
- From the point of view of mathematics we show how the existing image processing schemes can be adapted and improved to become suitable for the measured PS-OCT and DPC-OCT images. Especially the necessity of an appropriate pre-processing (as image denoising and decomposition), tailored to the features of phase-based OCT imaging, is illustrated.

We have demonstrated the performance of the described methods to obtain spatially-resolved and quantitative information about internal material states, as birefringence and stress, or about the topography of embedded phase structures. Suggestions for further improvements of the reconstruction scheme are discussed. We have exemplified the proposed procedures for different test samples in real-world applications and situations being relevant in the field of material testing.

The thesis is written deliberately in the field spanned between physics, in particular optics, and mathematics, in particular image processing. The work should illustrate the potential, which can be obtained by the interdisciplinary consideration of optical measurement techniques, mathematical data analysis, and aspects of material sciences.



## **Kurzfassung:**

Die Dissertation widmet sich der Thematik von phasensensitiver Bildgebungstechniken und Bildverarbeitung, die speziell zur Untersuchung von Strukturen im Mikrometer-Bereich verwendet werden können. Sie demonstriert das Potential, das sich unter Einbeziehung von Bildverarbeitungsmethoden für eine quantitative Analyse der untersuchten Materialien ergibt. Die verwendeten Proben sind meist technische Materialien. Aber die betrachteten Methoden sind im allgemeinen nicht nur auf technische Anwendungen beschränkt. Verschiedene Aspekte der Bildgebung entstammen ursprünglich biologischen Aufgabenstellungen und sind erst vor einiger Zeit in das Gebiet der Materialwissenschaft übertragen worden.

Hinsichtlich der optischen Untersuchungsmethoden wird der Schwerpunkt in dieser Arbeit auf die optische Kohärenztomographie (OCT) gesetzt, insbesondere auf deren phasensensitiven Realisierungen: Polarisationsensitive OCT Technik (PS-OCT) und (Differentielle) Phasenkontrast OCT Technik (DPC-OCT). Um Gemeinsamkeiten, Unterschiede und Einschränkungen von beiden Techniken zu analysieren wird ebenso auch Phasenkontrastmikroskopie im Vergleich betrachtet.

Wir schlagen zwei getrennte Methoden vor, die sowohl die Messung, die Verbesserung und die quantitative Auswertung der gemessenen Daten umfassen: Zum einen werden sogenannte Verzögerungsbilder, die mittels PS-OCT aufgenommen wurden, analysiert und daraus Materialgrößen, wie Anisotropie oder Doppelbrechung, ermittelt. Zum anderen, wird die Messung von Phasen-Gradientenfeldern durch das DPC-OCT Bildgebungsverfahren und die mathematische Rekonstruktion des daraus resultierenden optischen Weglängen-Profiles gezeigt.

- Vom Standpunkt der Physik demonstrieren wir, wie existierende phasensensitive OCT Techniken in ihrem optischen Aufbau modifiziert werden können, um eine verbesserte Bildaufnahme zu erreichen. Insbesondere betrachten wir, wie eindimensionale Methoden in DPC-OCT zu einem Verfahren erweitert werden, das letztendlich eine zweidimensionale Rekonstruktion von gemessenen Phasenstrukturen ermöglicht.
- Vom Standpunkt der Signalverarbeitung, erläutern wir die Möglichkeiten, die sich für die Auswertung von PS-OCT Verzögerungsbildern ergeben, wenn von eindimensionaler Betrachtungsweise der OCT Signale auf eine zweidimensional Bildanalyse übergegangen wird. Wir zeigen, wie Demodulationsverfahren, beruhend auf verallgemeinerter analytischer Signaltheorie und ursprünglich für interferometrische Anwendungen entwickelt, auch für PS-OCT Anwendungen erfolgreich verwendet werden können.
- Vom Standpunkt der Mathematik zeigen wir, wie existierende Bildverarbeitungsverfahren an die spezifischen Charakteristika von PS-OCT Bildern angepasst werden können. Wir demonstrieren insbesondere die Notwendigkeit einer geeigneten Vorverarbeitung (d.h. Bildverbesserung und Bildkorrektion) für die aufgezeichneten PS-OCT und DPC-OCT Daten.

Die Leistungsfähigkeit der beschriebenen Methoden zur Gewinnung von örtlich aufgelösten und quantitativen Informationen über lokale Doppelbrechung in Materialien, interne Spannungsverläufe oder Topographie von eingebetteten Phasenstrukturen konnte gezeigt werden. Verbesserungsmöglichkeiten der Mess- und Rekonstruktionsmethoden werden von uns ebenso diskutiert.

Die entwickelten Verfahren sind an verschiedenen Testobjekten in technisch-relevanten Situationen erprobt worden.

Die Dissertation ist bewusst fächerübergreifend zwischen Physik (Optik), und Mathematik (Bildauswertung), angefertigt worden. Sie soll das Potential demonstrieren, das sich aus einer interdisziplinären Betrachtungsweise von optischer Messtechnik, mathematischer Datenauswertung und Fragestellungen der Materialwissenschaft ergibt.



# Contents

<b>1</b>	<b>Introduction</b>	<b>17</b>
<b>2</b>	<b>Phase Contrast Microscopy Imaging: State of the Art</b>	<b>23</b>
2.1	Conventional phase contrast microscopy . . . . .	23
2.1.1	Imaging principle in PCM . . . . .	23
2.1.2	Imaging setup for Fourier plane filtering . . . . .	26
2.2	Differential interference contrast microscopy . . . . .	26
2.2.1	Imaging principle in DIC microscopy . . . . .	26
2.2.2	Imaging setup in DIC microscopy . . . . .	28
2.2.3	Quantitative imaging in DIC . . . . .	28
2.3	Spiral phase microscopy . . . . .	29
2.3.1	Imaging principle in spiral phase microscopy . . . . .	29
2.3.2	Properties of the spiral phase filter in optics . . . . .	30
2.4	Summary . . . . .	31
<b>3</b>	<b>Fundamentals of Analytic Signal Theory</b>	<b>33</b>
3.1	Image structures . . . . .	34
3.1.1	Classification of image structures . . . . .	34
3.1.2	Characterization of image structures . . . . .	34
3.1.3	Decomposition and analysis of image structures . . . . .	36
3.1.3.1	Fourier and Hilbert spectral analysis methods . . . . .	36
3.1.3.2	Empirical mode decomposition . . . . .	36
3.2	1D Analytic signal . . . . .	37
3.3	2D Monogenic signal . . . . .	39
3.3.1	Hilbert transform approaches in 2D . . . . .	39
3.3.2	Riesz transform . . . . .	41
3.3.3	Extension: Superposition of 2D AM-FM signals . . . . .	42

3.4	Demodulation of 2D AM-FM signals . . . . .	42
3.4.1	2D AM-FM signal model for the demodulation scheme . . . . .	42
3.4.2	The Hilbert transform and the quadrature component computation . . . . .	44
3.4.3	Influence of the algebraic space on the demodulation approach . . . . .	46
3.4.3.1	Computation of 2D quadrature component by the radial Hilbert transform (Spiral phase transform) . . . . .	46
3.4.3.2	Computation of 2D quadrature component by the Riesz transform . . . . .	49
3.4.3.3	Comparison: Radial Hilbert transform and Riesz transform . . . . .	50
3.4.4	Influence of the wave shape on the demodulation approach . . . . .	51
3.4.4.1	1D Signals . . . . .	51
3.4.4.2	2D Signals . . . . .	52
3.4.5	Influence of the background on the demodulation approach . . . . .	56
3.4.5.1	Error estimation . . . . .	56
3.4.5.2	Background correction by the EMD method . . . . .	57
3.5	Summary . . . . .	60
<b>4</b>	<b>Conventional OCT and Advanced Modifications</b>	<b>61</b>
4.1	OCT: Imaging principles . . . . .	61
4.1.1	OCT: Working principle and optical setup . . . . .	62
4.1.2	OCT: Reflectivity signal and image generation . . . . .	63
4.1.3	OCT: Imaging parameters . . . . .	66
4.2	Artifacts and noise in OCT imaging . . . . .	66
4.3	Advanced modifications of OCT imaging . . . . .	67
<b>5</b>	<b>PS-OCT for Birefringence and Stress Imaging</b>	<b>69</b>
5.1	PS-OCT: Imaging technique . . . . .	69
5.1.1	PS-OCT: Optical configuration . . . . .	70
5.1.2	PS-OCT: Image types . . . . .	72
5.1.3	PS-OCT: Fringe pattern parameters . . . . .	73
5.1.4	PS-OCT retardation imaging: Testing and samples . . . . .	74
5.1.5	Comparison of PS-OCT with conventional photoelasticity techniques . . . . .	75
5.2	PS-OCT: Speckles and speckle noise . . . . .	77
5.2.1	Laser speckles . . . . .	77
5.2.2	Speckles in OCT . . . . .	78
5.2.3	Speckle noise in reflectivity images . . . . .	79

---

5.2.4	Speckle noise in OCT retardation images . . . . .	79
5.3	PS-OCT: Modeling of retardation and birefringence/stress images . . . . .	79
5.3.1	Comparison: Retardation and phase . . . . .	80
5.3.2	Noise-free depth-resolved retardation signal . . . . .	81
5.3.3	Noisy depth-resolved retardation signal . . . . .	82
5.3.3.1	Illustration: Retardation signal generation . . . . .	85
5.3.3.2	Comparison: Simulated and measured depth-resolved retardation signals . . . . .	88
5.3.4	Modeling birefringence and retardation image . . . . .	90
5.3.4.1	Modulating function: Birefringence and stress . . . . .	90
5.3.4.2	Internal birefringence and stress model . . . . .	91
5.4	PS-OCT: Reconstruction methods . . . . .	94
5.4.1	1D Reconstruction method for continuous retardation . . . . .	94
5.4.2	2D Reconstruction method for continuous retardation . . . . .	97
5.4.2.1	Scaling . . . . .	97
5.4.2.2	Background and riding wave correction . . . . .	97
5.4.2.3	Denoising . . . . .	98
5.4.2.4	Computation of 2D quadrature image and orientation estimation . . . . .	99
5.4.2.5	Unwrapping . . . . .	100
5.4.3	Reconstruction of internal stress distribution . . . . .	103
5.4.4	Further comments on the reconstruction approach . . . . .	105
5.4.4.1	Comments on the denoising . . . . .	105
5.4.4.2	Comments on the demodulation . . . . .	109
5.4.4.3	Comments on the internal stress calculation . . . . .	109
5.5	PS-OCT: Results and discussion . . . . .	111
5.5.1	Evaluation on simulated fringe patterns . . . . .	111
5.5.2	Evaluation on measured cross-sectional retardation images . . . . .	118
5.5.2.1	Dilatation test . . . . .	118
5.5.2.2	Bending test . . . . .	119
5.5.3	Evaluation on measured en-face retardation images . . . . .	121
5.5.4	Discussion: PS-OCT imaging and reconstruction . . . . .	124
5.5.4.1	Consideration about testing and reconstruction . . . . .	124
5.5.4.2	Summary: Pros and Cons . . . . .	125

---

<b>6</b>	<b>DPC-OCT for Optical Path Length Mapping</b>	<b>127</b>
6.1	DPC-OCT: Imaging techniques . . . . .	128
6.1.1	DPC-OCT: Optical configuration . . . . .	128
6.1.2	DPC-OCT: Image types . . . . .	130
6.1.3	DPC-OCT: Test samples . . . . .	131
6.2	DPC-OCT: Measurement performance . . . . .	134
6.2.1	DPC-OCT: Raw-data phase drift . . . . .	134
6.2.2	Repetition accuracy . . . . .	137
6.2.3	Phase unambiguity range . . . . .	137
6.3	DPC-OCT: Reconstruction of phase and optical path length map . . . . .	138
6.3.1	En-face DPC-image extraction . . . . .	138
6.3.2	2D Unwrapping . . . . .	139
6.3.3	Phase map reconstruction . . . . .	139
6.3.3.1	1D phase reconstruction approaches . . . . .	140
6.3.3.2	2D phase reconstruction approaches . . . . .	145
6.4	DPC-OCT: Results and discussion . . . . .	149
6.4.1	Results: 1D reconstruction . . . . .	149
6.4.2	Results: 2D reconstruction . . . . .	151
6.4.3	Discussion: DPC-OCT imaging and reconstruction . . . . .	152
<b>7</b>	<b>Conclusions &amp; Outlook</b>	<b>159</b>
7.1	Conclusions . . . . .	159
7.1.1	PS-OCT imaging system . . . . .	160
7.1.2	DPC-OCT imaging system . . . . .	160
7.2	Outlook . . . . .	161
<b>8</b>	<b>Acknowledgments</b>	<b>163</b>

# Symbols

$\alpha$	attenuation parameter
$\alpha_D$	divergence angle
$\alpha_{Ch}$	chirp parameter
$\beta$	orientation/direction
$\beta_\pi$	orientation
$\beta_{2\pi}$	direction
$\beta_R$	regularization parameter
$\gamma$	step size
$\gamma_A$	exponential decay factor
$\gamma(z)$	coherence function
$\delta$	offset
$\delta_x$	lateral resolution
$\delta_z$	axial resolution
$\delta_R$	angular shift
$\delta()$	delta function
$\varepsilon$	strain
$\varepsilon_A$	approximation error
$\varepsilon_\phi$	phase error
$\iota$	intensity
$\iota_{AC}$	alternating intensity signal
$\iota_r$	reflectivity (intensity)
$\phi$	phase
$\phi_w$	wrapped phase
$\phi_c$	continuous phase
$\phi_r$	phase retardation
$\phi_{rw}$	wrapped phase retardation
$\phi_{rc}$	continuous phase retardation
$\phi_x$	differential phase in x
$\phi_y$	differential phase in y
$\Delta\phi$	phase difference
$\phi_{Off}$	phase modified by offset
$\Phi$	Fourier transform of $\phi$ .
$\vartheta$	optical path length
$\lambda$	wavelength
$\kappa$	coherence
$\mu$	mean value

$\sigma_S$	stress
$\sigma^2$	variance
$\sigma$	scaling parameter (Gaussian kernel bandwidth)
$\sigma_{Sp}^2$	Speckle variance
$\tau$	beam shear
$\xi$	scale
$\omega$	angular frequency
$\Delta$	(discrete) difference
$\Delta x, \Delta y$	beam shear (in x- and y-scanning direction)
$\mathbf{k}$	spatial frequencies related to optics
$\mathbf{u}$	spatial frequencies related to mathematics, $\mathbf{k} = \frac{2}{\pi} \mathbf{u}$
$k$	wave number in material
$k_0$	wave number in vacuum (air)
$n_M$	refractive index in medium
$n_0$	refractive index in air/vacuum
$\Delta n_B$	birefringence
$n$	noise (index)
$n_{iSp}$	intensity-related speckle noise
$\mathbf{n}$	noise in complex representation (retardation related)
$R_{Sp}$	real component of the speckle noise
$I_{Sp}$	imaginary component of the speckle noise
$f$	focus length
$d_H$	height, thickness
$\gamma$	noise parameter
$G(\omega)$	power spectral function
$E$	spatial and temporal EM-field
$u$	(time-independent) transmission function
$\mathbf{a}$	EM-field in context of OCT
$a, A$	amplitude (modulation)
$A$	magnitude of complex value
$I$	intensity
$I_{AC}$	alternating intensity
$I_0$	constant intensity offset
$R$	reflectance
$M_D$	modulation depth, visibility
$f_P(\mathbf{x}), I_P(x, y)$	in-phase signal
$f_Q(\mathbf{x}), I_Q(x, y)$	quadrature signal
$f_q(\mathbf{x})$	(true) quadrature signal
$S$	detector signal (representing photocurrent or voltage)
$b(\mathbf{x}), B(x, y)$	offset, background,
$P$	topological charge
$K$	Gaussian kernel

---

$x, y, z$	spatial coordinates
$u, v, w$	spectral coordinates
$r, \theta$	polar coordinates in spatial domain
$R, \Theta$	polar coordinates in spectral domain
$I, R$	imaginary and real component (as indices)
$\eta, \zeta$	spatial coordinates in complex representation
$z$	depth, (penetration depth)
$t$	time
$T$	time domain
$\Omega$	spatial domain
$\Gamma$	boundary of domain
$\mathbf{W}$	wrapping operator
$\mathbf{W}_D$	orientational unwrapping operator
$\mathbf{M}$	general smoothing operator
$h(x, y)$	point spread function (PSF)
$h_Z(x, y)$	complex point spread function (cPSF) in Zernike PCM
$h_{DIC}(x, y)$	complex point spread function (cPSF) in DIC microscopy
$h_{SPF}(x, y)$	complex point spread function (cPSF) in spiral phase microscopy
$H(u, v)$	optical transfer function (OTF), filter function
$\mathcal{H}$	Hilbert transform operator
$\mathcal{F}$	Fourier transform operator
$\mathcal{H}_R$	Radial Hilbert transform operator (Spiral phase operator)
$\mathcal{R}$	Riesz transform operator
$\mathcal{E}$	Energy operator
$\mathcal{E}_\theta$	Energy operator computed by spiral filter
$\mathcal{T}$	Teager-Kaiser operator
$\mathbf{H}$	matrix representation of difference operator
$\mathbf{H}_R$	spiral filter transfer function
$J$	structure tensor
$c$	eigenvalues
$\mathcal{D}$	diffusivity
$\mathcal{N}(\mu, \sigma^2)$	Normal distribution
$\mathbf{e}_\tau$	shear direction
$\mathbf{e}_n$	normal direction
$f(x, y)$	general 2D signal
$f_A(x)$	analytic signal (1D)
$f_{\mathbf{R}}(x, y)$	Radial Hilbert (spiral phase) transformed signal part
$f_{\mathbf{RI}}(x, y)$	Riesz transformed signal part
$f_{\mathbf{M}}(x, y)$	monogenic signal (2D)
$f_{MU}(x, y)$	multi-component signal
$f_m(x, y)$	mono-component signal

## Mathematical operations:

$(\cdot, \cdot)$	inner product
$\odot$	outer product
$\times$	cross product
$\otimes$	convolution
$\langle \rangle_T$	time average
$\langle \rangle$	spatial average
$\ (\cdot)\ _2$	Euclidean norm
$ \cdot $	absolute value
$\angle(\cdot)$	argument value
$\prec$	$m \times n$ matrix to $m \times n \times 1$ vector
$\mathbb{C}^n$	complex space
$\mathbb{R}^n$	real space
$\mathbb{Q}$	quaternionic space



## Abbreviations:

PCM	Phase contrast microscopy
DIC	Differential interference contrast
QPM	Quantitative phase microscopy
OCM	Optical coherence microscopy
CPM	Coherence probe microscopy
DHM	Digital holographic microscopy
FPF	Fourier plane filtering
FPf	Fourier plane filter
SLM	Spatial light modulator
SPM	Spiral phase microscopy
SPF	Spiral phase filter
CPI	Common path interferometry
LCI	Low coherence interferometry
OCT	Optical coherence tomography
PS	Polarization-sensitive
DPC	Differential phase contrast
FF	Full-field
PE	Photo elasticity
SAR	Synthetic aperture radar
HT	Hilbert transform
RHT	Radial Hilbert transform
RT	Riesz transform
TF	Transfer function
OTF	Optical transfer function
cTF	Complex transfer function
PSF	Point spread function
SNR	Signal-to-noise ratio
OPL	Optical path length
CED	Coherence enhancing diffusion
NLM	Non local mean
EM	Electromagnetic
AM	Amplitude modulated
FM	Frequency modulated
1D	One-dimensional
2D	Two-dimensional
1d	One-directional
tri	Triangular wave shape
rect	Rectangular wave shape
i1D	Intrinsic one-dimensional



# Preliminaries

## ■ Spatial Coordinate System Notations

- Generalized Cartesian spatial coordinate system  $\mathbf{x} = (x_1, \dots, x_n)$  with special case of 3D (resp. 2D) spatial coordinates representation  $(x, y, z)$  (resp.  $(x, y)$ ).
- Generalized Cartesian spectral coordinate system  $\mathbf{u} = (u_1, \dots, u_n)$  with special case of 3D (resp. 2D) spectral coordinate system  $(\mathbf{v}, \mathbf{v}, \mathbf{\omega})$  (resp.  $(\mathbf{v}, \mathbf{v})$ ).
- Generalized Cartesian spectral coordinate system  $\mathbf{k} = (k_1, \dots, k_n)$  related to wave number  $\mathbf{k} = \frac{2\pi}{\lambda} \mathbf{u}$  with special case of 3D (resp. 2D) k-space coordinate system  $(k_x, k_y, k_z)$  (resp.  $(k_x, k_y)$ ).

## ■ Signal and image domain

- Considering in general functions  $f : \mathbb{R}^n \rightarrow \mathbb{R}$  in the domain  $\Omega = (-\infty, \infty) \times \dots \times (-\infty, \infty)$ , and in case of temporal varying functions  $f : (0, \infty) \rightarrow \mathbb{R}$  in the time domain  $\mathbf{T} = (0, \infty)$ ; different use is otherwise indicated in the text.
- Considering finite data sets the spatial domain  $\Omega$  is given by:  
 $\Omega = (0, a_1) \times \dots \times (0, a_n) \subset \mathbb{R}^n$ , especially  $\Omega = (0, n) \times (0, m) \subset \mathbb{R}^2$  in case of  $f : \Omega \rightarrow \mathbb{R}$  representing an 2D image.
- Boundary of spatial domain:  $\Gamma = \partial\Omega \subset \mathbb{R}^n$ .

## ■ In our paper we assume complex-valued signals $f(\mathbf{x}) \in \mathbb{C}^n$ or as special case real-valued signals $f(\mathbf{x}) \in \mathbb{R}^n$ (in general $n = 1$ for the considered signals) with the properties:

- continuously differentiable function:  $f \in C$
- band-limited function with finite-energy:  $\int_{-\infty}^{\infty} |f(\mathbf{x})|^2 d\mathbf{x} < M$
- Fourier representation:

$$\mathcal{F} \{f(\mathbf{x})\} = F(\mathbf{u}) = \frac{1}{2\pi} \int_{-\pi}^{\pi} f(\mathbf{x}) \exp(-i2\pi\mathbf{u}\mathbf{x}) d\mathbf{x}. \quad (1)$$

In Chapter (3) we will also shortly consider quaternionic signals  $f(\mathbf{x}) \in \mathbb{Q}$ , where  $\mathbb{Q}$  describes the quaternionic space with the corresponding algebra.

## ■ Mathematical definition: Phase and amplitude

Considering complex-valued signals  $f(x) = A(x) \exp(i\phi(x))$ , the argument of the complex function describes the phase by  $\phi(x) = \angle(f(x))$  mathematically, and the amplitude  $A$  represents the magnitude of the quantity by  $A(x) = |f(x)|$ . Whereas the strength of signals is

expressed by its amplitude, the phase characterizes its temporal or spatial propagation in space or time and moreover, the displacement or delay of the signal find their expression in phase difference terms.

In the following chapters the phrase *phase* is used in slightly different contexts, and it should be carefully distinguished between the different meanings of the word. In particular, expressing e.g. *instantaneous* phase, *initial* phase and *global* phase. Considering e.g. a pure harmonic signal  $f(x) = \cos(\omega x + \phi_0)$  with the frequency  $\omega$ , the term  $\phi(x) = \omega x + \phi_0$  expresses the instantaneous phase or local phase  $\phi(x)$  of the signal at position  $x$ . The initial condition of the signal at  $x = 0$  is given by the initial phase term  $\phi_0$ . Taking the Fourier transform  $F(u) = \mathcal{F}\{f(x)\}$ , the argument  $\arg(F(u))$  describes the global phase (or Fourier phase)  $\phi_F(u)$  of the signal over all frequency components  $u$ . A phase shift in space or time represented by a change of the initial phase yields the well-known shift theorem

$$\mathcal{F}\{f(x - x_0)\} = \mathcal{F}\{f(x)\} \exp(-i 2\pi x_0 u) \quad (2)$$

The phase is often represented by using the arctan-function for the angle of the signal, causing a mapping of the phase to the interval  $[-\pi/2, \pi/2)$  (resp.  $[-\pi, \pi)$  (depending on the definition) and yielding the wrapped phase  $\phi_w(x)$ . Reconstructing the original phase term by phase unwrapping methods delivers the unwrapped phase  $\phi_{uw}(x)$  with  $\phi(x) = \phi_{uw}(x)$  in case of continuous phase functions.

Furthermore, it should be mentioned that in the chapters related to optical phase measurements (i.e. Chapter (2) and Chapter (6)) the phase is directly related to the phase of the electro-magnetic (EM) field or to the phase change introduced by the specimen. In chapters concerning image processing (i.e. Chapter (3) and Chapter (5)) this quantity corresponds to the local (1D or 2D) phase  $\phi(x, z)$  or  $\phi(x, y)$  of the image structures (e.g. fringes). On the other hand the fringes are encoding and representing the spatial shape of the wave and are therefore a measure for the phase of the EM-field.

■ Orientation:

For image processing besides amplitude and phase also the orientation  $\beta(x, y)$  of a structure  $f(x, y)$  represents a relevant quantity for description. The orientation can be interpreted [1], closely related to the gradient of  $f(x, y)$ , as the direction of the gradient. Hence, the orientation of a structure in a 2D domain is given as

$$\beta(x, y) = \arctan\left(\left(\frac{\partial f(x, y)}{\partial y}\right) / \left(\frac{\partial f(x, y)}{\partial x}\right)\right), \quad (3)$$

in every point  $(x, y)$ , where  $f(x, y)$  is differentiable. In this representation the *orientation*  $\beta$  represents an unoriented direction mapped into a interval of the length of  $\pi$ . In contrast, the term *direction* expresses an oriented direction mapped into a the interval of the length of  $2\pi$ . Where it is necessary to indicate this difference, which is question of the sign, we denote *orientation* with  $\beta_\pi$  and *direction* with  $\beta_{2\pi}$ .

Note: In practice an orientation estimation by means of the gradient is mostly impracticable, but a more robust estimation, based on statistical approaches or least-square methods, has to be chosen.

- Amplitude and phase objects:

Considering an object in the propagation path we can characterize this object by its complex-valued transmission function

$$u(x, y) = a(x, y) \exp(i\phi(x, y)). \quad (4)$$

The amplitude  $a$  expresses the attenuation of the wave by absorption, and the argument  $\phi$  describes the phase shift of the wave field caused by the object. Objects with  $0 < a < 1$  and  $\phi = 0$  are denoted as amplitude objects, whereas objects introducing no absorption ( $a = 1$ ) and only changing the phase of light according to its phase function  $\phi$  represent phase-only objects. Real phase objects exhibit a small absorption compared to the introduced phase shift.

In a general context the total phase change  $\Delta\phi(x, y) = \phi(x, y, z) - \phi_0(x, y, z_0)$  caused by the specimen can be seen as a measure for its geometrical thickness (geometrical path length) profile  $\Delta d_H(x, y)$  relative to the reference position ( $z = z_0$ ) and for its distribution of the refractive index difference  $\Delta n(x, y)$  related to the refractive index  $n_0$  of the surrounding medium, both expressed by the optical path length (OPL) map  $\vartheta(x, y)$  with

$$\Delta\phi(x, y) = k_0 \vartheta(x, y) = \frac{2\pi}{\lambda_0} \int_{z_0}^{d_H} \Delta n(x, y, z) dz, \quad (5)$$

with the wave number  $k_0 = \frac{2\pi}{\lambda_0}$ , and the vacuum wavelength  $\lambda_0$ .

As the refractive index depends on the sample structure itself, but also on internal state quantities as temperature, pressure, concentration, these parameters can be visualized indirectly by phase-sensitive imaging techniques.



# Thesis Structure

This thesis is structured as follows:

- Chapter 1:

Our motivation for the topic of phase-based imaging and phase reconstruction in microscopy and interferometry illustrating the broad range of options is provided for the reader.
- Chapter 2:

A survey about current phase contrast microscopy techniques is given. Their physical principles and their relation to Fourier plane filtering and interferometric microscopy are briefly explained, and their potential and limitations for quantitative phase measurements and analysis are regarded. Furthermore, elements comparable to our realized phase-sensitive optical coherence tomography (OCT) setups are highlighted.
- Chapter 3:

The mathematical fundamentals for 1D and 2D demodulation based on analytic signal theory are described. Additionally, a comparison of different generalizations of Hilbert transform in higher dimensions is drawn. The single fringe analysis and demodulation methods, which have already been established for conventional interferometry, are tested by us for different types of wave shapes extending the usual way of consideration about harmonic wave shape signals. The influence of non-perfect wave shapes and background on the demodulation results is demonstrated by simulations, which are related to measuring artifacts of real-world applications. Improvements in decreasing the resulting erroneous nonlinearities in phase are discussed shortly.
- Chapter 4:

Intensity-based optical coherence tomography (OCT) imaging, the imaging principles, and the signal generation in OCT as low-coherence interferometric technique are discussed. Imaging parameters describing the resolution of OCT imaging setup are shortly considered.
- Chapter 5 and 6:

Phase-sensitive OCT techniques, in particular, polarization-sensitive OCT (PS-OCT) and differential phase contrast OCT (DPC-OCT) are regarded. Two optical phase-sensitive OCT setups are demonstrated that have been developed or modified, and their phase-sensitive measurement principles are explained. The potential and limitations of DPC-OCT for quantitative phase evaluation and the potential and limitations of PS-OCT for the analysis of

derived quantities as birefringence and stress in a spatially resolved way are considered for different investigated test samples.

Furthermore, a signal and noise model based on complex speckle noise for PS-OCT is derived, which is used in combination with an inherent stress model as a basis for PS-OCT image simulations. These simulations and measured PS-OCT data are used to demonstrate the reconstruction approach based on 2D demodulation techniques in combination with image preprocessing methods.

With respect to DPC-OCT the similarities and differences in imaging and reconstruction to (conventional) DIC microscopy are regarded and exemplified with the measured and investigated samples.

■ Chapter 7:

In conclusion to our measurements and reconstruction results we give a summary about the impact, advantages and limitations of the realized phase-sensitive OCT imaging and reconstruction methods. An outlook onto newly upcoming phase-sensitive or phase-modulating imaging techniques applicable for sophisticated 3D microstructure investigation and material research, their potential extensions of coherent imaging techniques and the expected potential for a combination of coherent imaging techniques with modern mathematical techniques in the field of signal processing are finally presented.



# Chapter 1

## Introduction

Although we are living in the age of nano-structures, in daily life and for several technical applications the size range of the structures of interest is still at the *micron scale*. The increasing demand of industry for new functional materials requires appropriate methods for material characterization and inspection. Imaging methods working in the mesoscopic size range of a few micrometers provide a valuable extension of nanoscopic investigation methods for material and tissue characterization.

In the past the needs in the field of medicine and biology have undoubtedly influenced the development of appropriate imaging techniques for microobjects, e.g. cellular structures or tissue sections. Nowadays the driving forces behind the development and enhancement of appropriate micro-imaging techniques may also be found outside the field of medical application. Often the requirements are closely related to visualization tasks in the field of material sciences. To obtain a better understanding of modern materials, they have to be inspected in several ways for evaluation of their structural composition, their functional behavior or for recognition of possible defects and damage assessment. Especially optical methods, which are non-destructive techniques – enabling contactless measurements, providing information and allowing conclusions about expected functionality – are preferred techniques in various fields of material inspection.

Over the years the imaging modalities for biological or technical microstructures have reached a huge variety, therefore allowing different classification schemes. In particular, as possible classification criteria should be mentioned here:

- *Spectral range:*

With respect to the exploited spectral range the methods can be divided into visible (VIS), near infrared (NIR), X-ray or Terahertz (THz) imaging techniques, and the broad optical bandwidth of light can be used for imaging of the different materials and composites.

- *Dimensionality of data:*

With respect to the number of dimensionality of recorded data (channels) the methods can be grouped e.g. into grayscale, color, multispectral or hyperspectral imaging techniques.

- *Optical sectioning ability and scanning scheme:*

The imaging can be realized by wide-field or confocal techniques, dependent on the regarded probing volume, or as rastering ('flying point') or full-field methods with respect to the corresponding scanning scheme.

- *Contrast mechanism:*

A widespread classification of microscopic imaging techniques is given by the type of the exploited contrast. Due to the electromagnetic (EM) wave nature of light it can be absorbed, reflected, scattered, diffracted, retarded or furthermore, light can itself cause emission or nonlinear interactions inside the sample leading to e.g. fluorescence or higher harmonics generation. Hence, different resulting contrast mechanisms, e.g. linear and nonlinear amplitude, phase, differential phase, structural or chemical contrast, can be exploited for microscopic imaging [2].

Concerning the applied contrast mechanisms, we consider image contrast determined by phase and phase-related properties of the specimen later in the thesis. In microscopic imaging the first choice for imaging of structures is mainly influenced by their absorption or transmission behavior. Conventional transmission microscopy exploits the absorption contrast in general. However, several microbiological specimens, e.g. cells, lipid droplets, but also technical structures, e.g. inhomogeneities in glasses or polymers, organic surface protection coatings, oil films, etc. are often nearly transparent or translucent in the visible spectral range. This optical transparency limits the use of transmission microscopy as phase variations introduced by the specimen can not be recognized directly.

Fluorescence microscopy has become an established method for providing meaningful images of specimens. Although staining of objects with natural markers, pigments in conventional microscopy and with fluorescent dyes in fluorescence microscopy can provide a solution for visualization of transparent specimen, these techniques can not always be applied. Imaging of highly sensitive cellular samples (e.g. living sub-cellular structures) without simultaneously influencing them by chemical substances requires label-free imaging techniques. Therefore *phase-sensitive* and also spectral imaging techniques have never lost their importance. A continuous interest and a further development of these methods are guaranteed even nowadays.

The importance of phase for imaging is combined with the complex nature of light and the human perception system. Light, regarded as electro-magnetic wave can be described by its complex wave field  $\mathbf{E}$  at the spatial position  $\mathbf{r} = (x, y, z)$  and time  $t$ , propagating in a direction  $\mathbf{k}$ . Considering a plane harmonic wave

$$\mathbf{E}(\mathbf{r}, t) = E_0 \exp(i\phi(\mathbf{r}, t)) = E_0 \exp(-i(\omega t - (\mathbf{k} \mathbf{r} + \phi_0))), \quad (1.1)$$

and assuming a wave propagation in  $z$ -direction through a homogeneous medium, by decoupling the temporal and spatial varying term, the harmonic wave field can be described by its complex exponential form as

$$\mathbf{E}(z, t) = E_0 \exp(i\phi(z)) \exp(-i\omega t) \quad (1.2)$$

with the (spatial) phase term  $\phi(z) = n k_0 z + \phi_0$ .

When light propagates through a stained or turbid sample some amount of the light is absorbed or scattered, resulting in a modulation of the wave amplitude relative to the background. The

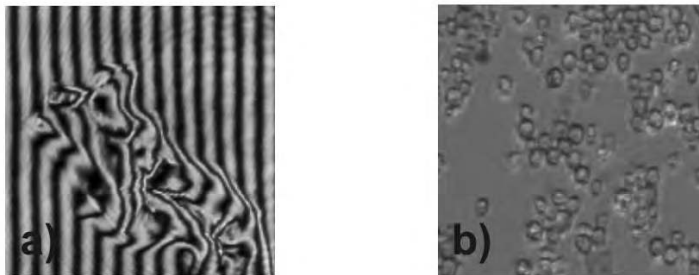


Figure 1.1: Phase-to-intensity mapping. a) Interferometric image showing typical fringe patterns, b) phase contrast image of cellular specimens, [185].

amplitude of the wave field directly determines the intensity  $I$ , the time average of the squared magnitude of the wave field with  $I \propto \langle \mathbf{E} \mathbf{E}^* \rangle_T$ . The phase (difference) is an expression of the position or of the delay of the wave field related to an initial or reference state.

As the human perception system is sensitive to amplitude changes, amplitude contrast is easy to visualize by a direct amplitude-to-intensity transform. However, humans are not able to directly recognize phase changes. In imaging, light waves traversing unstained, transparent objects cause only a faint amplitude contrast and weakly discernible structures, due to scattering and diffraction at the object edges. Even though the amplitude is mainly unchanged, the phase of the light propagating the sample is delayed with respect to the undisturbed phase of the surrounding medium. These phase changes, in the following called phase shifts or phase retardations (with respect to OCT), have to be visualized indirectly and analyzed by different phase-to-amplitude or phase-to-intensity mapping techniques. The mapping can be realized by different *microscopic* and *interferometric* phase imaging techniques. In interferometric images the phase of the wave field is expressed as fringe pattern (i.e. alternating lines of high and low intensity), as depicted in Figure 1.1 a). For phase microscopy mainly phase contrast mechanisms are exploited for the visualization of transparent objects, as shown in Figure 1.1 b).

Various *phase contrast microscopy* (PCM) techniques, e.g. Zernike PCM [3], Hoffmann modulation PCM [4], generalized PCM [5] have been developed over the years. Differential interference contrast (DIC) microscopy [6], imaging the phase gradient, can be considered as a modification of PCM techniques. Also Schlieren imaging can be associated to phase contrast techniques even though it is normally utilized for visualization of larger sized phase structures as appearing e.g. in thermal flow fields or ultrasonic pressure fields [7, 8].

Besides phase contrast microscopy, the extensively exploited field of (micro-)interferometric techniques for testing of transparent objects and determining their refractive index and thickness variations should be mentioned. In interferometric techniques the phase measurement is based on the superposition of a known reference wave with a sample wave having a defined phase relation to each other [9]. By recording multiple phase shifted images or applying single fringe analysis methods the imaged phase distribution can be determined. Combining interferometric principles with digital holographic reconstructions, several digital holographic microscopy (DHM) techniques [10] for the quantitative phase reconstruction of nearly transparent microobjects [11] have been realized in recent years.

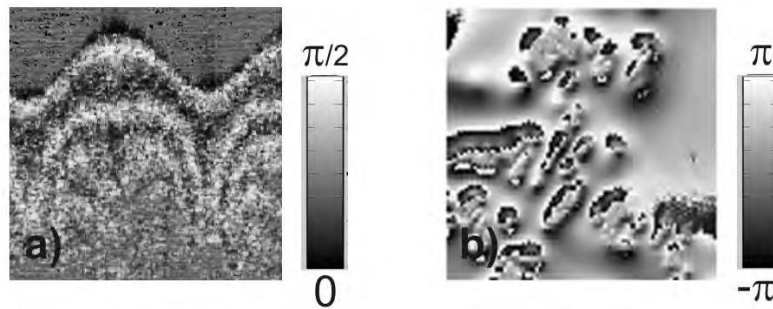


Figure 1.2: Phase-sensitive OCT imaging. a) PS-OCT phase retardation image, b) DPC-OCT differential phase image.

Arising from white light interferometry (WLI) [12] *optical coherence tomography* (OCT) as a low coherence interferometry (LCI) technique was invented in 1991 [13]. Starting first in medical diagnostic fields [14] and applied at the beginning for biological tissue characterization, recently, OCT techniques have been extended and complemented by functional imaging methodologies. Nowadays, OCT is utilized also for various applications in the field of material science. The capability of OCT techniques to recognize embedded microstructure and to investigate stratified specimens in sub-surface regions of the sample can be exploited for various technical material inspection tasks [15]. This potential extension of the exploitable probing range from surface to sub-surface regions gives rise to different imaging applications suitable for the characterization of structures in the size range of some microns.

Similar to microscopy, different contrast mechanism can also be utilized for OCT. Whereas in turbid, highly scattering media imaging is achieved by multiple scattering at randomly distributed point scatterers or layers, in the case of transparent samples phase contrast or differential phase principles can be included. Thereby, additional information about the internal homogeneity or anisotropic composition of the sample can be extracted by the modification of standard OCT to phase- or frequency-sensitive versions. These functional OCT setups, exploiting e.g. polarization dependence, second harmonic generation, or frequency shifts as a probing feature, deliver additional information about the specimens.

In case of polarization-sensitive OCT (PS-OCT) [17] the phase retardation or phase difference allows conclusions about anisotropies, e.g. resulting birefringence, or about stress distribution within the sample. In PS-OCT imaging the anisotropic material behavior causes typical fringe pattern, so-called *phase retardation* fringe patterns, as can be seen in Figure 1.2 a).

In case of differential phase contrast-OCT (DPC-OCT) the optical path length gradient due to thickness or refractive index variations can be extracted [18], as shown for the example in Figure 1.2 b). Furthermore, elastic properties of materials can be determined by means of optical coherence elastography [16].

Over the years a huge variety of different combinations and modifications of phase contrast, conventional interferometric and OCT techniques, partly extended by other contrast mechanisms, have been established leading to e.g. optical coherence microscopy (OCM) [19], nonlinear OCT [20], or molecular OCT [21] techniques.

In the following the regarded phase-sensitive techniques can be distinguished by the specific-

ties of their optical setups: The applied spectral bandwidth and coherence of the illumination source, the light path (common-path as in case of PCM and SPM; sheared-path as in case of DIC and DPC-OCT; amplitude-divided versions as realized in conventional and low coherence interferometry). They can be classified according to the recorded phase-related quantity in total phase, differential phase or phase retardation measuring techniques, differing in their resolution, their optical sectioning properties and measurable phase range. They all represent techniques for imaging phase structures in the micro- and submicrometer range exploiting the various characteristics of interference.

In addition to the demand for sophisticated qualitative visualization techniques for the investigated transparent objects or their derived properties, the need for appropriate mathematical reconstruction approaches has gained importance for an improved *qualitative* or even *quantitative* interpretation of the recorded images. Recognizable efforts have been performed recently in the mathematical field of phase recoveries and reconstruction for quantitative phase microscopy (QPM) [23] based on non-interferometric imaging and reconstruction methods. For interferometric techniques, especially for phase-sensitive transient or dynamic process monitoring, often performed by single shot measurements, some progress has been made in combination with single fringe pattern analysis in recent years [22]. Besides conventional interferometric fringe patterns, as shown in Figure 1.3 a), fringe patterns are also typical image structures for PS-OCT imaging, as depicted in Figure 1.3 b). But generally, fringes can also be found in other fields, as in Moiré and electronic speckle interferometry (ESPI), or in the field of biology (e.g. as finger prints, as shown in Figure 1.3 c), and also in a wider sense as natural 'fringe' patterns, e.g. as tree-rings in dendrochronology).

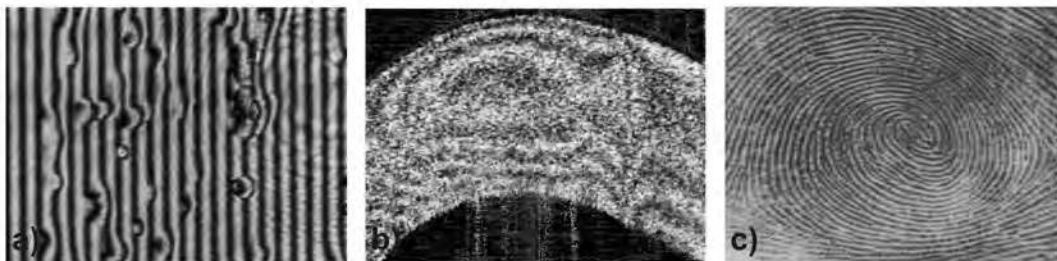


Figure 1.3: Fringe pattern images in different fields of application. a) Fringe pattern recorded by conventional interferometry, b) fringe pattern (retardation fringes) recorded by PS-OCT, c) a finger print as natural 'fringe' pattern.

PS-OCT retardation fringe patterns are challenging and differ from conventional interferometric fringes in some interesting points (e.g. their wave shape, their high amount of speckle noise or their strongly material dependent signal-to-noise ratio (SNR)). Dependent on the material scattering and attenuation properties retardation fringes can be clearly visible or almost be vanishing. Due to these characteristic features a higher complexity for signal analysis results and conventional interferometric analysis methods can not be directly applied for PS-OCT imaging.

In this thesis we present an extended procedure of how approaches of phase contrast microscopy (Chapter (2)) – from the point of view of physics – and of 2D signal analysis and demodulation techniques (Chapter (3)) – from the point of view of mathematics and signal processing – can be combined for phase-sensitive OCT imaging and image reconstruction (Chapters (4) – (6)).

We focus on two phase-sensitive techniques: PS-OCT and DPC-OCT to increase the performance of these techniques towards a spatially resolved quantitative analysis method. For DPC-OCT imaging techniques optical components otherwise applied in phase contrast microscopy (e.g. elements of DIC microscopy) are included in the realized measurement setup. At the same time we demonstrate mathematical approaches suitable for spatially resolved 2D phase reconstruction from measured DPC-OCT images. For PS-OCT imaging the performed signal analysis combines a 2D demodulation scheme with mathematical image enhancing methods. The combination of phase-sensitive imaging with the possibilities of advanced image processing provides the basis for an improved interpretability of the measured data and finally for obtaining quantitative information about the recorded phase-related quantities.

## Chapter 2

# Phase Contrast Microscopy Imaging: State of the Art

In this chapter, first, we want to consider established phase contrast microscopy techniques to explain the basic principles and capabilities for a *quantitative* phase measurement and reconstruction. Second, we demonstrate the connection of PCM to the applied phase-sensitive OCT techniques described in Chapter (4). And third, we highlight the similarities of methods (especially of filtering techniques) applied in optics and in mathematics, in particular, in image processing. But, we also mention their differences thereby.

In the explanation of imaging principles we will focus on (*Zernike*) *phase contrast microscopy* (PCM), the first introduced version of phase contrast microscopy, on *differential interference contrast microscopy* (DIC), a derivative of the original PCM technique and partially comparative to the realized DPC-OCT setup, and on *spiral phase microscopy* (SPM). The interesting correspondence between spiral phase microscopy in optics and spiral phase filtering in signal processing give rise to this choice.

On one hand PCM and interferometric techniques (as conventional or white light interferometry and OCT) often cover different application fields with either biological or technical background. On the other hand they can be considered under the unifying approach of (partially or low) coherent imaging techniques exploiting phase-related quantities for the visualization of the specimen. In Figure 2.1, an imaging example for the three further considered versions of phase contrast microscopy is given.

## 2.1 Conventional phase contrast microscopy

### 2.1.1 Imaging principle in PCM

For classical phase contrast microscopy, developed by Zernike in the 1930's for imaging of almost transparent biological structures [24], it is assumed that the spatial phase changes  $\Delta\phi(x,y)$  introduced by the specimen are small and significantly less than  $\pi/3$  [25]. This basic assumption, denoted as small-scale phase approximation (SSPA), and supposing a specimen being without absorption, allow to expand the complex object function  $u(x,y)$  by Taylor series of the first order

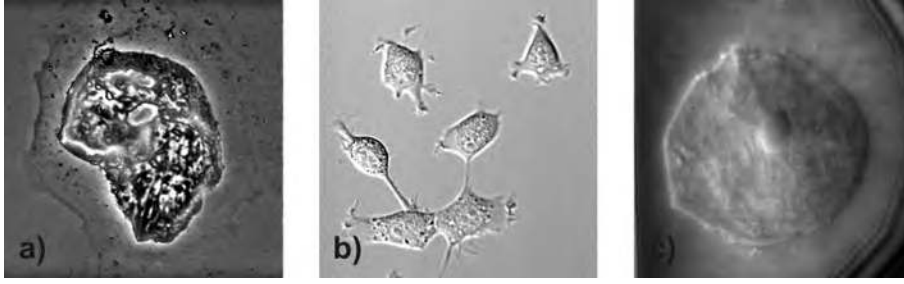


Figure 2.1: Phase contrast imaging examples of almost transparent cellular structures, recorded by a) (conventional) phase contrast microscopy, b) differential interference contrast microscopy, c) spiral phase microscopy, [185].

to

$$u(x, y) = \exp(i\Delta\phi(x, y)) \approx 1 + i\Delta\phi(x, y). \quad (2.1)$$

A light field passing through a phase object is partly diffracted at the phase structures. The undiffracted part of the illumination wave is propagating through the sample without any interaction, the diffracted part is influenced according to the inherent phase distribution of the sample. In (2.1) the first term represents the undiffracted wave component, the so-called zero-order wave, whereas the second term models the diffracted wave component. Zernike has shown that phase contrast can be achieved by differently shifting the diffracted and undiffracted parts, usually by  $\pi/2$  to each other in PCM, with the help of a phase filter in the back-focal plane of the microscope objective.

This imaging principle can be regarded from two points of view: as a common-path interferometry or as a Fourier plane filtering technique.

When interpreting PCM as a common-path interferometer (CPI) [26, 27], the imaging is performed comparable to a conventional interferometer (e.g. to a Michelson interferometer which has been chosen also for the OCT setup). The difference consists in the realized imaging paths: In CPI techniques both wave components, the object wave, carrying the phase information of the sample, and the reference wave, representing the undiffracted component, pass the sample and interfere in the image plane. PCM regarded as CPI technique therefore represents a self-interference method, in contrast to (conventional) OCT techniques where both imaging paths are split. Still both techniques have an interferometric imaging principle in common and are exploiting encoded phase information.

When interpreting PCM using the Fourier plane filtering (FPF) approach the diffraction pattern  $U(\mathbf{k})$  in the back focal plane

$$\mathcal{F}\{u(\mathbf{r})\} = U(\mathbf{k}) = (2\pi)^2\delta(\mathbf{k}) + i\Delta\Phi(\mathbf{k}), \quad (2.2)$$

represents the 2D spectral distribution over all spatial frequencies  $\mathbf{k} = (k_x, k_y)$  of the investigated phase object, which is modified by a so-called Fourier plane filter in this Fourier plane.

The Fourier plane filter (FPF) can be defined by its (generally complex-valued) filter function (or transmission function (TF))  $H(\mathbf{k})$

$$H(\mathbf{k}) = b(\mathbf{k}) \exp(i\theta(\mathbf{k})). \quad (2.3)$$



The factor  $b(\mathbf{k}) \in [0, 1]$  represents the attenuation of the amplitude of the spatial frequencies, and the parameter  $\theta(\mathbf{k}) \in [0, \pi)$  introduces a phase shift between the spatial frequencies.

In the observation plane  $(x', y')$  the phase contrast image  $I(x', y')$  is produced and can be described by

$$\begin{aligned} I(x', y') &\propto u(x', y')u^*(x', y'), & \text{with} \\ u(x', y') &= \mathcal{F}^{-1}(H(k_x, k_y) \mathcal{F}(u(x, y))) & \text{or} \\ u(x', y') &= h(x, y) \otimes u(x, y), \end{aligned} \quad (2.4)$$

with the impulse response function (or point spread function (PSF))  $h(x, y) = \mathcal{F}^{-1}\{H(k_x, k_y)\}$ , based on the correspondence between convolution ( $\otimes$ ) in spatial- and multiplication in Fourier domain.

Although different realizations for phase filtering and illumination schemes can be exploited in PCM, in principle they all can be described by the scheme of (2.4) differing only in the applied filter function. Microscopic imaging techniques as dark field microscopy, spiral phase microscopy or DIC-like phase microscopy imaging [175] may be regarded as modifications of the classical PCM. Their realization by FPF is discussed in the following.

For dark field (index DF) microscopy the undiffracted light component is set to zero in the Fourier plane within a small central region of the FPF (for a given aperture radius  $k_a$ ).

$$H_{DF}(\mathbf{k}) = \begin{cases} 0 & \text{for } |\mathbf{k}| \leq k_a \\ 1 & \text{for } |\mathbf{k}| > k_a, \end{cases} \quad (2.5)$$

In case of Zernike-PCM (index Z) the undiffracted on-axis component is phase shifted by a certain phase amount (usually by  $\pi/2$ ). The corresponding filter function  $H_Z$  can be described [29] by

$$H_Z(\mathbf{k}) = \begin{cases} \exp(\pm i\pi/2) & \text{for } |\mathbf{k}| \leq k_a \\ 1 & \text{for } |\mathbf{k}| > k_a, \end{cases} \quad (2.6)$$

resulting in a filtered diffraction image

$$U_Z(\mathbf{k}) = H_Z(\mathbf{k})U(\mathbf{k}) = \begin{cases} \pm i(2\pi)^2 \delta(\mathbf{k}) \mp \Delta\Phi(0) & \text{for } |\mathbf{k}| \leq k_a \\ i\Delta\Phi(\mathbf{k}) & \text{for } |\mathbf{k}| > k_a \end{cases} \quad (2.7)$$

as derived in detail in [30].

The back-transformed wave field at image plane  $(x', y')$  can be written as

$$u_Z(x', y') = \pm i + i \Delta\phi(x', y'). \quad (2.8)$$

The intensity of the resulting interference image under the assumption of the small-scale phase approximation can be noted as

$$I_Z(x', y') \propto u_Z(x', y')u_Z^*(x', y') \approx 1 \pm 2\Delta\phi(x', y'), \quad (2.9)$$

realizing a *linear* mapping from phase to intensity for small phase shifts. Limited by this approximation PCM can be exploited in a *quantitative* way only for very small phase shifts. Working still in the described linear regime quantitative PCM imaging for technical application fields has been demonstrated recently in [31].

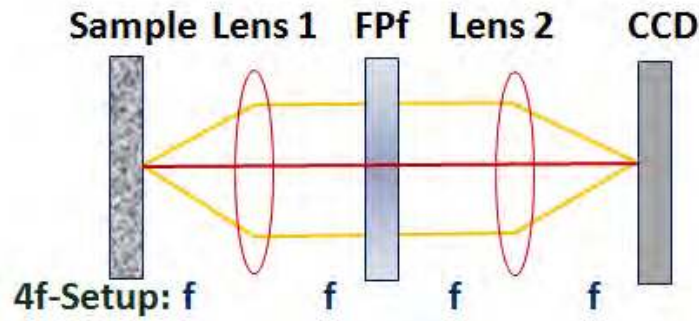


Figure 2.2: Scheme of a 4f-configuration for Fourier plane filtering.

Furthermore phase contrast images often suffer from imaging artifacts, in particular, halo- and shade-off effects, and a *quantitative* evaluation is complicated. To overcome the limitations given by the conventional PCM different approaches have been developed to increase the exploitable phase range for PCM [5]. Recently, a mathematical generalized approach to PCM has been demonstrated in [25] taking into account a higher order expansion of the Taylor series of the object wave field, which allows an extended *quantitative* imaging.

### 2.1.2 Imaging setup for Fourier plane filtering

The above described Fourier plane filtering can optically be realized by means of a so-called 4f-imaging configuration, as sketched in Figure 2.2. The Fourier plane filter (FPf) is used to modify the on-axis part of the undiffracted wave, focused in the central region of the FPf, relatively to the off-axis diffracted wave. The phase object is placed at the object plane  $\mathbf{x} = (x, y)$  and illuminated by the incident plane wave. The object plane is located in the front focal plane of lens L1 with focal length  $f$ . The lens L1 performs the Fourier transform  $\mathcal{F}$  of the imaging wave field. The Fourier plane filter is inserted in the common focal plane (Fourier plane) of both lenses modifying the projected spatial frequency distribution of the phase objects. After optically performing the inverse Fourier transform  $\mathcal{F}^{-1}$  with the second lens L2 the filtered image, showing a modified contrast, can be recorded. The specific design of the apertures (central, angular, point pattern) in PCM will not be considered here, but it should be noticed that the illumination aperture has to correspond to the chosen phase masks of the Fourier plane filter.

## 2.2 Differential interference contrast microscopy

### 2.2.1 Imaging principle in DIC microscopy

DIC microscopy, as a whole-field imaging microscopy technique [32], can be regarded as a derivative of phase contrast microscopy: Zernike PCM measures the phase difference  $\Delta\phi$  between the diffracted and the undiffracted propagating waves. In contrast, in DIC microscopy the phase difference  $\Delta\phi_{\tau}(x, y)$  between the two adjacent wave fields passing the object under a (*shear*) distance

$\tau$ , gives a measure for the phase gradient  $\nabla\phi$  *projected* onto the shear direction  $\mathbf{e}_\tau$ . In a transmission regime the phase gradient also expresses the gradient of the optical path length (OPL)  $\nabla\vartheta$ . Describing the measured phase difference by the projected OPL gradient as

$$\Delta\phi_\tau(x, y) = \frac{2\pi}{\lambda} (\nabla\vartheta(x, y), \tau\mathbf{e}_\tau) + \phi_0, \quad (2.10)$$

and supposing a shear in  $x$ -direction with  $\tau = \Delta x$  yields  $\Delta\phi_\tau(x, y) = \frac{\partial\phi(x, y)}{\partial x} \Delta x$  as the measurable phase-related quantity.

The recorded intensity  $I_{DIC}(x, y)$  can be related to the object transmission function  $u(x, y)$  and especially to the total phase difference  $\Delta\phi(x, y)$ , which is induced by the sample in the wave propagation direction. Following again the FPF approach the image formation can be written (according to (2.4)) as a convolution of the object transmission function with the 2D PSF  $h_{DIC}(x, y)$  of a DIC microscope [33],

$$I_{DIC}(x, y) = I_0 \left| \int_{\Omega} u(\tilde{x}, \tilde{y}) h_{DIC}(x - \tilde{x}, y - \tilde{y}) d\tilde{x} d\tilde{y} \right|^2, \quad (2.11)$$

assuming a (spatially coherent) incident illumination  $I_0$  here. The complex PSF  $h_{DIC}(x, y)$  with an inherent DIC shear  $\mathbf{e}_\tau = (\Delta x, \Delta y)$  can be expressed by [34]

$$\begin{aligned} h_{DIC}(x, y) &= \left( \frac{1}{2} \left[ \exp(-i \frac{\phi_0}{2}) h_\sigma(x - \Delta x/2, y - \Delta y/2) \right. \right. \\ &\quad \left. \left. - \exp(i \frac{\phi_0}{2}) h_\sigma(x + \Delta x/2, y + \Delta y/2) \right] \right), \\ &\text{with } h_\sigma(x, y) \propto \exp(-(x^2 + y^2)/2\sigma_D^2), \quad \sigma_D > 0, \end{aligned} \quad (2.12)$$

where the Gaussian kernel function  $h_\sigma(x, y)$  with the parameter  $\sigma_D$  denotes the approximated PSF of conventional transmission optics and expresses the diffraction limitation in microscopy. In case of a simplified, purely geometric optics model  $h_\sigma(x, y) = \delta(x, y)$  may be supposed. Assuming this geometric optics model for a conventional DIC microscope setup the measured intensity image  $I_{DIC}(x, y)$  can be described with an equation showing the interferometric imaging character of DIC microscopy

$$I_{DIC}(x, y) = I_0 \sin^2(\Delta\phi_\tau(x, y)/2 + \phi_0) = \frac{1}{2} I_0 (1 - \cos(\Delta\phi_\tau(x, y) + \phi_0)). \quad (2.13)$$

Considering phase objects with weak slopes  $\Delta\phi_\tau \ll \pi$ , as commonly can be assumed for cells and flat objects, equation (2.13) can be linearized. For a given bias retardation of  $\phi_0 = \pi/2$  and after removing the DC-component, we obtain a zero-mean DIC intensity image  $I'_{DIC}$

$$I'_{DIC}(x, y) = I_{DIC}(x, y) - \frac{1}{2} I_0 \propto \sin(\Delta\phi_\tau(x, y)) \propto \Delta\phi_\tau(x, y). \quad (2.14)$$

A linear mapping from a *directional phase derivative* (i.e. the phase gradient projected on the shear direction) to *intensity* can be realized for small phase derivatives. This *quantitative* relationship may be exploited for an approximative reconstruction of the phase map for transparent biological samples under the assumption of small phase gradients, as demonstrated recently in [165].

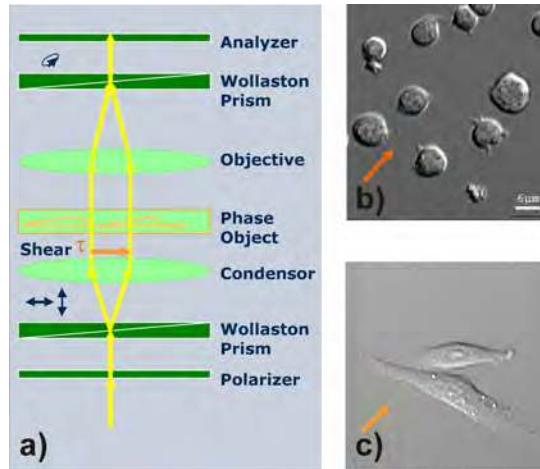


Figure 2.3: Differential interference contrast microscopy. a) Optical DIC microscope setup with indicated wave propagation and polarization directions, b) and c) DIC image of different cell types showing typical differential interference contrast in the diagonal direction, [185].

### 2.2.2 Imaging setup in DIC microscopy

A sketch of the optical DIC microscope setup is depicted in Figure 2.3 a). It contains two *Wollaston prisms* as essential optical elements. The first one performs the splitting and shearing of the incident linear polarized wave field and the second Wollaston prism combines the two wave fields after having passed the investigated transparent sample. The phase object causes a mutual phase shift between the two wave fields interfering after the second Wollaston prism. In general, the phase changes introduced by the specimen result in an elliptic polarization state of the interference signal. The ellipticity, extracted by the second polarizer, gives a measure for the phase difference in shear direction.

Hence, the DIC shear direction  $\mathbf{e}_\tau$ , which is in general diagonal, parallel or orthogonal to the scanning movement, determines the direction of the recorded phase derivative. The shear amount  $\tau$  determines the lateral resolution of the DIC imaging. Additionally the bias retardation  $\phi_0$  may modify the intensity distribution, e.g. a bias  $\phi_0 = \pi/2$  results in a pseudo 3D profile as can be seen in Figure 2.3 b) and c). Hence, the shadow-like appearance of the DIC-imaged specimen is not a result of illumination, but of interference between the two sheared waves.

### 2.2.3 Quantitative imaging in DIC

The question about phase reconstruction from the recorded DIC image is discussed in the field of quantitative DIC microscopy. Two principle ways for phase recovery are followed for quantitative DIC imaging: Approaches which are based on sophisticated optical configurations and mathematically based solution of (at least approximative) reconstruction.

For the general case of arbitrary sized phase objects the approximation of (2.14) is no longer valid. The nonlinear relation between measured intensity and phase or phase derivative of the investigated object has to be taken into account for a *quantitative* reconstruction. Similar to phase stepping methods in conventional interferometry, an optically modified type of DIC microscope is

suggested in [36] to obtain a linear dependence between intensity and differential phase. Therein a geometric phase shifting with optical phase plates (so-called PS-DIC) is demonstrated. Being able thereby to extract the linear phase gradient (by performing the measurements in two orthogonal shear directions and with different phase shifts due to the phase plates) the described PS-DIC technique allows a *quantitative* reconstruction of the OPL distribution of the specimen. However, PS-DIC requires a sophisticated optical setup compared to a conventional DIC microscope.

In [35] a rotational-diversity phase reconstruction approach has been suggested for *quantitative* DIC imaging combining optical and mathematical approaches. The mathematical reconstruction is based on the solution of a Czesars I-divergence minimization problem in case of having multiple rotated DIC scans available.

In conventional DIC microscopy usually only a single DIC scan is available. Being aware that the complete *quantitative* phase information perpendicular to the shear direction is lost for only a single DIC image being available, the phase map can not be fully recovered from a *single* image. But, the phase distribution (or OPL map) can be recovered approximatively in a *quantitative* way assuming weak phase objects and including additionally prior information (e.g. smoothness, positivity, etc.). Simplified reconstruction methods are described in literature, which are based on (iterative) line-integration and deconvolution approaches [159].

Following the principle of conventional DIC imaging and measuring the directional phase derivatives we have adapted DIC imaging methodology for the DPC-OCT imaging setup. The advantage of DPC-OCT imaging over DIC microscopy consists hereby in the linear relationship between the differential phase (or phase gradient) and the measured intensity, therefore being not restricted to small phase differences as in the case of PCM. Hence, additional phase stepping methods or comprehensive numerical reconstruction are not required for quantitative phase reconstruction in DPC-OCT imaging. Furthermore, DPC-OCT exhibits the ability of a depth-resolved *quantitative* phase imaging that can not be realized by means of conventional DIC microscopy, as will be regarded in detail in Chapter (6).

## 2.3 Spiral phase microscopy

### 2.3.1 Imaging principle in spiral phase microscopy

Spiral phase microscopy (SPM), also known as vortex microscopy, and spiral phase filtering (SPF) have found increased interest in last years. The use of SPF in the field of laser beam shaping [37] or for contrast enhancement [38] has been demonstrated. In the context of phase contrast microscopy and interferometry the concept of SPM has been suggested by [39] exploiting the above described concept of Fourier plane filtering, only with a helical phase filter function. Its transmission function  $H_{Sp}(\mathbf{k})$  is described by

$$H_{Sp}(\mathbf{k}) = i \frac{\mathbf{k}}{|\mathbf{k}|} = i \exp(i \Theta), \quad (2.15)$$

with the complex notation for vector  $\mathbf{k} = k_x + i k_y$  and polar angle  $\Theta = \angle \mathbf{k}$ .

In spatial domain the related PSF  $h_{Sp}(\mathbf{r})$  of the spiral phase filter (index Sp) is given by

$$h_{Sp}(\mathbf{r}) = \begin{cases} -\frac{\mathbf{r}}{2\pi r^3} = -\frac{\exp(i \Theta)}{2\pi r^2} & \text{for } r \neq 0 \\ 0 & \text{for } r = 0, \end{cases} \quad (2.16)$$

with  $\mathbf{r} = x + iy$ ,  $r = |\mathbf{r}|$  and the polar angle  $\theta = \angle \mathbf{r}$ . The PSF contains an isotropic radial (index  $r$ ) component  $h_{Sp,r}(r) = -\frac{1}{2\pi r^2}$ , and an angular (index  $\theta$ ) component  $h_{Sp,\theta}(\theta) = \exp(i\theta)$  depending on the angle  $\theta$ .

It should be emphasized that the spiral phase filter (SPF) included in the microscopic imaging system acts as Fourier plane filter on the complex-valued wave field of the propagating light. The image formation itself can be described again by the FPF scheme: Modifying the image contrast by applying the spiral phase filter function  $H_{Sp}(\mathbf{k})$  on the object transmission function. In this optical context the applied SPF can be used e.g. for edge detection, anisotropic structure enhancement [41], or for obtaining a visualization of the transparent sample comparable to the appearance of a phase object imaged by DIC methods [40].

In addition to the pure contrast or edge enhancement ability by (optical) spiral phase filtering, a method for *quantitative* phase imaging of a complex specimen is demonstrated in [42] using three by means of the spiral filter rotationally phase-shifted images for reconstruction.

### 2.3.2 Properties of the spiral phase filter in optics

Some interesting properties of spiral phase filter acting as an optical device should be mentioned already here, and they will appear again in the context of mathematics and signal processing in Chapter (3) by applying spiral phase filtering as a mathematical operation in an analog way.

- Phase filtering by applying a SPF mask represents a phase-only filtering (with exception for the DC component), i.e. the transfer function has a constant unit value of magnitude and only the angular phase  $\Theta$  is changing.
- Although the problem of designing "an isotropic odd 2D filter is not possible in the complex domain" [45], the SPF fulfills a weaker assumption for isotropy and for the required odd-property: The isotropy is fulfilled with respect to performing a 1D HT along each frequency line passing the center, and the transfer function is odd with respect to the sign change along each of these lines.
- The SPF has a singularity in its center for  $r = 0$ , which is of importance for the appearance of the filtered image. Using a programmable, pixelated spatial light modulator (SLM) as phase filter, the central pixel of the SLM can be set at a chosen phase value resulting in different direction of edge enhancement. In case of setting the central pixel to zero it results in isotropic edge enhancement [39].
- The SPF with a transfer function  $H_{Sp}(\mathbf{k}) = \exp(i P \Theta)$  with  $P = 2, 3, \dots$  represents a SPF with higher topological charges  $P$ . Recently SPFs with fractional values of  $P$  have been optically demonstrated [41].

The mathematically corresponding analogon to SPF as optical device is represented by the radial Hilbert transform (RHT), which will be considered in the following chapter in the field of signal analysis. Also in the field of image processing the RHT may be used for isotropic edge enhancement or to extraction of image features as corners and lines [46, 47]. But, applied in image processing the filter acts on the scalar-valued pixel intensity. This leads to slightly different behavior of the filter in image processing with respect to edge enhancement or orientational information extraction.

In Chapter (3) and Chapter (5) we consider the use of vortex filters in the context of monogenic signal theory and for fringe pattern demodulation.

## 2.4 Summary

In this chapter, we have shortly reviewed established phase-contrast based microscopic techniques, their imaging principles based on Fourier plane filtering and their unified representation as interference based, phase-sensitive imaging techniques. We have shown that they can be applied as *quantitative* techniques, but only under additional assumptions about weak phase objects or weak phase gradients or, as in the case of SPM, in combination with phase shifting techniques.

Fourier phase microscopy [48] or Hilbert phase microscopy [49, 50] could provide alternatives for *quantitative* phase imaging and phase-sensitive investigation of microstructures. But, Fourier phase microscopy as a global phase imaging technique with high performance for dynamical phase visualization of transient processes extracts only the total phase shift.

In contrast to phase microscopy the applied phase-sensitive OCT techniques allow a depth-resolved *quantitative* measuring of phase or phase ratios as demonstrated in the thesis for DPC-OCT imaging. PS-OCT as phase retardation imaging technique also enables to determine a cumulative phase resp. retardation representation over the depth direction. Both techniques will be explained in detail in Chapter (5) and Chapter (6).

Finally, it should be mentioned that also non-interferometric *quantitative* phase microscopy imaging and reconstruction methods, are existing [51, 52]. As demonstrated in [23] and recently shown for DIC imaging in [53] the phase reconstruction is performed by solving the so-called transport of intensity equation. Although this method provides an interesting idea for quantitative phase recovery we do not follow this approach in the thesis as the described reconstruction can not be transferred for the intended DPC-OCT setup.





## Chapter 3

# Fundamentals of Analytic Signal Theory

Before phase-sensitive OCT imaging techniques and reconstruction approaches are regarded in Chapter (5) and Chapter (6) as the main item of this thesis, we will introduce in this chapter the mathematical fundamentals which are prerequisites for signal analysis and fringe demodulation, in particular, for PS-OCT imaging. PS-OCT images often exhibit strong fringe patterns, so-called retardation fringe patterns. This type of fringe patterns expresses material inherent properties as birefringence, stress or retardation of the investigated specimen and will be regarded in detail in the following chapter.

Generally, 2D fringes patterns are characterized by their instantaneous phase, instantaneous frequency, local amplitude and local orientation. The extraction of the information encoded by the instantaneous phase, frequency or amplitude of the fringe patterns is the aim of different demodulation techniques. Demodulation techniques based on only a single fringe pattern (in contrast to phase-stepped versions) are called single fringe analysis or demodulation methods. In [43] the term 'natural demodulation' is introduced to this type of 2D signal demodulation in the field of interferometry.

In the mathematical field (i.e. in functional analysis) demodulation techniques are closely related to the analytic signal (or analytic function) theory, to the Hilbert transform delivering the complex extension or quadrature component, and to the monogenic signal theory for extending the analysis to a higher signal dimension.

In this chapter, we want to regard some basic relations valid for *analytic* and *monogenic* signals, different interpretations of the *Hilbert transform* in various contexts, and relate fringe patterns to *single-* and *multi-component* image structures. Furthermore, the conditions for the applicability of the 2D demodulation theory are considered. Additionally *simulations* are performed to explain and to estimate expected deviations and errors from the conventional demodulation scheme. Non-harmonic wave shapes or varying background, being typical effects in real-world PS-OCT imaging, are taken into account.

## 3.1 Image structures

### 3.1.1 Classification of image structures

Considering (grayscale) images represented as 2D functions  $f(x, y) \in \mathbb{R}$  we can classify the recorded image structures e.g. into structures at certain scales [54], into deterministic or random structures describing statistical properties of the observed specimen (e.g. material scattering or noise), or into structures requiring different degrees of freedom for description. Regarding image structures in a local neighborhood of  $(x, y)$  we can distinguish e.g. between local areas of constant intensity, edges, lines, junctions of lines or point patterns.

Classifying in general 2D image structures according to the degree of freedom [55], or correspondingly according to their local spectrum and following the definition of [56], the structures can be schematized into:

- Locally intrinsic zero-dimensional ( $i0D$ ) patterns (with a spectrum concentrated in the origin), representing a constant intensity value,
- Locally intrinsic one-dimensional ( $i1D$ ) patterns (with a spectrum concentrated in a single line through the origin), representing lines, edges or sinusoidal waves,
- Locally intrinsic two-dimensional ( $i2D$ ) patterns (with a spectrum not concentrated on a single line), representing e.g. crossing lines and junctions, corners or spots.

The image structures are called 'simple' if they can be described in a local neighborhood as a pattern with one single orientation, e.g. the signal is mainly varying only in one direction. We will model retardation fringes in Chapter (5) as being simple  $i1D$  structures in a local neighborhood.

### 3.1.2 Characterization of image structures

Images structures may be characterized by different quantities, e.g. by their intensity ( $I$ ), scale ( $\xi$ ), orientation ( $\beta$ ), but they also can be described by their local *phase*  $\phi$  or instantaneous *frequency*. E.g. edges (step function) and lines are not only a transition of intensity (i.e. they are not only characterized by e.g. their intensity gradient exceeding a given threshold), but they are also characterized by their local phase, having e.g. at edges the highest phase congruency (i.e. all Fourier modes are having the same phase state (modulo  $2\pi$ ) according to the definition given in [57]). These phase-related interpretations of structures and patterns require a different understanding of the image, what will be explained in the following.

Assuming that an arbitrary image may be described as a (real-valued) signal in the form of  $f(\mathbf{x}) = a(\mathbf{x}) \cos(\phi(\mathbf{x}))$ , in general we can not suppose simultaneously smooth functions for  $a(\mathbf{x})$  and  $\phi(\mathbf{x})$ . Hence, there results an infinite number of possible solutions for decomposing the signal  $f(\mathbf{x})$  into  $a(\mathbf{x})$  and  $\phi(\mathbf{x})$ . However, by additional constraints supposing e.g. smoothness of  $a(\mathbf{x})$  and  $\phi(\mathbf{x})$  and positivity of  $a(\mathbf{x})$  we can restrict the number of solutions. But by conditioning smoothness, a solution need not to exist in the single-component representation. Therefore, an

arbitrary image has to be represented as a *multi-component* (index MU) signal [58]:

$$f_{MU,R}(\mathbf{x}) = \sum_{m=1}^M f_m(\mathbf{x}) = \sum_{m=1}^M a_m(\mathbf{x}) \cos(\phi_m(\mathbf{x})), \quad (3.1)$$

$$\text{with } f_{MU,R} : \mathbb{R}^n \rightarrow \mathbb{R}, a_m : \mathbb{R}^n \rightarrow (0, 1], \phi_m : \mathbb{R}^n \rightarrow \mathbb{R}.$$

The signal  $f_{MU,R}$  can be considered as the real part of the in generally complex-valued multi-component signal

$$f_{MU}(\mathbf{x}) = \sum_{m=1}^M f_m(\mathbf{x}) = \sum_{m=1}^M a_m(\mathbf{x}) \exp(i \phi_m(\mathbf{x})), \quad (3.2)$$

$$\text{with } f_{MU} : \mathbb{R}^n \rightarrow \mathbb{C}, a_m : \mathbb{R}^n \rightarrow (0, 1], \phi_m : \mathbb{R}^n \rightarrow \mathbb{R}.$$

First we want to assume, similar to [58], a complex-valued signal modeled as a multi-component signal  $f_{MU}(\mathbf{x})$  by superposition of (globally) spatially varying, but locally coherent *single-component* signals  $f_m(\mathbf{x})$

$$f_m(\mathbf{x}) = a_m(\mathbf{x}) \exp(i \phi_m(\mathbf{x})); \quad \mathbf{x} \in \mathbb{R}^n. \quad (3.3)$$

The single-component signals are characterized by their smooth instantaneous amplitude function

$$a_m(\mathbf{x}) = |(f_m(\mathbf{x}))|, \quad (3.4)$$

a smooth instantaneous phase function

$$\phi_m(\mathbf{x}) = \angle(f_m(\mathbf{x})), \quad (3.5)$$

and an instantaneous frequency function

$$\mathbf{w}_m(\mathbf{x}) = \frac{\partial(\phi_m(\mathbf{x}))}{\partial \mathbf{x}}. \quad (3.6)$$

Furthermore, it should be remarked that the phase definition of (3.5) assumes a scalar interpretation of the phase. In connection with monogenic signal theory we will introduce a vector-related definition of the local phase for 2D signals. Furthermore, it has to be mentioned that also a 2D phase interpretation based on quaternionic signal analysis may be used for description of image structures [59]. Here, we want to suppose a signal being locally narrowband (i.e. signals with an amplitude and frequency that do not vary too rapidly) and being coherent (i.e. signals, whose structure is retaining over several length scales).

For fringes in PS-OCT retardation images it would be almost fulfilled, at least regarding a small neighborhood region and neglecting the noise. By performing a previous preprocessing for noise removal and a background correction the number of components may be decreased. Then, for a local region we can assume approximatively that one spatially frequency is dominant or can be extracted e.g. after a preceding bandpass filtering exploiting prior knowledge about the expected signal frequency spectrum.

However, if we consider fringes as 2D spatially varying signals (similar to the 1D case of instationary signals in case of temporal signals) over a larger image region the filtering would require a local adaptation, e.g. an adaptive bandpass filtering by windowed Fast Fourier Transform (FFT) methods. Especially, if the multi-component signal contains a dominant component superposed by a slowly varying second instationary signal component (as would result e.g. from a local non-zero mean background) the filtering becomes difficult. A time-frequency analysis for decomposition of the composed signal into its different signal modes (i.e. dominant signal, background and noise) would be required to determine interpretable phase values.

### 3.1.3 Decomposition and analysis of image structures

#### 3.1.3.1 Fourier and Hilbert spectral analysis methods

Fourier spectral analysis methods as short time FFT (SFFT) or Wigner-Ville distribution methods [60] are established techniques for signal decomposition and instantaneous frequency estimation. But, they represent a computationally expensive procedure, which is not followed by us.

As an alternative to usual Fourier spectral analysis methods we consider Hilbert spectral analysis methods. Therein no longer a decomposition of the signal by assuming constant coefficients  $a_m$  and frequencies  $\mathbf{w}_m$  is applied, but considering  $a_m(\mathbf{x})$  and  $\mathbf{w}_m(\mathbf{x})$  as functions. This concept allows to find a suitable and interpretable decomposition for instationary or spatially varying signals.

$$f(\mathbf{x}) = \sum_m a_m(\mathbf{x}) \exp(i \int \mathbf{w}_m(\mathbf{x}) d\mathbf{x}), \quad (3.7)$$

Based on Hilbert spectral analysis the empirical mode decomposition (EMD) can be derived as a possibility for an adaptive signal decomposition as recently demonstrated in [61]. The concept of EMD for instantaneous frequency and phase estimation is briefly regarded in the following.

#### 3.1.3.2 Empirical mode decomposition

Empirical mode decomposition (EMD) techniques may be used for the analysis of multi-component signals to obtain a meaningful interpretation of their local phase and frequency with respect to their single components. Suggested by [62] as an adaptive, data driven technique it allows a representation of the instationary, multi-component signal as sum of zero-mean instationary single-component signals (called intrinsic mode functions (IMF)) and a remaining low-frequency residual function. The IMFs are resulting from the inherent data structures. An IMF can easily be characterized by its two properties: [63]

- The number of extrema and the number of zero crossings must either be equal or differ at most by one over the whole data set.
- The mean value of both envelopes defined by either the local maxima and local minima is zero at any point.

This original 1D concept (for instationary signals) can be extended to higher dimensional signals (for spatially varying signals) in an analog way. In particular, it may be realized as bi-dimensional EMD (BEMD) method [64], which is applicable for decomposition of 2D AM-FM image structures. For the BEMD a suitable 2D method for the computation of the maxima/minima envelopes is required. We follow the approach in [64] using a Delaunay triangulation and a cubic spline interpolation on the resulting triangles for the maximum/minimum-envelope computation.

In case of bandpass filtering being insufficient for preprocessing of fringe patterns we apply the EMD method for the estimation of the locally varying non-zero mean background. The background is estimated hereby as the sum of the low-frequency IMFs and the residual of the decomposition (the degree of decomposition has been tested empirically by us). Finally, a local zero-mean signal with a locally dominant frequency can be obtained which is exploitable for quadrature computation and demodulation, see Section (3.4).

In the following, after performing a bandpass filtering or EMD as preprocessing, we suppose the functions  $f(\mathbf{x})$  as zero-mean, locally coherent (narrowband)  $i1D$  signals, for which analytic or monogenic signal theory successfully can be used for the extraction of their local phase, frequency or energy.

## 3.2 1D Analytic signal

The analytic signal definition of a real-valued 1D signal as complex-valued 1D signal representation was introduced by Gabor in 1946 [65]. Since that time analytic signal theory has developed to a well established approach in signal processing for instantaneous phase and frequency estimation. Based on analytic signal theory various demodulation techniques find their wide-spread use e.g. in communication technology [66, 67], for Laser-Doppler velocimetry [68] or in ultrasound applications [69].

The analytic signal theory is closely related with the Hilbert transform (HT).

Considering the function  $f(x) \in \mathbb{R}$  of the real-valued variable  $x$  a complex-extended signal  $f_A \in \mathbb{C}$  whose imaginary part can be determined by the Hilbert transform of the real signal part  $f(x)$

$$f_A(x) = f(x) + i \mathcal{H}\{f(x)\} = f(x) + i f_H(x), \quad (3.8)$$

is called the analytic signal [70].  $\mathcal{H}$  denotes the 1D Hilbert transform operator. The HT is mathematically defined as a linear mapping between two sets of functions  $\mathcal{H} : \mathbb{R} \rightarrow \mathbb{R}$  with

$$f_H(x) = \mathcal{H}\{f(x)\} = -\frac{1}{\pi} \int_{-\infty}^{\infty} \frac{f(\eta)}{\eta - x} d\eta = \frac{1}{\pi x} \otimes f(x). \quad (3.9)$$

It can be represented in the Fourier domain as

$$\mathcal{H}\{f(x)\} = -\mathcal{F}^{-1}\{i \operatorname{sgn}(\nu) \mathcal{F}\{f(x)\}\}, \quad (3.10)$$

with the transfer function  $H(\nu) = -i \operatorname{sgn}(\nu) = \exp(\pm i \frac{\pi}{2})$ . Hence, the HT acts as a filter function, shifting the Fourier phase of all spectral components by  $\pm \frac{\pi}{2}$  depending on the sign of the spectral component.

The 1D Hilbert transform (3.9) as a well-known integral transform is characterized by the following properties with respect to its transfer function  $H$ :

- Antisymmetry:  $H(\nu) = -H(-\nu)$
- Unit energy:  $|H(\nu)| = 1, \quad \forall \nu \neq 0$
- Suppression of DC component:  $H(0) = 0$

The analytic signal is characterized by an one-sided spectrum containing only zero-valued components on the left side of the Fourier spectrum  $F(\nu)$ , i.e. all Fourier coefficients are vanishing for  $\nu < 0$ .  $f_A(x)$  can be derived by removing all negative frequency components in the Fourier spectrum of the real signal  $f(x)$ .

Extending the analytic signal to the complex analytic function  $f_A(\zeta) = f_R(\zeta) + i f_I(\zeta)$  of the complex variable  $\zeta = \chi + i \varsigma$  defined in the upper half plane  $\Omega_C^+ = \{(\chi, \varsigma) : \chi \equiv x, \varsigma > 0\}$  (including the real axis as boundary), both components  $f_R(\zeta)$  and  $f_I(\zeta)$  have to satisfy the Cauchy-Riemann system

$$\frac{\partial f_R(\zeta)}{\partial \chi} = \frac{\partial f_I(\zeta)}{\partial \varsigma} \quad (3.11)$$

$$\frac{\partial f_R(\zeta)}{\partial \varsigma} = -\frac{\partial f_I(\zeta)}{\partial \chi}. \quad (3.12)$$

Being  $\zeta$  inside a closed contour  $\mathcal{L} \in \Omega_C^+$ ,  $f_A(\zeta)$  can be expressed according to Cauchy's definition [71] as

$$f_A(\zeta) = \frac{1}{2\pi i} \int_{\mathcal{L}} \frac{f_A(\zeta')}{\zeta' - \zeta} d\zeta'. \quad (3.13)$$

Restricting the analytic function at the real axis  $f_A(\zeta) = f_A(\chi, 0)$  the analytic signal of the real variable  $x$  as a complex function can be derived in the limit. The boundary values  $f_R(\chi, 0)$  and  $f_I(\chi, 0)$  are related by

$$f_A(x) = f_A(\chi, 0) = f_R(\chi, 0) + i f_I(\chi, 0) = f_R(\chi, 0) + i \mathcal{H}\{f_R(\chi, 0)\}, \quad (3.14)$$

where  $f_I(\chi, 0)$  represents the 1D Hilbert transform of  $f_R(\chi, 0)$ . The mutual relation between  $f_R$  and  $f_I$  can be expressed using Cauchy principal value notation ( $Pf$ ) as [71]

$$f_I(\chi, 0) = -\frac{1}{\pi} P \int_{-\infty}^{\infty} \frac{f_R(\eta, 0)}{\eta - \chi} d\eta \quad (3.15)$$

$$f_R(\chi, 0) = \frac{1}{\pi} P \int_{-\infty}^{\infty} \frac{f_I(\eta, 0)}{\eta - \chi} d\eta, \quad (3.16)$$

with  $\chi = x$  resulting in (3.9).

Regarding these relations from the point of view of system theory equations (3.15) and (3.16) are representing the mutual dependence of real and imaginary component of the system transfer function. Considering them from point of view of optics they deliver the well-known Kramers-Kronig relations, characterizing e.g. the dispersion dependence of complex susceptibilities in materials. From the mathematical point of view they are applied to deliver the complex extension of real-valued functions.

The fundamental importance of the 1D analytical signal representation is related to the possibility to decompose the 1D signal information into its *local amplitude* as modulus and into its *local phase*  $\phi_A(x)$  as argument of the complex-valued analytic signal with

$$A_A(x) = \text{abs}(f_A(x)) = \sqrt{f(x)^2 + \mathcal{H}(f(x))^2} \quad (3.17)$$

$$\phi_A(x) = \arctan \frac{\mathcal{H}(f(x))}{f(x)}. \quad (3.18)$$

This decomposition, denoted as so-called "split of identity" [47] of signal information, allows to independently extract information about local energy and local phase of the signal. Signal energy is related with local amplitude (i.e. amplitude and energy are mutually variant quantities) and the

local structure of the signal is related with local phase (i.e. amplitude and phase being invariant quantities). This so-called invariance-equivariance principle is fulfilled by decomposing the signal content into its energetic and structural component by means of the HT as demonstrated in [45]: The energetic information varies solely with the amplitude, whereas changes in signal structure find their expression in the local phase.

### 3.3 2D Monogenic signal

Applications of higher dimensional functional analysis in the field of image processing e.g. phase-based discrimination between lines and edges, 2D demodulation of arbitrary interferometric signals or phase-based fingerprint [72] and texture analysis [73] require a generalization of the 1D Hilbert transform to higher dimensions (in particular to 2D signals).

Regarding such real-world problems, the extension of the analytic signal definition to higher dimensions results in a generalized 2D analytic image representation [74] and later, in the monogenic signal and monogenic scale space theory [77] combined e.g. with quaternionic signal and wavelet approaches [45, 78].

We want to apply the analytic signal theory for demodulation of our measured 2D PS-OCT fringe patterns, so higher dimensional approaches for analytic functions are considered by us with respect to the intended 2D phase retardation and stress reconstruction, performed on real data in Chapter (5). Here, in Section (3.4), the influence of the different wave shapes and of varying background on phase and frequency recovery will be regarded at first on simulated 2D signals.

As in literature various understandings and interpretations of the 2D Hilbert transform exist, differing with respect to the regarded symmetry, to the applied algebra (complex, quaternionic, geometric algebra), a short overview about used definitions for the 2D Hilbert transform is given briefly in the following, according to [71, 45, 74].

#### 3.3.1 Hilbert transform approaches in 2D

The property of antisymmetry of the 1D HT operator in Fourier domain poses the question about the applied symmetry type in 2D applications: Line symmetry or point symmetry, resulting in directional (half-plane symmetric) definitions or radial approaches for the HT.

- **Line symmetry**

*Partial Hilbert transform*

with respect to the direction  $\mathbf{e}_n$  is defined as:

$$f_{H_p}(x, y) = \mathcal{H}\{f(x, y)\} = \frac{\delta(\mathbf{x} \times \mathbf{e}_n)}{\pi \mathbf{x} \mathbf{e}_n} \otimes f(x, y). \quad (3.19)$$

The equation (3.19) can be regarded as one-dimensional linewise convolution along the direction  $\mathbf{e}_n$ .

In case of  $\mathbf{e}_n$  being the  $x$ - or  $y$ -direction, (3.19) results in

$$\begin{aligned} f_{H_p}(x, y) &= \frac{\delta(y)}{\pi x} \otimes f(x, y), \\ f_{H_p}(x, y) &= \frac{\delta(x)}{\pi y} \otimes f(x, y). \end{aligned} \quad (3.20)$$

In the following the HT according to (3.19) and (3.20) is denoted as directional HT (dHT). We will regard this approach and apply the dHT on 2D signals and images in comparison with radial interpretations, but (3.19) remains intrinsically an one-dimensional method (*i*1D dHT).

*Total Hilbert transform*

with respect to the  $x$  and  $y$  axis is defined as:

$$f_{H_T}(x, y) = \mathcal{H}\{f(x, y)\} = \frac{1}{\pi xy} \otimes f(x, y). \quad (3.21)$$

Combining partial and total HT yields the complex HT. However, all these definitions of HT are performed with respect to a preferred direction and can not represent an isotropic approach.

#### ■ Point symmetry

*Radial Hilbert transform (RHT)*

$$\mathbf{f}_R(x, y) = \mathcal{H}_R\{f(x, y)\} = \mathbf{h}_R(x, y) \otimes f(x, y) = -\frac{1}{2\pi(x^2 + y^2)^{3/2}} \begin{bmatrix} x \\ y \end{bmatrix} \otimes f(x, y), \quad (3.22)$$

or expressed in Fourier domain as

$$\mathbf{F}_R(\mathbf{v}, \mathbf{v}) = \mathbf{H}_R(\mathbf{v}, \mathbf{v}) F(\mathbf{v}, \mathbf{v}). \quad (3.23)$$

The transfer function  $\mathbf{H}_R(\mathbf{v}, \mathbf{v})$  is given by the Fourier representation of the convolution kernel  $\mathbf{h}_R(x, y)$  as

$$\mathbf{H}_R(\mathbf{v}, \mathbf{v}) = \frac{i}{\sqrt{(\mathbf{v}^2 + \mathbf{v}^2)}} \begin{bmatrix} \mathbf{v} \\ \mathbf{v} \end{bmatrix} = i \frac{\mathbf{u}}{\|\mathbf{u}\|}. \quad (3.24)$$

The kernel  $\mathbf{h}_R$  can be split into its radial and angular component:

$$\mathbf{h}_R(r, \theta) = h_{Rr}(r) \mathbf{h}_{R\theta}(\theta) = -\frac{1}{2\pi r^2} \exp(i \theta), \quad (3.25)$$

or in Fourier domain as

$$\mathbf{H}_R(R, \Theta) = H_{Rr}(R) \mathbf{H}_{R\theta}(\Theta) = i \exp(i \Theta), \quad (3.26)$$

with an angular component describing – both in spatial and Fourier domain – a spherical harmonics, in the context of optics often denoted as vortex or spiral phase filter.

The RHT can be considered as (complex) analogue to the Riesz transform as defined next in (3.27), however staying in the complex-valued signal space. Hence, the three characteristic 2D image signal features: Amplitude, phase and orientation can not be decoupled independently by the RHT. Therefore, an additional orientation estimation is required.



### 3.3.2 Riesz transform

Switching from the complex space to the space  $\mathbb{R}^3$  spanned by the orthonormal basis vectors  $(\mathbf{e}_1, \mathbf{e}_2, \mathbf{e}_3)$ , and considering a quaternionic algebra  $\mathbb{Q}$  with  $\{1, i, j, k\}$ , in which  $\mathbb{R}^3$  is embedded as sub-space, a 3D representation of the signal can be derived by  $\mathbf{f}(\mathbf{x}) = f_1(\mathbf{x}) \mathbf{e}_1 + f_2(\mathbf{x}) \mathbf{e}_2 + f_3(\mathbf{x}) \mathbf{e}_3$  (instead of previously complex algebra  $\mathbb{C}$  with  $\{1, i\}$ ).

Introducing  $\mathbf{x} = ix_1 + jx_2 + x_3$  and  $\mathbf{u} = iu_1 + ju_2 + u_3$  and identifying  $f_3\mathbf{e}_3$  with the real-valued component  $f(x, y)$ ,  $f_1\mathbf{e}_1$  with  $i$ -valued and  $f_2\mathbf{e}_2$  with  $j$ -valued component,

the Riesz transform (RT)  $\mathcal{R}_{\mathcal{L}}$ , partially also denoted as spherical Hilbert transform [76], can be described as [75]

$$\mathbf{f}_{\mathbf{RI}}(\mathbf{x}) = \mathcal{R}_{\mathcal{L}}\{f(\mathbf{x})\} = \mathbf{h}_{\mathbf{RI}} \otimes f(\mathbf{x}) = -(i, j) \frac{\mathbf{x}}{2\pi \|\mathbf{x}\|^{3/2}} \otimes f(\mathbf{x}) = (if_1(\mathbf{x}), jf_2(\mathbf{x})). \quad (3.27)$$

The representation in Fourier domain is given as

$$\mathbf{F}_{\mathbf{RI}}(\mathbf{u}) = \mathcal{F}\{\mathbf{h}_{\mathbf{RI}} \otimes f(\mathbf{x})\} = \mathbf{H}_{\mathbf{RI}}(\mathbf{u})F(\mathbf{u}) = -(i, j)i \frac{\mathbf{u}}{\|\mathbf{u}\|} F(\mathbf{u}) = (1, k) \frac{\mathbf{u}}{\|\mathbf{u}\|} F(\mathbf{u}), \quad (3.28)$$

with notation  $(i, j)\mathbf{x} = ix_1 + jx_2$ , and  $(1, k)\mathbf{u} = u_1 + ku_2$ .

Applying the Riesz-transform on  $f(x, y)$  allows the definition of the monogenic signal  $\mathbf{f}_{\mathbf{M}}(x, y) \in \mathbb{Q}$  as a vector-valued signal representation according to [45] with

$$\mathbf{f}_{\mathbf{M}}(x, y) = f_3(x, y) + i f_1(x, y) + j f_2(x, y) = f(x, y) + \mathbf{f}_{\mathbf{RI}}(x, y) = f(x, y) - (i, j)\mathbf{f}_{\mathbf{R}}(x, y), \quad (3.29)$$

and the corresponding Fourier representation  $\mathbf{F}_{\mathbf{M}}(\mathbf{v}, \mathbf{v})$  is given by

$$\mathbf{F}_{\mathbf{M}}(\mathbf{v}, \mathbf{v}) = F(\mathbf{v}, \mathbf{v}) + \mathbf{F}_{\mathbf{RI}}(\mathbf{v}, \mathbf{v}) = F(\mathbf{v}, \mathbf{v}) - (i, j)\mathbf{F}_{\mathbf{R}}(\mathbf{v}, \mathbf{v}). \quad (3.30)$$

The monogenic signal  $\mathbf{f}_{\mathbf{M}}$  is characterized by its three independent sizes [45]: Local amplitude  $A_{\mathbf{M}}(x, y)$ , local phase  $\phi_{\mathbf{M}}(x, y)$  and local orientation  $\beta_{\mathbf{M}}(x, y)$  with

$$A_{\mathbf{M}}(x, y) = \sqrt{f^2(x, y) + |\mathbf{f}_{\mathbf{RI}}(x, y)|^2}, \quad (3.31)$$

$$\phi_{\mathbf{M}}(x, y) = \arg(\mathbf{f}_{\mathbf{M}}(x, y)) = \mathbf{e}_{\mathbf{M}} \arctan \left( \frac{\sqrt{f_1^2(x, y) + f_2^2(x, y)}}{f(x, y)} \right), \quad (3.32)$$

$$\beta_{\mathbf{M}}(x, y) = \arctan \left( \frac{f_2(x, y)}{f_1(x, y)} \right), \quad (3.33)$$

$$\text{with } \mathbf{e}_{\mathbf{M}} = \frac{(0, 0, 1)^T \times \mathbf{f}_{\mathbf{M}}}{|\mathbf{f}_{\mathbf{M}}|}.$$

It should be mentioned that the local phase, according to the definition in [45], is considered as vector with a direction corresponding to the rotation axis lying in the plane spanned by  $(i, j)$ .

### 3.3.3 Extension: Superposition of 2D AM-FM signals

Demonstrating the applicability of RT for the local description of composed image structures (e.g. superposition of fringe patterns), recently a generalization of the 2D analytic signal with respect to multi-component analysis of  $i2D$  structures has been suggested including approaches of Clifford analysis [79] and differential geometry [80, 55]. Using a multivector basis [81] for the description of oriented structures, this model characterizes the 2D pattern by its amplitude, phase, orientation and additionally by its apex angle. This generalized theory could finally allow the decomposition of 2D multi-component signals into their intrinsic  $i1D$  signal components.

## 3.4 Demodulation of 2D AM-FM signals

### 3.4.1 2D AM-FM signal model for the demodulation scheme

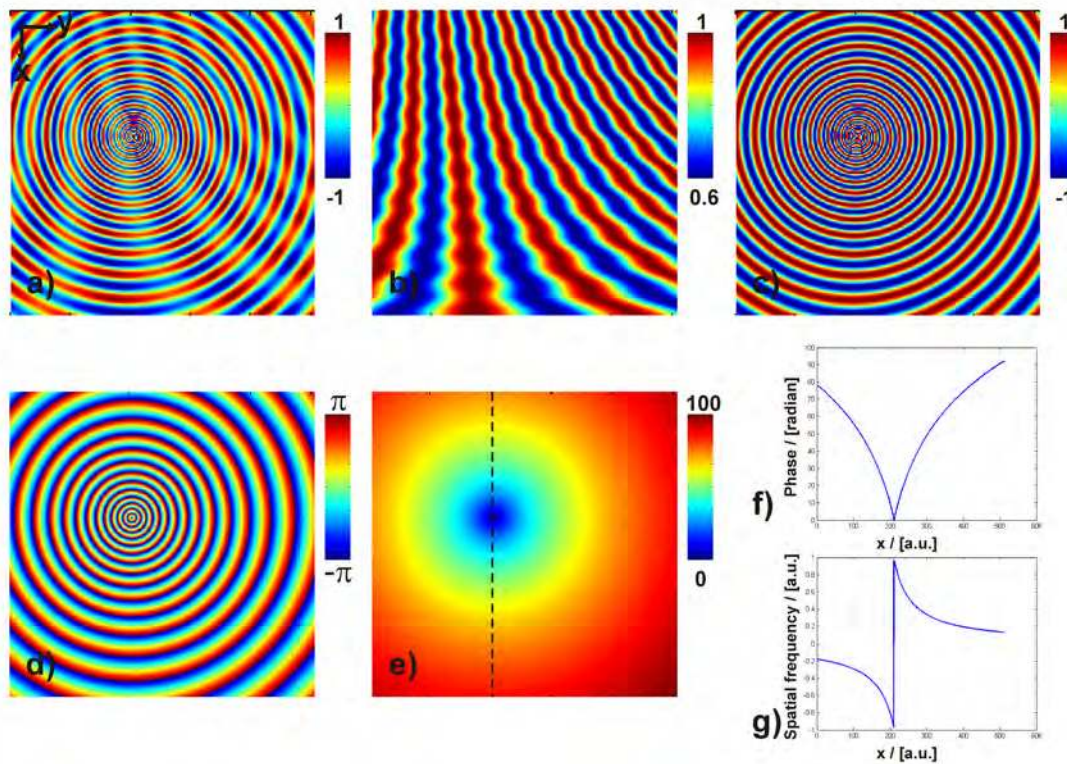


Figure 3.1: 2D AM-FM signal model. a) Simulated 2D AM-FM image, b) simulated amplitude image (describing the amplitude modulating function), c) simulated fringe pattern (being frequency modulated), d) simulated wrapped phase image, e) simulated continuous (unwrapped) phase image (describing the phase (or frequency) modulating function), f) continuous phase profile along the line indicated in (e), g) frequency profile as derivative of (f). Image (a) represents the input for the demodulation scheme, and amplitude (b) and phase (e) should be reconstructed by demodulation in the following.

PS-OCT retardation fringe patterns can be described in a simplified way as 2D amplitude and frequency modulated signals (2D AM-FM signals). A more detailed model of PS-OCT retardation images including noise simulations is given in Section (5.3).

Here, we introduce a 2D AM-FM signal model for demonstrating the principle of the 2D demodulation scheme, which is based on analytic and monogenic signal theory. In addition, we include an additive background term  $B(x,y)$ . The 2D AM-FM signal  $I_P(x,y)$ , denoted also as the in-phase component (index P), is represented for signals with harmonic wave shape (index S) as

$$I_{P,S}(x,y) = B(x,y) + A(x,y) \cos(\phi(x,y)), \quad (3.34)$$

with  $B(x,y)$ ,  $A(x,y)$  and  $\phi(x,y) \in C$ . The amplitude modulation (AM) function is denoted as  $A(x,y)$ , and  $\phi(x,y)$  represents the phase. This signal model with sinusoidal wave shape is used for basic considerations and for illustration of the scheme.

A 2D AM-FM signal in terms of

$$I_{P,T}(x,y) = B(x,y) + A(x,y) \text{tri}(\phi(x,y)), \quad (3.35)$$

is applied to describe the expected theoretical triangular (tri) wave shape (index T) of the retardation fringes.

For the sake of interest we also consider 2D AM-FM signals with a rectangular (rect) wave shape (index R) expressed as

$$I_{P,R}(x,y) = B(x,y) + A(x,y) \text{rect}(\phi(x,y)). \quad (3.36)$$

The aim of the AM-FM demodulation consists in the determination of the local values of amplitude  $A(x,y)$ , phase  $\phi(x,y)$ , and partially in estimating the background  $B(x,y)$ . Furthermore, the directional derivatives of the phase, representing the spatial frequencies  $\mathbf{w}(x,y)$ , are of interest. At the beginning, the additional background is supposed to be constant (here set to zero with  $B(x,y) = 0$ ). Later we will consider the influence of a varying background on the phase and frequency retrieval.

In our approach we apply a 2D demodulation scheme, as originally suggested in the field of classical interferometry by [43], which computes approximatively the quadrature component (index Q or q) as  $I_Q(x,y) = A(x,y) \sin(\phi(x,y))$  by the radial Hilbert transform. The applicability of the (generalized) analytic signal theory and the conditions for the computation of the quadrature term by means of the Hilbert transform are regarded in the following.

The simulated image, which we will use for illustration of the demodulation, is depicted in Figure 3.1: The 2D AM-FM signal (as shown in (a)) is composed by its AM-component (as shown in (b)) and its frequency-or phase modulation (FM or PM) component (as shown in (c)–(e)). The theoretical phase and frequency profiles along the dashed line are depicted in (f) and (g).

The 2D signal represents a pure theoretical fringe structure, with a bandlimited spectrum, containing a singularity in the center, and being amplitude and frequency modulated. We have chosen this pattern, because it describes a chirped and vortex-like signal, which is also of interest in case of SPM applications. Both spectra for the AM term  $A(x,y)$  and for the FM term  $\cos(\phi(x,y))$  are distinguished by their spectral ranges, whereas in the limit they are slightly overlapping.

### 3.4.2 The Hilbert transform and the quadrature component computation

The questions which have to be posed in connection with the applied demodulation scheme are:

- Under which conditions analytic signal theory yields a suitable approach for quadrature computation?
- How can the approximation error between Hilbert transform and quadrature component be estimated?
- How can errors due to non-harmonic wave shape, background or noise be limited?

First, considering the mathematical problem in  $ID$  and assuming a single-component signal, in particular, with the special cases of

a) a sinusoidal (tonal) signal  $f_P(x) = a(x) \cos(\phi(x)) = a(x) \cos(\omega_0 x + \phi_0)$ , and

b) a quadratic chirped sinusoidal signal  $f_P(x) = a(x) \cos(\phi(x)) = a(x) \cos(\omega_0 x + \alpha_{Ch} x^2)$ .

In Figure 3.2 a) and c), both signals are depicted, where  $a(x)$  is supposed to be constant here. The corresponding spectral magnitudes of the real-valued signal  $f_P(x) = \cos(\phi(x))$  and the complex-valued signal (index C)  $f_C(x) = \exp(i \phi(x))$  are depicted in Figure 3.2 b) and d). It should be noticed that for the chirped signal the magnitude of the complex-valued signal has a small contribution also for negative frequencies, (see in the following (3.39)).

Bedrosians theorem [82] states that the HT of a general product term  $a(x) c(x)$  can be expressed as

$$\mathcal{H}\{a(x) c(x)\} = a(x) \mathcal{H}\{c(x)\}, \quad (3.37)$$

only if the Fourier spectra for  $a(x)$  and  $c(x)$  are totally disjoint in frequency space.

Regarding, in particular,  $a(x)$  as a weak amplitude modulation due to inhomogeneous illumination or due to locally varying reference signals in the interferometric setup, and  $c(x) = \cos(\phi(x))$  as the frequency modulated function containing the encoded phase to be determined, the HT delivers only the conjugate component

$$\mathcal{H}\{a(x) \cos(\phi(x))\} = a(x) \mathcal{H}\{\cos(\phi(x))\}, \quad (3.38)$$

if phase and amplitude spectra are disjoint. Furthermore, the phase modulation has to be assumed being the high frequency component in contrast to the slowly varying amplitude modulation.

The Nuttall theorem [83] provides a quantitative measure for the approximation error  $\epsilon_A$  between the Hilbert transform  $f_Q(x) = a(x) \mathcal{H}\{\cos(\phi(x))\}$  of a signal (index Q), determined according to analytic signal theory, and the 'true' quadrature component  $f_q(x) = a(x) \sin(\phi(x))$  (index q). According to [83] the error can be estimated as

$$\epsilon_A = \int_{-\infty}^{\infty} |f_q(x) - f_Q(x)|^2 dx = 2 \int_{-\infty}^0 |F(\nu)|^2 d\nu, \quad (3.39)$$

with  $F(\nu) = \mathcal{F}\{a(x) \exp(i \phi(x))\}$ .

I.e. in case of bandlimited energy signals the error is bounded. Furthermore, it has been shown in [84, 85, 88] that for a signal generated by a wide sense homogeneous process, (i.e. having zero-mean and an autocorrelation function only dependent on distance), the 1D HT is the optimal

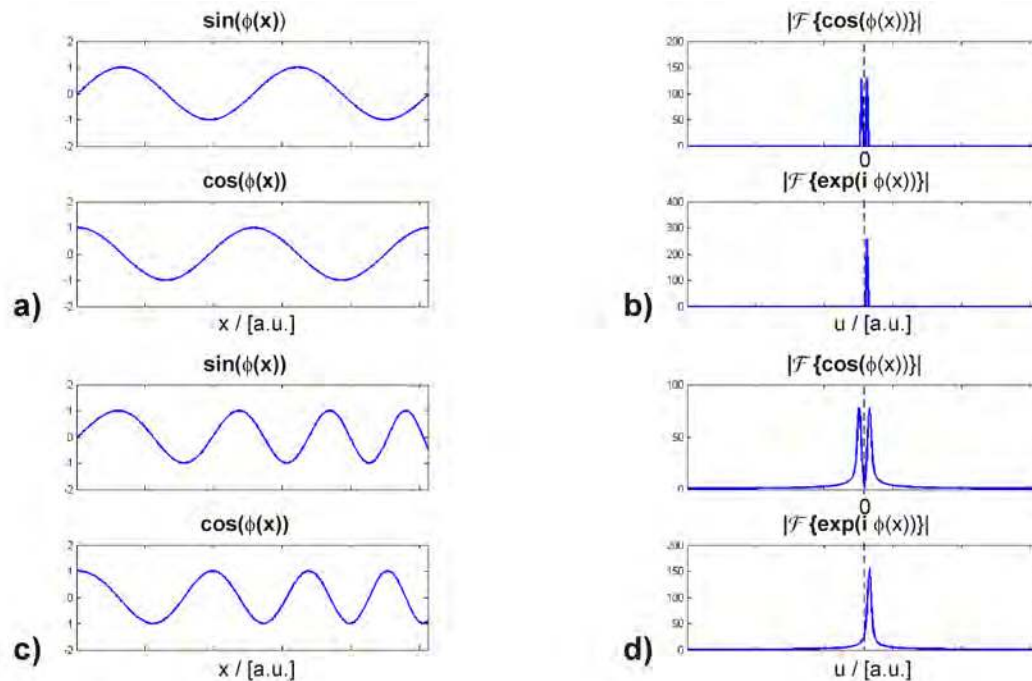


Figure 3.2: Illustration of the approximation error caused by computation of quadrature signal by HT according to the Nuttall theorem. a) Sinusoidal (tonal) signal with  $\phi(x) = \omega_0 x$ , b) spectral magnitude of  $f_P(x) = \cos(\phi(x))$  (top) and of  $f_C(x) = \exp(i\phi(x))$  (bottom) having no energy in the negative frequency range, c) chirped sinusoidal signal with  $\phi(x) = \omega(x)x = \cos(\omega_0 x + \alpha_{Ch} x^2)$ , d) spectral magnitude of  $f_P(x) = \cos(\phi(x))$  (top) and  $f_C(x) = \exp(i\phi(x))$  (bottom) having a small amount of the total spectral energy in the negative frequency range.

transform for computing the quadrature component of the signal in the sense of a least-square problem.

Second, regarding the problem in  $2D$ , the Bedrosian theorem with respect to the  $2D$  Hilbert transform (i.e. directional HT) is analyzed in [86]. It is shown there, that "a bounded linear translation invariant operator satisfies the Bedrosian theorem if and only if it can be represented as linear combination of partial Hilbert transforms". This result allows the splitting of local phase and amplitude by using the generalized analytic signal for the multi-dimensional case, as first introduced by [87].

If the Bedrosian theorem should be justified in case of applying the radial Hilbert transform operator (or spiral phase transform according to (3.22)), we argue first that the RHT operator is a bounded operator (with exception of the origin, but there it is mostly set to zero). Second, RHT can be interpreted as superposition of linewise  $1D$  Hilbert transforms performed in all angular directions through the origin. Fulfilling the required condition of disjoint spectral ranges for the amplitude- and frequency modulation component along these angular directions, also in the  $2D$  case a decomposition of the AM-FM modulated signal can be applied and the validity of Bedrosian theorem can be assumed correspondingly. However, it should be mentioned that the  $2D$  signals have to be (local) zero-mean signals equivalent to the  $1D$  case. Furthermore, a directional dependence is included in this approach, which requires an additional orientation estimation. (To reliably perform this orientation estimation the amplitude modulation should be weak, i.e.  $0 << a(x) \leq 1$ ). Recently in [88] it has been shown that the spiral phase transform provides the optimal least square solution for searching a transform approximatively computing the quadrature signal  $\sin(\phi(x,y))$  from  $\cos(\phi(x,y))$ .

As will be shown in Section (5.3) our simulated or measured and preprocessed PS-OCT retardation fringe patterns exhibit only a slowly varying amplitude modulation (as a result of multiple light scattering over depth, decreasing SNR and mathematically smoothing in regions with different variances). In contrast, the frequency modulation of the fringes is expressed almost everywhere in a higher spectral range. Under these assumptions and after performing a previous preprocessing (i.e. removing noise and higher harmonics) the  $2D$  demodulation approach for quadrature component computation, as described in the following, can be performed.

### 3.4.3 Influence of the algebraic space on the demodulation approach

For computation of the  $2D$  quadrature component we regard two approaches: Supposing  $B(x,y) = 0$  the quadrature component  $I_Q(x,y) = A(x,y) \sin(\phi(x,y))$  from the original signal  $I_P(x,y) = A(x,y) \cos(\phi(x,y))$  can be determined either by the radial Hilbert transform (RHT) (denoted also as spiral phase transform in literature) or by the Riesz transform (RT).

#### 3.4.3.1 Computation of $2D$ quadrature component by the radial Hilbert transform (Spiral phase transform)

We follow the approach in [43] for interferometric single fringe demodulation and performing the RHT by a filtering of the fringe pattern in Fourier domain with the spiral filter transfer function

$$F_{\Theta}(\mathbf{v}, \mathbf{v}) = \exp(i \Theta(\mathbf{v}, \mathbf{v})) \equiv \mathbf{H}_R(R, \Theta), \quad (3.40)$$

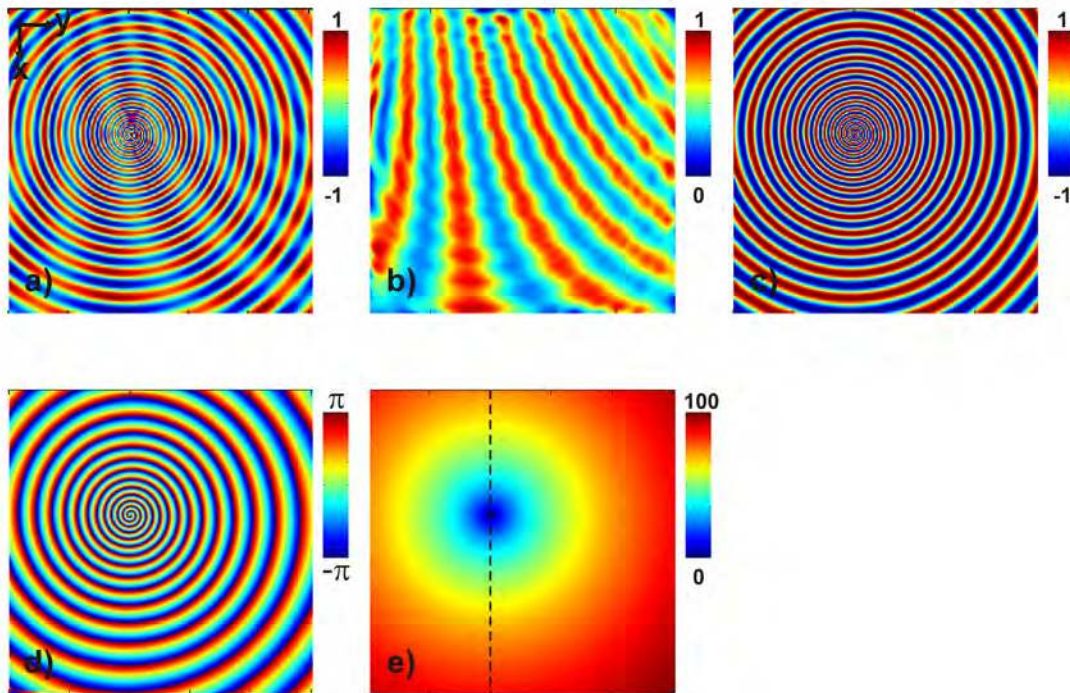


Figure 3.3: 2D demodulation scheme, applied on a 2D AM-FM signal with *harmonic wave shape*, based on the *radial Hilbert transform* approach. a) 2D AM-FM input image, b) reconstructed amplitude image, c) reconstructed sinusoidal phase image, d) reconstructed wrapped phase image, e) reconstructed continuous (unwrapped) phase image.

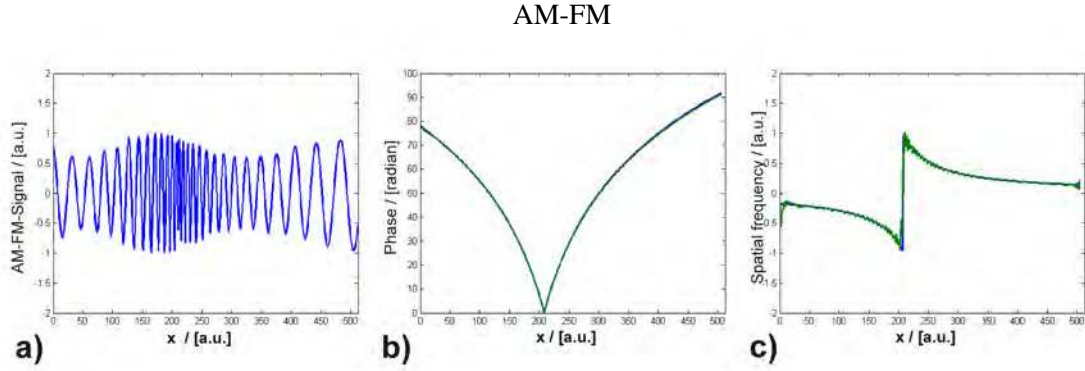


Figure 3.4: AM-FM signal along the line, indicated in Figure 3.3 e). a) AM-FM input signal with *harmonic wave shape*, b) reconstructed phase profile (*blue*: theoretical value, *green*: reconstructed value), c) reconstructed frequency profile (*blue*: theoretical value, *green*: reconstructed value).

which is defined analogue to (2.15).

*Note:* Whereas in Section (2.3) in the context of spiral phase microscopy the operator  $\mathbf{H}_R(R, \Theta)$  is applied to the EM-wave to modify the contrast in imaging, the spiral filter transfer function  $F_\Theta(\nu, \nu)$  is applied here to the fringe pattern, i.e. to a scalar-valued quantity, which is described as 2D real-valued function.

According to [43] the quadrature component is approximately obtained by the relationship

$$\mathcal{F}^{-1} \{ \mathcal{F} \{ I_P(x, y) \} \exp(i \Theta) \} = i \exp(i \beta(x, y)) I_Q(x, y), \quad (3.41)$$

where  $\beta(x, y)$  represents the *direction* of the fringes (i.e.  $\beta = \beta_{2\pi}$  according to (3)).

This method based on the early work of [89] represents an elegant solution of the computation of the quadrature component for a closed fringe pattern. It comprehends a different understanding of the Hilbert transform and different interpretation of a 2D signum function, compared to directional 2D HT approaches [90]. However, it requires an additional *orientation/direction estimation* step to remove the exponential orientation term  $\exp(-i \beta(x, y))$  in (3.41). Finally, in the case that the orientation (and direction) estimation of the fringes has been additionally performed, the quadrature signal  $I_Q(x, y)$  is obtained as

$$I_Q(x, y) = -i \exp(-i \beta(x, y)) \mathcal{F}^{-1} \{ \mathcal{F} \{ I_P(x, y) \} \exp(i \Theta) \}. \quad (3.42)$$

The amplitude modulation  $A(x, y)$  and the wrapped phase  $\phi_w(x, y)$  can be determined from the (measured or simulated) 2D in-phase component  $I_P(x, y)$  and the computed 2D quadrature component  $I_Q(x, y)$  in the usual way as

$$A(x, y) = |(I_P(x, y) + i I_Q(x, y))|, \quad (3.43)$$

$$\phi_w(x, y) = \angle(I_P(x, y) + i I_Q(x, y)). \quad (3.44)$$

The steps of the described demodulation scheme ((3.34), (3.43), (3.44)) are depicted in Figure 3.3 a)–d). As the phase in (3.44) is given in a mapped representation, an unwrapping of



the wrapped phase  $\phi_w(x,y)$  is required to extract the continuous phase  $\phi_c(x,y)$ , as shown in Figure 3.3 e). The spatial frequencies can be obtained finally as gradient of the unwrapped phase signal,

$$\mathbf{w}(x,y) = \nabla(\phi_c(x,y)). \quad (3.45)$$

In Figure 3.4 the the phase and frequency demodulation of an AM-FM signal along the line indicated in Figure 3.3 is depicted for a better visualization. Theoretical phase and frequency values and reconstruction values are correctly coinciding in case of an AM-FM model having sinusoidal wave-shape fringes.

### 3.4.3.2 Computation of 2D quadrature component by the Riesz transform

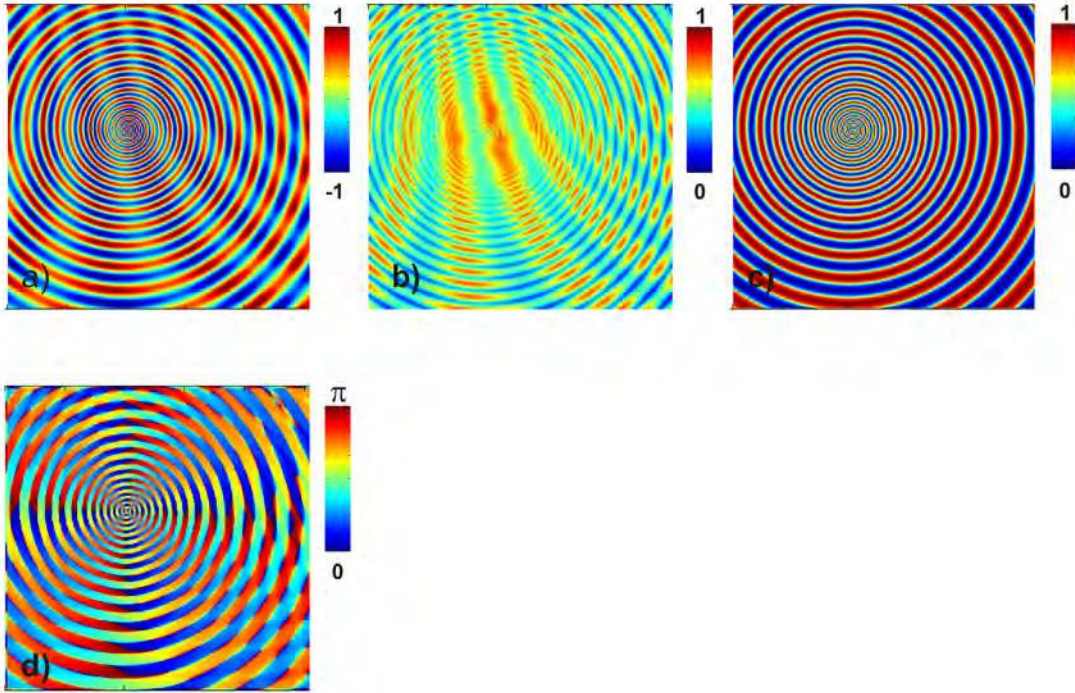


Figure 3.5: 2D demodulation scheme, applied on a 2D AM-FM signal with *harmonic wave shape*, based on the *Riesz transform* approach [45, 55]. a) 2D input AM-FM image, b) reconstructed amplitude image, c) reconstructed phase image, d) estimated orientation image.

Furthermore, as extension to the RHT approach we apply the concept of quadrature computation by the Riesz transform, defined in (3.27) and (3.28), according to the scheme proposed in [45, 55]. Therein, in the spatial domain the convolution with the RHT kernel  $\mathbf{h}_R$ , coupling the radial  $\frac{1}{2\pi r^2}$  and angular term  $\exp(i\beta)$  is replaced by the convolution with the Riesz kernel  $\mathbf{h}_{RI}$ , defined in quaternionic space. Having now four independent basis elements  $(i, j, k, 1)$  available, the

three quantities (amplitude, phase and orientation) can be represented independently, and phase and orientation are no longer entangled.

Following this approach and using the quaternionic signal representation, the 2D AM-FM signals may be split into its amplitude, phase and orientation component, as depicted in Figure 3.5. Additionally, here a bandpass filter has been included. This results in slight fluctuations in the reconstructed amplitude image (Figure 3.5 b)).

### 3.4.3.3 Comparison: Radial Hilbert transform and Riesz transform

The results of both approaches (Radial Hilbert transform and Riesz transform) are comparable with respect to the separation of the amplitude and phase image, compare Figures 3.3 and 3.5. The monogenic (vectorial) phase (see (3.32)) is represented here by its magnitude (i.e. without wraps), the sign would be encoded in the direction of the vector  $\mathbf{e}_M$ . The advantage of RT approach versus RHT consists that no additional orientation estimation is required. However, the switching to quaternionic algebra is a necessary step for the realization of this method. Comparing both efforts, we have chosen in the following the RHT as basis for the 2D signal demodulation. It should be noted that the RT approach seems of advantage in case of considering superposition of fringe patterns.

### 3.4.4 Influence of the wave shape on the demodulation approach

#### 3.4.4.1 1D Signals

First, we demonstrate the influence of the wave shape on the demodulation results and especially on the frequency estimation for a periodic 1D signal  $f_P(x)$ , being sinusoidal (S), triangular (T) or rectangular (R) pulse trains, as shown in Figure 3.6. There we have displayed the signal, its quadrature component  $f_Q(x)$ , computed by the HT (taking into account some approximation error), and its energy as magnitude of both components  $|f_P(x) + if_Q(x)|$ . Only in the case of a sinusoidal signal we obtain a constant unit energy. In the case of the other chosen wave shapes deviations from unit energy are recognizable, (i.e. the quadrature does not correspond exactly to the signal obtained by HT). This can also be explained in terms of Taylor series by the higher harmonics of the non-harmonic signals.

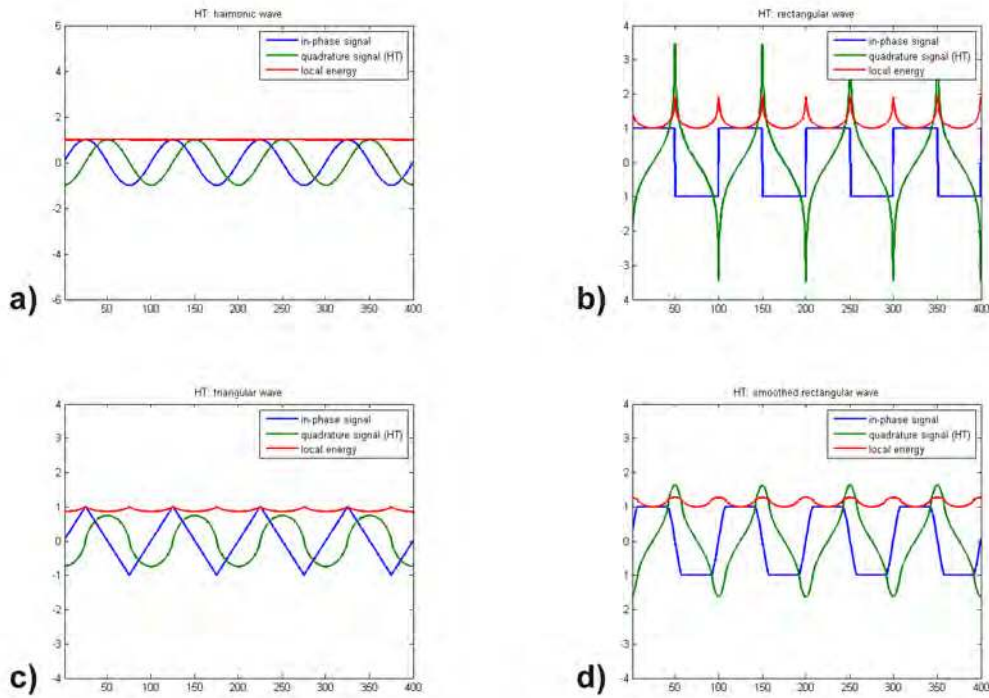


Figure 3.6: 1D periodic signals of different wave shapes (S,T,R). a) Sinusoidal signal  $f_{PS}(x), f_{QS}(x)$ , b) rectangular signal  $f_{PR}(x), f_{QR}(x)$ , c) triangular signal  $f_{PT}(x), f_{QT}(x)$ , d) smoothed rectangular signal  $f_{PR}(x), f_{QR}(x)$ . (blue: original signal  $f_P(x)$ , green: Hilbert transformed signal  $f_Q(x)$ , red: magnitude of the analytic signal  $|f_A|$ ).

As we can represent the periodic signals by its Fourier series

$$f_{PS}(x) = \sin(\omega x) \quad (3.46)$$

$$f_{PT}(x) = \sin(\omega x) - \frac{1}{9} \sin(3\omega x) + \frac{1}{25} \sin(5\omega x) \dots \quad (3.47)$$

$$f_{PR}(x) = \sin(\omega x) + \frac{1}{3} \sin(3\omega x) + \frac{1}{5} \sin(5\omega x) \dots, \quad (3.48)$$

and applying the HT delivers the corresponding conjugate signal terms

$$f_{QS}(x) = -\cos(\omega x) \quad (3.49)$$

$$f_{QT}(x) = -\cos(\omega x) + \frac{1}{9} \cos(3\omega x) - \frac{1}{25} \cos(5\omega x) \dots \quad (3.50)$$

$$f_{QR}(x) = -\cos(\omega x) - \frac{1}{3} \cos(3\omega x) - \frac{1}{5} \cos(5\omega x) \dots, \quad (3.51)$$

Hence, by computing the phase directly by the arctan-relation we would obtain a nonlinear phase function in case of triangular or rectangular wave shapes, as shown in Figure 3.7. Although the phase error between the nonlinear phase function and the linear phase function is low, as shown in Figure 3.8 a), and can be estimated by Taylor series expansion (with less than 0.12 rad for triangular pulses), the frequency as derivative of the phase functions shows erroneous peaks. A decreasing of the erroneous peaks in the frequency signal can be achieved by a preceding smoothing, e.g. by a low pass filtering or – as later regarded – by a regularization method. Due to the low pass filtering the higher harmonics are reduced, resulting in a decreasing of the erroneous peaks, as shown Figure 3.8 b),

For real-world signals these effects demonstrated here by simulations give us the motivation to combine the denoising and smoothing of wave shapes to obtain an approximately harmonic wave shape.

#### 3.4.4.2 2D Signals

Similar to our considerations about the influence of wave shape in 1D, the 2D demodulation scheme has been exemplified on the simulated 2D AM-FM image, being comparably modified by triangular and rectangular wave shapes. The demodulation scheme works in principle, but, similar to the 1D case, it leads to frequency peaks in case of a triangular wave shape (as shown in Figure 3.9 and Figure 3.10) due to the nonlinear phase function. The erroneous frequency peaks are still more amplified in the case of a rectangular wave shape signal (as can be seen in Figure 3.11 and Figure 3.12). Due to these artefacts, the direct demodulation scheme without any preprocessing (i.e. smoothing) seems impracticable.

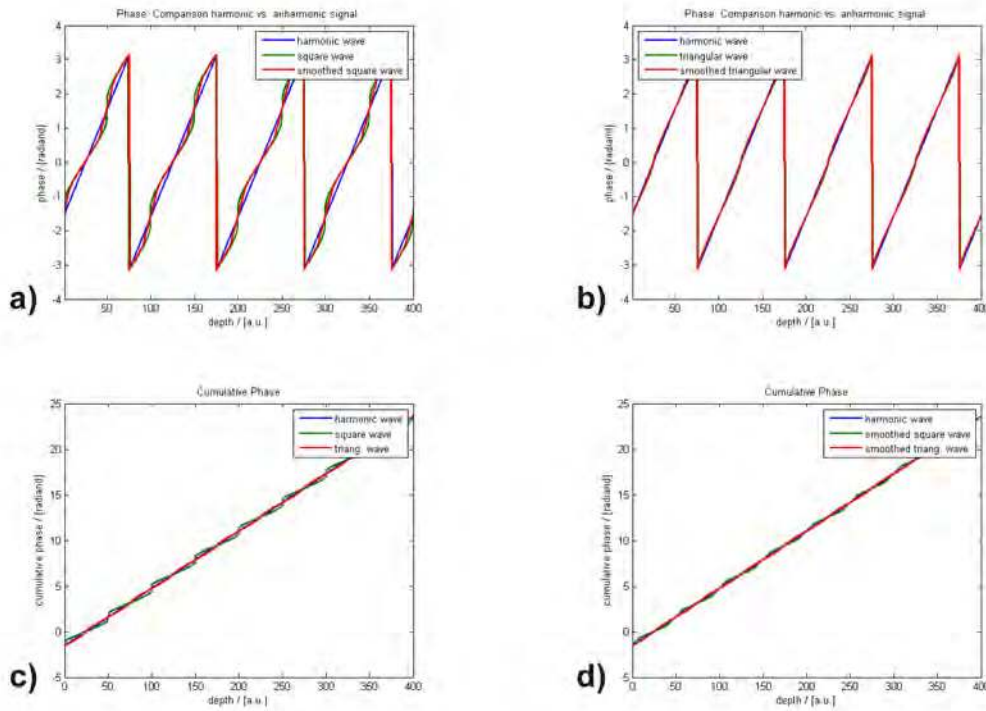


Figure 3.7: Illustration of the non-linearity of the phase, obtained by the HT approach. a) Wrapped phase dependent on wave shape (sinusoidal, rectangular), b) after smoothing the wave shape (sinusoidal, triangular), c) unwrapped phase dependent on wave shape (sinusoidal, rectangular, triangular), d) unwrapped phase after smoothing the wave shape.

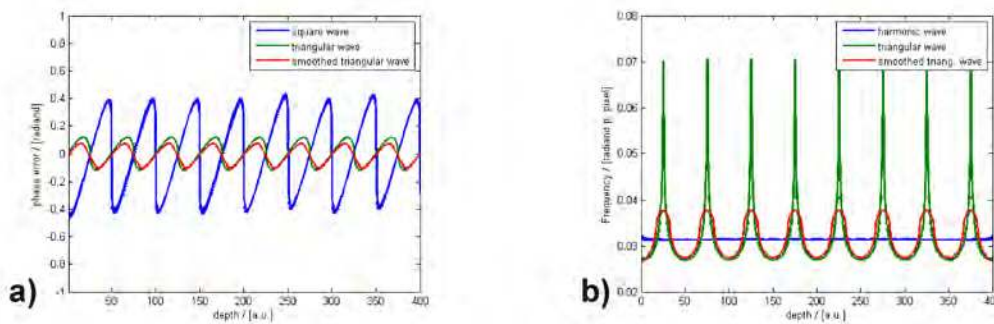


Figure 3.8: Phase error and frequency deviations in case of non-harmonic signal. a) Phase error obtained as deviation from linear phase, b) instantaneous frequency as derivative of instantaneous phase exhibiting erroneous peaks, but being reduced by a prior smoothing.

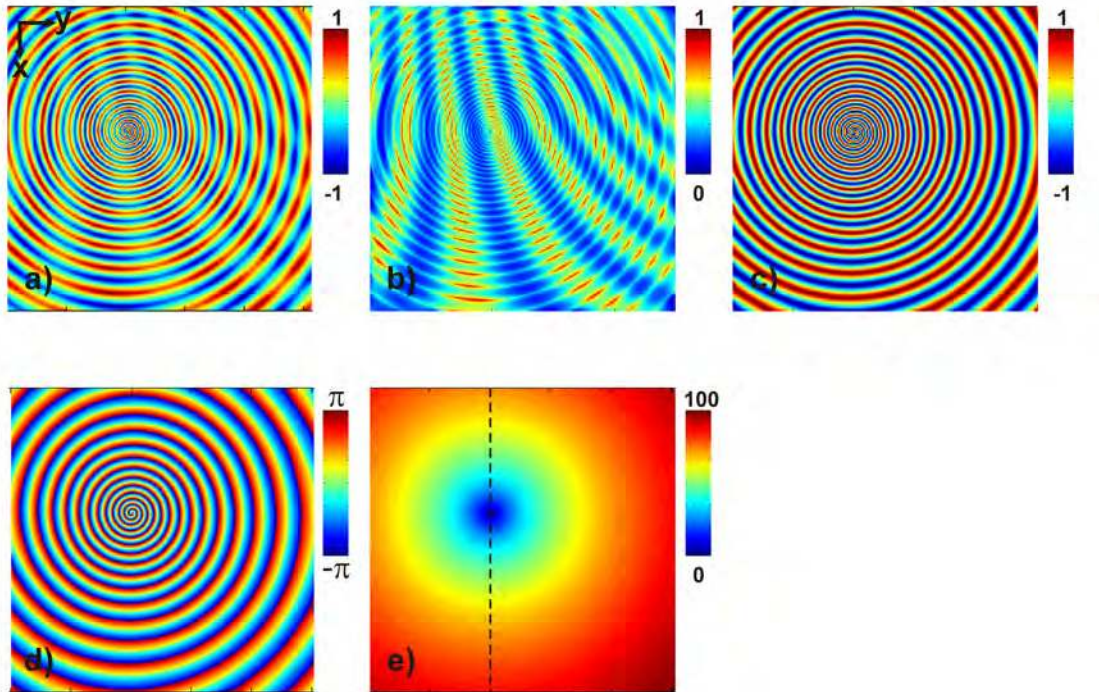


Figure 3.9: 2D demodulation scheme, applied on a 2D AM-FM signal with *triangular wave shape*. a) 2D AM-FM input image, b) reconstructed amplitude image, c) reconstructed sinusoidal phase image, d) reconstructed wrapped phase image, e) reconstructed continuous (unwrapped) phase image.

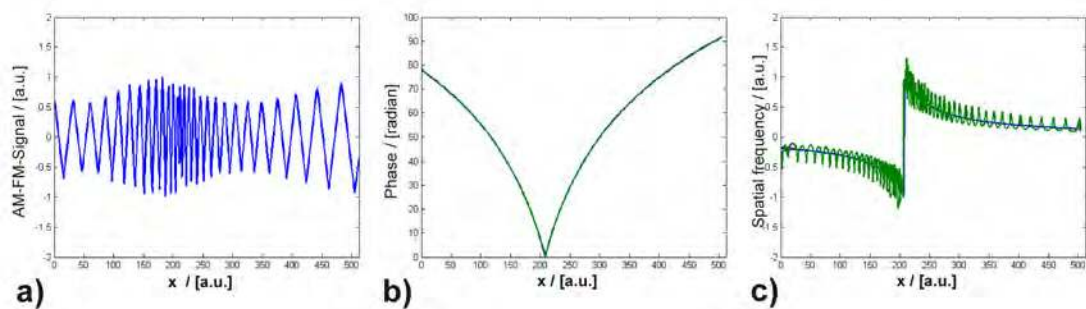


Figure 3.10: AM-FM signal along the line, indicated in Figure 3.9 e). a) AM-FM input signal with triangular wave shape, b) reconstructed phase profile (*blue*: theoretical value, *green*: reconstructed value), c) reconstructed frequency profile (*blue*: theoretical value, *green*: reconstructed value).

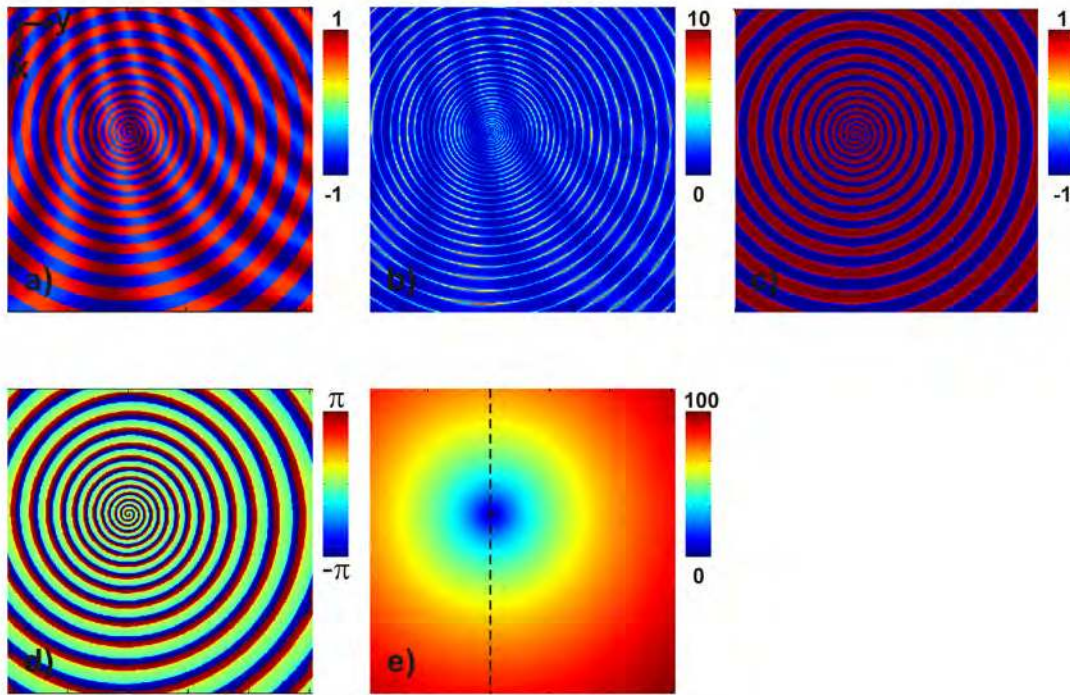


Figure 3.11: 2D demodulation scheme, applied on a 2D AM-FM signal with *rectangular wave shape*. a) 2D AM-FM input image, b) reconstructed amplitude image, c) reconstructed sinusoidal phase image, d) reconstructed wrapped phase image, e) reconstructed continuous (unwrapped) phase image.

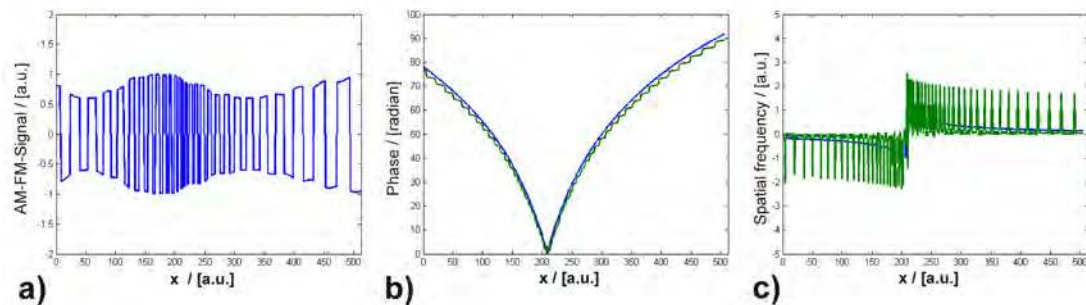


Figure 3.12: AM-FM signal along line, indicated in Figure 3.11 e). a) AM-FM input signal with rectangular wave shape, b) reconstructed phase profile (*blue*: theoretical value, *green*: reconstructed value), c) reconstructed frequency profile (*blue*: theoretical value, *green*: reconstructed value).

### 3.4.5 Influence of the background on the demodulation approach

Due to different imaging situations (e.g. having varying illumination) or due to inhomogeneous scattering properties of the sample (e.g. by a moving average over noisy inhomogeneous regions) an additive background term  $B(x,y)$  may occur. It can be considered as an additional offset. First, the influence of this offset term is estimated for a periodic 1D signal. Second, for our 2D AM-FM signal model a solution for background removal is presented.

#### 3.4.5.1 Error estimation

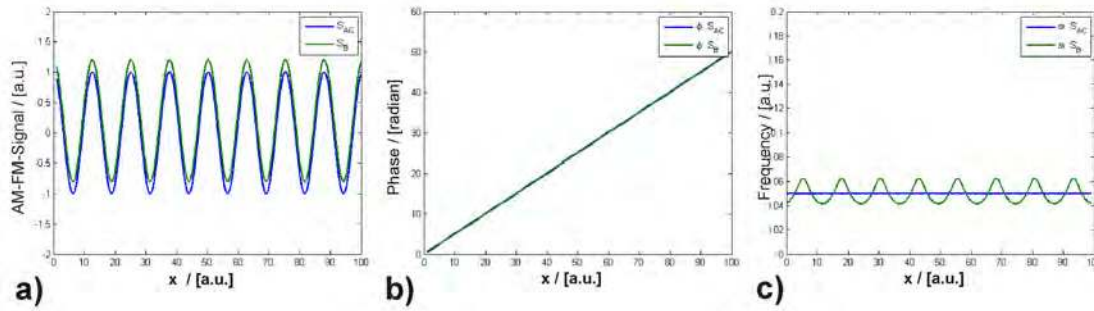


Figure 3.13: Influence of signal offset on phase linearity (1D signal). a) Periodic sinusoidal signal with and without an offset component, b) phase deviations, c) frequency error.

The demodulation method based on analytic signal theory supposes zero-mean signals. In case that this condition can not be fulfilled in measurements, the recorded signal  $I_P(x,y) = \cos(\phi(x,y)) + \delta(x,y)$  exhibits an offset due to illumination or also due to local smoothing effects. We want to estimate the influence of this offset, assuming here first a constant, normalized amplitude  $A(x,y) = 1$  and an constant offset  $\delta$ . An additional phase error  $\epsilon_\phi$  in the analysis is introduced, as the HT transform of a constant value yields zero. Hence, an offset would result in an erroneous phase value of

$$\phi_{Off}(x,y) = \arctan \frac{\sin(\phi(x,y))}{\cos(\phi(x,y)) + \delta}. \quad (3.52)$$

As shown in [91] and can be estimated by Taylor series the error is bounded by

$$\begin{aligned} \epsilon_\phi &= \phi_{Off}(x,y) - \phi(x,y) \\ &= \sin(\phi(x,y)) \delta \leq \delta, \end{aligned} \quad (3.53)$$

as long the modulation depth is higher than the offset value.

Similar to the influence of non-harmonic wave shapes, which causes erroneous frequency peaks as described before, now frequency errors are resulting due to the offset term, as illustrated for a periodic 1D signal, having a constant offset, in Figure 3.13 a)–c).



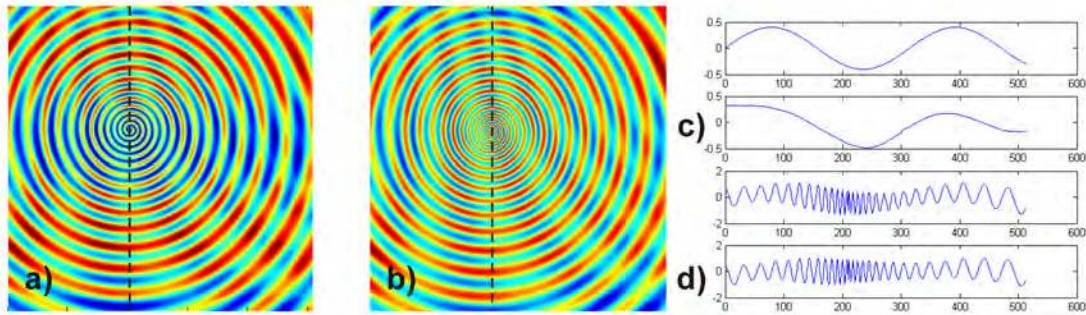


Figure 3.14: Demonstration of the background correction by empirical mode decomposition (EMD) method, applied on the 2D AM-FM signal. a) Simulated 2D AM-FM image, superposed with low frequency modulated background (being a local non-zero mean signal), b) recovered local zero-mean 2D AM-FM image after background correction with the EMD approach, c) *top*: simulated background profile corresponding to the line, indicated in (a), and *bottom*: estimated background profile with EMD, d) *top*: local non-zero mean signal along the line, indicated in (a), and *bottom*: local zero-mean (IMF) signal, obtained after background correction.

### 3.4.5.2 Background correction by the EMD method

In case of a constant additive background the correction becomes trivial by subtracting the DC component. Closer to reality seems a locally varying background representing a low frequency offset term. For estimating and correcting this varying background, prior to demodulation, the empirical mode decomposition is applied as explained in Subsection (3.1.3).

In Figure 3.14 a) our simulated 2D AM-FM image of Figure 3.1 a) is taken, now superposed by an locally varying offset, which we want to correct. Therefore we apply, in particular, now for a 2D image signal, the bi-dimensional EMD method for estimating the background as sum of lower frequency IMFs and the residual of the decomposition. Finally, the estimated background may be subtracted to yield a local zero-mean 2D AM-FM signal, as shown for the simulated fringe pattern in Figure 3.14 b)–d). The resulting almost zero-mean signal can be properly demodulated. Empirically we tested the level up to which the decomposition has to be performed to obtain a representative background estimation. Small artifacts can be recognized at the boundary of the image and would have to be treated additionally by a suitable continuation of the signals.

The influence of the varying offset and especially, the need for a background corrected signal (Figure 3.15 a)–c)), to obtain smooth phase and frequency signals (Figure 3.15 d)–f)) is illustrated here: By the correction of the local non-zero mean signal to an almost zero-mean one, the phase and frequency errors can be remarkably reduced, (as shown in Figures 3.15 f) and 3.16 a)). Additionally, the background correction can be combined with a regularized differentiation, (Figure 3.16 b)), what will be demonstrated for real data in Section (6.3).

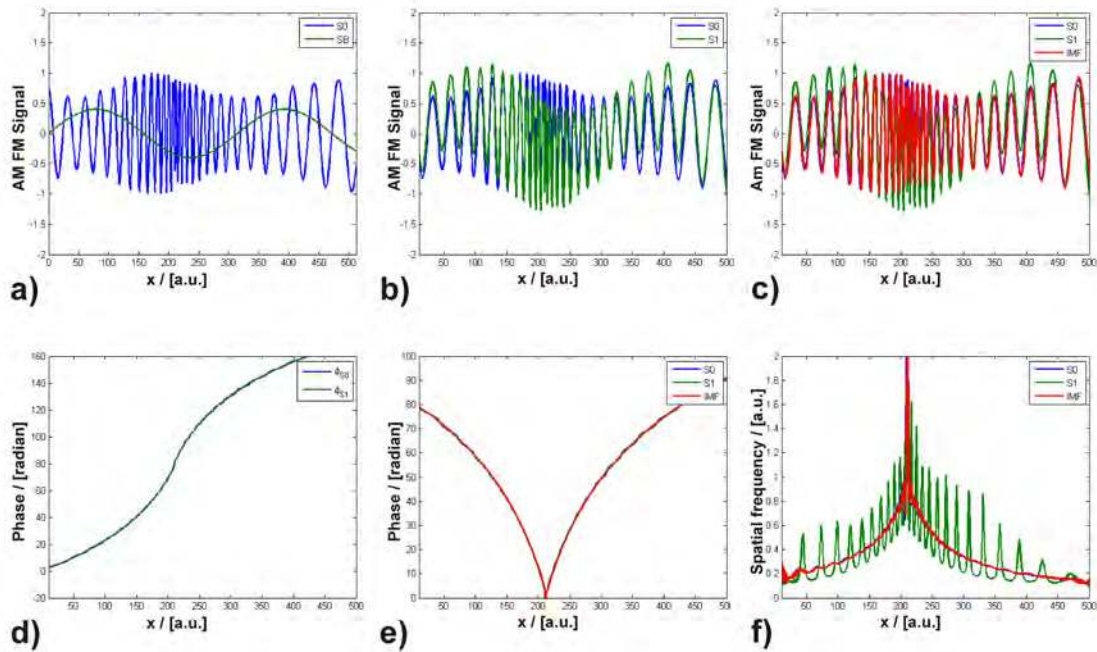


Figure 3.15: Illustration of the EMD method for reduction of demodulation errors, caused by local non-zero mean signals. (signal along the line, indicated in Figure 3.14 a). a) Local zero-mean signal (*blue*:  $S_0$ ) and background (*green*:  $S_B$ ), b) local zero-mean signal (*blue*:  $S_0$ ) and non-zero mean signal (*green*:  $S_1$ ) with superposed background, c) background corrected signal (*blue*:  $S_0$ , *green*:  $S_1$ , *red*: corrected signal IMF), d) reconstructed phase (applying the 1D HT), e) reconstructed phase (applying the 2D RHT), f) reconstructed frequency (*red*: performed on the EMD-corrected signal, *green*: performed on the local non-zero mean signal  $S_1$ , *blue*: performed on the local zero-mean signal  $S_0$ ). IMF denotes the background corrected signal here.

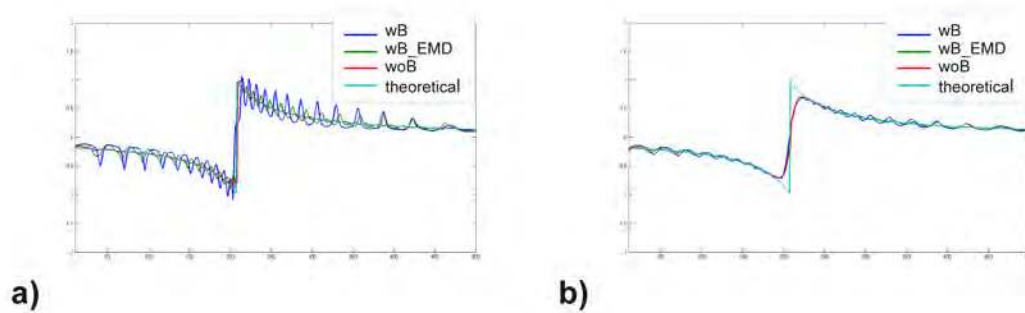


Figure 3.16: Comparison of estimated frequency along the line as indicated in Figure 3.15 a) and b). a) Recovered frequency (differentiation of phase performed without regularization), b) recovered frequency (differentiation of phase performed with regularization), (wB with background, woB without background, wB\_EMD with background and EMD corrected).

### 3.5 Summary

In this chapter we have derived the required mathematical fundamentals for the demodulation and phase reconstruction on simulated 2D AM-FM signals. We have demonstrated the chosen 2D demodulation scheme on a simulated 2D AM-FM image model. Furthermore, we have considered different limitations, which are to expect for PS-OCT signals with respect to wave shape and background.

In Section (5.3) we will describe our 2D retardation fringe pattern as locally *iID* structures if considered in a small neighborhoods, but as spatially varying 2D AM-FM signals, if considered in larger regions. They may be composed by multiple components, which necessitates an appropriate decomposition. Especially, as the measured 2D retardation signals and fringe structures can be disturbed in reality by severe noise, background effects and measurement artifacts, a direct use of the monogenic signal analysis approach for successful demodulation is restricted. Combining for the analysis of retardation fringe patterns the analytic (or monogenic) phase concept with an appropriate preprocessing (e.g. including denoising and background correction) allows finally the applicability of the described 2D demodulation scheme on noisy retardation signals with originally non-harmonic wave shape.

In case of PS-OCT imaging the whole procedure will be reviewed for the spatially resolved reconstruction of phase retardation, frequency and related optical quantities in Section (5.4).

## Chapter 4

# Conventional OCT and Advanced Modifications

Complementary to microscopic imaging also optical coherence tomography (OCT) represents an interesting interferometric imaging technique for the investigation of microstructures. Developed in the latest decades, nowadays a huge variety of modalities for OCT imaging exists [92]. Preferred objects, studied by OCT, are turbid or semi-transparent materials, whose backscattering behavior is exploited in conventional OCT imaging.

In contrast to conventional microscopy, where the probing is restricted to the uppermost surface layer of the sample in case of turbid materials, by OCT structural information from deeper sub-surface regions inside the material can be obtained. Depending on the specific optical parameters for the imaging and of the investigated specimen a depth range of up to 1-2 mm can be probed with an achievable resolution of few micrometers. Therefore, additional knowledge about interfaces, scattering structures, the 3D distribution of backscatterers and their material-dependent density can be provided by OCT imaging.

Considering light as electro-magnetic wave and a complex quantity, besides intensity-related also phase-related quantities can be exploited by OCT, similar to phase contrast microscopy, described in Chapter (2). Phase-sensitive modifications of OCT imaging, their basics and their potential for functional and quantitative imaging, will be considered in Chapter (5) and Chapter (6). In this chapter we will shortly explain *intensity-based* OCT imaging as the fundamental technique for the following phase-based versions.

### 4.1 OCT: Imaging principles

At the beginning, the particular features of OCT imaging, in which it is distinguished from microscopic phase imaging, should briefly be mentioned:

- First, the intensity and time-dependence of the *backscattered* or *back-reflected light*, depending on the reflectivity of the structures, is used as the measurable quantity.
- Second, the backscattered signals are *coherently amplified* (i.e. by interferometric signal generation). Thereby, OCT differs from conventional microscopy: Coherent amplification

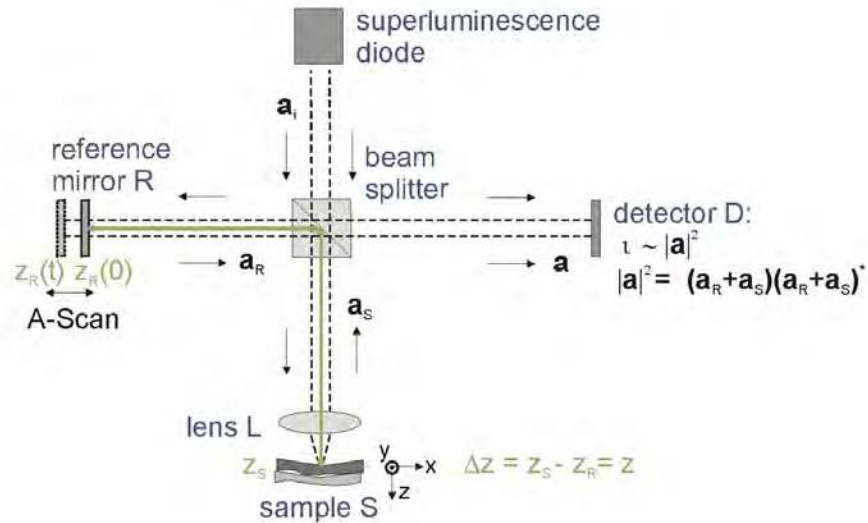


Figure 4.1: TD-OCT optical setup with indicated wave fields denoting initial ( $\mathbf{a}_i$ ), sample ( $\mathbf{a}_S$ ), reference ( $\mathbf{a}_R$ ), and interference ( $\mathbf{a}$ ) wave. The reference mirror can be moved along the  $z$ -axis.

enables the detection of weak signals from inside the specimen, which can no longer be detected by microscopic imaging.

- Third, OCT uses the *low-coherence* properties of light for detection. By exploiting specifically this low-coherence property the OCT-imaging can be realized in a depth-resolved way.

Based on these main characteristics the capability of conventional OCT for gaining structural information results and will be reviewed in more detail in the following.

#### 4.1.1 OCT: Working principle and optical setup

The working principle of OCT is based on low-coherence interferometry, i.e. OCT enables a coherent, interferometric imaging, which is additionally highly localized in depth. The optical setup of a conventional OCT system is sketched in Figure 4.1. The OCT-configuration contains as essential element an interferometer, here depicted as Michelson-type interferometer, as realized for our applications. The incident light wave is divided at the beam splitter into a sample and reference wave. The interference signal between the backscattered sample wave and the back-reflected reference wave, superposed at the photodetector, is measured. An interference signal can be obtained only if the optical path lengths of both sample and reference wave match to each other.

The interference signal is detected as long as the mutual optical path difference is lower than the coherence length  $l_c$  of the light source. Thereby, the coherence length describes the axial resolution range, within (measurable) interference can occur. It depends inversely on the spectral width  $\Delta k$  of the light source  $l_c \propto 1/\Delta k$ . In contrast to conventional interferometry, in OCT a spectral broad-band light source (e.g. super-luminescence diodes (SLD) or femto-second pulse lasers (fs-lasers), usually in the NIR spectral range) is used for illumination. Due to the broad bandwidth of the source the coherence length is very small (in range of some micrometers). Additionally, the reference mirror is oscillating. Due to the movable reference mirror the depth position, where both imaging arms are matching in their distances, is also moved through the sample. This results in an temporarily altering position of coherence gate, denoted therefore as time-gated signaling. This time-gated interference signal over depth  $z$  is recorded by a point detector. Including further an incremental lateral shifting of the sample, the specimen can be scanned subsequently by the raster scanning unit.

The explained time-gated coherent imaging regime of OCT is called Time domain(TD)-OCT. The later discussed OCT setup for our applications is realized as a TD-OCT in its basic configuration. By including additionally polarization- and phase-modifying optical components the conventional OCT setup can be extended to become phase-sensitive, as will be described in the following chapters.

It should be mentioned that beside the depicted time domain (TD) OCT setup also spectral domain (SD) OCT versions are extensively used, allowing a high-sensitive and high-speed imaging of the sample. The SD-OCT setup mainly differs from TD-OCT in the points: (1) The reference mirror is fixed, (2) additionally diffractive elements are included in front of the detector, which is replaced by a (3) spectrometer. The spectrum of the interference signal is analyzed by inverse Fourier transform. The strength of the spectral components contains the reflectivity information, the wave number encodes the corresponding depth. The coherence condition is full-filled for the individual wavelength components of the source at different depth position. Therefore, by Fourier transforming the spectrum the depth-resolved reflectivity map can be recovered [93, 94].

Summarizing, as main elements in the conventional TD-OCT setup should be mentioned:

- The interferometer, which is required for *coherent detection* and *amplification*,
- The *spectral broad-band* light source, which enables the low-coherence imaging,
- The *movable* reference mirror, for obtaining depth-resolved interference signals.

#### 4.1.2 OCT: Reflectivity signal and image generation

Conventional OCT systems are exploiting the backscattering properties of the material and the wave reflection at interfaces, which depends on the spatial distribution of the refractive index inside the investigated sample. The backscattering can also be influenced from the size and shape of the scattering particles. These sub-microscopic scattering effects will not be considered further, only the general dependence on refractive index and reflectance of the sample will be taken into account in the following.

First, regarding the OCT-signal generation as a *backscattering* process the magnitude of the measured detector signal  $S_D(z)$  can be related to the refractive index distribution  $n(z)$  of the sample

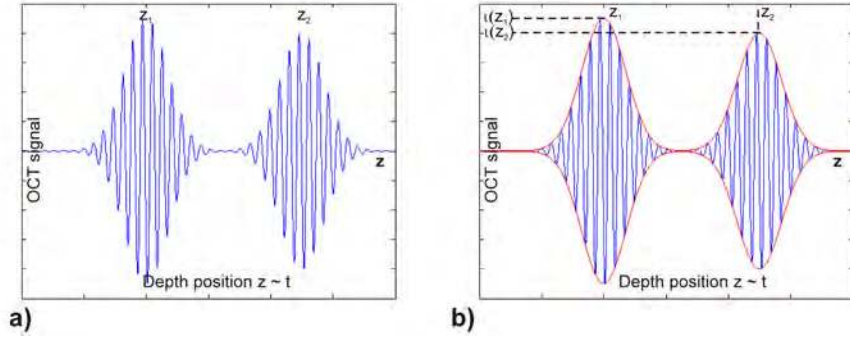


Figure 4.2: Reflectivity (intensity) signal of a sample with two interfaces at depth  $z_1$  and  $z_2$ . a) Interference burst signal in OCT imaging, b) reflectivity signal envelope.

over depth [95] by

$$S_D(z) \propto \left( \frac{\partial n(z)}{\partial z} \right)^2 + n(z) \frac{\partial^2 n(z)}{\partial z^2}. \quad (4.1)$$

This relation illustrates that the *change* of the refractive index represents the essential quantity, which delivers the recorded signal and explains the capability of OCT for imaging in particular, interfaces between different material layers.

Now, regarding signal generation in TD-OCT as an *interferometric* superposition, the generated detector signal is proportional to the total intensity of the interference signal as  $S_D \sim \mathfrak{I}$ . The interference signal results from the superposition of the two wave fields the sample wave  $\mathbf{a}_S = a_S \exp(-i\phi_S)$ , which is back-reflected/backscattered from the sample surface (or interface) and located at position  $z_S$ , and the reference wave  $\mathbf{a}_R = a_R \exp(-i\phi_R)$ , which is reflected from the reference mirror at position  $z_R$ . The total intensity signal yields

$$\begin{aligned} \mathfrak{I} &\propto (\mathbf{a}_S + \mathbf{a}_R)(\mathbf{a}_S + \mathbf{a}_R)^* \\ \mathfrak{I} &= \mathfrak{I}_R + \mathfrak{I}_S + 2\sqrt{\mathfrak{I}_R \mathfrak{I}_S} \cos(\Delta\phi), \end{aligned} \quad (4.2)$$

with  $\mathfrak{I}_R \propto \mathbf{a}_R \mathbf{a}_R^* = R_R \frac{\mathbf{a}_i \mathbf{a}_i^*}{2}$  and  $\mathfrak{I}_S \propto \mathbf{a}_S \mathbf{a}_S^* = R_S \frac{\mathbf{a}_i \mathbf{a}_i^*}{2}$ , being the intensity of reference and sample field. The intensity of the incident wave field is denoted by  $\mathfrak{I}_i \sim \mathbf{a}_i \mathbf{a}_i^*$ .  $R_R$  and  $R_S$  express the reflectivities of the reference mirror and the sample surface. The phase difference  $\Delta\phi = (\phi_S - \phi_R) = 2k \Delta z$  is related to the geometrical path length difference between sample and reference path  $\Delta z = (z_R - z_S) \equiv z$ , (by choosing  $z = 0$  appropriately to e.g. sample surface and assuming monochromatic light with wave number  $k = n k_0$ ).

Regarding now low-coherence interferometry, then the characteristic difference to conventional interferometry consists in the broad-band light source applied for illumination. Whereas in conventional interferometry the illumination light is described by only an (almost) discrete angular frequency  $\omega_0$ , now the light source can be characterized by its power spectral density function  $G(k)$ , having a broader spectral bandwidth  $\Delta k$  with the central wave number  $k(\omega_0)$ .

Furthermore, the source can also be described in spatial domain by its coherence function  $\gamma(z)$ , which is mutually related to the power spectral density function by the Fourier transform.

$$\gamma(z) = \mathcal{F} \{ \hat{G}(k) \}, \quad (4.3)$$



with  $\hat{G}(k)$  being the normalized power spectral density of the light source  $\hat{G}(k)$  [96]. These both functions  $\gamma(z)$  and  $G(k)$  describe the spectral behavior of the light source and give a measure for the expected coherence length  $l_C$ , which can be expressed as the full width at half maximum (FWHM) of the magnitude of the (complex) coherence function

$$l_C = \text{FWHM}(|\gamma(z)|). \quad (4.4)$$

Integrating –in case of broad-band sources– over all spectral components of the light source, i.e. including the coherence function  $\gamma(z)$  in (4.2), finally the measured LCI interference signal yields

$$\begin{aligned} \mathfrak{I}(z) &\propto \mathfrak{I}_{DC} + 2\sqrt{R_R R_S} |\gamma(z)| \cos(2k(\omega_0)z), \\ &\propto \mathfrak{I}_{DC} + 2 \operatorname{Re} \left\{ \gamma(z) \otimes \sqrt{R_R R_S} \delta(z - 2(z_S - z_R)) \right\}, \end{aligned} \quad (4.5)$$

with  $\gamma(z) = |\gamma(z)| \exp(i k(\omega_0) z)$ . The DC-component  $\mathfrak{I}_{DC}$  is proportional to the sum of reflectivities  $R_R + R_S$ , and is usually removed by bandpass filtering.

Furthermore, in OCT, as a version of LCI technique, the imaging is extended to interfaces or random scatterers at discrete depth positions  $z_{S_n}$  within the sample. We can describe the measured intensity signal  $\mathfrak{I}_{AC}$  as sum of all discrete burst-like interference signals by

$$\begin{aligned} \mathfrak{I}_{AC}(z) &\propto 2 \operatorname{Re} \left\{ \gamma(z) \otimes \sum_n^N \sqrt{R_R R_{S_n}} \delta(z - 2(z_R - z_{S_n})) \right\}, \\ &\propto \sum_n^N \sqrt{R_R R_{S_n}} \exp(-(z_R - z_{S_n})^2 \Delta k^2) \cos(2k(\omega_0)(z_R - z_{S_n})), \end{aligned} \quad (4.6)$$

commonly assuming a Gaussian-shaped coherence function

$$\gamma(z) = \exp\left(-\frac{z^2 \Delta k^2}{2}\right) \exp(i k(\omega_0) z). \quad (4.7)$$

Since the reference mirror is moving/oscillating with the speed  $v_R$ , a Doppler frequency shift

$$\omega_D = \frac{2 v_R n}{c} \omega_0 = 2 k(\omega_0) n \frac{z_R}{t} \quad (4.8)$$

is introduced and acts as OCT-signal carrier frequency, whose amplitude is modulated by  $|\gamma(z)|$ .

The envelope of the burst signal  $\mathfrak{I}_{AC}(z(t))$  can be extracted by applying the 1D HT in the conventional way (compare 3.9) and taking the magnitude of the analytic signal. The amplitude  $a(z)$  and the maximum position  $z_i$  of the envelope of the signal burst  $\mathfrak{I}_{AC}(z)$  characterize both the *reflectivity* and the *depth* of the investigated structures.

Finally the squared amplitude signal  $\mathfrak{I}_r \propto a^2$  and its course over depth  $\mathfrak{I}_r(z)$  represents the interesting relation to be investigated by (structural) OCT, describing the backscattering profile  $R_S(z) = \sum_n R_{S_n} \delta(z - z_{S_n})$  of the sample. It is accordingly called reflectivity signal  $\mathfrak{I}_r(z) \propto a^2(z)$ .

In Figure 4.2 a) the typical OCT signal response for a two layer structure is depicted, with overlaid envelopes in Figure 4.2 b).

In similarity to ultrasound imaging the depth-resolved reflectivity signal  $\iota_r(z)$  at a fixed lateral position  $x$  is named as *A-scan*. By sequential scanning at laterally adjacent sites and concatenating the recorded A-scans to cross-sectional images  $\iota_r(x, z)$ , so-called *B-scans* are obtained. By regarding the  $(x, y)$ -field of view, *en-face* images or *C-scans*  $\iota_r(x, y)$  are extracted. Therefore, finally by OCT imaging in total a 3D image stack  $\iota_r(x, y, z)$  can be recorded. For the performed analysis we consider 2D image slices out of the 3D data stack in the following, chosen either as cross-sectional or as en-face images.

### 4.1.3 OCT: Imaging parameters

For the resolving power of OCT the axial-, lateral resolution, depth of focus and sensitivity are the characteristic quantities. In case of a Gaussian power spectrum of the light source the (temporal) coherence length determines the axial resolution  $\delta_z$  of the system with

$$\delta_z \propto l_C \propto \frac{1}{\Delta k} \propto \frac{\lambda_0^2}{\Delta \lambda}. \quad (4.9)$$

The lateral resolution  $\delta_x$ , similar to microscopy, results from the numerical aperture (NA) of the focusing optics with  $\delta_x \propto \frac{\lambda_0}{NA}$ . In OCT imaging  $\delta_x$  and  $\delta_z$  are decoupled from each other. High resolution OCT systems achieve axial resolution around one micron. If samples have to be investigated over an extended depth range, a trade-off between resolution and depth of focus has to be found or dynamic focusing techniques may be applied. For the realized conventional OCT setup the axial resolution in air has been determined as  $\delta_z \sim 10\text{--}20 \mu\text{m}$  in case of using a commercial SLD (with commonly  $\lambda = 850 \text{ nm}$  or  $1550 \text{ nm}$ ,  $\Delta \lambda = 50\text{--}100 \text{ nm}$ ) as illumination source.

## 4.2 Artifacts and noise in OCT imaging

OCT images exhibit different imaging artifacts and noise components. Possible artifacts may be caused by over-exposure of the detectors at glossy or highly specular reflecting structures. Vibrations during measurements may also result in erroneous signals and may interrupt lateral structures. For highly dispersive samples dispersion compensation techniques have to be applied. Multiple scattering and backreflection at nearly parallel structures (comparable with the etalon effect) leads to delayed signals and ghost images.

With respect to the noise, different contributions have to be considered: Noise caused by the electronic setup (e.g. photon shot noise, amplification noise, thermal noise at resistors), and speckle noise, resulting from the fluctuations of the propagating wave field.

In our considerations we want to assume that the speckle noise due to surface roughness, internally multiple backscattering and random delays of the forward propagating beam inside the specimen is the dominant noise. In detail the phenomena of speckles and their influence on OCT imaging will be considered in Section (5.2).

### 4.3 Advanced modifications of OCT imaging

Conventional OCT, while imaging the structural composition of the sample, can be modified to obtain additional information about material behavior and functionality. Besides the OCT-intensity signal, phase and frequency of the interference signal can be exploited for the investigation of dynamical or transient phenomena, for the visualization of optical anisotropies or for the analysis of stress states inside the specimen.

Exploiting the complex nature of the light as vector wave, i.e. utilizing not only the scalar-valued *intensity*, but also the *phase*, *frequency* or *retardation* of the wave for signal generation allows to extend the information amount obtainable by OCT techniques.

Applying OCT techniques to probing specimens containing moving particles and measuring the Doppler frequency shift of the backscattered interference signal arising from the moving scatterers give the base for Doppler OCT methods. Enabling a local characterization of the spatial and temporal velocity distribution of e.g. particle flows in micro devices, phase or frequency-sensitive modifications of OCT have been demonstrated both in biological application field (e.g. for in vivo noninvasive blood flow measurements [106]) and in the field of technical fluid dynamics. These OCT-versions may be exploited for the investigation of laminar and turbulent flows in micro-channels [107], for turbulence monitoring [108] or for the evaluation of transient mixture processes [109].

Extending standard OCT by polarization-sensitive elements (as polarizing beamsplitters, prisms and wave plates), these techniques can be applied for the investigation of optically anisotropic materials (i.e. varying with respect to their refractive index or birefringence). Phase-related features (as optical path length or refractive index, regarded in Chapter (6)) or polarization-related features (as phase retardation and optical axis orientation, regarded in Chapter (5)) can be extracted by modifications of conventional OCT setups to phase-sensitive configurations. For phase-sensitive OCT-techniques different realizations have been described in literature exploiting either phase or frequency information in the time domain [114, 106], or in the Fourier domain [115].

In general phase information shows a much higher sensitivity with respect to deformation, thickness or refractive index variations of the sample compared to intensity-based measurements. Based on phase-sensitive techniques an axial resolution corresponding to the (sub-)nanometer range [110, 112] can be achieved in OCT imaging modalities, whereas the axial resolution of current intensity-based OCT systems is limited to about one micrometer size range.

In our work we perform phase-sensitive OCT measurements using two optical configurations:

- First, by a polarization-sensitive OCT (PS-OCT) setup, enabling two-dimensional depth-resolved retardation imaging inside the probed specimen, as will be regarded in the following chapter.
- Second, by a modified differential phase contrast OCT (DPC-OCT) setup, measuring locally differential phase values and delivering finally the lateral phase derivatives as en-face images from the recorded *3D sample*, as will be regarded in Chapter (6).



## Chapter 5

# PS-OCT for Birefringence and Stress Imaging

In this chapter we focus on a modification of phase-sensitive OCT imaging, which exploits in particular the state of polarization of the light. The investigated specimens are again turbid, scattering materials, similar as in conventional OCT, but now they exhibit additionally a locally distributed internal birefringence. The birefringence causes in general a change of the polarization state, introducing a phase retardation between both orthogonally polarized wave components of the measured interference signal. This phase retardation represents the main quantity of interest for PS-OCT imaging, as a type of polarimetric imaging [113], and can be visualized in so called *retardation* images. So, imaging the phase retardation becomes a possibility to visualize the magnitude of anisotropy of the investigated specimen. Furthermore, the obtainable information can be extended by information about the optical axis orientation within the material.

In the following we will briefly describe the *PS-OCT imaging technique*, the modifications to conventional OCT and characteristic features of the (phase) retardation images. Especially the importance of speckles and the interplay between the backscattering signal and the speckle noise in retardation images will be discussed. A complex *speckle noise* model, as mostly applied in coherent imaging, will be adapted to become suitable for *modeling* of PS-OCT retardation signals and for simulation of noisy retardation images. Based on these simulated data and furthermore, on measured data in different real-world test applications we demonstrate a *2D reconstruction* method for the birefringence and stress distribution. We show the capability of the developed procedure as a comprehensive approach for recovering spatially resolved information and conclusions about birefringence or stress states within the materials under investigation in PS-OCT imaging.

### 5.1 PS-OCT: Imaging technique

The striking potential of PS-OCT imaging consists in its applicability for the investigation of optically anisotropic materials. These materials may exhibit an birefringence, being already inherent or caused due to different external influences (e.g. the effect of stress, load, temperature, extrusion or moulding in production processes, etc.). The resulting birefringence within the material may emerge as stress/strain-, flow-, or temperature-induced birefringence [117, 118, 119]. We want

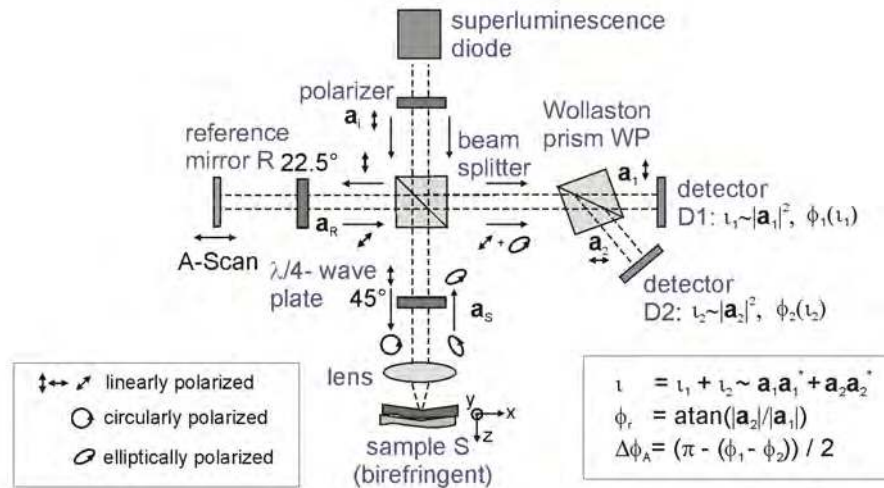


Figure 5.1: Schematic representation of the TD-PS-OCT optical setup. Especially the polarizing components, both quarter wave plates (under  $45^\circ$  and  $22.5^\circ$  orientation) and the polarizing beam-splitter (here realized as a Wollaston prism), introduced in addition to the conventional OCT setup, should be mentioned. The polarization states of the different wave components are schematically indicated.

especially to consider induced birefringence states, as they contain the encoded information about the causing quantities, and focus on imaging of optical anisotropies in materials mainly due to stress-induced birefringence.

### 5.1.1 PS-OCT: Optical configuration

As explained in the previous chapter for conventional OCT imaging, for recording a (cross-sectional) reflectivity image only a single detector is necessary. Now, in phase-sensitive OCT the phase relations between wave components, having orthogonal polarization directions to each other, are exploited. Both polarization components of the interference signal therefore are recorded by two detectors. The depth-resolved change of the initial polarization state, which is caused by the sample, yields the essential information, measured in PS-OCT imaging. To facilitate the measurement of changing polarization states through the material the OCT setup has to be modified and extended in the following way [116]:

- In contrast to the conventional OCT system light with a defined state of *polarization* is required in case of PS-OCT imaging.
- By introducing additionally two *quarter wave plates* (with correct axis orientations) in the

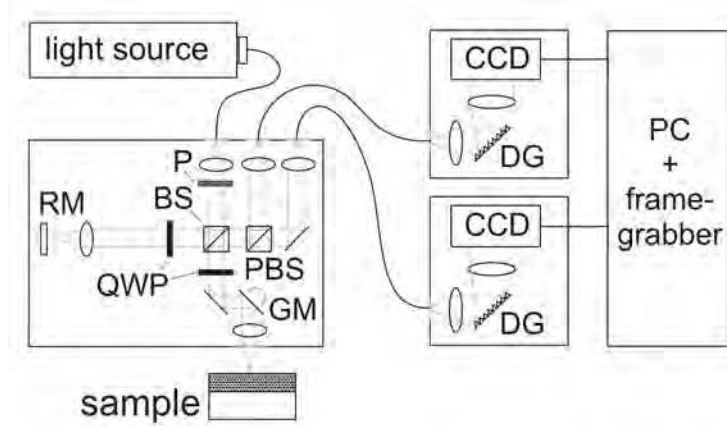


Figure 5.2: Schematic representation of the SD-PS-OCT optical setup, containing diffractive components in addition to the TD setup. (BS beam splitter, QWP quarter wave plate, P polarizer, DG diffractive grating, RM reference mirror, CCD charge coupled device camera)

imaging setup, a polarization-sensitive interference of sample and reference wave can be achieved.

- Additionally, a *polarizing beam splitter* in front of the detectors allows the splitting of both horizontally and vertically polarized wave components, which interfere separately at the *two detectors*.

The scheme for a PS-OCT configuration, realized again as a Michelson configuration and operating in the TD regime, is depicted in Figure 5.1. Similar to the conventional OCT also PS-OCT imaging may be performed in the spectral domain (SD). The corresponding SD-PS-OCT setup is sketched in Figure 5.2. In this case the two amplitude and phase signals are given by computing the inverse Fourier transform of both recorded spectra, and relating both magnitudes and phases to each other.

The data acquisition for our PS-OCT imaging application has been performed by means of both versions, as TD-PS-OCT and SD-PS-OCT configuration.

By the described optical setup modifications the acquisition of two individual signals ( $\iota_1$  and  $\iota_2$ ) is finally enabled. Both signal components, representing the interference signal of both polarization components, can be expressed, as

$$\iota = \begin{pmatrix} \iota_1 \\ \iota_2 \end{pmatrix} \propto \begin{pmatrix} \mathbf{a}_1 \mathbf{a}_1^* \\ \mathbf{a}_2 \mathbf{a}_2^* \end{pmatrix} = \begin{pmatrix} |a_1|^2 \\ |a_2|^2 \end{pmatrix} \quad (5.1)$$

$$\propto \begin{pmatrix} (\mathbf{a}_{R1} + \mathbf{a}_{S1})(\mathbf{a}_{R1} + \mathbf{a}_{S1})^* \\ (\mathbf{a}_{R2} + \mathbf{a}_{S2})(\mathbf{a}_{R2} + \mathbf{a}_{S2})^* \end{pmatrix}, \quad (5.2)$$

in an analogue way to the conventional OCT.

In Figure 5.3, the schematic PS-OCT signals are depicted for a structure with two interfaces.

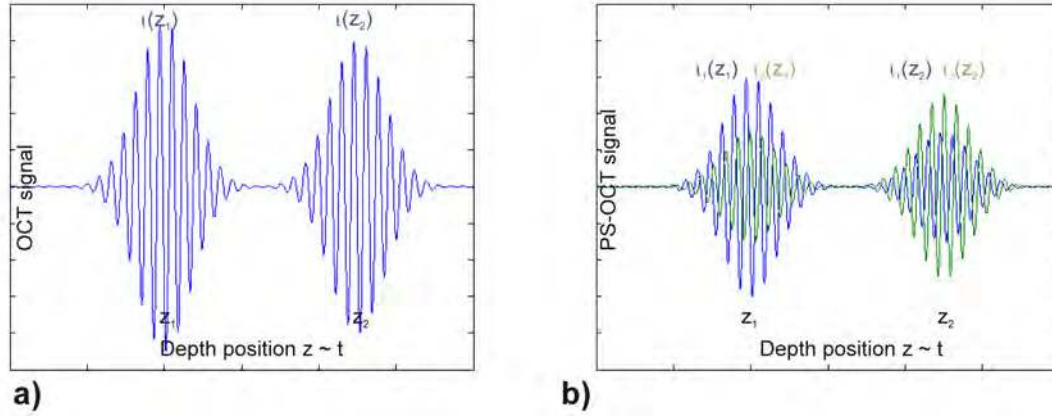


Figure 5.3: Illustration of a PS-OCT signal bursts. a) Conventional OCT interference signal (A-scan), b) dual channel PS-OCT interference signals (A-scan).

### 5.1.2 PS-OCT: Image types

Since there are two detectors in use, recording in their both channels the horizontally and the vertically polarized components of the interference signal, their mutual amplitude ratio (between  $a_1$  and  $a_2$ ) and phase relation between ( $\phi_1$  and  $\phi_2$ ) can be exploited for imaging. These mutual relations can be regarded either by means of the Stokes vector representation [120] or by means of the *reflectivity, retardation and optical axis orientation* OCT image representation [121]. In the latter case, the dependencies between amplitude and phase signals and the resulting images in PS-OCT can be expressed as [122]:

- **Reflectivity (intensity) image:**  $\iota_r(x, z)$ :

The reflectivity image is obtained as sum of the intensity signals  $\iota_1$  and  $\iota_2$  recorded at both detectors (1) and (2).

$$\iota_r(x, z) = \iota_1(x, z) + \iota_2(x, z) \propto a_1(x, z)^2 + a_2(x, z)^2. \quad (5.3)$$

It represents the total intensity comparable with the reflectivity image in conventional OCT.

- **Retardation image:**  $\phi_r(x, z)$ :

In birefringent materials a phase delay between the two orthogonally polarized wave components is caused due to the difference of the refractive indices  $n_O$  and  $n_E$  of the ordinary and extraordinary wave  $\Delta n = n_O - n_E$ , resulting in different phase velocities of both wave component. In general, the delay causes an elliptical polarization state, being here a measure for the internal birefringence. The ellipticity of the signal is recorded by the two detectors measuring either the horizontally or vertically polarized interference signal. Regarding the amplitude ratio of both detector signals the phase retardation between the two components can be represented as

$$\phi_{rw}(x, z) = \arctan \frac{|a_2(x, z)|}{|a_1(x, z)|}, \quad (5.4)$$

with index  $w$  denoting the wrapped phase retardation, which is mapped into the interval  $[0, \pi/2)$ . The index  $c$  names the cumulative (or continuous) phase retardation, which is



obtained by the accumulation of all incremental phase retardation values  $d\phi_{rc}$  over depth caused by the internal birefringence distribution  $\Delta n_B(x, z)$

$$\phi_{rc}(x, z) = \int_{\phi(z_0)}^{\phi(z)} d\phi_{rc} \propto \int_{z_0}^z \Delta n_B(x, z') dz'. \quad (5.5)$$

■ **Optical axis orientation image:**  $\Delta\phi_a(x, z)$ :

The orientation of the fast optical axis of the material can be calculated from the phase difference between both interference signal as

$$\Delta\phi_a(x, z) = \frac{\pi - (\phi_1(x, z) - \phi_2(x, z))}{2}, \quad (5.6)$$

by applying the 1D Hilbert transform on the interferograms of both detector signals.

■ **Birefringence image:**  $\Delta n_B(x, z)$

Retardation images may indicate inherent or induced birefringence distributions. The birefringence can be determined from the slope of the (cumulative) retardation image, which will be explained in detail in Section (5.3). The birefringence image is given as

$$\Delta n_B(x, z) = \frac{\lambda}{2\pi} \frac{\partial(\phi_{rc}(x, z))}{\partial z}. \quad (5.7)$$

### 5.1.3 PS-OCT: Fringe pattern parameters

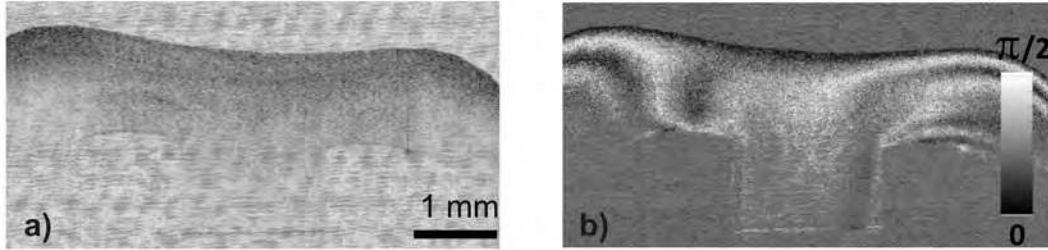


Figure 5.4: PS-OCT imaging examples of injection-molded plastic component. a) Cross-sectional reflectivity image, b) cross-sectional retardation image with inhomogeneous regions.

If a (continuous) birefringence distribution  $\Delta n_B(x, z)$  causes a phase retardation  $\phi_{rc}(x, z)$ , then the wrapped retardation image  $\phi_{rw}(x, z)$  may show fringe patterns as typical image structure in PS-OCT imaging, even if the reflection image does not reveal any structural information. In Figure 5.4 a), the reflectivity image of an injection-moulded plastic component is depicted, characterized by an isotropic backscattering behavior with slightly decaying intensity over depth. However, the corresponding retardation image exhibits typical fringe patterns, which indicate optical anisotropies within the specimen, as depicted in Figure 5.4 b) in comparison.

As already explained in Section (3.1), a fringe pattern is characterized by its *local amplitude*, its *instantaneous spatial frequencies* or *local phase*, and its *local orientation* as particular features considered in an local neighborhood.

Furthermore, the *modulation depth*  $M_D$  represents a characteristic parameter for the fringe visibility or fringe modulation contrast, which in retardation images is strongly dependent on the probed material and the achievable penetration depth. It can be determined as

$$M_D = \frac{\Delta I}{I_m} = \frac{I_{max} - I_{min}}{I_{max} + I_{min}}, \quad (5.8)$$

as ratio between modulation  $\Delta I$  and mean  $I_m$ , where  $I_{max}$  and  $I_{min}$  denotes the (noise-free) extrema values of the visualized fringes.

The SNR, in case of analyzing fringe patterns, is mostly defined by the ratio of the fringe modulation to the noise variance  $\sigma^2$  as

$$SNR_{Fringe} = 20 \log\left(\frac{\Delta I}{\sigma}\right). \quad (5.9)$$

The spatial distribution of the retardation fringes, expressed by their local descriptors, especially phase and frequency, encodes the information about local birefringence and related quantities, which we want finally to extract by the demodulation methods.

The modeling and the analysis of the fringe pattern will be considered in Section (5.3) and Section (5.4). The importance of speckles therein for image formation and fringe visibility reduction in PS-OCT will be explained in Section (5.2). Here, first the investigated specimens and test situations in PS-OCT imaging are described, and then a comparison with photoelasticity imaging is drawn.

#### 5.1.4 PS-OCT retardation imaging: Testing and samples

The test samples are chosen with respect to their use for different real-world strain/stress test applications, as there have been performed: A tensile test, a bending test, and an evaluation for the optimization of photolithographic patterning process. The materials are probed by PS-OCT with respect to their internal anisotropies, especially with respect to their inherent or stress-induced birefringence. They are chosen from different polymer and photo-resist materials. In particular, we focus on:

- **Sample PS1:** Polyurethane (PU) elastomer test sample,
  - being the specimen for tensile testing due to its elasticity property,
  - with the dimensions of  $\sim 5 \times 1 \text{ mm}^2$ , as shown in Figure 5.5 a),
  - investigated by the FD-PS-OCT setup ( $\lambda_0=1550 \text{ nm}$ ,  $\delta_z=19 \mu\text{m}$  in air).
- **Sample PS2:** Low density polyethylene (LDPE) polymer test sample,
  - being the specimen for bending testing due to its bending property,
  - with the dimensions of  $\sim 10 \times 1 \text{ mm}^2$ , as shown in Figure 5.5 b), -investigated by the TD-PS-OCT setup ( $\lambda_0=1550 \text{ nm}$ ,  $\delta_z=19 \mu\text{m}$  in air).
- **Sample PS3:** Photo-resist (PR) mould structure,
  - being a transparent specimen for the optimization of the photolithographic patterning process,
  - with the dimensions of  $\sim 3 \times 2 \text{ mm}^2$ , as shown in Figure 5.5 c),
  - investigated by an en-face scanning PS-OCT setup ( $\lambda_0=800 \text{ nm}$ ,  $\delta_z=3 \mu\text{m}$ ).

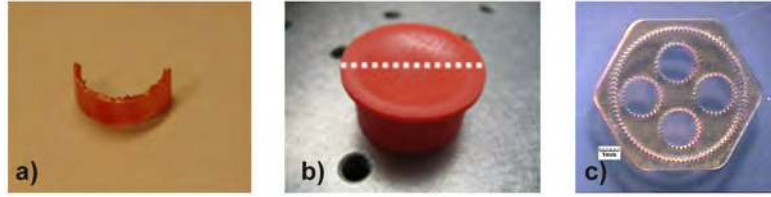


Figure 5.5: Representation of specimens utilized in PS-OCT retardation imaging for birefringence analysis and for strain/stress testing. a) Polyurethane elastomer specimen, b) low density polyethylene specimen, c) photo-resist mould structure for miniaturized gear wheel production.

### 5.1.5 Comparison of PS-OCT with conventional photoelasticity techniques

Nowadays, for the characterization of internal birefringence and stress states in loaded or deformed materials a huge variety of numerical methods based on finite element or boundary element methods are available [123, 124]. They are also applied as state of the art techniques for the computation and prediction of local birefringence or stress distributions [125, 126]. But nevertheless, the experimental verification of the calculated results remains of essential importance.

Photoelasticity (PE) techniques represent the classical experimental method for the analysis of strain/stress states in materials [127, 128]. However, fully transparent birefringent specimens are required in PE setups, which work usually in transmission mode. Therefore, PE imaging is only feasible in connection with transparent birefringent models, which are scaled to the sample of interest, or for weakly scattering, almost transparent specimens [129].

In contrast, PS-OCT enables especially the investigation of anisotropies and stress states in turbid birefringent materials. A scheme of the principle optical setup for both PE and PS-OCT imaging is shown comparatively in Figure 5.6 a) and b).

Furthermore, an important difference of the two methods is given by the specific recording of the retardation signal. PE measurements allow only the determination of the global, total (T) retardation  $\phi_T(x, y)$  through a (thin) specimen of thickness  $\Delta z$  in transmission direction, with

$$\phi_T(x, y) \propto \overline{\Delta n_B}(x, y) \Delta z. \quad (5.10)$$

In comparison, by applying PS-OCT imaging a depth-resolved, cumulative retardation  $\phi_{rc}(x, y, z)$  is obtained according to (5.5). Hence, in PE measurements the birefringence (or stress) can only be determined as average value over thickness  $\overline{\Delta n_B}(x, y)$ . Whereas, in PS-OCT the birefringence may be characterized as a spatially resolved quantity and especially, as the local slope of the cumulative retardation over depth, as  $\Delta n_B(x, y, z) \propto \frac{\partial \phi_{rc}(x, y, z)}{\partial z}$  according to (5.7). In PS-OCT, as a coherent imaging method and by measuring in particular, turbid scattering samples, retardation images are much more corrupted, compared to their PE-counterparts, by the inherent speckle patterns. The speckle character in PS-OCT imaging in comparison to PE is demonstrated in Figure 5.6 c) and d) for two technical structures under load. Therefore, an additional denoising during birefringence and stress analysis is almost required for a quantitative analysis of PS-OCT images.

In the following we will review the phenomenon of speckles in coherent imaging, first for OCT imaging, and second, with emphasis on PS-OCT retardation imaging.

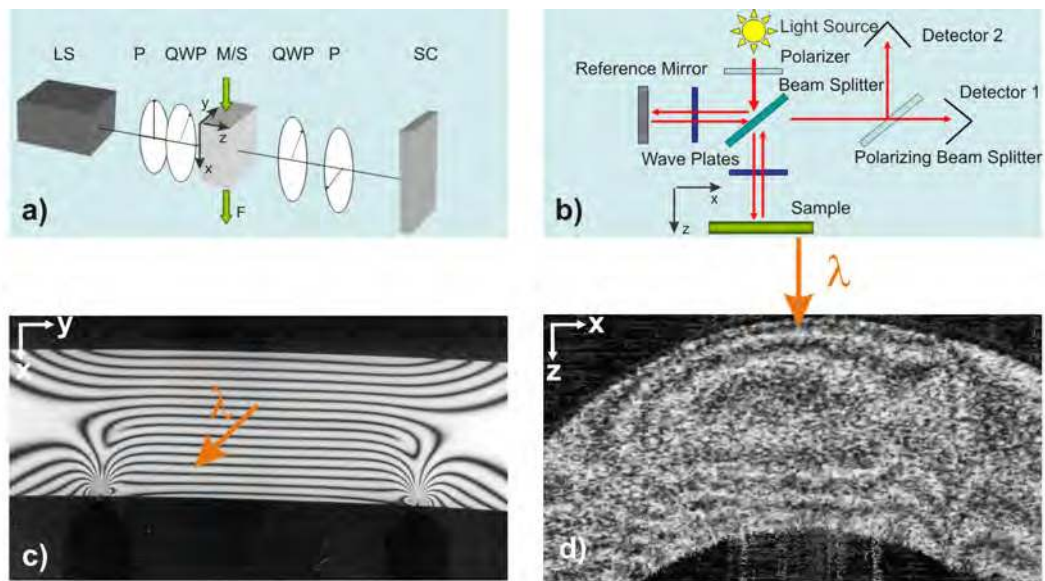


Figure 5.6: Comparison of PS-OCT with conventional photoelasticity (PE) imaging. a) Scheme of the classical PE configuration working in transmission mode, b) scheme of the PS-OCT optical setup working in reflection mode, c) transparent test model under a two point load with photoelastic fringes, imaged by PE technique, [185], d) polymer bending test samples with typical retardation fringes, examined by PS-OCT. (LS light source, P polarizer with indicated orientation, QWP quarter wave plates, M model, S sample, SC camera, F force/load)

## 5.2 PS-OCT: Speckles and speckle noise

Speckles are a phenomena of various coherent imaging techniques, ubiquitously encountered e.g. in interferometry, holography, or synthetic aperture radar (SAR) imaging. Speckles may further arise by imaging through the atmosphere or are caused in wave guiding applications. In some coherent imaging techniques speckles can be considered ambiguously: As noise, degrading the image, but they can also deliver valuable information, as used e.g. in electronic speckle interferometry. Being of this twofold nature, they are also a phenomenon of OCT imaging. Here we want to consider first speckles generally as laser speckles, then speckles in OCT, and based on this, finally, we want to derive a modeling of speckles in PS-OCT for a homogeneous birefringent material.

### 5.2.1 Laser speckles

The speckle formation can be described as a random stochastic process. Speckles are caused by random interferences due to stochastic fluctuations (in scale of the wavelength) in the wave propagation path, e.g. by atmospheric fluctuations, by random roughness distributions of the back-reflecting surfaces or, as in OCT, by the random scatterer distribution inside the investigated sample. The superposition of these independent random-phased wave components gives rise to the speckle noise. Speckles can be described statistically with respect to their amplitude and phase as complex-valued random variables or as scalar-valued random variable with respect to their intensity. Taking into account that in coherent imaging techniques light is exploited as a complex quantity, also a complex-valued model and notation for the speckle noise  $\mathbf{n}_{Sp}$  should be chosen.

Assuming a wide-sense stationary stochastic process, fully-developed speckles can be expressed according to [101] by their random real and imaginary part  $(R_{Sp}, I_{Sp})$  as  $\mathbf{n}_{Sp} = R_{Sp} + i I_{Sp}$ . Usually, speckles can be modeled by a random walk approach as an addition of random phasors ( $\mathbf{c}_{Spk} = c_{Spk} \exp(i\phi_{Spk})$ ) with

$$R_{Sp} = \sum_k^N c_{Spk} \cos(\phi_{Spk}), \quad (5.11)$$

$$I_{Sp} = \sum_k^N c_{Spk} \sin(\phi_{Spk}), \quad (5.12)$$

provided that amplitudes  $c_{Spk}$  and phases  $\phi_{Spk}$  are statistically independent from each other and for each  $n \neq m$ . Furthermore, the phase components  $\phi_{Spk}$  are uniformly distributed in the interval  $[-\pi, \pi)$ .

For a sufficiently large number of steps  $N$  and applying the central limit theorem the joint probability density function  $p_{(R_{Sp}, I_{Sp})}(R_{Sp}, I_{Sp})$  is given by [101]

$$\begin{aligned} p_{R_{Sp}, I_{Sp}}(R_{Sp}, I_{Sp}) &= \frac{1}{2\pi\sigma_{Sp}^2} \exp\left(-\frac{R_{Sp}^2 + I_{Sp}^2}{2\sigma_{Sp}^2}\right) \\ &= \frac{1}{2\pi\sigma_{Sp}^2} \exp\left(-\frac{R_{Sp}^2}{2\sigma_{Sp}^2}\right) \exp\left(-\frac{I_{Sp}^2}{2\sigma_{Sp}^2}\right), \end{aligned} \quad (5.13)$$

describing a circular complex Gaussian random variable, which can be separated into two independent Gaussian probability density functions for the real and imaginary components with equal variances  $\sigma_{S_p}^2$ .

Considering speckles as phasors  $\mathbf{n}_{S_p} = a_{S_p} \exp(i \phi_{S_p})$  with the random magnitude  $a_{S_p} = \sqrt{R_{S_p}^2 + I_{S_p}^2}$  and the random phase  $\phi_{S_p} = \arctan(\frac{I_{S_p}}{R_{S_p}})$ , the marginal probability density functions for magnitude and phase are given by

$$p_{a_{S_p}}(a_{S_p}) = \frac{a_{S_p}}{\sigma_{S_p}^2} \exp\left\{-\frac{a_{S_p}^2}{2\sigma_{S_p}^2}\right\}, \quad (5.14)$$

and

$$p_{\phi_{S_p}}(\phi_{S_p}) = \frac{1}{2\pi}, \quad (5.15)$$

representing a Rayleigh density function for the random amplitude and a uniform distribution for the random phase of the speckle noise.

Characterizing the speckles by their intensity  $\mathfrak{I}_{S_p} \sim (a_{S_p} a_{S_p}^*)$  as scalar-valued random variable the corresponding density function can be derived from (5.14), yielding the well-known exponential speckle statistics

$$p_{\mathfrak{I}_{S_p}}(\mathfrak{I}_{S_p}) = \frac{1}{2\sigma_{S_p}^2} \exp\left(-\frac{\mathfrak{I}_{S_p}}{2\sigma_{S_p}^2}\right). \quad (5.16)$$

Considering a (conventional) interferometric setup, where sample and reference path show two independent, almost equal-strength speckle fields  $\mathfrak{I}_{S_{p1}}$  and  $\mathfrak{I}_{S_{p2}}$  with the mean  $\mathfrak{I}_m$ , and regarding finally the sum of these two speckle fields  $\mathfrak{I}_{S_{p12}} = \mathfrak{I}_{S_{p1}} + \mathfrak{I}_{S_{p2}}$ , then the probability density function for the resulting speckle intensity may be approximately described as Gamma-distribution by

$$p_{\mathfrak{I}_{S_{p12}}}(\mathfrak{I}_{S_{p12}}) = \frac{\mathfrak{I}_{S_{p1}} + \mathfrak{I}_{S_{p2}}}{\mathfrak{I}_m^2} \exp\left(-\frac{\mathfrak{I}_{S_{p1}} + \mathfrak{I}_{S_{p2}}}{\mathfrak{I}_m}\right). \quad (5.17)$$

## 5.2.2 Speckles in OCT

With respect to the origin of the speckles two aspects have to be taken into account for OCT imaging: Laser speckles as general phenomenon in coherent imaging techniques and speckles determined by the material statistics of the object under investigation.

For the modeling of the specific scattering properties of materials an extensive amount of sophisticated methods exists, often including Monte-Carlo based simulations in the model approach for the description of the random nature of the backscattering process [97]. Exploiting these material dependent speckle phenomena in OCT, speckles are not only to consider as noise but they also provide the OCT image information content, e.g. varying materials may be distinguished by their different statistics [98], or with respect to their autocorrelation functions [99]. Hence, speckles in OCT imaging play a twofold role, they are both signal-carrying speckles and signal-degrading speckles [100].

### 5.2.3 Speckle noise in reflectivity images

In general scalar-valued speckle noise  $n_{isp}$  is considered as multiplicative noise [102] in the measured intensity image  $\iota_n(x,y)$  corrupting the theoretical intensity image  $\iota(x,y)$  by

$$\iota_n(x,y) = \iota(x,y)n_{isp}, \quad (5.18)$$

assuming a mean value of one.

In literature different probability distributions are suggested for multiplicative speckle noise depending on the special coherent imaging technique.

In OCT imaging the assumption of superposition of equal-strength speckle fields (as assumed in (5.17)) is not generally fulfilled. Due to the different reflectivities of the sample structures and of the mirror surface the reference wave field has often a multiple higher intensity than the sample wave, but on the other hand a much lower noise variance. Hence, and taking into account the coherent amplification, the probability density function for the amplitude of the sample wave can be regarded as essential contribution for the speckle noise in reflectivity images, amplified by a multiplicative factor due to the reference mirror. Therefore, the speckle noise probability density function in conventional OCT can be described by an almost Rayleigh-distribution function [95],[100] (compare (5.14)). Furthermore, for OCT imaging often logarithmic compression is used [103]. A frequently applied approximation and simplification for the noise in *logarithmic reflectivity* image is given by assuming an additive white Gaussian noise.

### 5.2.4 Speckle noise in OCT retardation images

Whereas reflectivity images are scalar-valued intensity images and the noise is related to the intensity as scalar quantity in a multiplicative way, for the explanation and the modeling of speckles in *retardation* images we use a complex-valued noise model. In PS-OCT imaging we have in general two detector signals, as explained in Section (5.1), which can be considered as real and imaginary component of a complex-valued image. (Note: In the realized measurement configuration, in general only the ratio of both components, as measured retardation image, had been available.) Taking into account this complex character, the model supposes that the (complex) noisy retardation signal can be described as *sum of a deterministic known phasor and a random-valued phasor* [101], which is the complex speckle noise.

This model will be explained in the following and is applied for our simulation of retardation images.

## 5.3 PS-OCT: Modeling of retardation and birefringence/stress images

Here we want to derive a model of noisy retardation images, including further relevant stress states. The model should be typical for the specimens in the regarded test situations, which have been examined by PS-OCT imaging. Afterwards, based on the theoretical considerations, the simulation of retardation images is performed. The generated images are used for a first verification of the reconstruction method in the following.

### 5.3.1 Comparison: Retardation and phase

It should be emphasized that retardation images and conventional phase-based images (as would be obtained e.g. by classical interferometry or SAR imaging) are distinguished in particular in their characteristic wave shape.

According to (5.4) the retardation signal  $\phi_{rw}(z)$  is given by the relation

$$\phi_{rw}(z) = \arctan \frac{|a_2(z)|}{|a_1(z)|} = \arctan(|\tan(\phi_{rc}(z))|). \quad (5.19)$$

The physical relevant condition – only be able to measure intensity values  $\iota_{1,2}$  at both detectors – is expressed here by  $|a_{1,2}| = \sqrt{\iota_{1,2}}$ , i.e. only positive values for the measured signals are regarded. The (phase) retardation definition (5.19) is modified from the standard phase notation,

$$\phi_w(z) = \arctan \frac{a_2(z)}{a_1(z)} = \arctan(\tan(\phi_c(z))), \quad (5.20)$$

by the positivity assumption. Hence, we are restricted for the following complex signal notation to the first quadrant of the unit circle. As the result of this positivity constraint for the measured signals we obtain a periodicity of  $\pi$  for the wrapped retardation instead of the usual periodicity of  $2\pi$  in standard phase representation.

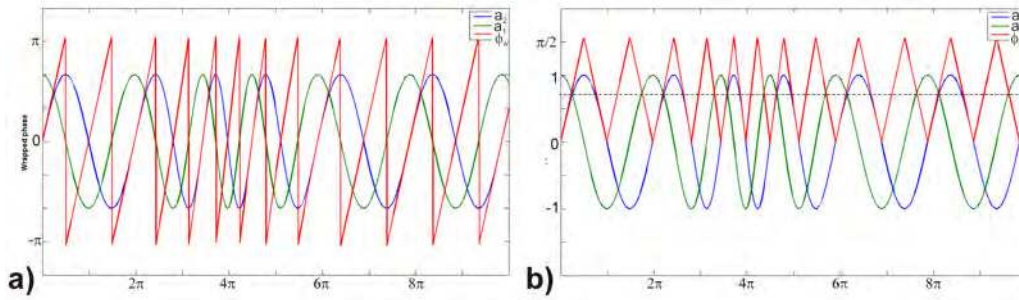


Figure 5.7: Comparison of a) wrapped phase and b) wrapped retardation of two sinusoidal signals with spatially varying frequency.

Furthermore, it should be emphasized that according to (5.19) the wrapped retardation  $\phi_{rw}(z)$  is shaped as a triangular (tri) wave in contrast to the 'sawtooth' profile of the conventional wrapped phase, as illustrated in Figure 5.7. The depth-resolved wrapped retardation we will describe as phase or frequency modulated triangular wave with

$$\phi_{rw}(z) = \text{tri}(\phi_{rc}(z)) \quad (5.21)$$

with

$$\begin{aligned} \text{tri}(\phi_{rc}) &= \phi_{rc} - k\pi \quad \text{for } k\pi \leq \phi_{rc} \leq k\pi + \frac{\pi}{2}, \quad k = 0, 1, \dots \\ \text{tri}(\phi_{rc}) &= k\pi - \phi_{rc} \quad \text{for } k\pi - \frac{\pi}{2} \leq \phi_{rc} \leq k\pi, \quad k = 0, 1, \dots \end{aligned} \quad (5.22)$$

Due to this modification of the wave shape the usual demodulation scheme can not be applied directly or causes partly erroneous results, as has been demonstrated in Section (3.4). We show for



our reconstruction task an adaptation of the quadrature computation and demodulation scheme in the following, taking into account the triangular wave shape and changed periodicity of retardation signals.

### 5.3.2 Noise-free depth-resolved retardation signal

The backscattered intensity signals over depth  $\iota_1(z)$ ,  $\iota_2(z)$  at both detectors can be expressed as [104]

$$\begin{aligned}\iota_1(z) &\propto \cos^2(\phi_{rc}(z)) = \cos^2(k_0 z \Delta n_B), \\ \iota_2(z) &\propto \sin^2(\phi_{rc}(z)) = \sin^2(k_0 z \Delta n_B),\end{aligned}\quad (5.23)$$

assuming at first a homogeneous birefringent material with  $\Delta n_B$  and  $\phi_{rc}(z) \propto k_0 z \Delta n_B$ .

Starting our simulation, we consider the 'theoretical' amplitude signals  $a_1(z)$  and  $a_2(z)$  with

$$\begin{aligned}a_1(z) &\propto \cos(\phi_{rc}(z)), \\ a_2(z) &\propto \sin(\phi_{rc}(z)).\end{aligned}\quad (5.24)$$

Furthermore, both signals  $a_1(z)$  and  $a_2(z)$  are amplitude modulated over depth by the attenuation function  $a(z)$

$$\begin{aligned}a_1(z) &= a(z) \cos(\phi_{rc}(z)), \\ a_2(z) &= a(z) \sin(\phi_{rc}(z)),\end{aligned}\quad (5.25)$$

expressing the internal absorption and scattering processes. As assumed, these processes can be described by an exponential decay with

$$a(z) = a_0 \exp(-\alpha z),\quad (5.26)$$

characterized by the attenuation parameter  $\alpha$ .

For our modeling, both signal components  $a_{1/2}(z)$  are interpreted as the real and imaginary component of a phasor with a complex amplitude  $a(z)$  and a phase  $\phi_{rc}(z)$  by

$$\mathbf{a}(z) = a(z) \exp(i \phi_{rc}(z)) = a_1(z) + i a_2(z).\quad (5.27)$$

Taking this interpretation into account, a complex-valued approach for the description of the retardation signal and a description as phasor will be chosen in the following. First, the noise-free deterministic retardation phasor is considered, afterwards the noise modeling is included. The positivity constraint will be included in the statistical formulation (5.32) by the restriction of the (complex) retardation values to the first quadrant.

The noise-free retardation phasor is depicted as polar plot in Figure 5.8 a) for illustration of the description. The exponential decaying amplitude  $a(z)$  results in a spiral-shaped curve.

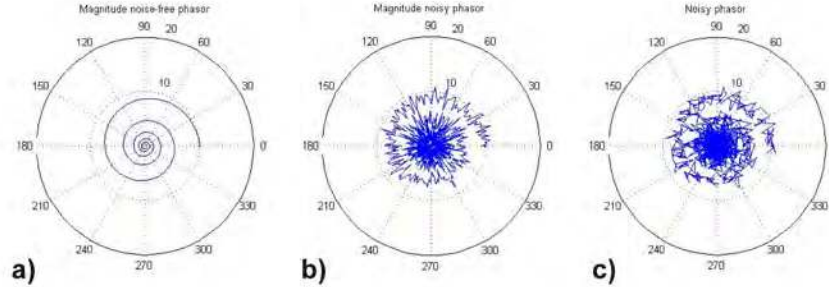


Figure 5.8: Polar plot representation of the (complex) retardation signal phasor. a) Noise-free signal phasor  $\mathbf{a}(a, \phi_{rc})$ , b) noisy signal phasor (with noise-free phase)  $\mathbf{a}_n(a_n, \phi_{rc})$ , c) noisy signal phasor  $\mathbf{a}_n(a_n, \phi_{rcn})$ .

### 5.3.3 Noisy depth-resolved retardation signal

In the performed PS-OCT experiments the investigated materials show different absorptions and scattering behavior. In substance the speckle variance depends on the transparency, thickness, or internal backscatterer distributions of the specimens. Although there is a huge amount of literature generally related to speckle noise [105], only little literature is available about modeling of speckles for especially PS-OCT retardation images. A method based e.g. on Monte Carlo simulation for PS-OCT noise modeling is described in [130].

In general, images taken by coherent optical imaging techniques and representing intensity quantities, are modeled to be corrupted by multiplicative speckle noise. Regarding only the phase, the noise is mostly assumed being uniform distributed. Taking into account an interferometric modeling of the imaging process, in [131] it is shown that the transition from the multiplicative noise model to the additive complex noise model can be performed in case of averaging over some adjacent sites. We suppose that this averaging is fulfilled after some multiple scattering events within the material.

For simulation of noisy retardation images we incorporate the previously described complex-valued random walk model of speckles in coherent imaging applications. We assume that the sum of random phasor components contributes to the speckle formation due to the random scattering of light inside the material (similar to the speckle formation at rough surfaces). Hereby, in our modeling, our main aim consists in the simulation of retardation images, having a similar appearance and being comparable in their statistics with the measured retardation data. In our simulated retardation images we want to consider only materials with continuously distributed backscatterers over depth, i.e. the aim does not consist in modeling material layers or interfaces here. Furthermore, we regard only materials with constant optical axis orientation value in our modeling. The various material characteristics can be represented in our approach in a simplified way by different attenuation parameters or changing noise variances of the generated speckles.

In the following a model of noisy retardation image is demonstrated, which allows to simulate

the observed phenomenon of vanishing retardation fringes over depth in some bulk materials. This reduced visibility of the fringe pattern is related to the absorption and (multiple) scattering behavior of the investigated specimens and therefore a strongly material-dependent feature in PS-OCT imaging.

As already mentioned, for the modeling of OCT *retardation images* and the speckle noise  $\mathbf{n}_{Sp}$  therein, we prefer the assumption of a complex-valued speckle noise, described in Subsection (5.2.4). The complex model, applied in the following, differs from the scalar-valued speckle noise  $n_{Sp}$  approach in Subsection (5.2.3) for *reflectivity images*, where the noise is regarded as a multiplicative one. Considering only the magnitude of the phasor as noisy quantity, the corresponding (complex-valued) retardation signal over depth is shown in Figure 5.8 b).

Now, the *retardation signal* is expressed as a (complex) sum of the known (deterministic) phasor  $\mathbf{a}(z)$  (modeling the noise-free signal) and a random phasor characterizing the speckle noise contribution  $\mathbf{n}_{Sp}$

$$\mathbf{a}_n(z) = \mathbf{a}(z) + \mathbf{n}_{Sp}. \quad (5.28)$$

The phasor of the noisy signal  $\mathbf{a}_n(z)$ , illustrated in Figure 5.8 c), is given as

$$\mathbf{a}_n(z) = a_n(z) \exp(i \phi_{rc n}(z)) = a_{n1}(z) + i a_{n2}(z). \quad (5.29)$$

In this approach we assume that the variance  $\sigma_{Sp}^2$  for both complex speckle noise components represents a constant value.

As we have derived in (5.15) the speckle phase can be assumed to be uniformly distributed, justifying an angular isotropic model of  $\mathbf{n}_{Sp}$ . Therefore, we can rotate the coordinate system in an appropriate way. Without loss of generality we suppose that the real and imaginary component of signal phasor  $\mathbf{a}(z)$  are degraded by each, the real and imaginary component of the speckles. According to (5.11)–(5.12) we can derive

$$\begin{aligned} a_{n1}(z) &= a(z) \cos(\phi_{rc}(z)) + \sum_k^N c_{Spk} \cos(\phi_{Spk}), \\ a_{n2}(z) &= a(z) \sin(\phi_{rc}(z)) + \sum_k^N c_{Spk} \sin(\phi_{Spk}). \end{aligned} \quad (5.30)$$

In Figure 5.9, the resulting noisy phasor signal  $\mathbf{a}_n$  is sketched. The speckle noise  $\mathbf{n}_{Sp}$  is drawn as an isotropic 'cloud' around a deterministic signal phasor  $\mathbf{a}$ .

According to [101] it can be shown that the marginal probability density function of the noisy signal *amplitude*  $a_n$  is described by a Rician density function as

$$p_{a_n}(a_n) = \frac{a_n}{\sigma_{Sp}^2} \exp\left(-\frac{a_n^2 + a(z)^2}{2\sigma_{Sp}^2}\right) J_0\left(\frac{a_n a(z)}{\sigma_{Sp}^2}\right), \quad (5.31)$$

with  $J_0$  denoting a first order modified Bessel function.

For sufficiently large signal amplitudes  $a(z)$  the Rician density function (5.31) tends approximately to a Gaussian distribution, and (5.31) converges to a Rayleigh distribution for signal amplitudes  $a(z) \rightarrow 0$ .

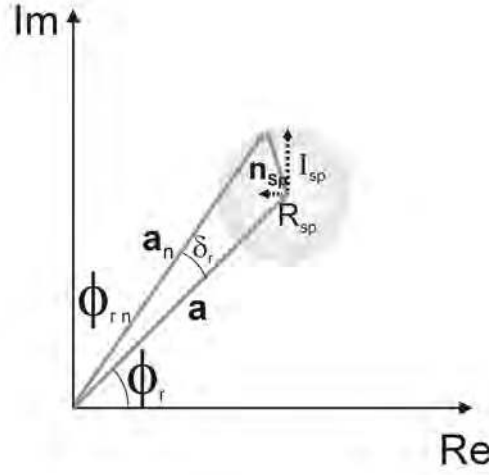


Figure 5.9: Schematic representation of a noisy signal phasor in polar plot representation. The noisy signal  $\mathbf{a}_n$  can be seen as sum of the noise free phasor  $\mathbf{a}$  and the complex speckle noise  $\mathbf{n}_{sp}$  (with a real and imaginary noise component  $I_{sp}$  and  $R_{sp}$ ), causing a variation of the magnitude and a rotation of the phase  $\phi_{rn} = \phi_{rc} + \delta_r$  of the deterministic phasor signal.

The marginal probability density function  $p_{\phi_{rn}}(\phi_{rn})$  for the random *phase* or *retardation* is given by

$$p_{\phi_{rn}}(\phi_{rn}) \approx \frac{1}{\sqrt{2\pi}\sigma_{Sp}/a(z)} \exp\left(-\frac{(\phi_{rn} - \phi_{rw})^2}{2(\sigma_{Sp}/a(z))^2}\right), \quad (5.32)$$

approximately describing again a Gaussian distribution for sufficiently large signal amplitudes  $a(z)$ . Its mean value equals  $\phi_{rw}$ , whereas the variance is given by

$$\sigma_{\phi_{rw}}^2 = \frac{\sigma_{Sp}^2}{a^2(z)}. \quad (5.33)$$

For  $a(z) \rightarrow 0$  and taking into account the periodicity of wrapped phase or retardation, (5.32) yields an uniform distribution function for the phase  $\phi_{wn}$  in the interval  $[-\pi, \pi)$ . As we are restricted to *positive values*  $|a_1|$  and  $|a_2|$ , the measured retardation as random variable  $\phi_{rn}$  is uniformly distributed in the interval  $[0, \pi/2)$ .

An exponential decay has been assumed for the attenuation function according to (5.26), i.e. the deterministic phasor is exponentially decreasing with the penetration depth. As a result, in the retardation signal we obtain with decreasing amplitude  $a(z)$  an increasing variance  $\sigma_{\phi_{rw}}^2(z)$  over depth, which is expressed as

$$\sigma_{\phi_{rw}}^2(z) \propto \sigma_{Sp}^2 \exp(2\alpha z). \quad (5.34)$$

Hence, this approach allows to model the *retardation* signal over depth as a random variable with an *increasing* noise variance. The increase depends on the attenuation parameter  $\alpha$ .

Finally, as shown in (5.13), the real and imaginary part of the speckles, modeled by the random walk approach, are normal distributed ( $\mathcal{N}$ ), independent and identically distributed random

quantities. Therefore, we can assign them to two Gaussian white noise components

$$n_1 = \sum_k^N c_{Sp_k} \cos(\phi_{Sp_k}), \quad (5.35)$$

$$n_2 = \sum_k^N c_{Sp_k} \sin(\phi_{Sp_k}), \quad (5.36)$$

for a sufficiently high number of steps  $N$ . Both noise components  $n_1$  and  $n_2$ , being normal distributed with  $n_1 \sim \mathcal{N}(0, \sigma_1^2)$  and  $n_2 \sim \mathcal{N}(0, \sigma_2^2)$ , represent the fluctuations in the two imaging and detection processes of both channels. As both channels are balanced, the same variances  $\sigma_1^2 = \sigma_2^2 = \sigma_{\phi_{Sp}}^2$  may be supposed. Additionally, other additive noise sources, representing e.g. the amplification or discretization, could be included by an increased variance.

Supposing now that both, real and imaginary signal part, are degraded by two independent additive noise components, we can finally show that the measured amplitude signals at both detectors can be expressed as

$$\begin{aligned} a_{n1}(z) &= a(z) \cos(\phi_{rc}(z)) + n_1, \\ a_{n2}(z) &= a(z) \sin(\phi_{rc}(z)) + n_2. \end{aligned} \quad (5.37)$$

### 5.3.3.1 Illustration: Retardation signal generation

Before the formation of a noisy (2D) retardation image with focus on the underlying anisotropy or stress model will be regarded in detail, here the retardation signal generation over depth, according to (5.25)–(5.37) for a single line (A-scan), starting from the noisy amplitude and intensity signals at both detectors in quadrature, should be illustrated in Figure 5.10 a)–c). A homogeneous birefringent material has been assumed for this illustration of 1D signal generation.

By the preprocessing step, depicted in Figure 5.10 d), an enhanced visibility of the smoothed retardation signal  $\tilde{\phi}_{rw}(z)$  over depth is achieved. For the 1D scheme the smoothing is performed by a moving average filter. In generally for the retardation images, the denoising operation can be realized in a more sophisticated way, e.g. by an adaptive median filter, wavelet filter, anisotropic diffusion methods, etc., as will be shown in Section (5.4). However, the averaged retardation signal can represent a non-zero mean signal. To correct the background we apply here the one-dimensional EMD method of Section (3.1) to imply a local zero-mean signal, as shown in Figure 5.10 e). After the – here only schematically illustrated preprocessing – a zero-mean retardation signal  $\tilde{\phi}_{rw}(z)$ , with decreasing amplitude and modulation depth, is finally obtained.

Considering now an *inhomogeneous internal birefringence* (or spatially distributed stress states) of an anisotropic material, a retardation fringe pattern with a spatially varying amplitude, frequency or phase is expected. After the schematically illustrated preprocessing the signal can be treated as an AM-FM signal, and (conventional) demodulation methods can be realized. We further assume that after the preprocessing, i.e. after denoising, smoothing, and therefore reduction of the higher harmonics, an almost harmonic wave shape can be supposed for  $\tilde{\phi}_{rw}(z)$ . The preprocessed signal can now approximately be described as

$$\tilde{\phi}_{rw}(z) \equiv I_P(z) \sim A(z) \cos(\phi_{rc}(z)), \quad (5.38)$$

taking into account only the fundamental mode.

By combining the retardation A-scans  $\phi_{rw}(z)$  in lateral ( $x$ ) direction to cross-sectional images (B-scans) the preprocessed (cross-sectional) retardation image  $I_P(x, z)$ , which is used for demodulation, approximately can be described as

$$I_P(x, z) \sim A(x, z) \cos(\phi_{rc}(x, z)). \quad (5.39)$$

The background  $B(x, z)$ , being a constant offset or having a locally varying low frequency baseline, has already been removed prior to the subsequent demodulation step.

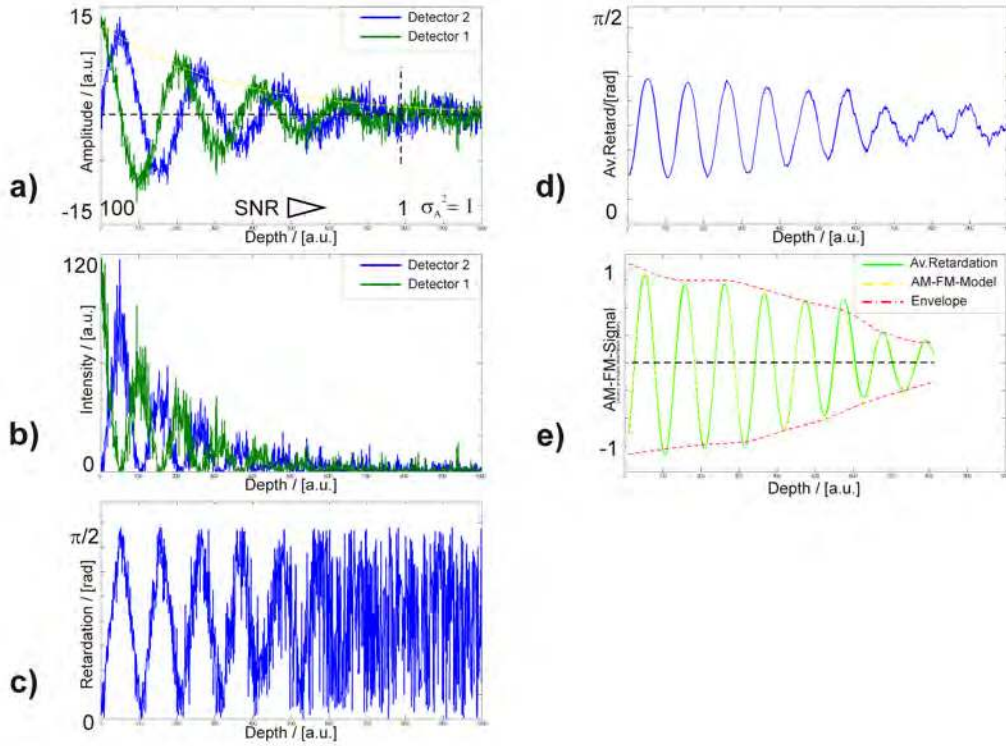


Figure 5.10: PS-OCT retardation signal generation (A-Scan) according to the random walk-model, resulting in increasing noise variance over depth in retardation image. a) Noisy amplitude signal over depth (parallel and orthogonal polarized E-field components), b) noisy intensity signal over depth (measured at detector 1 and 2), c) noisy retardation signal over depth, d) smoothed retardation signal over depth, e) zero-mean, normalized retardation signal over depth with overlaid envelope.

Summarizing, the different steps for retardation image generation with indicated noise behavior and the resulting retardation image are illustrated once more in Figure 5.11. The retardation  $\phi_{rc}(z)$  is modeled here for representing a locally inhomogeneous birefringence distribution in the material, (e.g. as would result from an almost point load acting on the material).

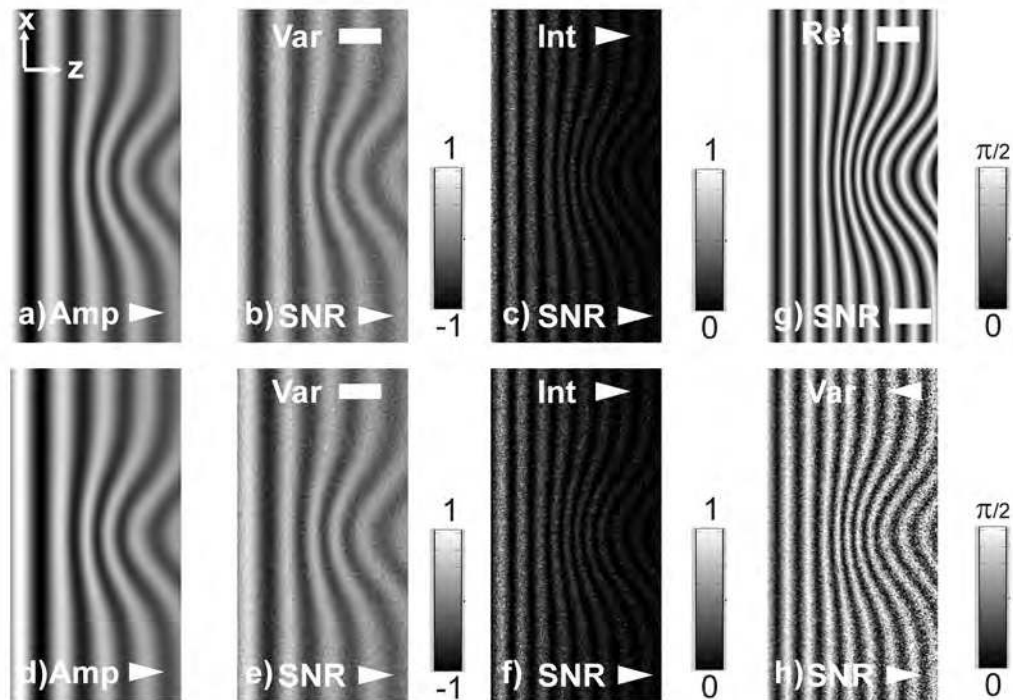


Figure 5.11: Generation of the cross-sectional PS-OCT retardation image according to the modeled sample M1.

a) Simulated cross-sectional amplitude image, corresponding to the cosine component, i.e. in-phase signal, b) simulated cross-sectional amplitude image, corresponding to (a) with additive Gaussian noise of constant variance over depth, c) simulated cross-sectional intensity image (at detector 1) corresponding to (b), d)–f) cross-sectional images, corresponding to the sine component, i.e. quadrature signal at detector 2, analog to (a)–(c), g) resulting cross-sectional retardation image *without* noise, h) resulting cross-sectional retardation image *with* noise. White symbols indicate increasing, constant or decreasing direction of the denoted quantity.

*Note:* (a) the amplitude signal over depth is decreasing due to attenuation, (b) the SNR is decreasing due to decreasing signal amplitude, (c) the SNR is decreasing, (g) the SNR is constant over depth.

(h) the resulting variance is increasing and hence, SNR is decreasing over depth. The amplitude images are only of theoretical nature, but required for modeling. The intensity images are the measurable quantity.

### 5.3.3.2 Comparison: Simulated and measured depth-resolved retardation signals

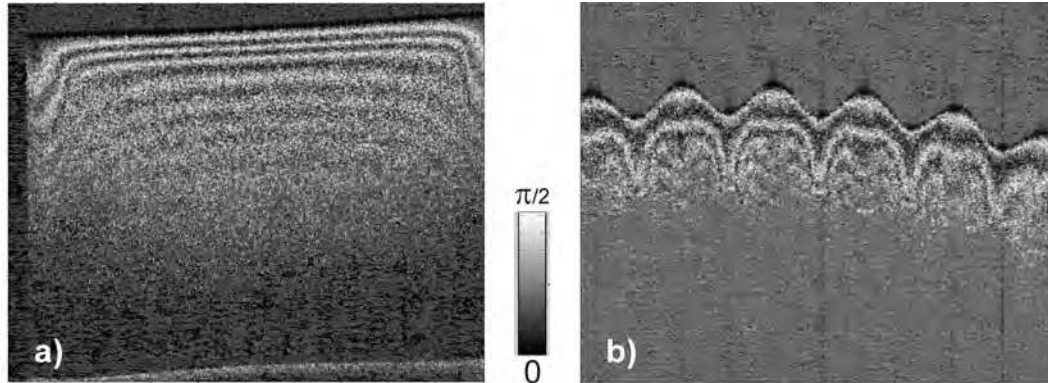


Figure 5.12: Comparison of cross-sectional retardation images, taken from a) a highly scattering, bulk polymer material, b) a weakly scattering, thin polymer material.

We compare the generated images with measured retardation data, especially with respect to the observed and simulated decrease of fringe visibility. Considering a variety of recorded retardation images there can be found examples for both: Retardation images showing a more or less constant modulation depth of the fringe pattern and having an almost constant noise variance over depth; and retardation images of specimens showing strongly disappearing fringes over depth. The first case can be referred to thin or weakly scattering, nearly transparent specimens, whereas the latter one may occur especially in thick bulk materials with highly multiple scattering properties, as illustrated in Figure 5.12. We have modified the classical 'sum of known phasor and noise' model, which supposes a constant deterministic phasor, in our approach by an exponentially decreasing signal phasor. Different attenuation parameters are chosen for the various materials. This varying exponential decay represents the solely additional assumptions, which we need for simulating a decreasing fringe visibility.

In Figure 5.13, examples for the altering fringe modulation contrast over depth are presented, comparatively for both measured and simulated data. For the image processing tasks, demonstrated in the following, retardation scans with an increasing variance over depth are of more interest.



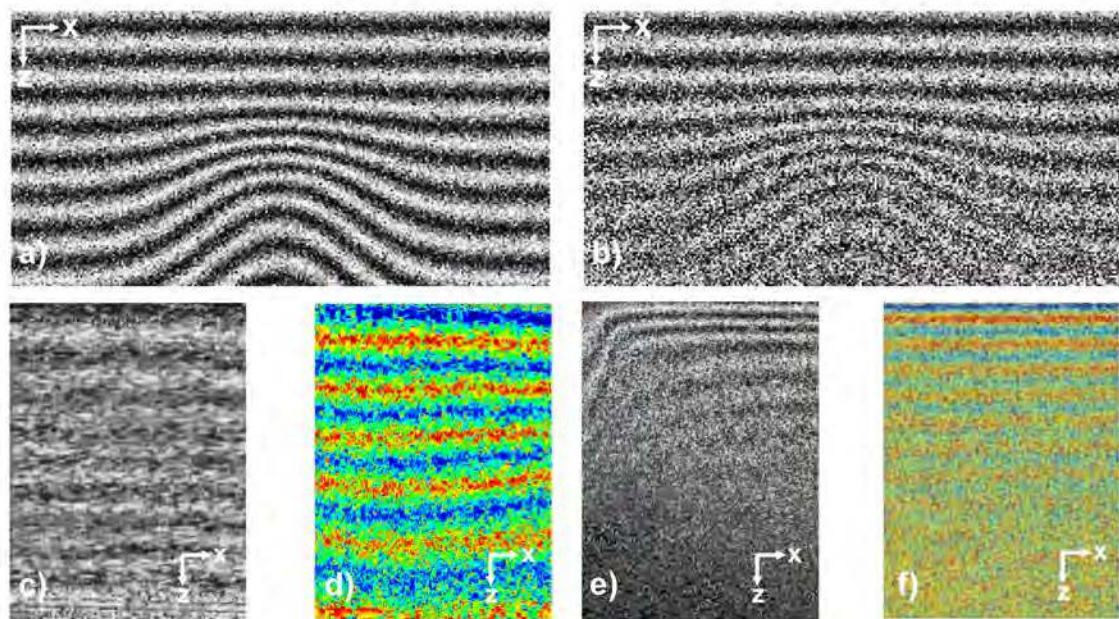


Figure 5.13: Comparison of simulated and measured retardation scans for different samples in PS-OCT. a) Simulated cross-sectional retardation representing a weakly scattering material, b) simulated cross-sectional retardation scan representing a strongly scattering material, c) and d) measured retardation image comparable with simulated data of (a), e) and f) measured retardation image comparable with simulated data of (b).

### 5.3.4 Modeling birefringence and retardation image

#### 5.3.4.1 Modulating function: Birefringence and stress

As shown in the previous example of Figure 5.11, retardation images with an underlying stress-induced birefringence distribution show typically fringe patterns. They can be described according to (5.39) and Chapter (3) as AM-FM signals.

The amplitude modulation function  $A(x, z)$  in (5.39) is supposed as a continuous, weakly decreasing function over depth. – From the imaging point the AM modulation is manifested in a decreased fringe visibility over depth. In the performed image processing, this AM term becomes recognizable after the smoothing operation, especially for retardation images, which show a strongly decreasing SNR over depth.– The frequency (FM) or phase modulation (PM) function  $\mathbf{w}(x, z)$  and  $\phi_{rc}(x, z)$ , are of main interest for the modeling and the reconstruction. They are given by the optical anisotropic material itself, which causes a locally changing phase or frequency modulation of the spatial fringe pattern.

The frequency modulation function  $\mathbf{w}(x, z)$  or the phase modulation function  $\phi_{rc}(x, z)$ , related by

$$\mathbf{w}(x, z) = \begin{pmatrix} w_x \\ w_z \end{pmatrix} = \nabla \phi_{rc}(x, z), \quad (5.40)$$

characterize the inherent or the stress-induced local birefringence  $\Delta n_B(x, z)$ . For appropriate specimens, which show an internal stress state

$$\sigma_S(x, z) = \frac{1}{C_{opt}} \Delta n_B(x, z), \quad (5.41)$$

with being  $C_{opt}$  the material dependent stress-optical coefficient, both spatial frequencies are determined by

$$w_x(x, z) = \frac{\partial(\phi_{rc}(x, z))}{\partial x} \propto \int_{z_0}^z \frac{\partial(\Delta n_B(x, z'))}{\partial x} dz', \quad (5.42)$$

$$w_z(x, z) = \frac{\partial(\phi_{rc}(x, z))}{\partial z} \propto \Delta n_B(x, z) \quad (\text{or } \propto \sigma_S(x, z)). \quad (5.43)$$

The recovery of the underlying spatially distributed birefringence  $\Delta n_B(x, z)$  or stress distribution  $\sigma_S(x, z)$ , encoded in the phase or frequency modulated fringes, is the aim of the mathematical reconstruction to be demonstrated in the following section for the simulated and, moreover, for the measured data.

### 5.3.4.2 Internal birefringence and stress model

For the previously demonstrated 1D signal generation, describing the A-scan signal generation, a material was supposed with a homogeneous internal birefringence. Thereby, a linear cumulative retardation  $\phi_{rc}(z) = w_z z \propto \Delta n_B z$  with a constant spatial frequency component  $w_z(z) = w_z$  in depth is expected. Now, for expressing the behavior of real materials, an inhomogeneous birefringence distribution will be supposed.

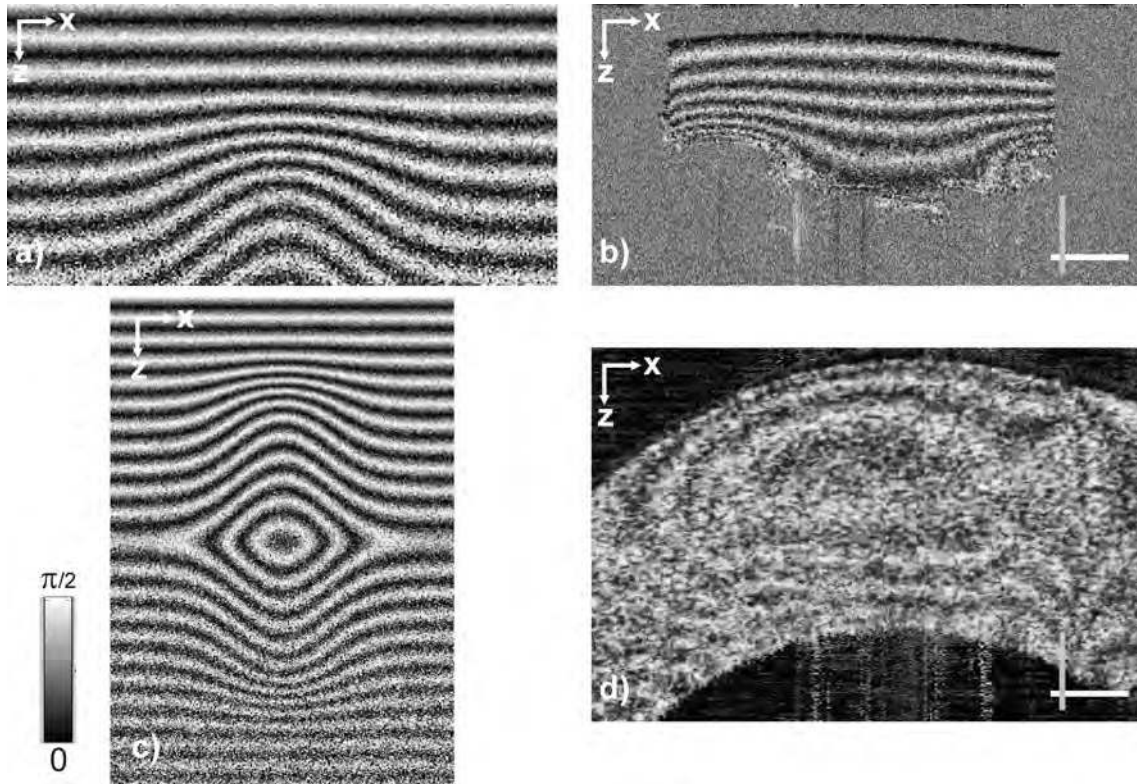


Figure 5.14: PS-OCT cross-sectional image (B-Scan): Comparison of simulated and measured PS-OCT retardation scans. a) Simulated retardation scan M1, which models the strained elastomer sample PS1, b) measured retardation scan of the strained elastomer sample PS1, c) simulated retardation scan M2, which models the bent sample PS2, d) measured retardation scan of the bent polymer sample PS2, which exhibits internally strained and compressed regions.  $z$  denotes depth direction. The white/gray bar corresponds to 500 / 250  $\mu\text{m}$  in (b) and 1000 / 500  $\mu\text{m}$  in (d).

The investigated materials, which are inspected by PS-OCT imaging under real-world test situations (e.g. by tensile and bending test experiments), show an inhomogeneous birefringence and internal stress distribution in general. This internal stress states should be modeled in a simplified way in our simulation, however, by including characteristic representations of stress states.

Stress can occur in possible types: as tensile stress (positive stress) in regions which are dilated, and compressive stress in regions which are compressed. Shear stress will not be regarded in the realized applications. In case of stress-induced birefringence, the recorded retardation image describes the local stress difference between both principal components (perpendicular to the wave propagation) in a cumulative or wrapped way. Modeling the internal birefringence and the internal

stress we have simulated two main cases of relevant specimen structures:

- **Simulated sample M1:** The underlying model for this simulation is characterized by an unimodal 2D Gaussian distribution simulating an exponentially varying birefringence inside the specimen. For materials, which show stress-induced birefringence, it can be assigned to a 2D positive stress distribution. A tensile stress state, as would be arising e.g. in a tensile test, may be described by a similar pattern, (compare also Figure 5.14 a) and b)).
- **Simulated sample M2:** Here, the model is characterized by a bi-modal 2D Gaussian distribution characterizing two differently signed modes of birefringence, (Figure 5.15 a) and c)). Bending tests may induce similar stress states, (compare also Figure 5.14 c) and d)).

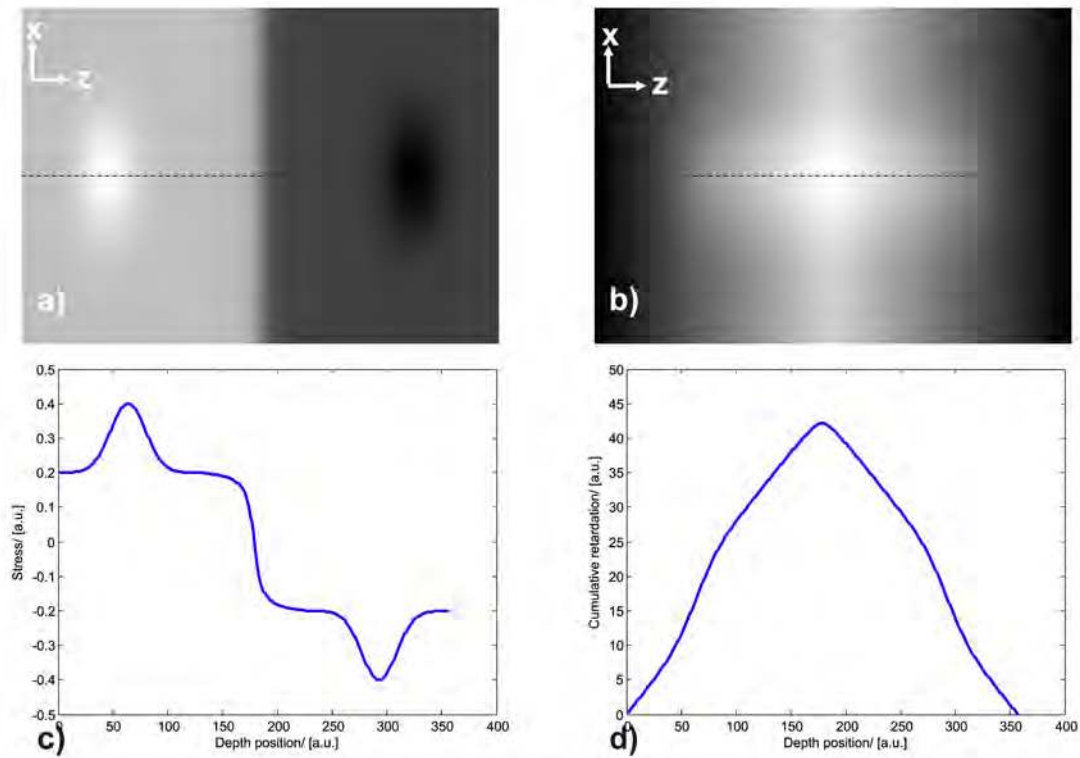


Figure 5.15: Model of the local birefringence distribution inside a material corresponding to the simulated sample M2. a) Internal birefringence distribution, b) internal continuous retardation according to (a), c) birefringence profile along indicated dashed line in (a), d) continuous retardation along indicated dashed line in (b).

For our simulation we have chosen the model parameters (with respect to the internal birefringence distribution  $\Delta n_B(x, z)$ , fringe frequency  $\mathbf{w}(x, z)$ , depth attenuation function  $a_0(x, z)$ ) to be comparable to the probed test samples under the relevant test situations. The simulated images are generated with different SNR and increasing variance over depth by applying speckle statistics as derived and demonstrated in the previous section. A rectangular cross-section has been supposed for modeling, neglecting cross-sectional deformations (e.g. volume changes or necking) during stretching or bending. The birefringence distribution, as shown in Figure 5.14 a) and c), gives

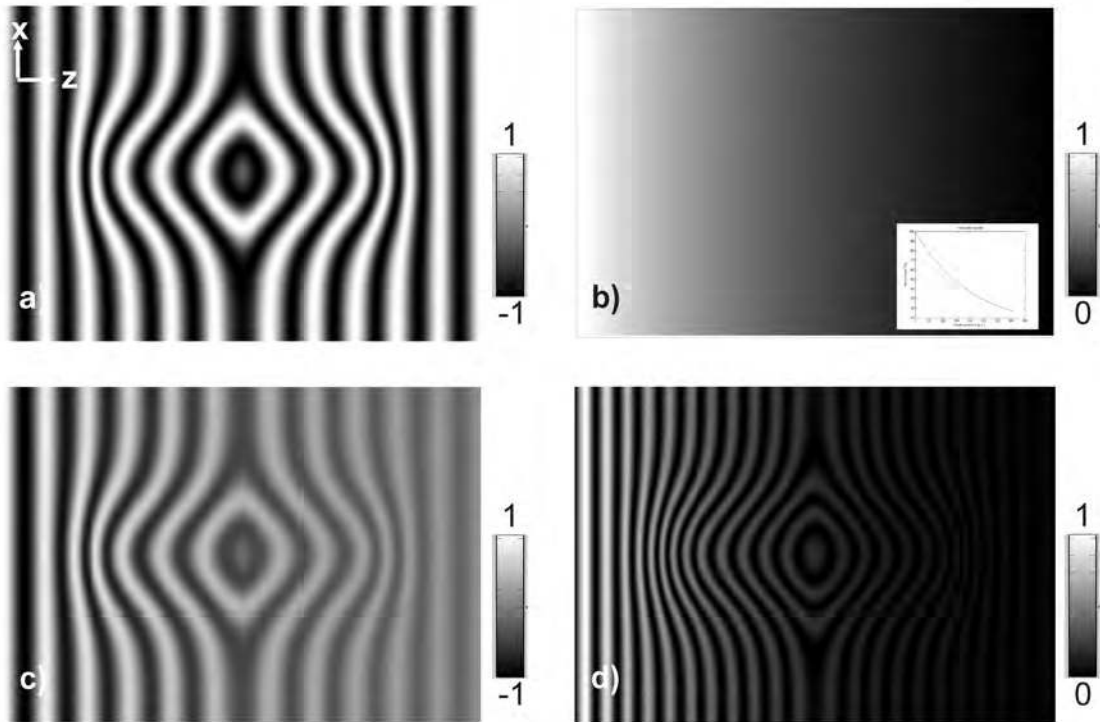


Figure 5.16: Cross-sectional image (B-Scan) at detector 1 corresponding to the simulated sample M2. a) Cross-sectional (theoretically supposed) amplitude image without depth attenuation, b) depth attenuation supposed as exponential decay function, c) cross-sectional (theoretically supposed) amplitude image including the depth attenuation, d) cross-sectional intensity image as would be measurable at detector 1 according to the stress distribution of Figure 5.15) a).

an example to simulate an anisotropic specimen with an internal compressive and tensile stress region and a neutral region between. Similar stress states are expected for the real-world specimen in realized bending beam experiments. A comparable stress distribution is underlying the analyzed retardation images in the following in Section (5.4).

Integrating the local birefringence values  $\Delta n_B(x, z)$  in depth direction yields the continuous retardation  $\phi_{rc}(x, z)$ , according to (5.5), depicted in Figure 5.15 b) and d).

In Figure 5.16 the depth-resolved (theoretically considered) amplitude and intensity cross-sectional images, which would be measured at one of the detectors corresponding to the regarded stress model, are depicted. The cross-sectional (noisy) retardation images, simulated according to the described approach, now are used for the verification of our 2D reconstruction method.

## 5.4 PS-OCT: Reconstruction methods for spatially resolved retardation, birefringence or stress imaging

In our thesis we develop a two-dimensional reconstruction scheme for local birefringence and stress distribution recovered from PS-OCT retardation images. Some efforts have been made, solving this problem by 1D approaches for PS-OCT imaging. However, to the best of our knowledge, no full 2D reconstruction scheme has been performed till now for local birefringence analysis in PS-OCT. In the context of 2D interferometric signal demodulation similar 2D approaches exist, however not in the special field of PS-OCT retardation imaging.

The analysis of the strain-stress behavior of the material is also the essential topic in the field of elastography. In the context of elastography and Moiré pattern displacement analysis the extraction of information from the photoelastic fringe pattern is demonstrated e.g. in [140]. The described methods therein are based on a time-frequency analysis or on wavelet approaches to recover the local strain tensor field. Although tensor analysis gives a comprehensive representation of the internal stress field, these approaches are not suitable for PS-OCT imaging, since not the entire stress tensor field can be imaged by a single PS-OCT retardation image. By rotating either the sample or the camera for taking several images under different angles, a comparable complete tensor field representation could theoretically be extracted by PS-OCT. But, this requires an extended experimental setup and leads to another topic. Here, we will focus on single frame analysis for PS-OCT imaging and recoverable information from only a single retardation image.

First, existing 1D reconstruction approaches will be considered, and afterwards our 2D procedure for PS-OCT will be demonstrated.

### 5.4.1 1D Reconstruction method for continuous retardation

For our special PS-OCT application, the local phase or the instantaneous spatial frequencies of the fringes encode the anisotropy or birefringence, induced or inherent in the sample, as described in (5.5) and (5.43). For analyzing the local birefringence states and the underlying inducing quantities (e.g. stress fields), the reconstruction task consists in an estimation of the instantaneous frequency or, as they are related, of the local phase.

Regarding the problem of frequency estimation from a more general point of view, the general task of frequency estimation for an oscillating signal  $f(x)$  or  $f(t)$ , has been extensively investigated in different fields of applications in recent years, (e.g. in velocimetry [134], or radar techniques [135]). Different methods, based on zero-crossing analysis [136] or autocorrelation techniques [150] can be found. Related to interferometric use, one of the most common techniques is suggested in [137], which applies a FFT-based method for the phase recovery. Although these FFT and autocorrelation methods are optimized for an estimation of the center frequency of the signal, they can not easily be used for a description of the instantaneous frequency or phase, if they are not transposed e.g. to a windowed realization or into the wavelet domain.

Other methods of frequency estimation are derivative-based approaches. They use e.g. the 1D Teager-Kaiser energy operator (TKEO)  $\mathcal{T}$  for frequency estimation [138]. This operator is defined by combining first and second order derivatives by

$$\mathcal{T} = \left( \frac{df(x)}{dx} \right)^2 - f(x) \left( \frac{d^2f(x)}{dx^2} \right), \quad (5.44)$$

and the frequency  $\omega$  can be obtained by

$$\omega = \sqrt{\mathcal{T} \left\{ \frac{\partial f(x)}{\partial x} \right\} / \mathcal{T} \{f(x)\}}. \quad (5.45)$$

But especially for noisy signals (5.45) may result in problems.

A further group of frequency estimation methods is based on quadrature demodulation, exploiting the 1D HT for the analysis of temporal varying 1D signals and for the determination of their local phase and frequency. We will focus on quadrature demodulation, and especially on the computation of the quadrature component by HT, as it provides instantaneous phase and frequency with acceptable computational efforts. In [139] the 1D HT analysis is exploited for phase estimations in time series of speckle interferograms.

With respect to the special application on PS-OCT images a method for stress distribution measurement and analysis based on Stokes vector images is shown in [141]. Therein an approach is demonstrated, which is based on a 1D demodulation scheme for oscillating Stokes vector signals, continued by a numerical differentiation, to obtain the internal stress distribution. In [142] a 1D phase recovery from wrapped retardation data for an almost straight fringe pattern is performed. The 2D problem is reduced to a 1D solution by regarding only laterally averaged retardation values. These 1D quadrature signal computation can be applied for the determination of the instantaneous values of retardation and birefringence as long as the fringes are almost straight. But in generally, it would result in *phase clipping*, i.e. the phase values are 'mirrored' at the symmetry line, as illustrated in Figure 5.17. Furthermore, these 1D analysis approaches do not exploit the 2D character of the fringes and the contained 2D information of the pattern.

In the following, we want to investigate how elements of 2D quadrature demodulation can be included in the mathematical analysis of PS-OCT retardation imaging.

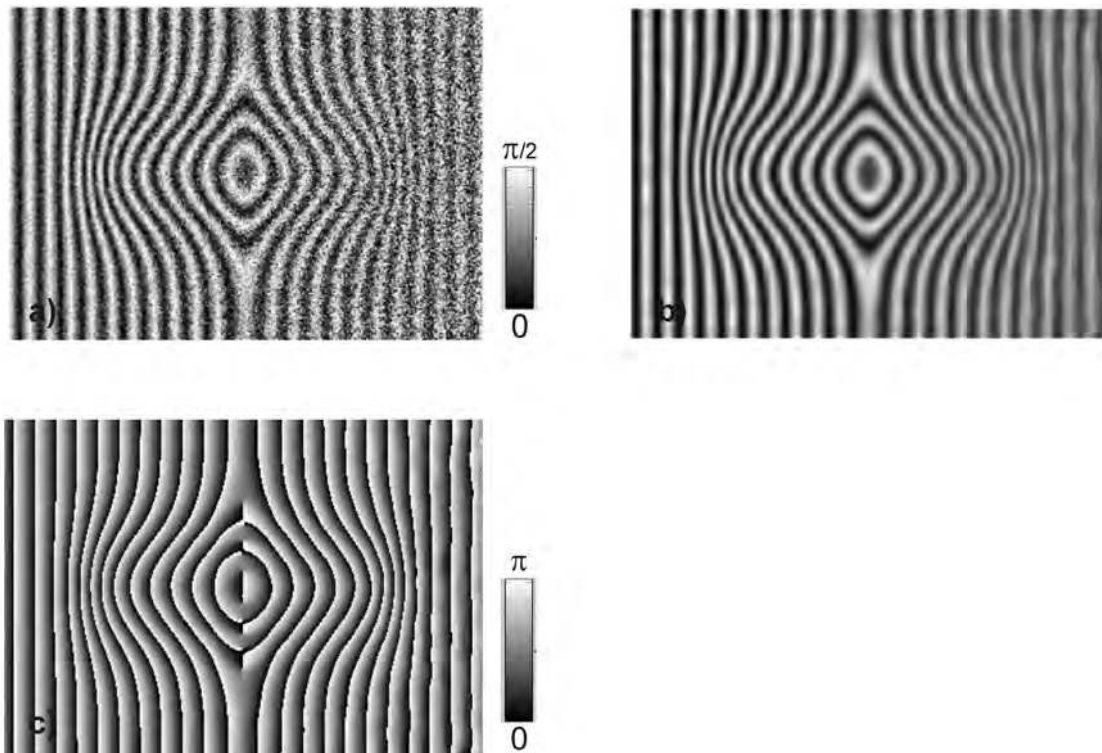


Figure 5.17: Illustration of the phase clipping for a closed fringe pattern structure. a) Simulated fringe pattern, b) smoothed fringe pattern, c) wrapped phase image. The quadrature image computation in (c) is based on the *i*1D dHT (according to (3.20)).



## 5.4.2 2D Reconstruction method for continuous retardation

Now considering retardation images as 2D signals with inherent 2D information encoded in the fringes, we aim to extend the concept of intrinsic 1D demodulation of retardation signals [141] to a true two-dimensional approach. In our method, the main emphasis on the 2D reconstruction is placed on the computation of a two-dimensional quadrature signal (called quadrature image). Therefore, we include in the demodulation scheme of retardation images the radial HT (or spiral phase transform), originally described and demonstrated in [43] in the context of interferometry.

But, in contrast to applications in conventional interferometry or photoelasticity [143], there are several extensions necessary so that this method is feasible for the birefringence or stress/strain analysis in the provided PS-OCT retardation images. In addition to the already demonstrated use in interferometry, for application in PS-OCT several preprocessing steps including *scaling*, zero-mean *background correction*, and *denoising* are necessary to perform a reliable phase reconstruction and to fulfill the prerequisites for the 2D *demodulation* method. As the retardation is reconstructed in a wrapped representation, furthermore an *unwrapping* step has to follow. In a final step a numerical *differentiation* has to be performed to obtain the 2D internal stress distribution.

In the following, these steps are described in more detail and some interesting aspects are demonstrated.

### 5.4.2.1 Scaling

The measured PS-OCT retardation images are mapped in the interval  $[0, \pi/2)$ . As for the following demodulation zero-mean signals are supposed, the retardation data  $\phi_{rw}(x, z)$  are scaled to the interval  $[-\pi/2, \pi/2)$ .

The denoised, zero-mean, background corrected (in-phase) retardation image  $I_{Pr}(x, z)$ , for which we assume a modeling according to (5.29)–(5.39), is normalized to the unit interval  $[-1, 1)$ .

### 5.4.2.2 Background and riding wave correction

The assumption of zero-mean signal is a necessary, but not a sufficient condition for the application of the HT for computation of the quadrature component. Real-world fringe pattern (regarded as multi-component signals) are often a superposition of different components: The main fringe pattern, interpretable as a 2D AM-FM signal with a locally dominant frequency, some slowly varying additive background signal, and some kind of speckle noise, as already mentioned in Section (3.1). The additive background may be caused by inhomogeneous illumination or may result by smoothing effects in the signal processing.

In our application we are interested in the phase of the dominant frequency signal component, as the dominant frequency encodes the information about the local quantities related to the retardation. A preceding bandpass filtering is performed, a preprocessing approach, which we have demonstrated in [156]. Additionally, we have tested the EMD method (Section (3.1)) for the estimation of the background. As this method is more interesting we have focus on it.

### 5.4.2.3 Denoising

Retardation fringe patterns, obtained by coherent imaging techniques, mostly exhibit strong speckle noise. Hence, the denoising of the fringe pattern is a prerequisite for all following steps. Although in general similar strategies can be applied for different interferometric techniques (as WLI, ESPI, Digital Holography), additionally, an adaptation to the specific interferometric image features is required. Especially in case of PS-OCT retardation images, the salient feature can be found in the material-dependent speckle noise with increasing strength over depth. It is reasoned by the multiple random scattering effects within the material, as already explained in Subsection (5.3.3).

In literature various methods for removing speckle noise are quoted, starting from simple median filtering [144] to an extensive collection of wavelet-based methods, e.g. the conventional wavelet shrinkage method [145] has been tested by us. But they have been proven to be insufficient for the measured retardation fringe patterns.

Retardation fringe patterns have also in the mathematical sense a strong anisotropy or coherence (of the image structures). The (mathematical) anisotropy may change its strength dependent on the investigated material to a more isotropic speckle pattern of random backscatterers with increasing imaging depth. Often our applications are featured by especially the diminishing of the anisotropic character of structures with increasing depth, and the isotropic character of the structures becomes the dominant behavior, (i.e. being almost *iID* structures in surface near regions and becoming random structures with increasing depth.) Therefore, we investigate denoising schemes, which are adaptive to the changing anisotropy-isotropy within the image. Although several image enhancing methods, based on anisotropic wavelets or curvelets [146], described in literature for enhancement of flow-pattern, textures or elongated structures, could be applied, we have especially chosen coherence enhancing diffusion (CED) methods. CED methods exploit the local coherence value  $\kappa(x, z)$  of the fringe pattern in a local neighborhood. The anisotropic or isotropic diffusion behavior (expressed by the diffusivity  $\mathcal{D}(x, z)$ ) is self-adaptive according to this coherence feature. Furthermore, the concept of scale space may be included in the denoising approach by smoothing the original image and the diffusion tensor image with the Gaussian kernels  $K_\sigma$  and  $K_\rho$  at the scales corresponding to  $\sigma$  and  $\rho$ .

We follow the approach of [147, 148], based on the anisotropic diffusion equation

$$\begin{aligned} \frac{\partial u}{\partial t} &= \operatorname{div}(\mathcal{D}\nabla u) && \text{in } \Omega \times T, \\ u(\mathbf{x}, 0) &= f(\mathbf{x}) && \text{on } \Omega \times 0, \\ (\mathcal{D}\nabla u \mathbf{e}_n) &= 0 && \text{on } \Gamma = \delta\Omega \times T, \end{aligned} \quad (5.46)$$

where here  $u(\mathbf{x}, t)$  denotes a temporal and spatial varying function, which is developed over time. The measured cross-sectional retardation image  $\phi_{rw}(x, z)$  is represented by  $f(\mathbf{x}) = f(x, z)$  and gives the initial condition for the diffusion equation. Here, Neumann boundary conditions are assumed.

In CED methods the local diffusivity  $\mathcal{D}(x, z)$  is adapted according to the structure tensor  $J_\rho$ ,

which can be computed as

$$\begin{aligned}
 J_\rho(\nabla u_\sigma) &= K_\rho \otimes (\nabla u_\sigma \odot \nabla u_\sigma^T), \\
 \text{with } K_\rho &= \frac{1}{(2\pi\rho^2)} \exp\left(-\frac{|\mathbf{x}|^2}{2\rho^2}\right), \\
 K_\sigma &= \frac{1}{(2\pi\sigma^2)} \exp\left(-\frac{|\mathbf{x}|^2}{2\sigma^2}\right), \quad (\rho, \sigma > 0) \\
 u_\sigma &= K_\sigma \otimes u(\mathbf{x}, t),
 \end{aligned} \tag{5.47}$$

and whose eigenvectors determine the direction of diffusion. The difference of the eigenvalues  $c_1$  and  $c_2$  of the structure tensor  $J_\rho(\nabla u_\sigma)$ , that describes the coherence at each pixel of the fringe pattern by

$$\kappa = (c_1 - c_2)^2, \tag{5.48}$$

steers the diffusion character. In case of isotropic structures both eigenvalues, having similar values,  $\kappa$  tends to zero. In case of anisotropic structures the eigenvalues are different and the eigenvectors  $v_1$  and  $v_2$  (i.e. the eigenvector of the smaller eigenvalue) determines the direction of the diffusion. Therefore, the diffusivity becomes a function of the coherence  $\mathcal{D}(\kappa, v_1, v_2)$ , and the smoothing becomes adaptive to the underlying fringe pattern.

Furthermore, the effect of increasing variance over depth can be treated in our approach by utilizing a weighted initial function  $\nabla u_g$  in (5.46) as

$$\begin{aligned}
 \frac{\partial u_g}{\partial t} &= \text{div}(\mathcal{D}\nabla u_g) \quad \text{in } \Omega \times T, \\
 u_g(\mathbf{x}, 0) &= \bar{\sigma}(x, z)^2 f(\mathbf{x}) \quad \text{on } \Omega \times 0,
 \end{aligned} \tag{5.49}$$

where  $\bar{\sigma}(x, z)^2$  expresses an locally averaged variance map of the simulated (measured) retardation  $\Phi_{rw}(x, z)$ .

We apply the CED method for closing interrupted lines and enhance the information content of the retardation fringe pattern. Furthermore, having also a slight amount of diffusion in the direction perpendicular to the fringes leads to a smoothing of the (theoretically triangular) wave shape. It helps to suppress the frequency components due to the higher harmonics, and therefore being of advantage for the following demodulation. Therein, in our application the denoising is slightly different from standard denoising tasks where sharp and preserved edges are usually desired. We aim for obtaining the zero-crossings.

#### 5.4.2.4 Computation of 2D quadrature image and orientation estimation

For the PS-OCT measurement setup the conditions of Nuttall and Bedrosian (i.e. supposing narrowband signals with bounded energy in general, treating the in average decreasing visibility of the fringes over depth by a slowly varying amplitude modulation, in contrast to the fast varying fringes) are approximatively fulfilled for the dominant fringe pattern. However, when working directly with un-preprocessed data the inherent noise, offset or wave shape would essentially disturb the demodulation and birefringence/stress extraction, as seen in the simulations of Subsections (3.4.4), (3.4.5).

After performing the required preprocessing of PS-OCT retardation images we may apply the spiral phase transform approach as described in Section (3.4). The CED denoised fringes act as input for the in-phase signal  $I_P(x, y)$ .

As already mentioned, the computation of the quadrature image by the spiral phase transform requires an additional estimation of fringe orientation. We pursue two approaches of orientation estimation:

First, the orientation estimation is performed by means of the complex *energy operator*  $\mathcal{E}_\Theta$  [149]. The energy operator can be computed in course of the spiral filtering approach by the subsequent application of the radial Hilbert transform operator  $\mathbf{H}_R(R, \Theta)$ , as defined in (3.26) and (3.40) on the fringe image  $f(x, y)$  or  $f(r, \theta)$ , as

$$\begin{aligned} \mathcal{E}_\Theta \{f(r, \theta)\} &= \mathcal{F}^{-1} \{ \mathbf{H}_R \{ \mathbf{H}_R \{ \mathcal{F} \{ f(r, \theta) \} \} \} \} \\ &- f(r, \theta) \left( \mathcal{F}^{-1} \{ \mathbf{H}_R \{ \mathcal{F} \{ f(r, \theta) \} \} \} \right)^2. \end{aligned} \quad (5.50)$$

This approach can be interpreted analogue to (5.44) as radial realization of the Teager-Kaiser operator. Its argument provides a pointwise estimation of the orientation in case of fringe patterns exhibiting only low noise levels and sinusoidal wave shapes.

The second possibility for orientation estimation is based on the *structure tensor*, which delivers also an orientation estimation. This approach has the advantage that it can be combined with the CED denoising step, since the orientation estimation is also inherent there.

Both orientation estimations deliver the *orientation*  $\beta = \beta_\pi$ , defined in  $[0, \pi)$ . However, for the application of the RHT, according to [43], the *direction*  $\beta = \beta_{2\pi}$ , defined in  $[0, 2\pi)$ , has to be determined. The mapping  $\mathbf{W}_D$  of the orientation  $\beta_\pi$  to the corresponding direction  $\beta_{2\pi}$

$$\mathbf{W}_D : [0, \pi) \rightarrow [0, 2\pi) \mid \beta_\pi \rightarrow \beta_{2\pi}, \quad (5.51)$$

is denoted as so-called orientational unwrapping [75]. The orientational unwrapping step represents a very instable problem in case of noisy images. It may be performed with an improved stability working on preprocessed images or by using rather the structure tensor method in comparison to the energy tensor approach for the orientation field estimation, as illustrated in the following.

#### 5.4.2.5 Unwrapping

In our approaches we separate denoising and unwrapping. After performing CED-diffusion filtering to improve the fringe coherence, and the computation of the 2D quadrature signal  $I_Q(x, z) \sim A(x, z) \sin(\phi_{rc}(x, z))$  from the measured, denoised and enhanced (in-phase) signal  $I_P(x, z) \sim A(x, z) \cos(\phi_{rc}(x, z))$  the *wrapped phase* is determined as

$$\phi_w(x, z) = \arctan \frac{I_Q(x, z)}{I_P(x, z)}. \quad (5.52)$$

It should be mentioned that the wrapped representation of the retardation, determined according (5.52), exhibits no longer the triangular wave shape, but is now transformed into the conventional wrapped phase representation  $\phi_w$ , which is restricted to the interval  $[0, \pi)$ . We use in the

following the notation  $\phi_w$  and the term *wrapped phase* image for this computed wrapped retardation representation to distinguish from the original retardation image  $\phi_{rw}$  with its triangular wave shape. (But keeping in mind that the retardation is the underlying quantity here – distinguished from the wrapped phase images in Chapter (6).)

The mapping of the continuous phase to a wrapped one can be described by the wrapping operator  $\mathbf{W}$

$$\mathbf{W}(\phi_c) = \phi_w + 2\pi n, \quad \text{with } n = 1, 2, \dots, \quad (5.53)$$

where the phase  $\phi_c$  should be assumed as continuous, smooth function. The aim of unwrapping consists in the reconstruction of the smooth continuous phase  $\phi_c$ .

Considering the unwrapping of (discrete) 1D signals, it can be seen as subsequent removal of all phase jumps (i.e. discontinuities of  $2\pi$ ) by performing the following scheme:

$$\begin{aligned} \phi(m) = \phi(0) + \sum_{n=0}^{m-1} \Delta\phi(n) &= \phi(0) + \sum_{n=0}^{m-1} \mathbf{W}\{\Delta(\mathbf{W}\{\phi(n)\})\} \\ \mathbf{W}\{\Delta(\mathbf{W}\{\phi(n)\})\} &= \mathbf{W}\{\Delta(\phi_w(n))\} = \mathbf{W}\{\phi_w(n+1) - \phi_w(n)\}, \end{aligned} \quad (5.54)$$

what can be interpreted as a path integration approach.

Unwrapping of 2D phase images represents an own comprehensive topic. Especially the influence of noise makes this problem a non-trivial one. Separation of the 2D unwrapping into two 1D unwrapping processes would be theoretical possible under the condition of irrotational gradient fields of  $\phi(x, z)$  guaranteeing the path independence along a contour  $L \in (x \times z)$

$$\oint_L \nabla\phi(\mathbf{x})d\mathbf{x} = 0, \quad (5.55)$$

or fulfilling the integrability condition

$$\frac{\partial^2\phi(x, z)}{\partial x\partial z} = \frac{\partial^2\phi(x, z)}{\partial z\partial x}. \quad (5.56)$$

However, for real data we can not assume this path independence due to the inherent noise. Additionally, measuring artifacts can especially cause rotational gradient fields. A subsequent 1D unwrapping would lead in practice to streaking artifacts. In case of (CED) denoised retardation images having a higher SNR compared to the original retardation phase images, these streaking artifacts are reduced, but erroneous stripes due to measurement artifacts, fringe singularities and specular reflexes can occur. Therefore, we apply in the following a 2D unwrapping scheme.

In literature, a huge amount about phase unwrapping methods may be found, (reviewed e.g. in [151]). The main 2D unwrapping approaches are distinguished in path-following methods, minimum norm methods, global FFT-based methods, etc.

We have chosen for the necessary unwrapping step depending on the OCT-application a path following method as it can be adapted to the specific features of the phase or retardation images.

The path-following approach using an adaptive quality map provides a robust solution as we have tested on our preprocessed PS-OCT images. It requires a heuristic measure (e.g. derivatives, variance, or SNR) for the quality and reliability estimation of the phase values.

The quality criterium  $Q$  is determined in our PS-OCT application by (the reciprocal of) the local variance  $\sigma^2(x, z)$  and the deviation  $\Delta(x, z)$

$$\Delta(x, z) = \left| \left( \nabla\phi(x, z) - \sum_{\tilde{x}, \tilde{z} \in \Omega_R} \nabla\phi(\tilde{x}, \tilde{z}) \right) \right|, \quad (5.57)$$

as distance between the local phase gradient and the averaged gradient within some neighborhood  $\Omega_R$ . Hence, the unwrapping path is determined by the quality criterium  $Q(\sigma^2(x, z), \Delta(x, z))$  describing the local SNR and signal smoothness. Regions with high SNR and accordingly high reliability are unwrapped at first, and regions with low SNR are considered afterwards, following the approach described in [153]. Applying this ordering scheme, the unwrapping is performed as a path tracking approach [152] and solved finally according to [154] as minimization problem

$$\sum_{\tilde{x}, \tilde{z} \in \Omega_R} (\nabla\phi(x, z) \mathbf{e}_n) + \beta_R (\mathbf{e}_n(x, z) - \mathbf{e}_n(\tilde{x}, \tilde{z}))^2 s(\tilde{x}, \tilde{z}) \rightarrow \min!, \quad (5.58)$$

which results in the equation system

$$\begin{aligned} & \begin{pmatrix} \sum_{\tilde{x}, \tilde{z} \in \Omega_R} (\phi_x(\tilde{x}, \tilde{z})^2 + \beta_R s(\tilde{x}, \tilde{z})) & \sum_{\tilde{x}, \tilde{z} \in \Omega_R} (\phi_x(\tilde{x}, \tilde{z}) \phi_y(\tilde{x}, \tilde{z})) \\ \sum_{\tilde{x}, \tilde{z} \in \Omega_R} (\phi_x(\tilde{x}, \tilde{z}) \phi_y(\tilde{x}, \tilde{z})) & \sum_{\tilde{x}, \tilde{z} \in \Omega_R} (\phi_y(\tilde{x}, \tilde{z})^2 + \beta_R s(\tilde{x}, \tilde{z})) \end{pmatrix} \begin{pmatrix} e_{n_x}(x, z) \\ e_{n_z}(x, z) \end{pmatrix} \\ & = \begin{pmatrix} \beta_R \sum_{\tilde{x}, \tilde{z} \in \Omega_R} (e_{n_x} s(\tilde{x}, \tilde{z})) \\ \beta_R \sum_{\tilde{x}, \tilde{z} \in \Omega_R} (e_{n_z} s(\tilde{x}, \tilde{z})) \end{pmatrix} \end{aligned} \quad (5.59)$$

The positions, where  $\mathbf{e}_n$  has already been estimated, are indicated with  $s(\tilde{x}, \tilde{z}) = 1$ . The parameter  $\beta_R$  stabilizes the unwrapping. The size of the neighborhood has to be chosen to be small in comparison to the size of the image structures.

As a second approach for unwrapping a global FFT-based 2D unwrapping approach has been considered, (especially in case of DPC-OCT imaging), which performs the unwrapping, similar also to the phase from gradient reconstruction, by solving the Laplace problem, (for details compare Section (6.3)).

### 5.4.3 Reconstruction of internal stress distribution

The internal stress distribution  $\sigma_S(x, z)$  can be derived from the reconstructed cumulative retardation  $\phi_{rc}(x, z)$  by numerical differentiation in  $z$ -direction. However, due to the influences of the wave shape, background and noise the reconstructed retardation signal may still obtain some spurious oscillations. Hence, performing differentiation by a simple difference quotient would result in an amplification of this erroneous oscillation signals, as demonstrated in Figure 5.18 a). (It should be referred to the simulations in Section (3.4).)

We have performed the numerical differentiation by additionally including spline interpolation, Tikhonov regularization [168, 184], or a combination of both, to obtain a smooth internal stress distributions within the material, as shown in Figure 5.18 b)–d). We have optimized the parameters (i.e. interpolation size and regularization parameter) to find a trade-off between smoothing and noise suppression in an empirical way, taking into account prior knowledge about the expected stress profiles. The numerical realization of the stress computation is illustrated in Figure 5.19 for different strength of regularization.

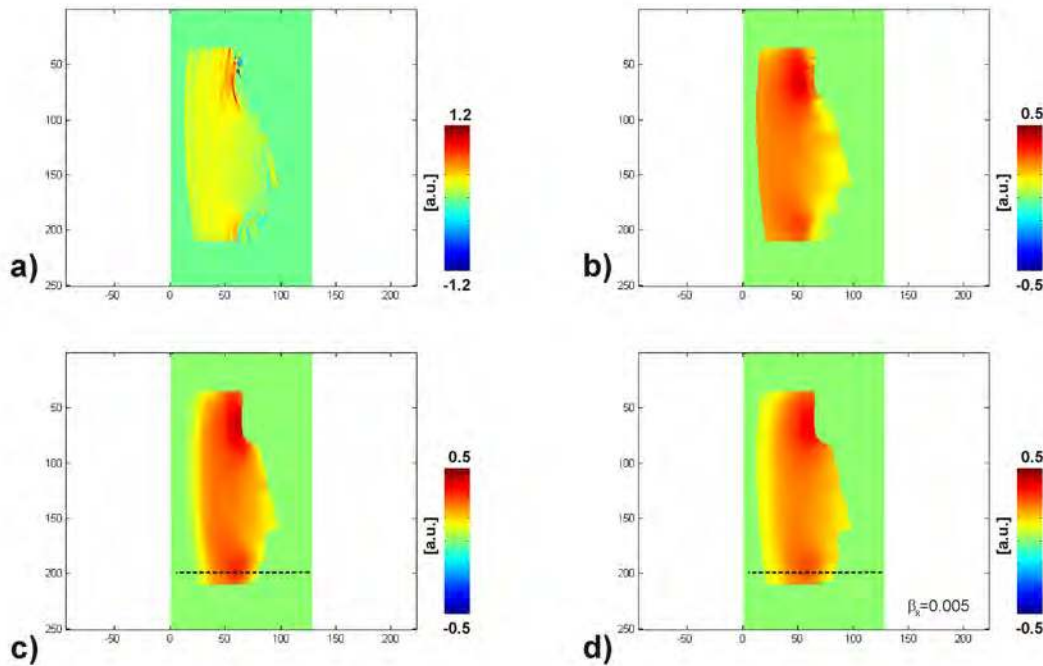


Figure 5.18: Comparison of the internal stress distribution. The internal stress distribution is obtained by numerical differentiation of the cumulative retardation image. The numerical differentiation is performed a) on cumulative retardation data (by a straight forward filtering with a  $[1 \ 0 \ -1]$  kernel), b) on regularized cumulative retardation data, c) on cubic spline interpolated cumulative retardation data, d) on cubic spline interpolated and regularized cumulative retardation data; (The comparison is shown for the tensile test sample PS1.)

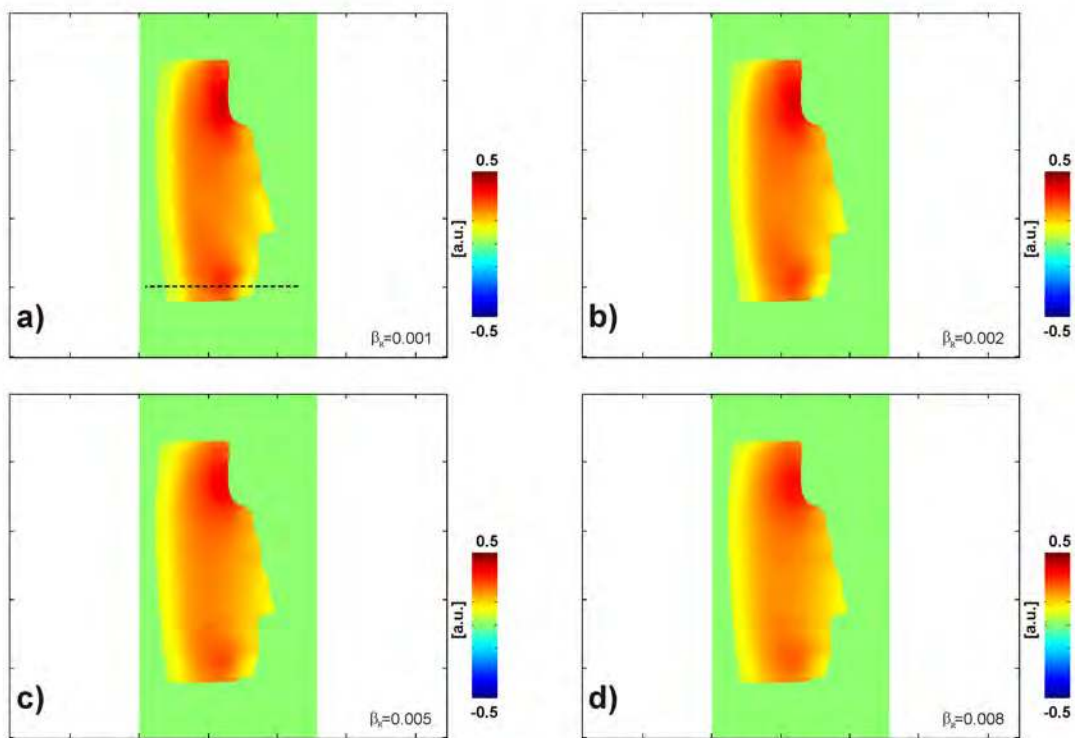


Figure 5.19: Comparison of the internal stress distribution. The regularization parameters  $\beta_R$  is increasing with a)  $\beta_R=0.001$ , b)  $\beta_R=0.002$ , c)  $\beta_R=0.005$ , d)  $\beta_R=0.008$ . (Spline interpolated cumulative phase retardation data have been chosen as input.)



### 5.4.4 Further comments on the reconstruction approach

#### 5.4.4.1 Comments on the denoising

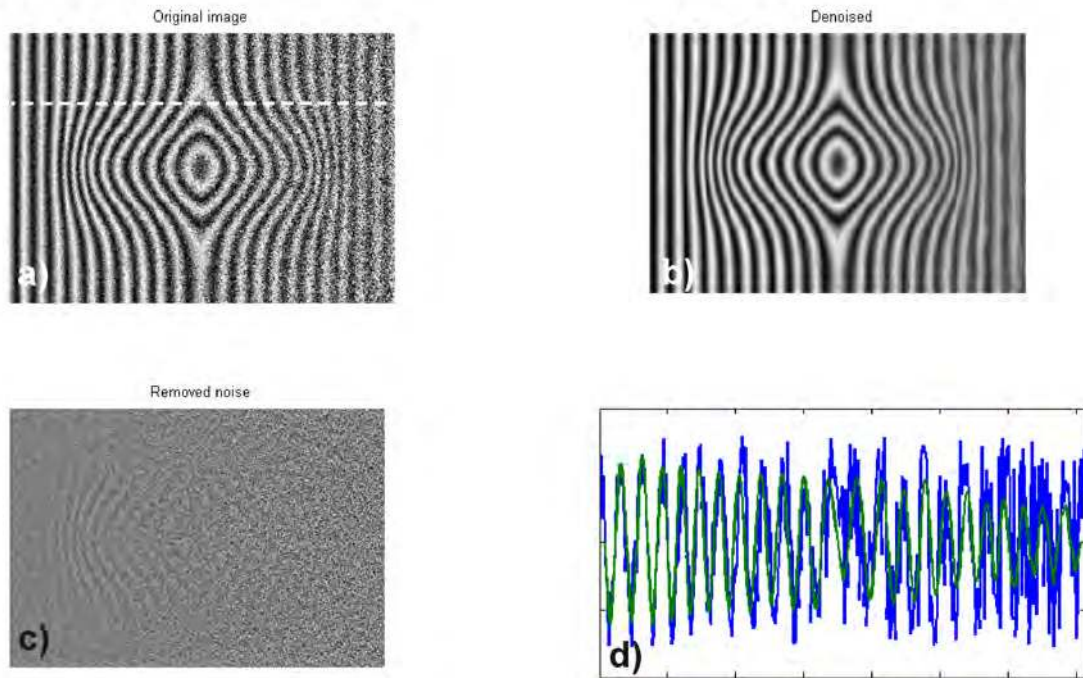


Figure 5.20: Illustration of CED-based denoising method on a simulated cross-sectional retardation image. a) Original retardation image, b) enhanced retardation image, c) residual noise, d) profile along indicated line (*blue*: noisy retardation signal, *green*: reconstructed).

The denoising has been realized in our procedure by CED methods. However, we would not restrict that CED denoising is the only appropriate denoising possibility. Also a variety of anisotropic wavelet and directional filtering based approaches have been available and have been partially tested by us [156]. However, by our experience in PS-OCT applications, CED denoising gives properly adapted results, as it improves the coherence structure of the fringes and we may also include the variance-depth dependency. In comparison to the CED-based denoising, shown in Figure 5.20, also the non-local mean (NLM) approach [157], shown in Figure 5.21, has been investigated as a further denoising method [184]. A direct comparison between both methods is given in Figure 5.22. Both approaches show partially restrictions, exemplified on simulated and measured image data of the tensile test experiment.

The NLM-based denoising yields good results in case of simple fringe patterns, as performed on the simulations. In case of fringe pattern images with lower SNR, the NLM method have been proven less adaptive to the varying coherence structure in comparison to the CED method, as shown in Figure 5.23.

The CED-based denoising may cause in boundary regions with low SNR, (i.e. at regions at

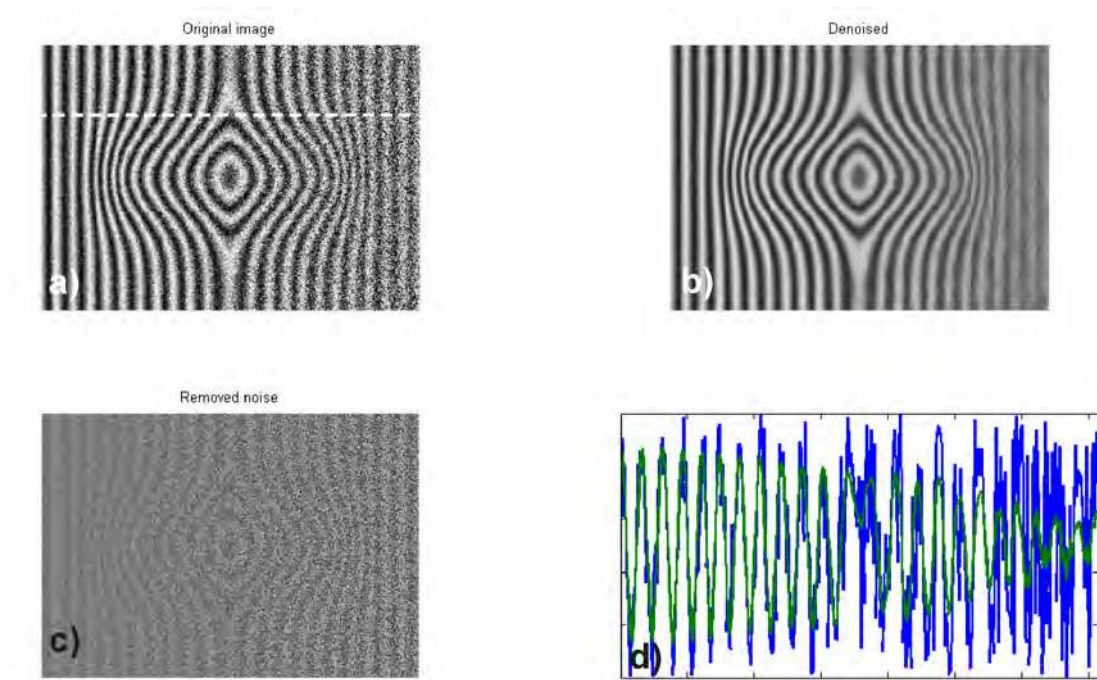


Figure 5.21: Illustration of NLM-based denoising method on a simulated cross-sectional retardation image. a) Original retardation image, b) enhanced retardation image, c) residual noise, d) profile along indicated line (*blue*: noisy retardation signal, *green*: reconstructed).

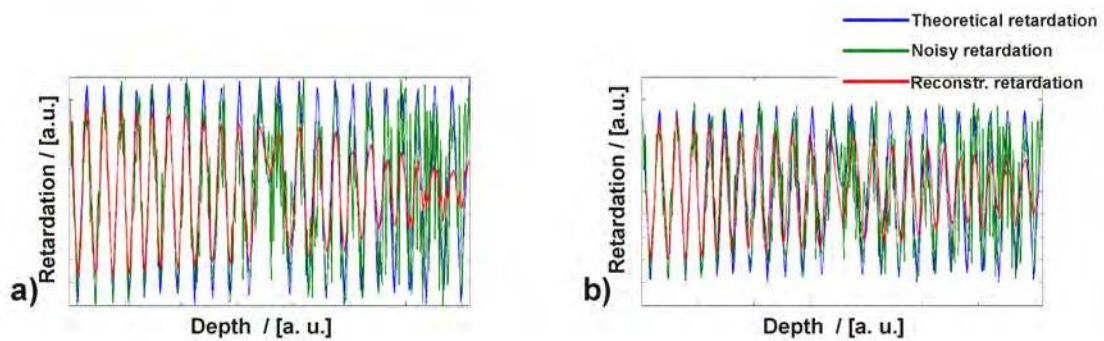


Figure 5.22: Comparison of both denoising methods (NLM and CED). Signal profile along indicated line in Figures 5.20 and 5.21. a) Applying NLM method (*blue*: theoretical retardation signal, *green*: noisy retardation signal, *red*: denoised retardation signal), b) applying CED method (*blue*: theoretical retardation signal, *green*: noisy retardation signal, *red*: denoised retardation signal).

the bottom side of the probed sample), an additional offset term, which results from erroneous diffusion components of background regions outside the investigated object. It could be restricted by a properly masking and discretization, but this seems rather complicated on irregularly shaped objects.

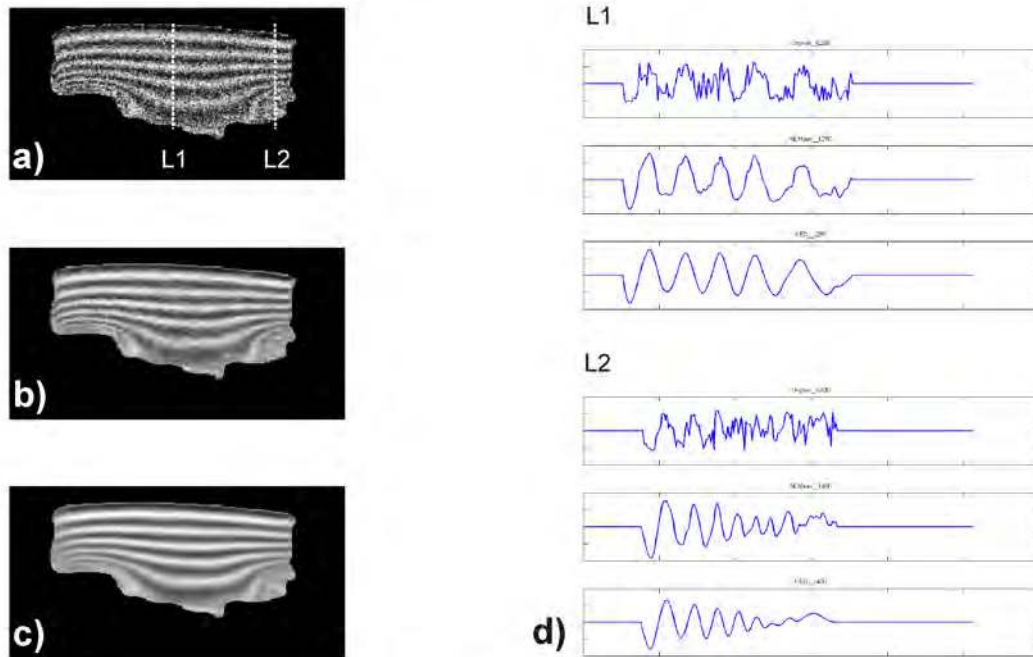


Figure 5.23: CED and NLM denoising results in comparison, considering a representative cross-sectional retardation scan of the tensile test sample (PS2). a) Measured cross-sectional retardation image having severe speckle noise, b) denoised cross-sectional retardation image applying NLM method, c) denoised cross-sectional retardation image applying CED method, d) profile along indicated lines L1 and L2 (*top, middle, bottom* are corresponding to (a), (b), and (c)).

With respect to the realized CED filtering, by including a weighting of the initial retardation image with the average variance map, as described in (5.49), the results could partially be improved. This approach leads to a locally increased gradient and to a stronger diffusion for regions of higher averaged variance. The incorporation of the variance allows to work with smaller Gaussian kernel parameter in the CED filtering, which otherwise would result in some remaining noise, which is illustrated in Figure 5.24 b) and c).

However, a limit of SNR exists, where both CED methods erroneously start to enhance random noise structures, as illustrated in Figure 5.25.

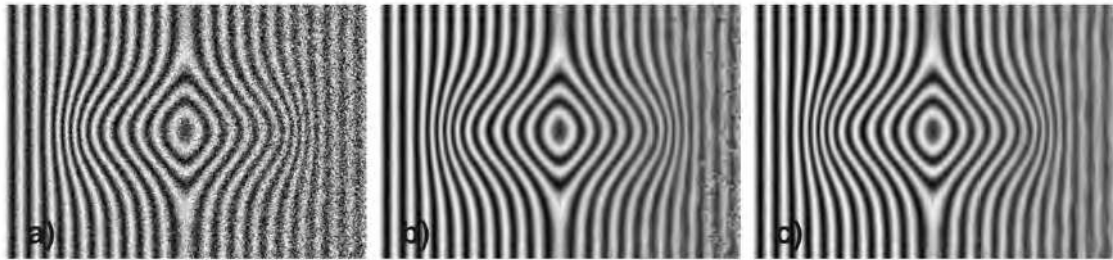


Figure 5.24: Comparison of CED denoising. a) Simulated noisy retardation image, b) CED denoising performed in the conventional way, c) including additionally the variance map as the initial condition in the CED denoising; otherwise applying the same parameter set as in (b).

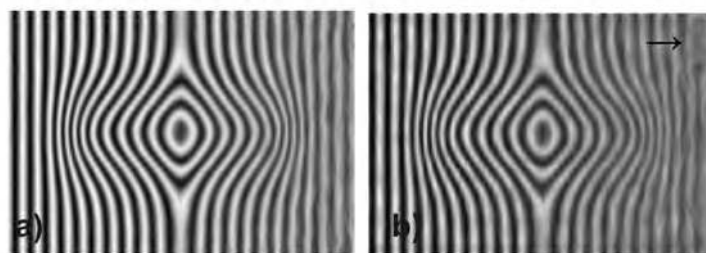


Figure 5.25: Illustration of the limits of CED denoising. a) CED denoised image (SNR:  $>2$  dB), b) CED denoised image (SNR:  $>0$  dB). Increasing variance over depth leads to decreasing SNR and fringe visibility, which results in erroneous structures after the denoising in (b).

#### 5.4.4.2 Comments on the demodulation

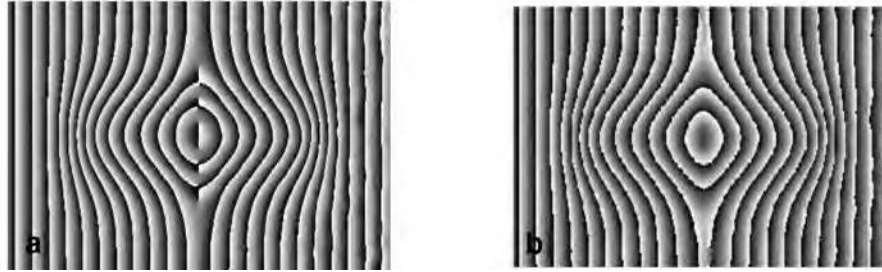


Figure 5.26: Illustration of phase clipping and the advantage of the 2D approach. The quadrature image computation is based on a) the directional HT method (as half-plane symmetric approach), which leads to clearly recognizable phase clipping in the central region, b) the radial HT method (as isotropic approach), where the phase clipping is avoided; exemplified on a simulated fringe pattern.

The performance of the suggested 2D approach is manifested in particular for patterns containing closed fringe structures. For these patterns the application of the directional HT ((*i*1D dHT), according to (3.20)), as an intrinsic 1D operation, would result in a phase clipping. In contrast, the approach based on the radial HT ((2D RHT), according to (3.22)) enables the reconstruction of the quadrature component of the image in the correct way, under the condition that the orientation and direction of the fringe pattern have been estimated additionally.

In Figure 5.26, the computed wrapped phase images, each obtained by the 1D directional or 2D radial HT realization, are depicted in comparison. For almost straight-lined fringes (i.e. having a defined single direction) the (*i*1D) directional HT can appropriately be applied. However, for curved fringes the phase clipping, resulting from the 1D consideration of the fringes, should be remarked.

In Section (3.4) we have explained the interfering influence of the background as locally varying offset term, superposed on the fringe pattern. For correcting this additional offset and for diminishing errors, the EMD approach can additionally be included. The improvements, which can be obtained by the combination of the radial HT (RHT) approach and the EMD-based background correction, exemplified again on the measured image data of the tensile test experiment, are illustrated in Figure 5.27. Especially in regions of lower SNR and curved fringes, which are typical here for the bottom side of the investigated sample, the differences are recognizable.

#### 5.4.4.3 Comments on the internal stress calculation

The whole birefringence and stress/strain analysis is performed as an 2D approach, including denoising, background correction and demodulation. But, the numerical differentiation step of the cumulative retardation is performed only as 1D directional derivative in depth direction. This is reasoned by the optical measurement principle, where only the cumulative accumulation of phase retardation in depth direction can be recorded. However, mathematically the potential of more information – by evaluating the whole gradient field of the cumulative retardation – would be

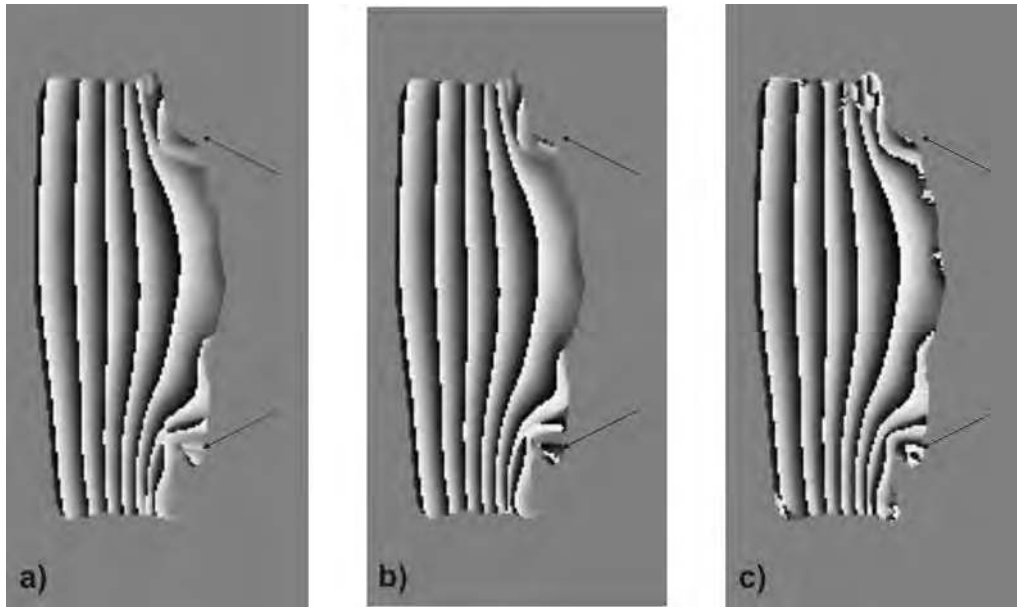


Figure 5.27: Comparison of wrapped phase images. The computation of the quadrature image is based on a) directional HT method, b) radial HT method, c) radial HT method combined with a bi-dimensional EMD background correction; exemplified on a measured retardation image (sample PS1), which curved fringes in the narrowings. An improved wrapped phase representation is noticeable in (c), especially for the regions, which are indicated by the arrows.

given by the demonstrated 2D approach. This possibility and its use for evaluating inhomogeneous birefringence in lateral direction should be discussed in the frame of future experiments.

Whereas in simulated data the wave shape is the crucial feature, which finally causes the erroneous signals in differentiation, in real data different measurement phenomena and artifacts, e.g. the decreasing modulation depth and the diminishing SNR, erroneous fringe vortices in deeper material regions, optical reflexes and signal drop-outs, may occur and deteriorate the reconstruction, which especially becomes visible during the differentiation step.

## 5.5 PS-OCT: Results and discussion

We have demonstrated our reconstruction procedure for recovering depth-resolved birefringence or internal stress information on different technical materials under relevant real-world test situations. These experimental applications are representative for situations in material testing being of increased interest, e.g. for the evaluation of elasto-mechanical properties of materials, especially strain-stress behavior of polymers or composites, and especially for observing the evolving internal anisotropies.

The samples have been probed and the reconstruction has been performed for three applications, in particular for:

- Dynamical stress/strain experiments, as a tensile test and a bending test,
- Evaluation of static strain/stress fields, arising in a photolithographic patterning process.

For the evaluation of the birefringence and stress reconstruction we performed the following steps:

- First, an evaluation of our reconstruction procedure has been performed by *simulations*.
- Second, for testing of technical materials, a homogeneous sample with a well-defined rectangular cross-section has been considered. The sample was almost uniformly stressed by increasing loads and shows an almost *homogeneous* birefringence. Comparative data [158], obtained by an additional load cell testing experiment, were available for the evaluation.
- Third, after the previous verification of our procedure by the comparative test experiments, samples of an arbitrary cross-section with locally *inhomogeneous* birefringence have been investigated.

### 5.5.1 Evaluation on simulated fringe patterns

The whole procedure developed for the evaluation and characterization of internal birefringence and stress distribution has been validated by means of simulated fringe patterns. The simulated sample M2 with a 2D inhomogeneous birefringence has been investigated, (compare Figure 5.14). The given internal stress distribution is used as reference and ground-truth, for which the stress reconstruction has been examined.

The cross-sectional retardation images have been modeled according to the scheme described in Subsection (5.3.4). The simulated retardation image, used for the reconstruction in the following, is depicted in Figure 5.28 a). We have chosen this sample to illustrate the performance of the 2D approach versus (intrinsic) 1D approaches. The simulated retardation image has been degraded according the noise model, described in Subsection (5.3.3), by (complex) speckle noise of different variances, as shown in Figure 5.28 b) and c). The noise variance in these images increases over depth, and vice versa the SNR decreases with the penetration depth. We have tested the simulations with noise variances up to reaching the limit, where the fringes starts to disappear in depth (i.e. up to a  $\text{SNR} \leq 0$  dB according to (5.9)), to emulate the decreasing visibility of the retardation fringes in highly scattering, bulk materials, (compare Figure 5.13).

The fringe orientation is calculated using the energy tensor approach for retardation images, as illustrated in Figure 5.29 a)–c). Especially the orientational unwrapping results in instabilities in case of higher noise variances, as can be seen in Figure 5.29 d)–f).

These instabilities can be reduced by a denoising step, either performed directly on the noisy (complex) orientation image, e.g. by a simple median filter as shown in Figure 5.30 b), or applied on the original fringe pattern. In particular, by using the CED filtering an enhanced orientation field estimation can be obtained by means of the structure tensor, as shown in Figure 5.30 c). After the preceding denoising of the fringe pattern, the stability of the orientation estimation and especially of the orientational unwrapping can be improved remarkably. Hence, for realizing our whole reconstruction method, we aim at a denoising of the fringe pattern to obtain a smooth wrapped retardation image, as can be seen in Figure 5.31 a)–f), where a CED filtering has been successfully applied.

Afterwards the quadrature transform on the smoothed fringe pattern image is determined, according to (5.50), which delivers the wrapped phase image  $\phi_r(x, z)$ , as depicted in Figure 5.28 d)–f). This wrapped phase data have been unwrapped, yielding the cumulative retardation image  $\Phi_{rc}(x, z)$ . Finally, the stress or birefringence distribution  $\Delta n_B(x, z)$  is obtained by means of numerical differentiation of the unwrapped cumulative retardation. The results are shown in Figure 5.31 g)–i). For the denoising performed by median filtering the recovered stress distribution, due to the remaining noise is disturbed over depth, whereas the quality of reconstruction is improved remarkably after CED denoising.

The influence of the wave shape on the reconstructed stress distribution is depicted in Figure 5.32 a) and b). As derived in Section (3.4) the triangular wave shape results in additional erroneous oscillations in the recovered stress image. By including a spline interpolation prior to differentiation this effect has been reduced, as shown in Figure 5.32 c). The reliability of our procedure, especially the advantage of a preprocessing, could be confirmed by the comparison with the simulated input data. In Figure 5.33 the corresponding profiles of the reconstructed stress distribution are shown. As can be recognized in Figure 5.33 b)–d), the erroneous oscillations are reduced in case of an additional smoothing and denoising.



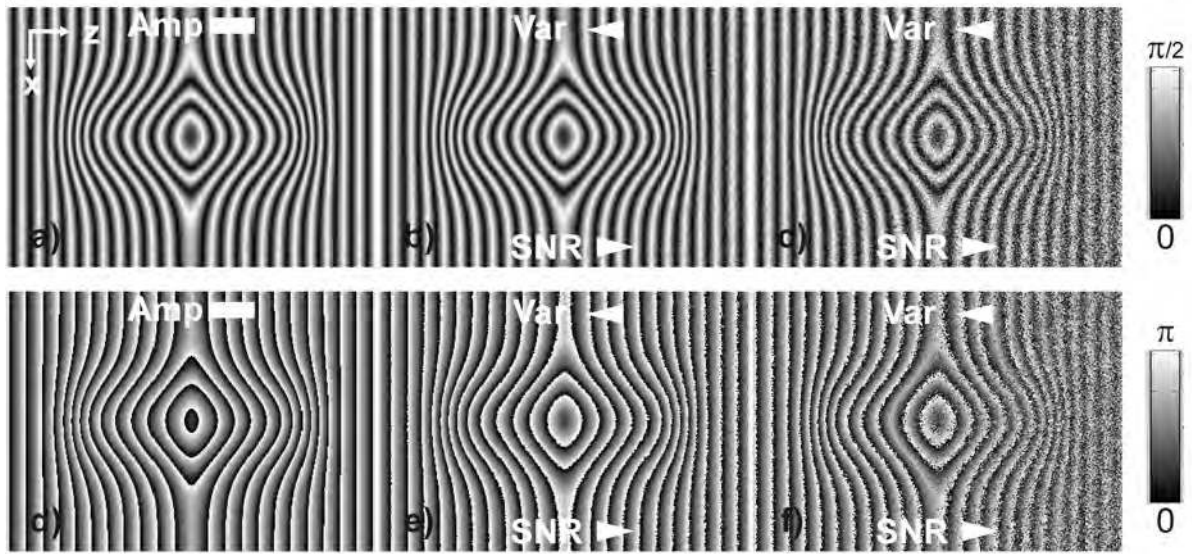


Figure 5.28: Cross-section (B-Scan) of the simulated retardation image. Retardation is scaled between  $[0, \pi/2)$ , wrapped retardation is scaled between  $[0, \pi)$ . a) Retardation image without noise, b) retardation image with speckle noise variance  $\sigma_{Sp}^2 = 0.1$ , c) retardation image with speckle noise variance  $\sigma_{Sp}^2 = 0.4$ , d)–f) wrapped phase images corresponding to (a)–(c). Speckle noise variance is related to the amplitude image, according to (5.37).

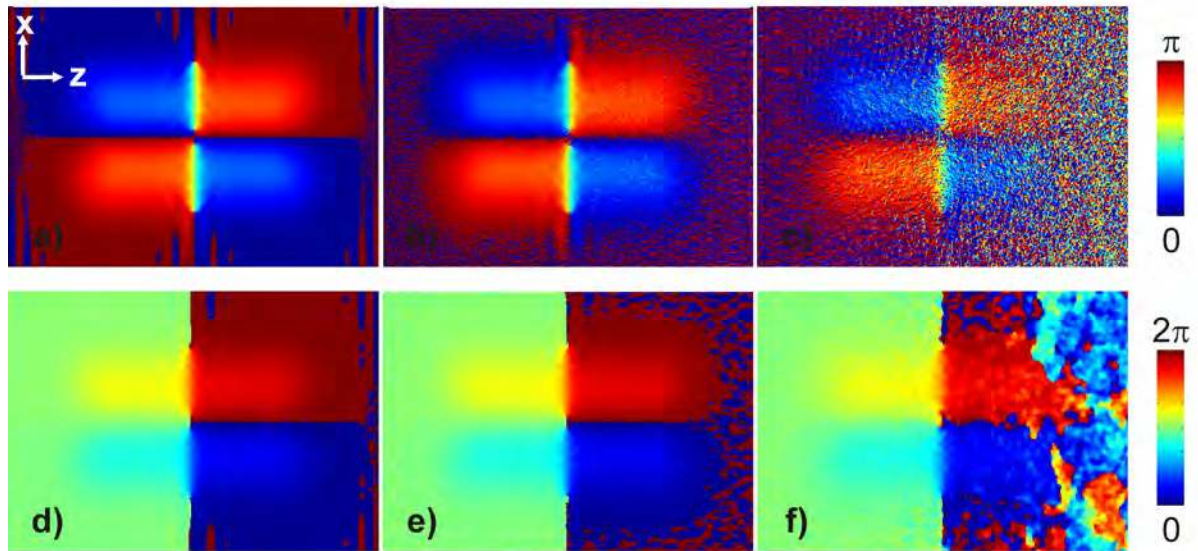


Figure 5.29: Fringe orientation and direction computed by the energy tensor approach for simulated retardation images with different noise levels. Orientation is scaled between  $[0, \pi)$ , direction is scaled between  $[0, 2\pi)$ . a) Fringe orientation image corresp. to Figure 5.28 a), b) fringe orientation image corresp. to Figure 5.28 b), c) fringe orientation image corresp. to Figure 5.28 c), d)–f) fringe direction image corresp. to a)–c) computed by orientational unwrapping. Orientational unwrapping artifacts due to increased noise level are clearly recognizable in (f).

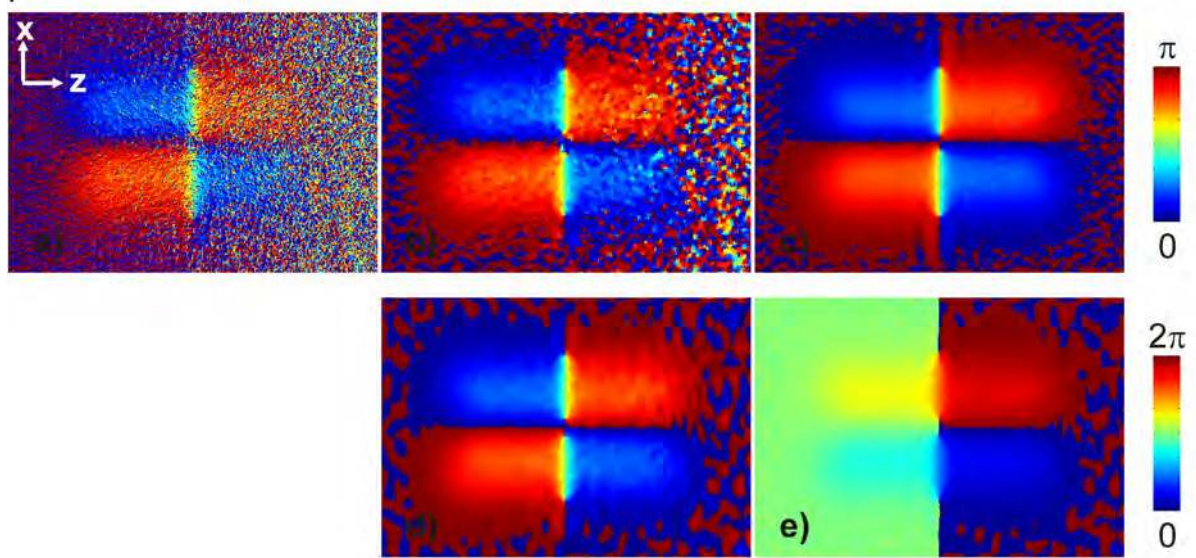


Figure 5.30: Influence of denoising on fringe orientation and direction estimation. a) Noisy orientation image obtained by the energy tensor approach, b) orientation image denoised by (complex) median filtering, c) orientation image obtained by the structure tensor approach, d) orientation image after a preceding CED-smoothing on the noisy retardation fringe image, e) direction image after the orientational unwrapping of (d). Improvement in the orientational unwrapping are visible in (d) in comparison to Figure 5.29 f).  $\sigma_{Sp}^2 = 0.4$ .

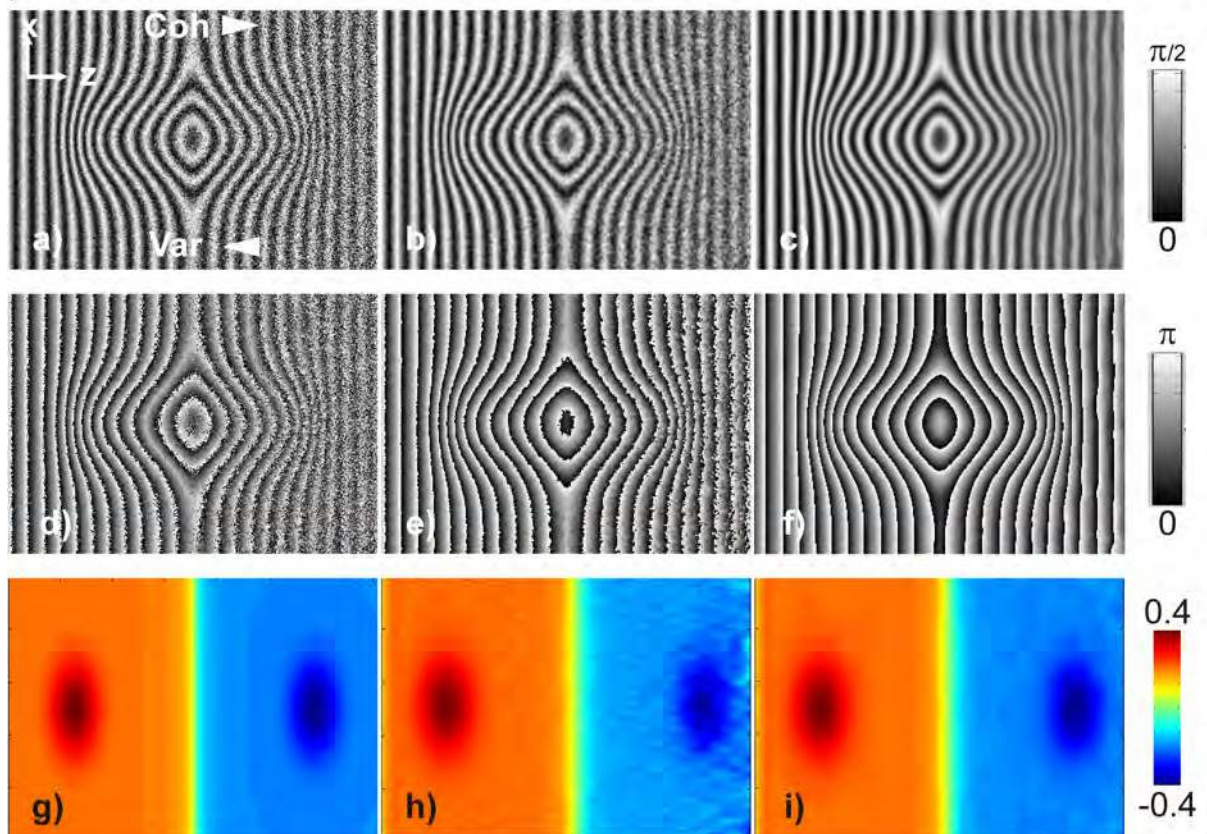


Figure 5.31: CED-based smoothing of noisy retardation image and its influence on resulting reconstructed internal stress distribution a) Original noisy retardation image, b) retardation image denoised by averaging, c) retardation image denoised by the CED approach including depth profile correction, d)–f) wrapped phase images corresp. to a)–c), g) initial stress distribution, h) reconstructed stress distribution correspond. to (b), i) reconstructed stress distribution correspond. to (c).  $\sigma_{Sp}^2 = 0.4$ .

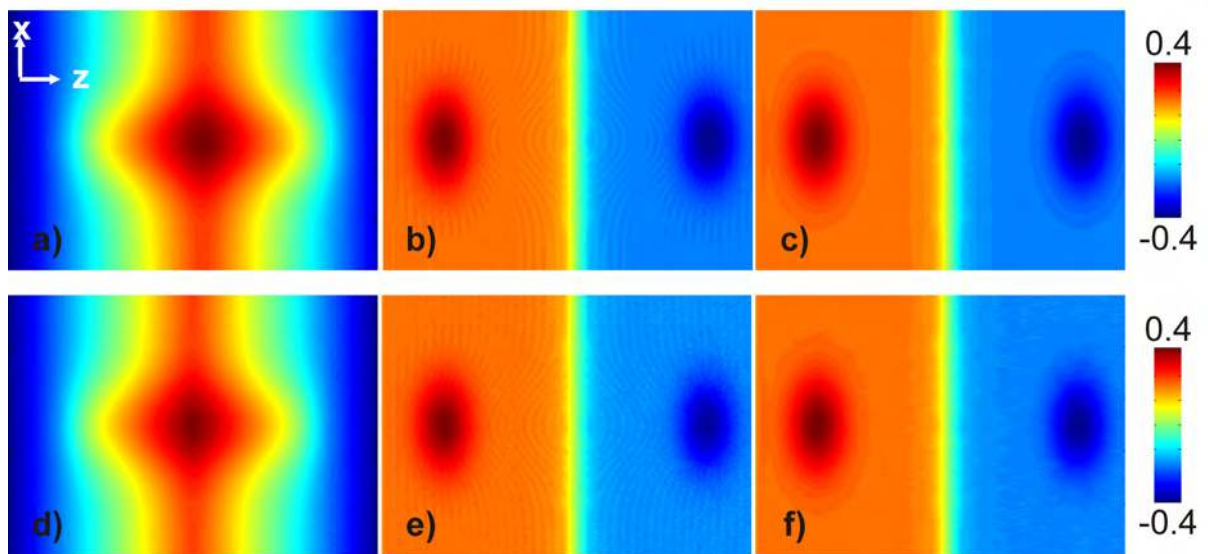


Figure 5.32: Demonstration of the influence of the triangular wave shape and noise on the demodulation results. Reconstructed a) cumulative phase retardation, b) stress distribution, c) smoothed stress distribution; (a)–(c): input data without noise, d) cumulative phase retardation, e) stress distribution, f) smoothed stress distribution; (d)–(f): input data with noise. In (c) and (f) in comparison to (b) and (e), a decrease of the erroneous ripples by an additional smoothing prior to demodulation can be recognized.  $\sigma_{Sp}^2 = 0.4$ .

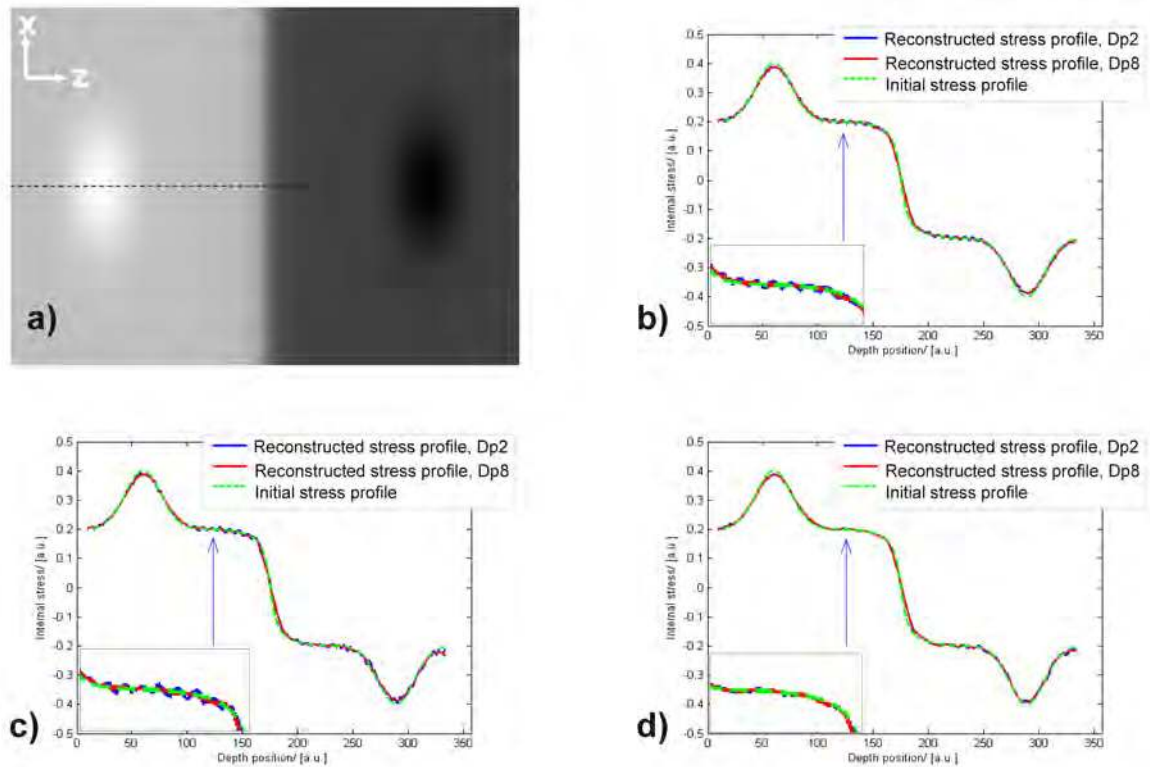


Figure 5.33: Comparison of initial and reconstructed stress profiles (along the indicated line in (a)). a) Simulated input stress distribution. b)–d) Reconstructed stress profiles, recovered from simulated b) noise-free retardation image, showing small oscillations, c) noisy retardation image, showing oscillations and small noise artifacts, d) noisy retardation image with a preceding CED-smoothing. The oscillations are clearly reduced in (d) in comparison to (b) and (c), visualized in the insets for a relevant signal part, (green: initial input stress profile, red and blue: reconstructed stress profile in different interpolations).  $\sigma_{Sp}^2 = 0.4$ .

## 5.5.2 Evaluation on measured cross-sectional retardation images

### 5.5.2.1 Dilatation test

For the final evaluation of the stress reconstruction procedure experimental data obtained by a tensile experiment have been regarded in comparison. A tensile test machine, which facilitates reproducible elongations of the samples under defined applied forces, has been used for the stretching. During the stretching the sample PS1 (elastomer) has been strained by an externally applied force up to a maximum stress value (almost reaching the ultimate stress limit) for the elastomer. Afterwards the sample has been relaxed to its approximate initial state.

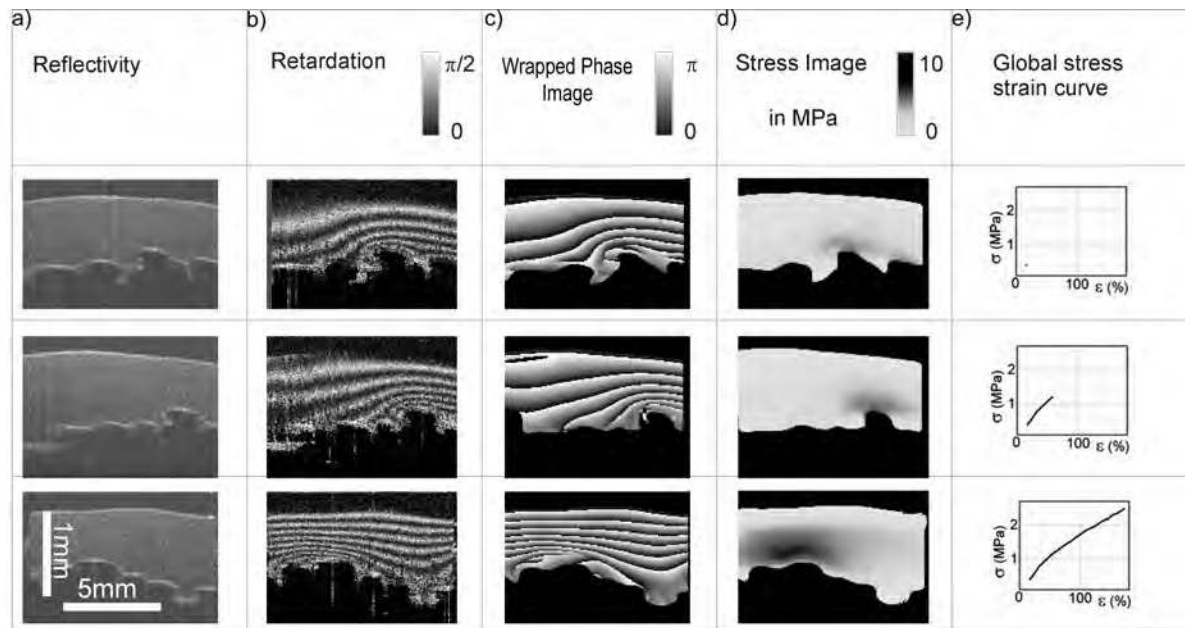


Figure 5.34: Representation of evolving internal stress distributions within the stretched elastomer sample (PS1), imaged under increasing external forces. The probed specimen shows anisotropic properties and stress-induced birefringence especially in the narrowing regions. a) Measured cross-sectional reflectivity images at different elongations, b) measured cross-sectional retardation images according to (a), c) reconstructed cross-sectional wrapped phase image, d) reconstructed cross-sectional internal stress image, e) measured strain/stress curve, illustrating the elastic behavior of the sample.

The evolving birefringence or stress states are analyzed on the consecutively recorded cross-sectional retardation images taken during the tensile test experiment. By means of the mathematical reconstruction procedure, as described in the previous chapter (subsequently by denoising, quadrature transform, 2D unwrapping and differentiation) on the individual frames, the distribution of the locally depth-resolved internal birefringence is finally obtained. The corresponding local stress distribution can be determined according to (5.41) with a stress-optical coefficient

( $C_{opt} = 19 \times 10^{-4} \text{ MPa}^{-1}$  [121]) for the investigated specimen. In Figure 5.34 a) and b), the measured reflectivity and retardation images at different states of elongations are shown. Correspondingly the reconstructed wrapped phase images and stress distributions are depicted in Figure 5.34 c) and d). The experimentally determined strain-stress behavior of the sample is presented for comparison in Figure 5.34 e).

First, evaluating the *qualitative* result, the reconstructed local stress pattern is in accordance with the physically expected stress distribution, i.e. locally higher stress states are observed at narrowings or constrictions of the cross-section. With rising strain also the reconstructed local stress values are increasing in the usual way.

Second, for the *quantitative* evaluation of the mathematically recovered stress data in this tensile test experiment, the mean values of the computed internal stress data have been compared with the experimentally determined global stress data at different elongations. The mean values of the computed internal stress data are obtained by averaging the reconstructed stress distribution over the cross-sectional area of the sample in the current frame. These values may be related to the external forces applied by the tensile test apparatus. The quantitative comparison with the experimental data at different elongations is depicted in Figure 5.35 a).

Reaching the maximal stretching value and being relaxed afterwards, the internal stress state returns to almost the initial state at the beginning. It should be noticed, that the investigated sample, having previously been stressed in other tensile test experiments, exhibits residual anisotropies within the material. The anisotropies have already been inherent to the sample prior to the validated test experiment. Presumably, the observed remaining anisotropies are connected with the irreversible uncoiling and reorientations of the polymer-chains inside the sample.

As can be seen from the globally measured strain-stress curve, a mechanical hysteresis loop is formed, as mostly prevalent in strain-crystallizing and filled elastomers, [174]. The hysteresis behavior could also be verified by our mathematical reconstruction: Exhibiting a nearly constant (computed) mean stress value at the beginning of the procedure, running through an hysteresis loop back at the end of the stretching to almost the initial value. However, in the reconstructed data (being also recognizable in the corresponding fringe patterns) an offset/bias can clearly be observed, both at the beginning and at the end of the tensile procedure, as shown in Figure 5.35 b). As previously explained, the offset is conditioned by the anisotropies within the material. From the experimental test realization and the mathematical reconstruction both contributions, stress-induced birefringence and material anisotropies can not be separated completely. A correct explanation of these effects would require an extended knowledge about the elastic behavior of the specific polymer type, which would go beyond of the scope of the performed experiments and reconstruction.

### 5.5.2.2 Bending test

Furthermore, the reconstruction has been tested for the evaluation of internal spatially distributed stress states emerging in a bending experiment of the sample. The sample (S2) has been chosen and clamped by its ends during the bending, which results in double 'S'-shape of the specimen. A more complicated distribution of internal stress with alternating tensile and compressive regions is expected, as depicted in the scheme of Figure 5.36. This results in a retardation fringe pattern with closed retardation fringes. The maximum of the cumulative retardation is located close to the

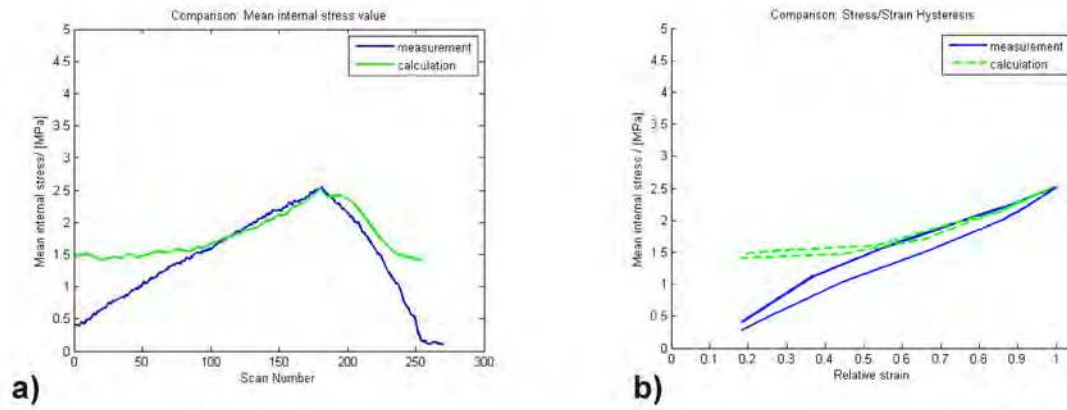


Figure 5.35: Comparison of applied external and mathematical reconstructed global strain/stress data during the stretching and relaxation process. a) Measured vs. mathematically reconstructed global stress data over time, b) stress/strain hysteresis behavior of the investigated polymer material.

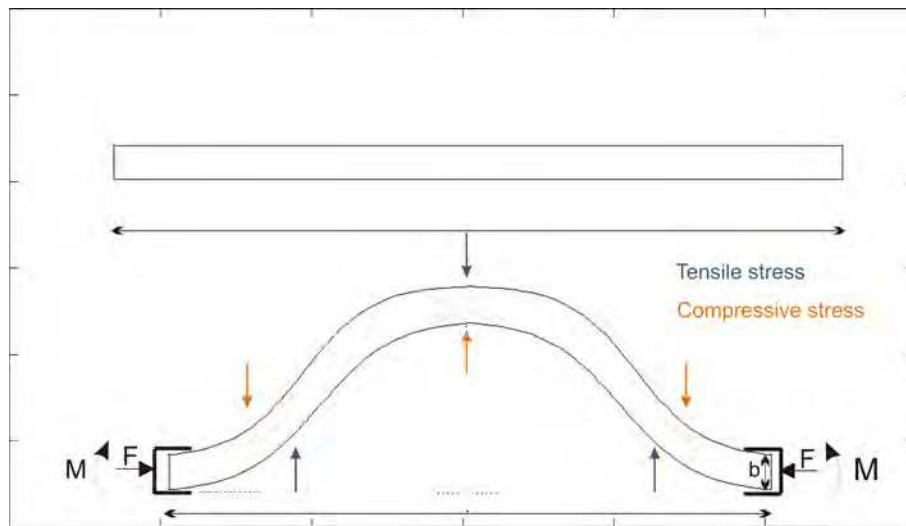


Figure 5.36: Scheme of a bent slab structure with resulting tensile and compressive stress regions as expected for the bending test, ( $F$ ,  $M$  acting force and moment,  $b$  material thickness)



center, where the neutral line separates tensile and compressive stress regions. For this application in particular, the realized 2D demodulation approach shows its performance by exploiting the full information.

In Figure 5.37, the performed reconstruction steps for internal birefringence and stress distribution extraction are demonstrated. Although the measured data exhibit severe noise and measurement artifacts (in this special case zero-valued data representing measurement drop-outs and an additional kink, as can be seen in Figure 5.38 a), a qualitative consistence of the reconstructed stress images with the theoretically expected stress distribution could be verified. The recovered internal stress distribution, depicted in Figure 5.38 b), is obtained here by numerical differentiation of the exponentially fitted cumulative retardation. For the central region of the slab the resulting stress profile in depth direction is visualized in Figure 5.38 c). It shows nicely the altering stress values between the tensile and compressive region with a neutral region in between.

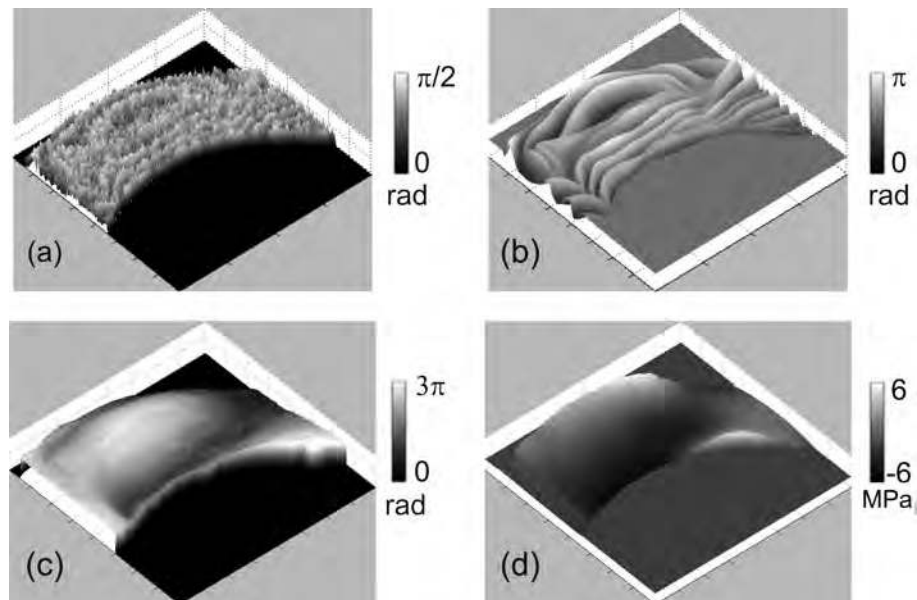


Figure 5.37: Illustration of the reconstruction procedure for a cross-sectional PS-OCT retardation scan, exemplified on the bent polymer sample (PS2). a) Original retardation image, b) (CED) denoised and wrapped phase image [184], c) cumulative (unwrapped) retardation image, d) resulting birefringence and corresponding stress image.

### 5.5.3 Evaluation on measured en-face retardation images

Finally, we have exemplified our reconstruction method for an en-face PS-OCT scanning application. The PS-OCT images are taken at the photoresist/wafer interface of test sample S3 representing a lithographically manufactured mold structure for miniaturized gear wheels, as shown in Figure 5.39 a). The mold structures are etched in a thick photo-resist layer. In particular, the region of interest is located between the neighboring wheel molds. There, by the PS-OCT imaging technique, the residual stress distribution arising after the exposure of the photo-resist material in the lithographic process has been investigated [158].

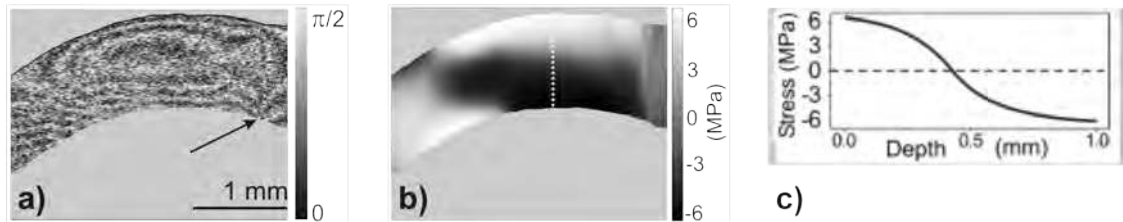


Figure 5.38: Representation of the measured fringe pattern and resulting stress distribution in the bent polymer sample of Figure 5.37 a). a) Noisy retardation fringe pattern, the arrow indicates a kink due to an existing material defect, the fringes are almost closed in the center and running towards the located material defect, b) cumulative retardation interpolated by a cubic polynomial, c) stress profile along the indicated line in (b), showing the transition between tensile and compressive stress.

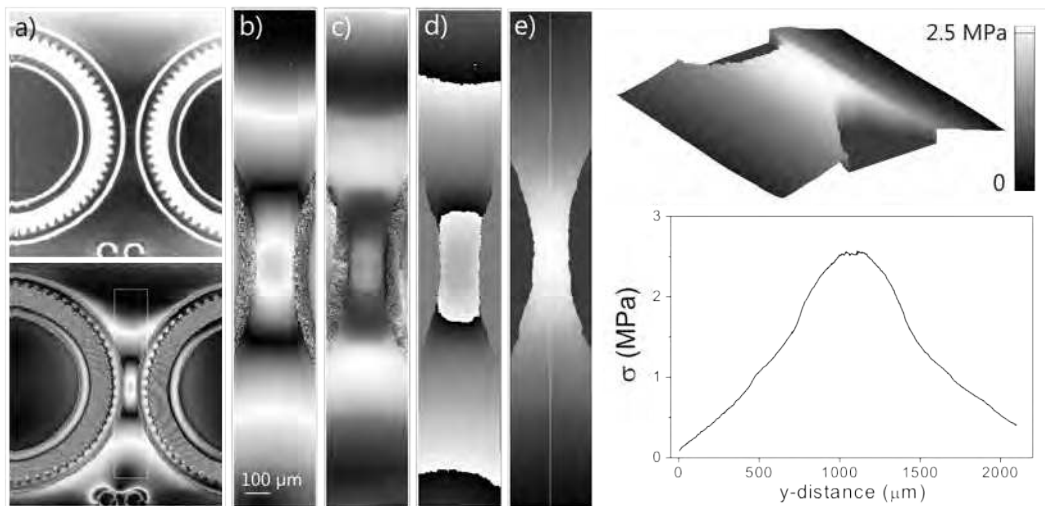


Figure 5.39: Illustration of the internal stress reconstruction performed on en-face PS-OCT retardation scans. A mould structure for miniaturized gear wheels represents the sample (PS3) under investigation. a) Original intensity (*top*) and retardation (*bottom*) images, b) enlarged view of area indicated in retardation image (a), c) quadrature image, d) wrapped phase image, e) stress image (plane and 3D view, as well as the profile along indicated dotted line).

With respect to the reconstruction the crucial point in this application consists in the noise variance differing locally due to the composition of the imaged materials: Whereas the birefringent photo-resist regions exhibit almost no noise and the fringes are clearly visible, inside the recessed regions a high amount of reflected speckle noise can be observed. On the other hand, these noisy regions exhibit no retardation and hence no fringe patterns, as depicted in Figure 5.39 b). Therefore, the denoising step of the fringes can be omitted in the reconstruction method. However, the 2D unwrapping method has been modified by an extended path-following approach, which exploits not only the local gradient of the retardation as quality measure, but ranks the different regions by a reliability criterium corresponding here solely to the local variance or SNR of the region. This ranking guarantees the stability of the unwrapping and quadrature transform computation over the whole region of interest, as shown in Figure 5.39 c)–e).

This application is more similar to a reflective photoelasticity experiment, and rather different from the previously considered cumulative cross-sectional PS-OCT imaging with its described capability of depth-resolved imaging. Here, in case of en-face PS-OCT techniques, the differentiation step need not be performed, as the stress values are averaged over the imaging depth. The unwrapped retardation value yields directly the birefringence after being scaled with the stress-optical coefficient of  $C_{opt} = 2.6 \times 10^{-4} \text{ MPa}^{-1}$  for the investigated photo-resist material [155]. The complete *quantitative* lateral stress map can be obtained, which exhibits stress values up to 2.5 MPa in the narrowing region between the wheel molds.

## 5.5.4 Discussion: PS-OCT imaging and reconstruction

### 5.5.4.1 Consideration about testing and reconstruction

Although all reconstructed data are comparable in their size with stress data obtained by comparative analysis techniques, it should also be noticed that different sources of measurement and reconstruction artifacts may have been occurred in our measurements, which possibly restrict the accuracy of the procedure.

With respect to the **measurements** we have to notice that inaccuracies may be introduced due to

- *Test sample:*

For performing the tensile stress experiment as a dynamical real-world application and for the following analysis the use of normalized standard tensile test elements would lead to better comparable and interpretable data.

Using as tensile test material an arbitrarily shaped specimen with a changing cross-sectional profile and with inherent inhomogeneities only roughly known can lead to different possible interpretations of the result. But, on the other hand samples with locally anisotropic regions represent more interesting and relevant specimens for depth-resolved stress measurements especially in dynamical tensile and fracture test experiments.

- *Hysteresis:*

Residual anisotropies in polymers may occur by previous tensile test experiments resulting in modified stress-optical coefficient values and in hysteresis behavior.

- *Irreversible processes:*

Combined with the hysteresis behavior of polymers the beginning of flow and plasticity deformations change the linear relationship between stress and strain. Furthermore, in case of varying cross-sectional areas of the sample the yield stress may be reached dependent on the effective local stress distribution at temporally different states.

- *Sample displacement:*

A slight change of the probing volume during the stretching process by the displacement of the sample may result in a different initial (residual) stress value and can cause a locally dependent biasing. Therefore, the tensile test setup should be stabilized by a unit allowing a well-defined reproducible sample position.

For the reconstruction step the noise variance or the SNR mainly determines the limiting factor for analysis. Only up to a certain material depth, dependent on material and backscatter distribution, the birefringence measurement and analysis can be reliably performed. With respect to the **mathematical reconstruction** of internal birefringence or stress states we have to notice that artifacts can be introduced due to:

- **Smoothing:**

Inducing vortex-like structures (i.e. singularities) in the fringe patterns may occur during the CED- or other denoising process in regions of very low SNR, where fringes are no longer

visible due to multiple scattering and material absorption. From the mathematical point of view these vortex artifacts can be removed by a preceding Helmholtz decomposition [151]. But, a correct limitation of the possible regions of interest for analysis by appropriate binary masking can reduce this artifact in an easier way.

- **Unwrapping artifacts:**

Incorrect unwrapping of complicated fringe pattern can be a result of the erroneously induced vortices. However, also partially remaining noise results in instabilities during the unwrapping procedure. With an adapted regularized unwrapping the influence of noise can be reduced.

- **Noise and wavy substructures amplification:**

Noise and wavy substructures amplification in the differentiation step can occur in the case of insufficient regularization or interpolation. On the other hand an over-smoothing may result in the case of a too strong regularization. A trade-off between both effects has to be found empirically or in an automatized way considering the backscatter statistics of the material.

#### 5.5.4.2 Summary: Pros and Cons

For PS-OCT imaging we have demonstrated how spatially resolved birefringence or stress states can be analyzed and interpreted in a two dimensional way to obtain qualitative and quantitative statements about inherent or induced anisotropies in turbid or semi-transparent polymer materials and about their related optical and elastic properties (e.g. uniaxial directions of polymer chains, internal birefringence or stress distribution). We have shown how the developed complex image analysis procedure, exploiting elements of single fringe analysis – as 2D quadrature transform and phase unwrapping – originally used for interferometric techniques, can successfully be adapted, extended and combined with image denoising techniques for a meaningful 2D analysis of PS-OCT retardation images. Both for simulations and for different real-world PS-OCT applications we have demonstrated the proof-of-principle of a 2D retardation image evaluation in extension to previously developed 1D analysis of other research groups. In addition, we have investigated the performance and the limitations of the proposed 2D demodulation technique for PS-OCT.

- **Advantages**

*Quantitative and spatial information:* The determination and reconstruction of local and spatially resolved complex birefringence and/or stress states inherent in (non-transparent) materials allows an advanced evaluation for non-destructive probing of materials in a quantitative way.

*Information content:* As we do not prefer any direction in the quadrature component computation the exploitation of the full 2D spatial frequency information of the retardation fringe pattern can be guaranteed.

*Complexity:* Closed and complicated retardation fringes being not necessarily convex can be analyzed. Phase stepping approaches requiring an extended experimental setup can be avoided using single fringe approaches.

**■ Limitations**

*SNR:* Measurement artifacts and an excessive noise may result that the reconstruction fails, in particular caused by instabilities in the unwrapping steps (orientational and phase unwrapping).

*Offset:* Locally varying background due to illumination or absorption by the specimen has to be corrected, e.g. by using empirical mode decomposition methods or partially by preceding band-pass filtering.

*Resolution:* Being limited by the resolution of the imaging unit, by the power of the light source and by the penetration depth of the light, also the performance of mathematical reconstruction to obtain quantitative local information can be reduced.

*Singularities:* In case of computation of a (complex) retardation fringe pattern, which exhibits inherent vortex structures, an additional consideration has to be performed, e.g. by separation of the pattern into its rotational and irrotational (complex) field components.

## Chapter 6

# DPC-OCT for Optical Path Length Mapping

Specimens investigated by phase-sensitive OCT techniques are mostly transparent samples and possess only few or no scattering centers, which are the carrier of image content in conventional OCT imaging. Hence, imaging contrast can only be obtained at material interfaces with refractive index differences or steep gradients. Interfaces usual represent embedded structures inside the sample which we want to investigate by phase-sensitive OCT techniques. Measuring the depth-resolved phase of the OCT interference signal at these interfaces the phase is an expression of the OPL according to (5) and it is therefore a measure for the cumulative phase change of the propagating wave field introduced by refractive index or thickness variations.

Measuring the absolute phase value of the OCT interference signal is often without importance or irrelevant as there is no continuous signal over the whole depth of the sample and regions with low intensity (reflectivity) signal and high noise level are situated between the different interfaces. However, a relative phase measure can be obtained at each interface comparing phase differences at adjacent lateral scanning positions or phase ratios between different interfaces. In [115] a phase-sensitive OCT setup working in FD is demonstrated measuring the phase shift introduced by the sample in comparison with a reference beam reflected from the sample surface in a common-path interferometer configuration. Besides measuring the phase difference related to a reference wave field, the mutual differential phase changes between laterally adjacent sites at the investigated interface can be exploited, as shown first by [18]. Following this DPC-OCT approach, in our work we extent the differential phase measuring technique, originally performed only in one direction (denoted in the following as one-directional (1d)-scanning), to a phase-sensitive OCT-configuration where both directional phase derivatives can be obtained. By means of the rotatable probing head a orthogonal-scanning regime, denoted in the following as two-directional (2d)-scanning, can subsequently been realized. Thereby being now able to measure the entire phase gradient field for different interfaces inside the sample, finally the total phase or OPL map at the interface can be reconstructed by classical gradient-based reconstruction schemes. In the following sections the DPC-OCT measuring setup and the whole OPL reconstruction procedure will be described.

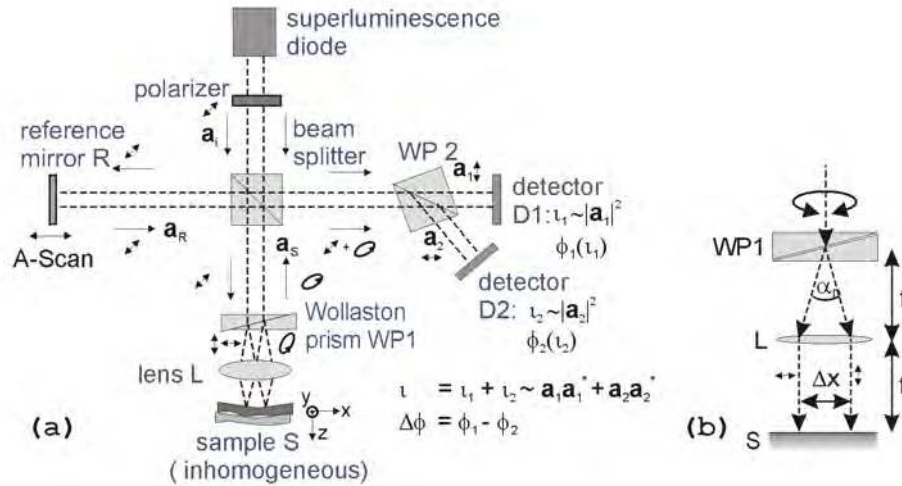


Figure 6.1: Optical configuration for DPC-OCT imaging. a) DPC-OCT optical setup scheme with indicated polarization directions, b) configuration of the probing head with rotatable Wollaston prism ( $f$ , focal length;  $\alpha_D$ , divergence angle;  $\Delta x$ , probing beam shear).

## 6.1 DPC-OCT: Imaging techniques

### 6.1.1 DPC-OCT: Optical configuration

For the performed measurements the previously demonstrated PS-OCT setup has been modified to a (differential) phase-sensitive OCT configuration. The optical setup for differential phase contrast OCT imaging is schematically sketched in Figure 6.1. Similar to a conventional OCT the basic optical setup consists also of a Michelson interferometer operating with a low coherence light source, in our case a SLD (Superlum SLD 761-MP3-DIL-D-1550) with a center wavelength  $\lambda_0=1550$  nm and a central bandwidth  $\Delta\lambda=50$  nm, resulting in an axial resolution  $\delta_z=19$   $\mu\text{m}$  in air according to (4.9). The setup is extended by including two Wollaston prism (WP) as crucial elements into the interferometric configuration. Due to the splitting and shearing of the probing beam by WP1 the phase difference between the two displaced wave components can be determined as phase delay between the two resulting interference signals, which can be separated due to their different polarization states at WP2. In Figure 6.2 a) the developed 2D DPC-OCT system is shown with indicated interferometric paths for the reference and probing wave. WP1 can be rotated to change the shear direction, allowing to measure the complete phase gradient field by subsequent scanning. The rotatable part of the stage, consisting of the Wollaston prism (WP1) and the imaging lens, is enlarged depicted in Figure 6.2 b).

Some crucial points concerning the measurement and imaging procedure in DPC-OCT are highlighted for a better understanding:



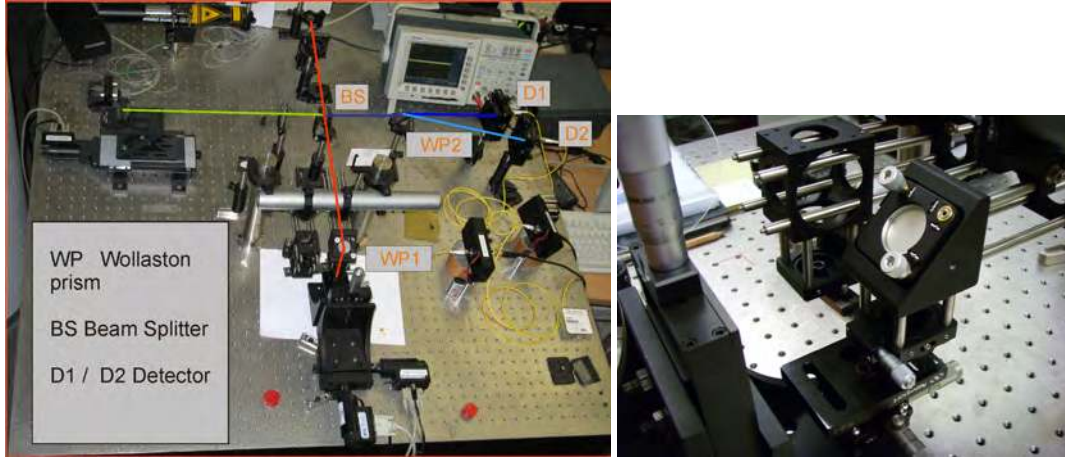


Figure 6.2: a) DPC-OCT measurement configuration, b) enlarged view of the beam shearing unit.

*Beam shearing:* The Wollaston prism WP1, which can be freely rotated around the beam axis, is placed in the back focal plane of the imaging lens L within the probing beam. The investigated structure has to be located in the front focal plane of the imaging achromatic lens. This arrangement allows a polarization dependent splitting and shearing of the probing beam into two adjacent parts, separated due to their different polarization states. The WP introduces a lateral shear  $\tau$  between the two wave components, so that the two beams are focused at two adjacent sites of the sample. In the realized setup the lateral displacement of the two focal spot positions is determined by the deviation angle ( $\alpha_D = 5^\circ$ ) of the Wollaston prism and by the focal length ( $f = 4.5$  mm) of the achromatic imaging lens, defining the lateral resolution of the system by

$$\delta_x = 2 \tan\left(\frac{\alpha_D}{2}\right) f, \quad (6.1)$$

which about  $6 \mu\text{m}$  for the specific setup. As the WP is rotatable in our configuration, the shear can be introduced both in  $x$ - or  $y$ - scanning direction as  $\tau_x = \Delta x$  or  $\tau_y = \Delta y$ . The two slightly displaced and focused beams are reflected at the depth-resolved interfaces and inhomogeneities within the sample. Due to refractive index changes over depth or thickness variations an OPL difference and consequently a phase shift  $\Delta\phi_{x,y}$  is introduced between the two sheared beams resulting in general in an elliptical polarization state after passing the WP1 in the backwards direction.

*Polarization steering:* It should be emphasized that the incident wave field  $\mathbf{a}_i$  has to be linearly polarized and oriented at  $45^\circ$ , as indicated in the scheme, allowing a decomposition of the reference wave into two orthogonally polarized, equal-valued wave components  $\mathbf{a}_{R1}$  and  $\mathbf{a}_{R2}$  with zero phase delay. In the beam splitter BS the backreflected sample wave, having in general an elliptical polarization, is mixed with the reference wave field. By including a second Wollaston prism WP2 in front of the two detectors D1 and D2 the interference signal  $\iota \propto (\mathbf{a}_R \mathbf{a}_S)$  is split into its two orthogonally polarized components  $\iota_1 \propto \mathbf{a}_{R1} \mathbf{a}_{S1}$  and  $\iota_2 \propto \mathbf{a}_{R2} \mathbf{a}_{S2}$ . At both detectors D1 and D2 two depth-resolved signals  $S_1(z) \propto \iota_1(x + \tau_x/2, z)$  and  $S_2(z) \propto \iota_2(x - \tau_x/2, z)$  or  $S_1(z) \propto \iota_1(y + \tau_y/2, z)$  and  $S_2(z) \propto \iota_2(y - \tau_y/2, z)$  are recorded describing the sheared interference between sample and reference wave.

*Calibration:* The probing configuration has to be calibrated to guarantee a horizontal alignment of the system. For these purposes we use the plane surface of a mirror as gauging object.

Furthermore, the changeable additional bias introduced by the WP1 is chosen to be zero. In case of a plane reflecting surface as reference sample the setup has to be calibrated that both detectors are balanced, i.e. receiving the same intensity signal.

### 6.1.2 DPC-OCT: Image types

Similarly to PS-OCT imaging also in DPC-OCT imaging two partial (sheared) reflectivity images are recorded. The total reflectivity image is obtained as

$$\iota_{rx}(x, y, z) = \iota_{rx1}(x, y, z) + \iota_{rx2}(x, y, z) \propto a_{1x}^2(x, y, z) + a_{2x}^2(x, y, z), \quad (6.2)$$

in case of the beam shear in  $x$ -direction and by an analogous expression for  $a_{1,y}$  and  $\iota_{ry}$  introducing the beam shear in  $y$ -direction.

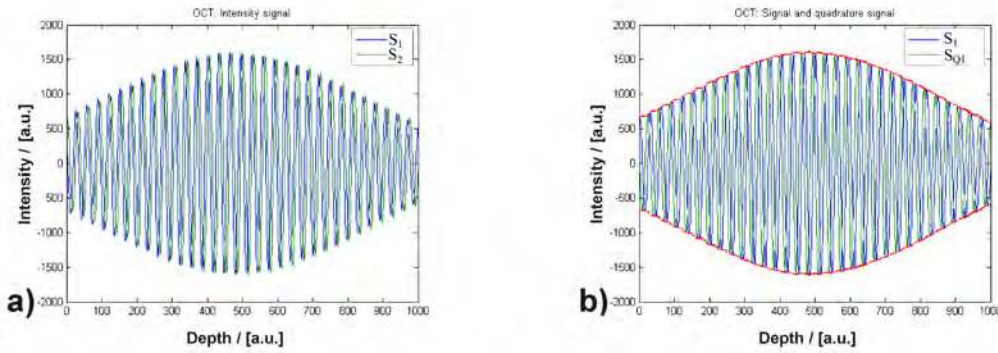


Figure 6.3: Detail of an A-Scan reflectivity signal. a) Detector signal (reflectivity)  $S_1(z)$  and  $S_2(z)$ , b) detector signal (reflectivity)  $S_1(z)$  and its quadrature signal  $S_{Q1}(z) = \mathcal{H}(S_1(z))$ .

Besides the reflectivity image the directional phase shifts  $\Delta\phi_x$  and  $\Delta\phi_y$  between both detector (reflectivity) signals  $S_1(z)$  and  $S_2(z)$  at adjacent lateral positions are of especial interest and can be obtained as phase difference between the instantaneous phase signals  $\phi_{1x}(z)$  and  $\phi_{2x}(z)$  (or as  $\phi_{1y}(z)$  and  $\phi_{2y}(z)$ ) by

$$\begin{aligned} \Delta\phi_x &= \phi_{2x} - \phi_{1x}, \\ \Delta\phi_y &= \phi_{2y} - \phi_{1y}. \end{aligned} \quad (6.3)$$

For each lateral position  $(x, y)$  the depth-resolved instantaneous phase values are given by the argument of the analytically continued detector signals by application of the 1D HT on  $S_1(z)$  and  $S_2(z)$  as

$$\begin{aligned} \phi_{1x}(x, y, z) &= \arctan \frac{\mathcal{H}(S_1(x + \tau_x/2, y, z))}{S_1(x + \tau_x/2, y, z)}, \\ \phi_{1y}(x, y, z) &= \arctan \frac{\mathcal{H}(S_1(x, y + \tau_y/2, z))}{S_1(x, y + \tau_y/2, z)}, \\ \phi_{2x}(x, y, z) &= \arctan \frac{\mathcal{H}(S_2(x - \tau_x/2, y, z))}{S_2(x - \tau_x/2, y, z)}, \\ \phi_{2y}(x, y, z) &= \arctan \frac{\mathcal{H}(S_2(x, y - \tau_y/2, z))}{S_2(x, y - \tau_y/2, z)}, \end{aligned} \quad (6.4)$$

illustrated in Figures 6.3 and 6.4 for the reflectivity and resulting phase signals at both detectors.

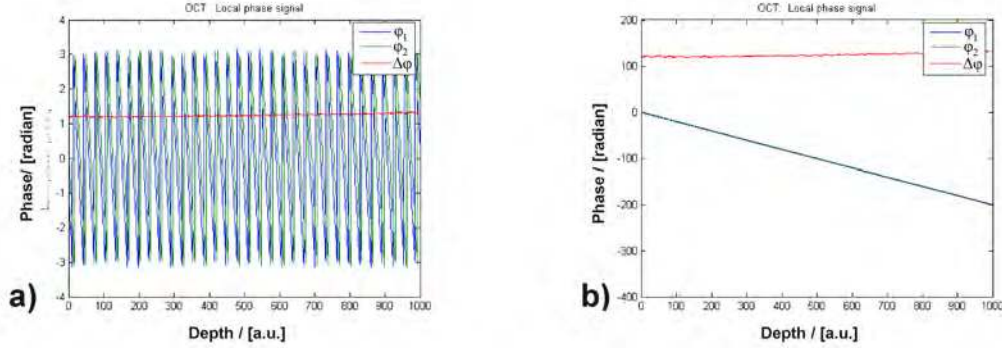


Figure 6.4: Detail of the instantaneous phase of the A-Scan signal in Figure 6.3. a) Instantaneous wrapped phase  $\phi_1(z)$  and  $\phi_2(z)$  of signal  $S_1(z)$  and  $S_2(z)$ , b) instantaneous unwrapped phase of signal  $S_1(z)$  and  $S_2(z)$  and phase difference  $\Delta\phi_i$  (red) corresponding to Figure 6.3.

Choosing a fixed depth position  $z = z_0$  and scaling the directional phase shifts  $\Delta\phi_i$ ,  $i = (x, y)$  with the beam shear  $\tau_i$  yields approximately the phase gradient  $\nabla\phi_i = (\phi_x, \phi_y)$  with

$$\begin{aligned}\phi_i(x, y) &= \frac{\partial(\phi(x, y))}{\partial i} \sim \frac{\Delta\phi_i}{\tau_i} \\ &= \frac{\phi_{2i}(x, y) - \phi_{1i}(x, y)}{\tau_i}, \quad i = (x, y).\end{aligned}\quad (6.5)$$

Both directional derivatives  $\phi_x(x, y)$  and  $\phi_y(x, y)$ , determined in the described way at each scanning position  $(x, y)$  and over the whole imaging depth  $z$ , represent the measured data of the two DPC-OCT 3D image stacks. Each individual image pair  $(\phi_x(x, y), \phi_y(x, y))$ , denoted as en-face DPC-OCT images, expresses the phase gradient  $\nabla\phi$ , or -after scaling- the optical path length gradient  $\nabla\vartheta$ . This measured gradient field delivers in the following the input data for the phase reconstruction, described in Section (6.3). To obtain a robust measurement the raw data of the A-scan (with a maximal sampling resolution of 40000 pts/mm) are averaged consecutively over depth.

### 6.1.3 DPC-OCT: Test samples

Whereas in conventional OCT imaging turbid, scattering samples are mostly under investigation, in phase-based OCT imaging techniques the specimens are composed of transparent objects with changing refractive index distribution or with embedded layer structures of varying lateral height profile.

Therefore, different transparent materials (varnish structures, silicon molded microbeads, wax particles, etc.), which act mainly as phase objects, have been probed by the developed DPC-OCT setup. Especially we want to focus on layered and embedded structures.

A set of representative samples has been chosen for demonstration of measurement and reconstruction with the main focus on validation, SNR or steep phase gradients:

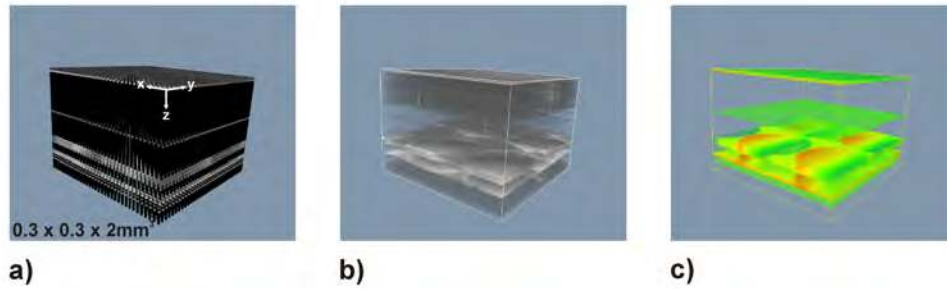


Figure 6.5: 3D visualization of an embedded microlens array imaged by DPC-OCT, test sample S1. a) 3D reflectivity data stack, b) 3D reflectivity image view with selected sections, c) 3D differential phase image view corresponding to (b) with a shear in x-direction.

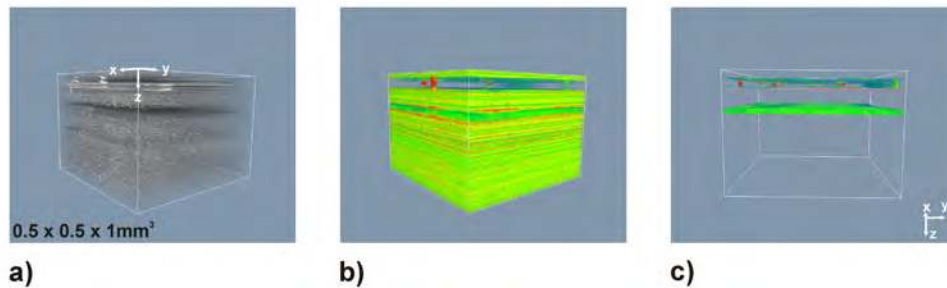


Figure 6.6: 3D visualization of an oil layer with embedded particles imaged by DPC-OCT, test sample S2. a) 3D reflectivity image view, b) 3D differential phase image view corresponding to (a), c) rotated view of b) with selected sections.

- **Sample S1:** Microlens array (Suss MicroOptics, Switzerland), being a specimen with known dimensions in order to validate our DPC-OCT imaging setup and the performed OPL-reconstruction method.  
 Imaging volume:  $0.3 \times 0.3 \times 2 \text{ mm}^3$   
 Voxel size:  $3 \times 3 \times 5 \text{ }\mu\text{m}^3$
- **Sample S2:** Oil layer with embedded microparticles, representing a specimen with a high noise level due to scattering effects at rough surfaces and impurities.  
 Imaging volume:  $0.5 \times 0.5 \times 1 \text{ mm}^3$   
 Voxel size:  $5 \times 5 \times 5 \text{ }\mu\text{m}^3$
- **Sample S3:** Acrylic, soft polymer film as a structure with an uneven surface and steep slopes to act as specimen with a high phase gradient resulting in phase wrapping effects.  
 Imaging volume:  $0.2 \times 0.2 \times 1 \text{ mm}^3$   
 Voxel size:  $2 \times 2 \times 5 \text{ }\mu\text{m}^3$

In Figures 6.5–6.7 the recorded 3D image stacks of the three test samples are visualized showing reflectivity and differential phase OCT maps. Layers containing no interference signal are partly removed for better visualization of relevant structures.

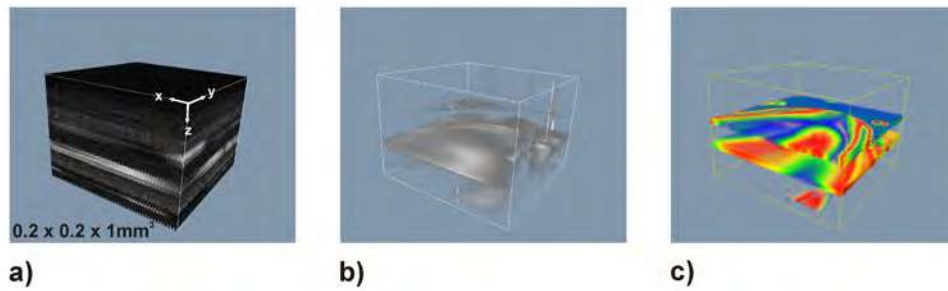


Figure 6.7: 3D visualization of transparent polymer layer imaged by DPC-OCT, test sample S3. a) 3D reflectivity data stack, b) 3D reflectivity image view with selected sections, c) 3D differential phase image view corresponding to (b).

It should be emphasized, that not only the surface of the specimen is investigated, but in particular DPC-OCT enables to visualize embedded phase structures within the sample, as schematically illustrated for the microlens array in Figure 6.8.

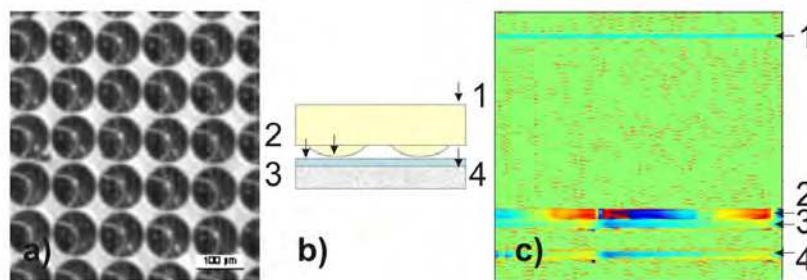


Figure 6.8: Test sample (S1) arrangement in DPC-OCT measurement. a) Microscopic image of the investigated microlens array, b) sketch of the microlens array, it is turned upside down with its bulk substrate on top and lenses at the bottom side, c) DPC-OCT cross-sectional image, with indicated interfaces. (Interfaces: (1) surface, (2) microlenses, (3) glass slide surface, (4) glass slide bottom side.)

## 6.2 DPC-OCT: Measurement performance

### 6.2.1 DPC-OCT: Raw-data phase drift

The accuracy of our DPC-OCT measurements was determined at first by using a defined test sample, (here given by a microscope cover glass of known dimensions and roughness), which represents a two-interface object (air/glass and glass/air). The reflectivity signal bursts at one detector, resulting from the individual interfaces, are shown in Figure 6.9.

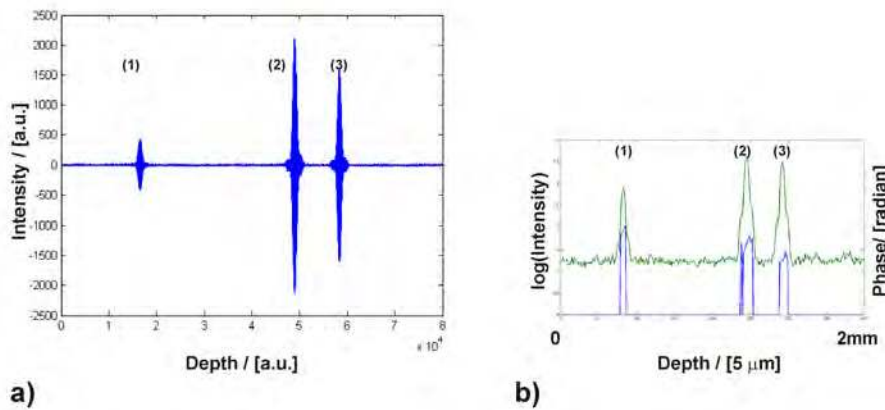


Figure 6.9: a) Reflectivity signal (raw data) of a two-interface test sample (microscope cover glass) with indicated signals: (1) artifact (ghost), (2) slide front surface, (3) slide bottom side, b) averaged (log)intensity and differential phase values over depth.

For the evaluation of the phase stability the raw data (i.e. the non-averaged data at a fixed lateral position  $(x, y)$ ) of the A-scan signal over the duration of the signal burst are regarded. The central part of the reflectivity burst, exceeding a predefined threshold and corresponding to about 1–2 pixel in the averaged representation, has been taken into consideration. The dependency of the phase difference over depth and the variance of the differential phase are depicted in Figure 6.10.

A slight drift in the phase difference over depth is recognizable on the data, averaged over 10 scans, as shown in Figure 6.11. The drift is noticeable as well at the front as at the back side of the slide (burst (2) and (3)), which may be caused by the side lobes of the SLD spectrum. The surface signal burst (2) also shows a small oversaturation in its center. For explaining the slightly higher degree of the phase drift at the slide bottom side, probably also dispersion can contribute to an additional drift of the measured phase difference values. This drift could be corrected by an exponential fitting. After fitting the standard deviation of the phase difference yields  $\sigma_{\Delta\phi_D} = 0.016$  and  $\sigma_{\Delta\phi_D} = 0.013$  rad (for bursts (2) and (3)) with respect to a mean phase difference of  $\mu_{\Delta\phi_D} = 1.24$  rad and  $\mu_{\Delta\phi_D} = 1.61$  rad.

The influence of noise and dispersion is illustrated by us with the help of a simulation. As depicted in Figure 6.12 a), first a sinusoidal interference burst simulating reflectivity signals in materials without dispersion has been assumed.

The interference burst (intensity) signal has been degraded by Gaussian white noise of different variances. In the differential phase (over depth) the noise results in phase fluctuations and causes a

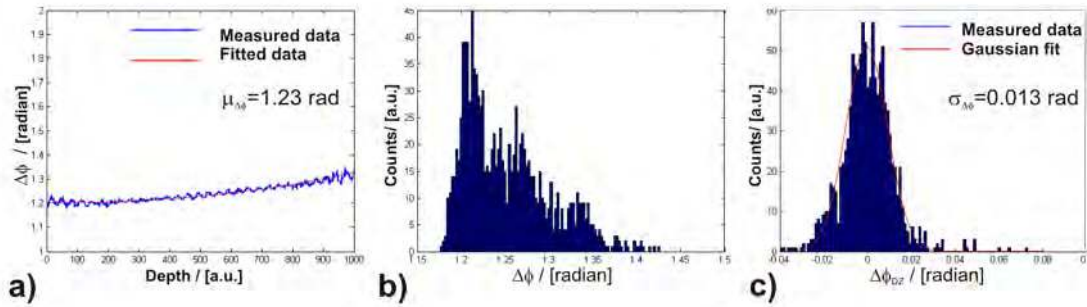


Figure 6.10: Deviation of the phase difference over depth (single A-scan). a) Phase difference over depth corresponding to burst (3), b) phase difference distribution corresponding to (a), c) phase difference distribution after drift correction.

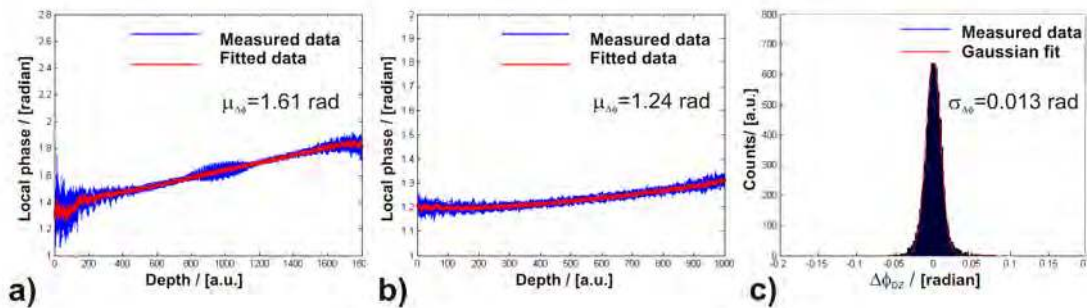


Figure 6.11: Deviation of the phase difference over depth (*red*: averaged over 10 A-scans). Phase difference signal over depth a) corresponding to burst (2), b) corresponding to burst (3), c) phase difference distribution, corresponding to burst (3), after zero-mean and drift correction with overlaid *red*: Gaussian fit.

fanning-out of the phase difference dependent on the value of the intensity envelope (Figure 6.12 b) and c)), i.e. dependent on the SNR ratio in the reflectivity image. It demonstrates that a reflectivity signal threshold has to be chosen for a reliable differential phase measurement, as we have done in our measurements.

Dispersion causes a chirped burst, as depicted in the simulated signals of Figure 6.13 a) and d). Finally the signal chirp results in a drift of the phase difference between the two interference bursts and may influence the accuracy of the measurement. However, on real data we have estimated that the error due to phase drift is almost to neglect, (less than 1% after exponential fitting correction).

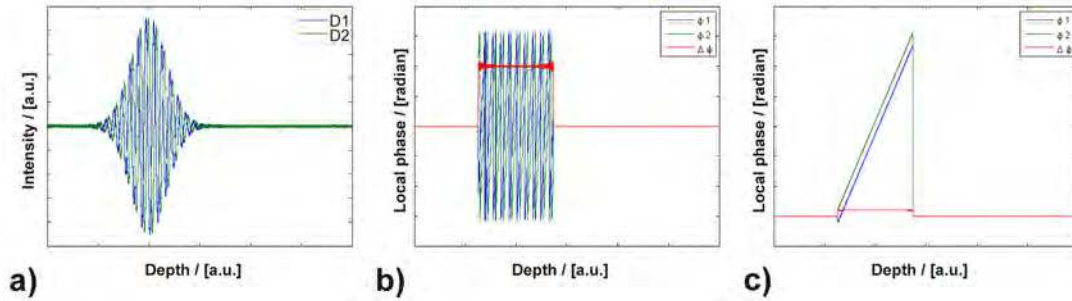


Figure 6.12: Sinusoidal interference burst with additive Gaussian white noise with variance  $\sigma^2 = 0.003$ . a) Noisy reflectivity bursts of both detector signals D1 and D2, b) noisy instantaneous wrapped phase (over depth)  $\phi_1$  and  $\phi_2$  of both detector signals, c) noisy instantaneous unwrapped phase (over depth) of both detector signals and differential phase (red line). The differential phase signal of (c) is overlaid in (b) (red line) for better visualization.

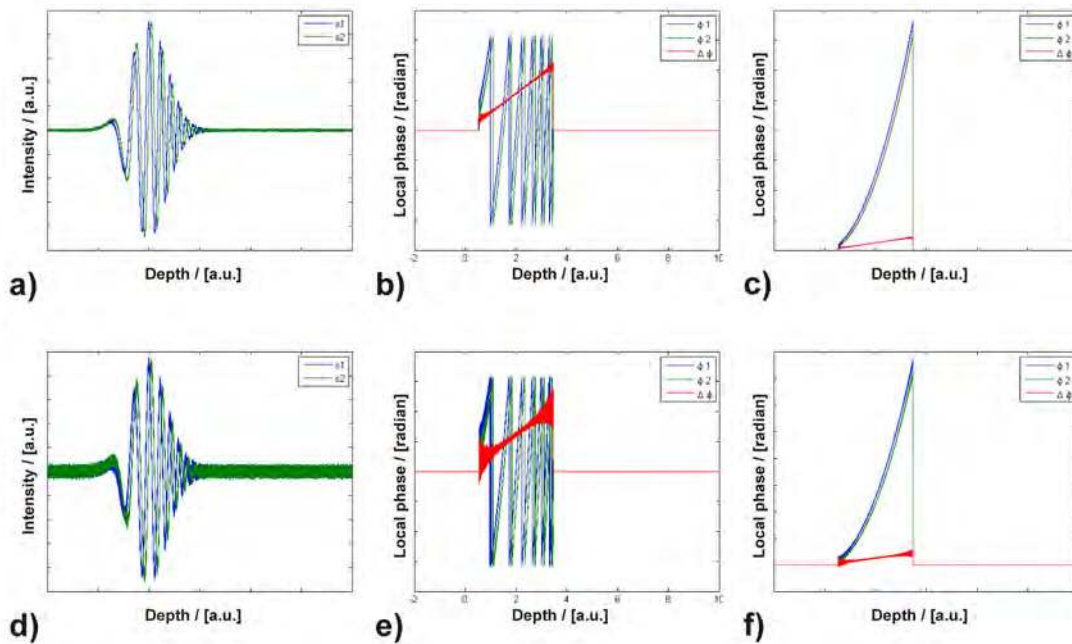


Figure 6.13: Chirped interference burst with additive Gaussian white noise with variance  $\sigma^2 = 0.003$  (top) and  $\sigma^2 = 0.015$  (bottom). a), d) Noisy reflectivity bursts of both detector signals, b), e) noisy instantaneous wrapped phase (over depth) of both detector signals D1 and D2, c), f) noisy instantaneous unwrapped phase (over depth) of both detector signals and differential phase. The differential phase signal of (c) and (f) is overlaid in (b) and (e) (red line) for better visualization.



### 6.2.2 Repetition accuracy

For the estimation of the achievable accuracy of the setup, we have ascertained the phase distribution by repeating 2500 A-scans on a simple glass slide and by evaluating the 40 dB reflection of the bottom surface. Despite the rather long interferometer arms ( $>0.5$  m), the standard deviation of the phase fluctuations was determined to be only 0.0055 rad corresponding to 0.7 nm OPL at a center wavelength of 1550 nm. Improvements are expected by switching to 800 nm and by miniaturizing the setup [173].

### 6.2.3 Phase unambiguity range

Each depth-resolved OCT-signal  $S_1(z(t))$  and  $S_2(z(t))$  at both detectors can be regarded as a sequence of interference bursts. The instantaneous phase of each burst is determined by the 1D HT according to (6.4), hence an ambiguity range of  $2\pi$ , corresponding the peak-to-peak distance inside the signal burst, is remaining. Although larger phase differences may be considered by additionally estimating the positions of the envelopes of both signals [150], here rather the prior knowledge about smooth functions is exploited for the phase reconstruction.

### 6.3 DPC-OCT: Reconstruction of phase and optical path length map

The aim of our reconstruction is the recovery of the phase from the two orthogonally scanned DPC-OCT 3D image stacks. The whole reconstruction procedure for the phase and OPL map, demonstrated for the extracted 2D en-face DPC-OCT images of the test samples, consists of several steps. These steps have to be combined and adapted to each other. Both measurement and reconstruction are performed with the focus on realizing these methods as 2D approaches. For comparison also 1D-based reconstruction approaches are regarded, suitable for conventional 1D DPC-OCT imaging.

In particular, we want to denote three essential steps for the phase reconstruction in the realized DPC-OCT imaging: The *extraction of the en-face scans*  $\phi_x^{(i)}(x,y)$  and  $\phi_y^{(i)}(x,y)$  at relevant interfaces ( $i$ ) out of the recorded 3D data stacks delivers the input data for the following reconstruction. A *2D unwrapping* task is required in the case of a discontinuous phase gradient field  $\nabla\phi_w(x,y)$  to recover the continuous gradient field  $\nabla\phi_c(x,y)$ . Finally the *reconstruction of the phase/OPL map* from the unwrapped continuous gradient field  $\nabla\phi_c(x,y)$  can be performed.

These main steps will be discussed in the following. However, it should be mentioned that for the whole reconstruction procedure also further preprocessing steps may be required, e.g. *registration* of the mutual orthogonal scans, *removal* of imaging artifacts, or *scaling* of the finite differences (i.e. scaling of the discretized derivatives).

#### 6.3.1 En-face DPC-image extraction

Applying the scheme for instantaneous phase computation of the A-scan signal by 1D HT, according to (6.3)–(6.5), we can obtain the local phase value for each position  $(x,y,z)$  in the recorded 3D data stack. Therefore, the local phase difference between laterally adjacent sites at a fixed depth position  $z$  can be determined. To select both en-face scans  $\phi_x^{(i)}(x,y)$  and  $\phi_y^{(i)}(x,y)$  at the interface position ( $i$ ) properly the reflectivity signal (over depth) at the considered layer is taken as reference. Inside the axial resolution range (extended in depth to about 2–3 pixel) the corresponding en-face DPC-OCT image is chosen with respect to the maximum value of the reflectivity signal, as illustrated in Figure 6.14.

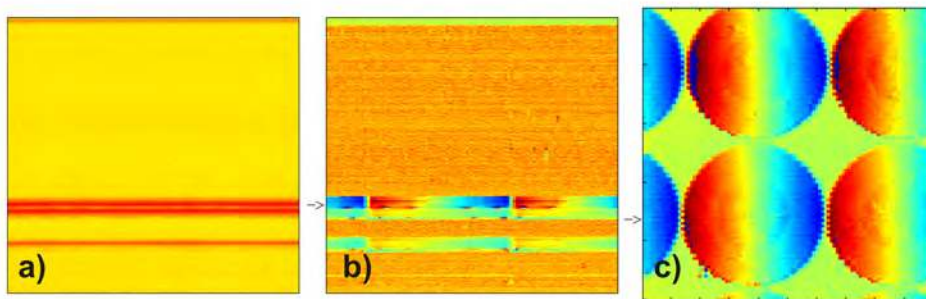


Figure 6.14: En-face DPC-image extraction, illustrated for the microlens array. a) cross-sectional reflectivity scan, b) cross-sectional DPC-OCT image, c) en-face image as indicated by the arrows.

### 6.3.2 2D Unwrapping

Due to the unambiguity range in the DPC-OCT measurement the data are recorded as wrapped values mapped to the interval  $[-\pi, \pi)$ . This can lead to a discontinuous, wrapped phase gradient field  $\nabla\phi_w(x, y)$ . Thereby we have to distinguish between single erroneously wrapped pixels, arising e.g. due to noise and scattering effects in the measuring system, and larger wrapped regions. We want to assume, that the wrapped regions are closed domains without phase singularities.

For the unwrapping of single wrapped pixels we apply a median filter for preprocessing. Median filtering has proven to be sufficient in our applications in case of moderate scattering samples, although a slight blurring by the filtering is introduced. In case of unwrapping a larger connected region we pursue two approaches:

A) An unwrapping method is performed based on *solving the Laplace equation* on the domain  $\Omega$  for the phase  $\hat{\phi}(x, y)$ , to be recovered, which can be described as

$$\begin{aligned} \frac{\partial^2 \hat{\phi}(x, y)}{\partial x^2} + \frac{\partial^2 \hat{\phi}(x, y)}{\partial y^2} &= \rho(x, y) \quad \text{on } \Omega, \\ \rho(x, y) &= \frac{\partial \phi_x(x, y)}{\partial x} + \frac{\partial \phi_y(x, y)}{\partial y}, \\ &\sim \frac{\Delta_{wx}(\Delta\phi_{wx}(n, m))}{\Delta x} + \frac{\Delta_{wy}(\Delta\phi_{wy}(n, m))}{\Delta y}, \\ \text{with } \Delta_{wx}(\Delta\phi_{wx}(n, m)) &= 0.5 * W(\Delta\phi_{wx}(n+1, m) - \Delta\phi_{wx}(n-1, m)), \\ \Delta_{wy}(\Delta\phi_{wy}(n, m)) &= 0.5 * W(\Delta\phi_{wy}(n, m+1) - \Delta\phi_{wy}(n, m-1)). \end{aligned} \quad (6.6)$$

The measured data  $\phi_x(x, y)$  and  $\phi_y(x, y)$  are partially derived. Their derivatives are being regarded mod  $(2\pi)$ , denoted by the wrapping operator  $W$ , yielding the right hand side of the (6.6). Here we want to assume Neumann boundary conditions

$$(\nabla\phi(x, y)\mathbf{e}_n) = 0 \quad \text{on } \delta\Omega, \quad (6.7)$$

with  $\mathbf{e}_n$ , denoting the normal direction on the boundary  $\delta\Omega$ . Practically, the boundary condition can be fulfilled by a mirrored continuation of the image.

B) A *path-following unwrapping* approach is chosen, as described in [151], depending on a quality criterium to be defined. The quality criterium can be adapted according to relevant image features (in our case variance, SNR, gradient, or deviation of the gradient from the local mean of a gradient). In Figure 6.15 the wrapped and unwrapped en-face scans of the microlens test sample are depicted.

### 6.3.3 Phase map reconstruction

Here we consider the reconstruction of the phase/OPL map from the unwrapped continuous gradient field  $\nabla\phi_c(x, y)$ . For our reconstruction we suppose smoothness and differentiability of the phase map (i.e.  $\phi(x, y) \in C^2$ ), to be recovered, although this assumption is not always completely fulfilled for all regions in the measured data. First, the reconstruction is regarded under the initial condition, that only one differential phase image (e.g.  $\phi_x(x, y)$ ) is available from measurements

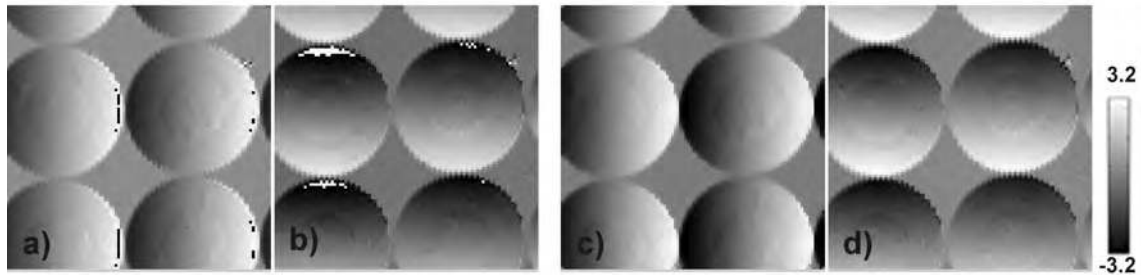


Figure 6.15: Illustration of the 2D phase unwrapping for the extracted en-face DPC-OCT images. For the unwrapping of the microlens test sample data the path-following method is chosen here. a) Wrapped DPC-OCT image  $\phi_{wx}(x,y)$ , containing wrapped domains in case of the steeper curved boundary, b) wrapped DPC-OCT image  $\phi_{wy}(x,y)$ , c) unwrapped DPC-OCT image  $\phi_x(x,y)$ , d) unwrapped DPC-OCT image  $\phi_y(x,y)$ .

and the phase map has to be recovered. This leads to the 1D line-integration methods being described in the following. Second, the reconstruction is shown under the condition, that now -by the realized DPC-OCT imaging setup- both differential phase derivatives are given, which will be considered after the 1D reconstruction approaches.

### 6.3.3.1 1D phase reconstruction approaches

In literature several line-integration approaches [159] are described for signal reconstruction from its differential signal. They can be applied here for reconstruction of phase or generally of topological surface maps. The approaches explicitly suppose that only one directional derivative is known, or that the derivative in perpendicular direction can be neglected by considering plane objects. Partially they assume smoothness of the recovered function in the direction orthogonally to the scanning direction [167].

Originally we applied these 1D reconstruction methods for enhanced segmentation of DIC images, where due to optical DIC-microscope limitations – being equipped with Wollaston prism under a fixed shear direction – only a single directional phase derivative image is recordable. Here, we will regard in a common approach the measured differential phase images, which in the context of DPC-OCT are the measured differential phase contrast images  $\phi_x(x,y)$ , and in the context of DIC imaging these are the measured DIC images  $I_{DIC}$ . Deviations from the common approach are accordingly noticed in the following passages. However, one main difference should be emphasized already here: In DIC imaging a nonlinear relationship between measured intensity and phase gradient (or OPL gradient) is given according to (2.13), which can only be linearized under the assumption of weak phase objects. On the other hand, in DPC-OCT imaging the phase gradient is obtained directly, as expressed in (6.3) and (6.5). Therefore, the phase gradient scales linearly with the measured differential phase images.

We have tested different 1D reconstruction approaches, namely *forward/backward line-integration*, *exponential line-integration*, *1D Hilbert transform*, *deconvolution*, and *optimization*, which will be regarded now. For illustration of their reconstruction potential the microlens test

sample is chosen as representative input data. Since having radial symmetric specimen structures, the strength of asymmetry, caused by 1D reconstruction, is nicely visualized.

#### ■ Forward/backward line-integration

We will assume that the measured DPC-OCT image  $\phi_x(x, y)$  is recorded with a shear in  $x$ -direction. The total phase  $\phi(x, y)$  is reconstructed by numerical linewise integration of the (zero-mean) directional phase derivative  $(\phi_x(x, y) - \bar{\phi}_x)$ , where

$$\bar{\phi}_x = \left( \int_{B_1}^{B_2} \phi_x(x, y) dx \right) / \left( \int_{B_1}^{B_2} dx \right)$$

denotes the linewise average of  $\phi_x(x, y)$ . The integration is performed in forward and backward direction between the image boundary  $B_1$  and  $B_2$  as

$$\phi(x, y) = 0.5 \left( \int_{B_1}^x (\phi_x(x', y) - \bar{\phi}_x) dx' - \int_x^{B_2} (\phi_x(x', y) - \bar{\phi}_x) dx' \right) \quad (6.8)$$

to balance the errors. The integration of (6.8) in shear direction could theoretically be used for retrieving  $\phi(x, y)$ , but measurement errors are propagating in integration direction by this straight-forward integration. Furthermore, the boundary values are not properly known, the assumption of having a constant boundary value is not fulfilled for real structures, being extended over the whole scan, and resulting in additional error terms therefore, as illustrated in Figure 6.16 a).

#### ■ Exponential line-integration

To improve the numerical integration an iterative line-integration method by exponential averaging in shear direction is proposed in [159], expressed as

$$\phi(x, y) = \frac{1}{2} \left( \int_{B_1}^x (\phi_x(x', y) - \bar{\phi}_x) \exp(-\gamma_A |x - x'|) dx' - \int_x^{B_2} (\phi_x(x', y) - \bar{\phi}_x) \exp(-\gamma_A |x - x'|) dx' \right), \quad (6.9)$$

as shown in Figure 6.16 b). The parameter  $\gamma_A > 0$  in the exponential decay term acts as attenuation factor for reducing the error propagation over spatial distance.

As this bi-directional attenuated integration can be interpreted as a convolution with an exponential decay function, we perform the computation for all line-integrational approaches in Fourier domain speeding up the computing time in comparison to integration in spatial domain.

$$\phi(x, y) = \mathcal{F}^{-1} \left\{ \mathcal{F} \left\{ \phi_x(x, y) - \bar{\phi}_x \right\} \frac{i \nu}{(\gamma_A^2 + \nu^2)} \right\}. \quad (6.10)$$

In the limit of  $\gamma_A \rightarrow 0$  (6.10) results in the conventional integration in FD

$$\phi(x, y) = \mathcal{F}^{-1} \left\{ \mathcal{F} \left\{ \phi_x(x, y) - \bar{\phi}_x \right\} \frac{i}{\nu} \right\} \quad \text{for } \nu \neq 0. \quad (6.11)$$

#### ■ 1D Hilbert transform-based method

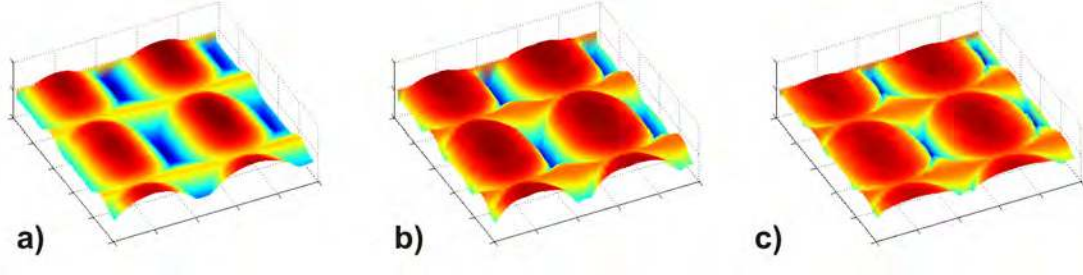


Figure 6.16: Qualitative comparison of line integrational methods for phase map recovery. Computation performed by a) line integrational method, b) exponential line integrational method, c) (i)1D Hilbert transform approach (1iteration).

In [160] the application of the directional HT on (DIC) differential phase images is suggested, which may be properly realized in Fourier domain,

$$\phi(x,y) \sim \mathcal{F}^{-1} \left\{ i \operatorname{sign}(v) \mathcal{F} \left\{ \phi_x(x,y) - \bar{\phi}_x \right\} \right\}. \quad (6.12)$$

(Figure 6.16 c)).

In [161] we propose an iterative Hilbert Transform (IHT)- algorithm for differential phase contrast images recorded by DIC microscopy. Regarding in general the measured differential image  $I_M(x,y)$  being the DIC or DPC-OCT image, the IHT approach consists in the initial step:

$$\begin{aligned} \mathcal{H}_{\alpha,0} \{I_0\} &= hI_0 = HI_0 \quad \text{with } I_0(x,y) = \phi_x(x,y), \\ \mathcal{D}\{hI_0\} &= I_1, \\ \Delta I_1 &= I_0 - I_1 \quad \text{for } n=0, \end{aligned} \quad (6.13)$$

and the following iteration scheme:

$$\begin{aligned} \mathcal{H}_{\alpha,n} \{\Delta I_n\} &= hI_n, \\ \mathcal{D}\{hI_n\} &= hI_{n+1}, \\ \Delta I_{n+1} &= \Delta I_n - hI_{n+1}, \\ \phi_n(x,y) \sim HI_n &= HI_{n-1} + hI_n \quad \text{for } n=1,2,\dots, \end{aligned} \quad (6.14)$$

with  $\mathcal{H}_{\alpha,n}$  denoting the Hilbert operator with an additionally included low pass filtering and  $\mathcal{D}$  standing for the convolution with the differential operator

$$\begin{aligned} \mathcal{H}_{\alpha,n} \{\cdot\} &= \mathcal{F}^{-1} \left\{ \mathcal{F} \{\cdot\} - i \operatorname{sign}(v) \frac{\alpha}{\alpha + n |v|} \right\} \quad \text{with } \alpha > 0 \quad \text{and } n=1,2,\dots, \\ \mathcal{D}\{\cdot\} &= [1 \ 0 \ -1] \otimes \{\cdot\}. \end{aligned}$$

#### ■ Deconvolution approaches

Furthermore a deconvolution approach is tested, describing the measured DIC/DPC image

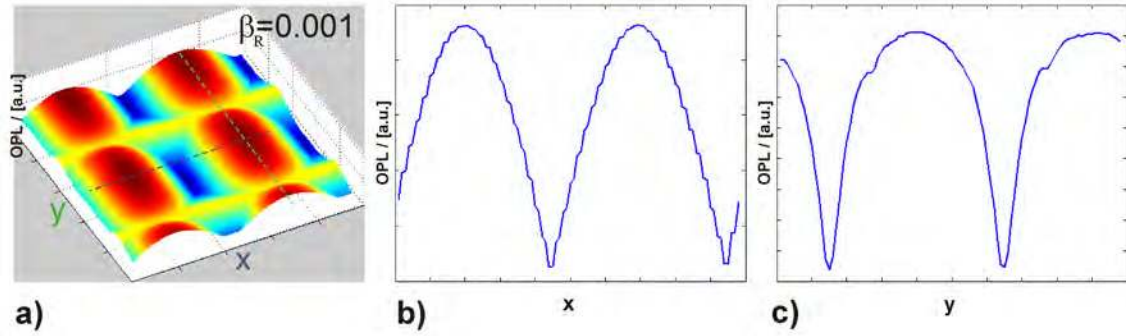


Figure 6.17: OPL reconstruction of the microlens sample applying a Wiener filter-based deconvolution,  $\beta_R = 0.001$ . a) 3D view of reconstructed OPL map of the microlens array, b) OPL profile in  $x$ -direction, c) OPL profile in  $y$ -direction.

as convolution of the (phase) image to be recovered with an intensity-PSF  $h_I$ , as otherwise used in conventional microscopy.

$$I_M(x, y) = h_I(x, y) \otimes \phi(x, y) + n(x, y), \quad (6.15)$$

with the intensity-based PSF  $h_I = h_{Ix}$  (or  $h_{Iy}$ ) for a shear either in  $x$ - or  $y$ - direction given as

$$\begin{aligned} h_{Ix}(x, y) &= \left( \delta\left(x + \frac{\Delta x}{2}, y\right) - \delta\left(x - \frac{\Delta x}{2}, y\right) \right) \otimes h_\sigma, \quad \text{and} \\ h_{Iy}(x, y) &= \left( \delta\left(x, y + \frac{\Delta y}{2}\right) - \delta\left(x, y - \frac{\Delta y}{2}\right) \right) \otimes h_\sigma, \end{aligned} \quad (6.16)$$

with  $I_M(x, y)$  denoting the measured (zero-mean) DIC/DPC image and  $n(x, y)$  being some additive noise. In comparison to (2.11) and (2.12), where the convolution of the *complex* transmission function by a *complex* PSF  $h_{DIC}$  is performed, here scalar-valued sizes are convolved. (For DIC imaging again phase objects with a weak phase gradient are supposed.)

In our DPC-OCT setup the illumination beam diameter is much smaller than the aperture of the imaging lens and therefore diffraction effects can be neglected assuming  $h_\sigma = \delta(x, y)$ . But, for DIC microscopy working in a wide-field regime we have to consider diffraction at microscope apertures by assuming a Gaussian kernel for  $h_\sigma$  (with an estimated spread of 4-5 pixels for the considered images).

By solving the inverse problem

$$\phi(x, y) = \mathcal{F}^{-1} \left\{ \mathcal{F} \{ I_M(x, y) \} / H(\mathbf{v}, \mathbf{v}) \right\} \quad (6.17)$$

to recover the phase map  $\phi(x, y)$  from the measured image  $I_M(x, y)$ , we have the obvious problem of a zero-crossing in the DIC/DPC optical transfer (OTF) function: The OTF of our differential phase measuring setup is approximatively described for this approach by

$$H(\mathbf{v}, \mathbf{v}) = -2i \sin(\pi \mathbf{v} \Delta x + \phi_0) H_\sigma(\mathbf{v}, \mathbf{v}), \quad (6.18)$$

where  $H_\sigma(\mathbf{v}, \mathbf{v})$  being the OTF of a diffraction limited microscope system. Additionally also the influence of the noise at higher frequencies as usually occurring in conventional (non-coherent) microscopic systems should be noticed.

In [163] a deconvolution approach is suggested based on Wiener filtering for phase retrieval. In this case the reconstruction is performed in Fourier domain as

$$\Phi(u, v) = \frac{H^*(u, v)}{|H(u, v)|^2 + \beta_R} \Phi_x(u, v) \quad \text{with } \beta_R \geq 0, \quad (6.19)$$

where  $\Phi(u, v)$ ,  $\Phi_x(u, v)$  and  $H(u, v)$  are the Fourier transform of  $\phi(x, y)$ ,  $\phi_x(x, y)$  and  $h_I(x, y)$ .

The Wiener filter, which can be related in Fourier domain to a Tikhonov regularization functional [164], improves the stability of the solution reducing the influence of noise and avoiding division by zero by adding a regularization parameter  $\beta_R > 0$ . We have tested this method in [161] for DIC images, and here for a single DPC-OCT scan, (Figure 6.17).

#### ■ Optimization approaches

In [165] we have suggested a positive projection  $P_+$  based Landweber iteration [166] for solving the minimization problem

$$(\mathbf{H}\phi - \mathbf{I}_M)^2 \rightarrow \min! \quad \text{with } \mathbf{H}\phi = h_I \otimes \phi \quad (6.20)$$

to recover the phase map from the measured DPC/DIC image. This approach exploits the prior knowledge about the positivity constraint of the OPL map. It varies from the in [166]

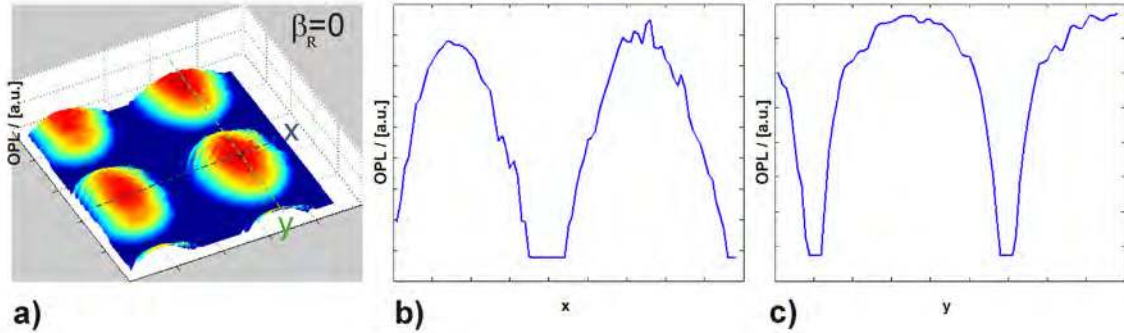


Figure 6.18: OPL reconstruction for ML array performed by P+ Landweber iteration. a) 3D view of reconstructed OPL map of the microlens array, b) OPL profile in  $x$ -direction, c) OPL profile in  $y$ -direction.

described approach that the reconstruction to be performed uses in our case the first derivative of the measured phase instead of the signal reconstruction based on the second derivative there. The following iteration is performed:

$$\begin{aligned} \hat{\phi}_{k+1} &= P_+ \left[ \hat{\phi}_k + \gamma (\mathbf{H}^T \mathbf{I}_M - \mathbf{H}^T \mathbf{H} \hat{\phi}_k) \right] \\ \phi_0 &= 0 \\ \mathbf{I}_M &= \mathbf{H} \phi \quad \text{with } \mathbf{I}_M \prec I'_{DIC}(x, y) \quad \text{or } \mathbf{I}_M \prec \phi_x(x, y), \end{aligned} \quad (6.21)$$

where  $\phi$  is the theoretical phase value to be reconstructed and  $\hat{\phi}_k$  is the estimated phase value at iteration step  $k$ . The matrix  $\mathbf{H}$  representing the differential imaging contains the



discrete differences of two Gaussian kernels, here  $\gamma$  denotes the step size.  $\mathbf{I}_M$  and  $\widehat{\phi}_k$  have to be interpreted as vectors in (6.21). The operator  $P_+$  is adapted to the DIC/DPC problem by the application of a combined median and minimum filter (med and min) and threshold step between the iterations

$$P_+ \left\{ \widehat{\phi}_k \right\} = \begin{cases} \widehat{\phi}_k & \text{if } \widehat{\phi}_k \geq c \\ c & \text{if } \widehat{\phi}_k < c \end{cases}, \quad (6.22)$$

where the threshold  $c$  is chosen as a weighted sum

$$c = c_1 \text{med}(\widehat{\phi}_k) + c_2 \text{min}(\widehat{\phi}_k) \quad \text{with} \quad c_1 + c_2 = 1 \quad (6.23)$$

to suppress the stripe-like artifacts (Figure 6.16) during integration, as shown in Figure 6.18.

Furthermore, for objects about which we have the prior knowledge of (partially) smoothness, we follow the approach of [167] and have included in (6.20) an additional penalization term to imply the smoothness in the direction perpendicular to the shear direction and solving the minimization problem

$$(\mathbf{H}\phi - \mathbf{I}_M)^2 + \beta_R (\mathbf{B}\phi)^2 \rightarrow \min! \quad \text{with} \quad \mathbf{B}\phi = h_{I_y} \otimes \phi. \quad (6.24)$$

An appropriate value for  $\beta_R$  needs additionally to be determined, adapted to the measurement/sample configuration, the SNR and/or the noise type. A trade-off between smoothing properties and noise removal has to be found, [168]. We have chosen, as also in the other regularized reconstruction methods, an empirical way adapting this parameter to our prior knowledge about the samples. In Figure 6.19, in our opinion, the best result of all the 1D reconstruction methods is shown, the stripes are suppressed and the lens shape is only slightly asymmetric.

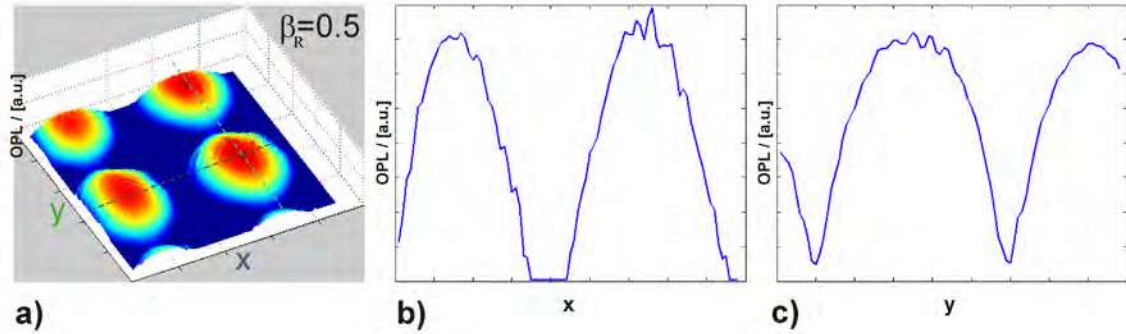


Figure 6.19: OPL reconstruction for ML array performed by constrained (P+) Landweber iteration and additional regularization perpendicular to the shear direction,  $\beta_R = 0.5$ . a) 3D view of reconstructed OPL map of the microlens array, b) OPL profile in  $x$ -direction, c) OPL profile in  $y$ -direction.

### 6.3.3.2 2D phase reconstruction approaches

Real images often do not fulfill the integrability condition of (5.56) due to the inherent noise or imaging artifacts. Furthermore, discretization effects may deteriorate the reconstruction by

line-integration methods. Therefore we have realized an 2D DPC-OCT system delivering two orthogonally sheared images as directional derivatives of the phase/OPL map. The phase recovery task, having now two orthogonally scanned DPC-OCT images available, leads to the (well-known) mathematical problem of reconstruction an image from its gradient field.

There are different methods described in the literature, mainly based on the algorithms of Horn and Brooks [169], Chellappa [170], Agrawal [171] and Weickert [172]. We have investigated components of these methods for the phase reconstruction from the measured differential phase images.

■ **Phase map reconstruction of the phase map as Laplace problem (Frankot-Chellappa method)**

Having both measured DPC scans  $\phi_x, \phi_y$  given we can reconstruct the phase/OPL map as

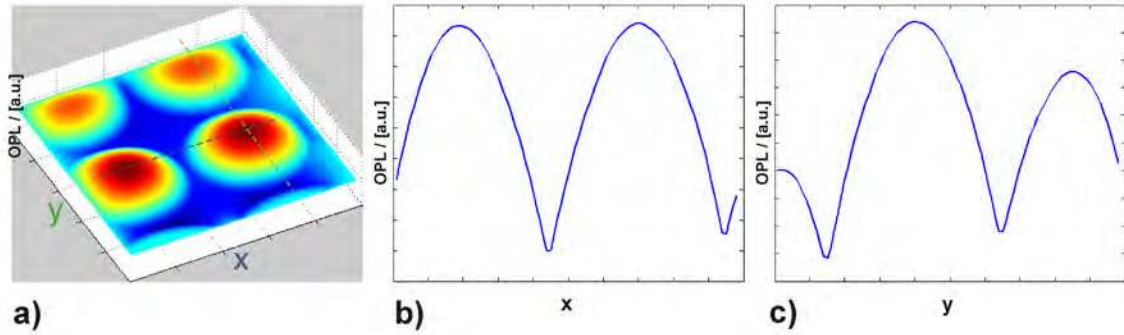


Figure 6.20: OPL reconstruction for ML array performed by Frankot-Chellappa method. a) 3D view of reconstructed OPL map of the microlens array, b) OPL profile in  $x$ -direction, c) OPL profile in  $y$ -direction.

an optimization problem in the Fourier domain as suggested originally in [170]. There the energy functional (or distance function)  $\mathcal{E}(\hat{\phi}(x,y))$  on the domain  $\Omega$

$$\mathcal{E}(\hat{\phi}(x,y)) = \int_{\Omega} |(\phi_x(x,y) - \hat{\phi}_x(x,y))|^2 + |(\phi_y(x,y) - \hat{\phi}_y(x,y))|^2 dx dy \quad (6.25)$$

has to be minimized in Fourier domain to enforce the integrability of the function  $\hat{\phi}(x,y)$  to be reconstructed. The minimization of (6.25) can be achieved for

$$\begin{aligned} \Phi(\mathbf{u}) = \Phi(\mathbf{v}, \mathbf{v}) &= \frac{-i \mathbf{v} \Phi_x(\mathbf{v}, \mathbf{v}) - i \mathbf{v} \Phi_y(\mathbf{v}, \mathbf{v})}{v^2 + v^2} \quad (6.26) \\ \text{with } \phi_x(\mathbf{x}) &= \sum_{\mathbf{u}} \Phi_x(\mathbf{u}) \exp(i \mathbf{u} \mathbf{x}), \\ \phi_y(\mathbf{x}) &= \sum_{\mathbf{u}} \Phi_y(\mathbf{u}) \exp(i \mathbf{u} \mathbf{x}), \end{aligned}$$

where  $\Phi_x(\mathbf{u})$  and  $\Phi_y(\mathbf{u})$  are the Fourier coefficients of  $\phi_x(\mathbf{x})$  and  $\phi_y(\mathbf{x})$ .

Equation (6.26) can be considered as the Fourier domain formulation of the Laplace problem

$$\begin{aligned} \nabla^2 \hat{\phi}(x,y) &= \hat{\phi}_{xx}(x,y) + \hat{\phi}_{yy}(x,y) = f(x,y) \quad \text{on } \Omega \quad (6.27) \\ \text{with } f(x,y) &= \nabla^2 \phi(x,y) = \phi_{xx}(x,y) + \phi_{yy}(x,y), \end{aligned}$$

being  $\phi_{xx}(x,y)$  and  $\phi_{yy}(x,y)$  the derivatives of the measured differential phase images.

It can be solved on the discretized images by a Fast Fourier Transform (FFT)-based approach taking into account the periodicity of the image, which is in general not fulfilled. However, boundary artifacts, inherent to FFT-based methods, can be reduced by image continuation and windowing. But this will at the same time deteriorate the results for extended sample features, as can be seen in Figure 6.20.

#### ■ Reconstruction by Shape-from-Shading (Shape-from-Gradient field) method

A further method for reconstruction of a function  $\phi(x,y)$  from its derived quantities is

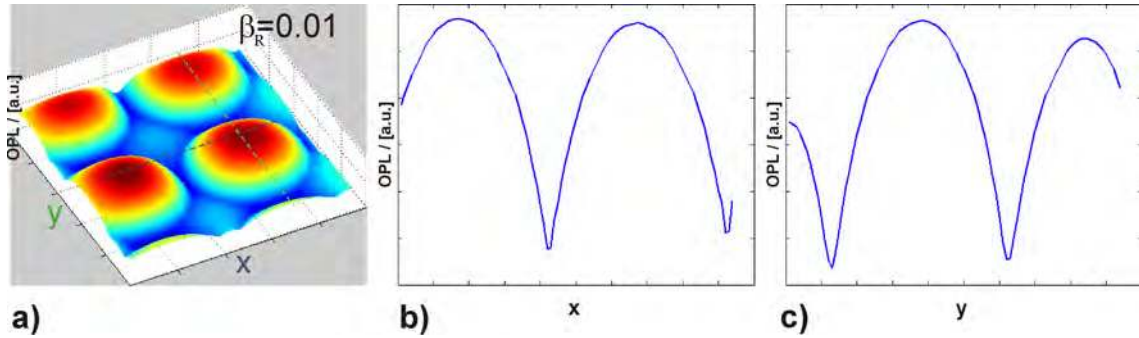


Figure 6.21: OPL reconstruction for ML array performed by SFS method,  $\beta_R = 0.01$ . a) 3D view of reconstructed OPL map of the microlens array, b) OPL profile in  $x$ -direction, c) OPL profile in  $y$ -direction.

described in [172].

In this approach the function  $\phi(x,y)$  can be mathematically reconstructed on the domain  $\Omega$  with a regularized Shape-from-Shading (SfS) (or Shape-from-Gradient (SfG)) method. The advantage of this method is given by the fact that both measured directional derivatives can symmetrically be included and further being free of boundary assumption as would be required for the previously described FFT-based reconstruction method. This allows to reconstruct the phase structure in an isotropic way, as can be shown in Figure 6.21.

The SfS method can be performed by minimizing the energy functional

$$\mathcal{E}(\hat{\phi}(x,y)) = \int_{\Omega} (f(x,y) - \mathbf{R}(\hat{\phi}_x, \hat{\phi}_y))^2 + \beta_R (\hat{\phi}_{xx}^2 + 2\hat{\phi}_{xy}^2 + \hat{\phi}_{yy}^2) dx dy \quad (6.28)$$

with scalar-valued functions  $f(x,y)$  and  $\mathbf{R}(x,y) = (\mathbf{e}_L(\hat{\phi}_x, \hat{\phi}_y, 1))$ , describing the "illumination" from the direction  $\mathbf{e}_L$ .

Using both measured orthogonal DPC images  $\phi_x(x,y)$  and  $\phi_y(x,y)$  of the individual layers (corresponding to an "illumination"  $\mathbf{e}_L = (1,0,0)$  and  $\mathbf{e}_L = (0,1,0)$  from  $x$ - and  $y$ - directions), we add this energy functional in combination of both directions to

$$\mathcal{E}(\hat{\phi}(x,y)) = \int_{\Omega} (\mathbf{f}(x,y) - \mathbf{R}(\hat{\phi}_x, \hat{\phi}_y))^2 + \beta_R (\hat{\phi}_{xx}^2 + 2\hat{\phi}_{xy}^2 + \hat{\phi}_{yy}^2) dx dy \quad (6.29)$$

with the vector-valued function of the measured data  $\mathbf{f}(x,y) = \begin{pmatrix} f_1(x,y) \\ f_2(x,y) \end{pmatrix} = \begin{pmatrix} \phi_x \\ \phi_y \end{pmatrix}$  and

the vector-valued function  $\mathbf{R}(\hat{\phi}_x, \hat{\phi}_y) = \begin{pmatrix} R_1(\hat{\phi}_x, \hat{\phi}_y) \\ R_2(\hat{\phi}_x, \hat{\phi}_y) \end{pmatrix} = \begin{pmatrix} \hat{\phi}_x \\ \hat{\phi}_y \end{pmatrix}$  denoting the derivatives of the total phase  $\hat{\phi}$  to be reconstructed.

Hence, according to the approach of [172] we have to solve the following partial differential equation

$$\begin{aligned} 0 &= \frac{\partial}{\partial x} \left( (f_1 - R_1(\hat{\phi}_x, \hat{\phi}_y)) R_{1\hat{\phi}_x}(\hat{\phi}_x, \hat{\phi}_y) \right) + \frac{\partial}{\partial y} \left( (f_1 - R_1(\hat{\phi}_x, \hat{\phi}_y)) R_{1\hat{\phi}_y}(\hat{\phi}_x, \hat{\phi}_y) \right) \\ &+ \frac{\partial}{\partial x} \left( (f_2 - R_2(\hat{\phi}_x, \hat{\phi}_y)) R_{2\hat{\phi}_x}(\hat{\phi}_x, \hat{\phi}_y) \right) + \frac{\partial}{\partial y} \left( (f_2 - R_2(\hat{\phi}_x, \hat{\phi}_y)) R_{2\hat{\phi}_y}(\hat{\phi}_x, \hat{\phi}_y) \right) \\ &+ \beta_R (\hat{\phi}_{xxxx} + 2\hat{\phi}_{xxyy} + \hat{\phi}_{yyyy}), \end{aligned} \quad (6.30)$$

where  $\hat{\phi}_{x\dots y\dots}$  denote the higher order derivatives.

With

$$\begin{aligned} R_{1\hat{\phi}_x}(\hat{\phi}_x, \hat{\phi}_y) &= \frac{\partial R_1}{\partial \hat{\phi}_x} = 1, \\ R_{2\hat{\phi}_x}(\hat{\phi}_x, \hat{\phi}_y) &= \frac{\partial R_2}{\partial \hat{\phi}_x} = 0, \\ R_{1\hat{\phi}_y}(\hat{\phi}_x, \hat{\phi}_y) &= \frac{\partial R_1}{\partial \hat{\phi}_y} = 0, \\ R_{2\hat{\phi}_y}(\hat{\phi}_x, \hat{\phi}_y) &= \frac{\partial R_2}{\partial \hat{\phi}_y} = 1, \end{aligned}$$

the equation system (6.30) can be simplified to

$$\begin{aligned} 0 &= \frac{\partial}{\partial x} (f_1 - \hat{\phi}_x) + \frac{\partial}{\partial y} (f_2 - \hat{\phi}_y) \\ &+ \beta_R (\hat{\phi}_{xxxx} + 2\hat{\phi}_{xxyy} + \hat{\phi}_{yyyy}) \\ &= (\phi_{xx}(x, y) - \hat{\phi}_{xx}(x, y)) + (\phi_{yy}(x, y) - \hat{\phi}_{yy}(x, y)) \\ &+ \beta_R (\hat{\phi}_{xxxx} + 2\hat{\phi}_{xxyy} + \hat{\phi}_{yyyy}). \end{aligned} \quad (6.31)$$

It is solved by a Jacobi-like iteration scheme. As stopping criterium we apply the defect norm.

$$\begin{aligned} \hat{\phi}^{k+1} &= \hat{\phi}^k - \gamma \mathbf{D} ((\phi_{xx}(x, y) - \hat{\phi}_{xx}^k(x, y)) + (\phi_{yy}(x, y) - \hat{\phi}_{yy}^k(x, y))) \\ &+ \beta_R (\hat{\phi}_{xxxx}^k + 2\hat{\phi}_{xxyy}^k + \hat{\phi}_{yyyy}^k) \\ \hat{\phi}^0 &= 0 \\ \mathbf{D} &= (\text{diag} \mathbf{H})^{-1}, \end{aligned} \quad (6.32)$$

where  $\mathbf{H}$  is the resulting system matrix.

In case that the regularization parameter  $\beta_R \rightarrow 0$ , equation (6.29) results in (6.25).

## 6.4 DPC-OCT: Results and discussion

Originally line-integration methods were investigated by us with respect to their potential for qualitative analysis and for enhancement of segmentation of huge cell populations imaged by DIC techniques, as demonstrated in [161]. In the thesis we have regarded these approaches anew in the context of phase reconstruction for one-directionally scanned DPC-OCT images in comparison to the orthogonal-scanning DPC-OCT and 2D reconstruction approaches.

The phase reconstruction based on the described 1D and 2D approaches of Section (6.3) are evaluated on the DPC scans recorded by the realized DPC-OCT setup. The improvements, achieved due to the included 2D approaches for measurement and reconstruction in combination with image processing, against 1D methods are discussed in the following.

### 6.4.1 Results: 1D reconstruction

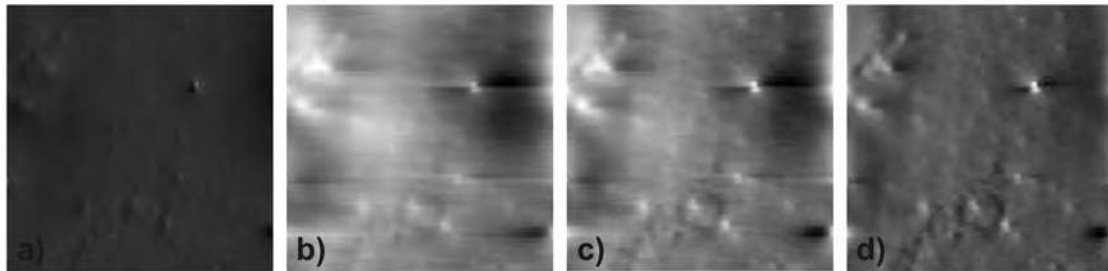


Figure 6.22: DPC image phase recovery: Comparison of 1D line-integration methods with different decay factor  $\gamma_A$ . a) DPC image with a shear in  $x$ -direction, b) phase reconstruction by forward/backward line-integration ( $\gamma_A = 0$ ), c) phase reconstruction by exponential line-integration ( $\gamma_A = 0.5$ ), d) phase reconstruction by exponential line-integration ( $\gamma_A = 0.8$ ).

As can be seen in Figure 6.22 all line-integration approaches, explained in Subsubsection (6.3.3.1), are showing more or less artifacts, especially streaking effects along the integration path due to

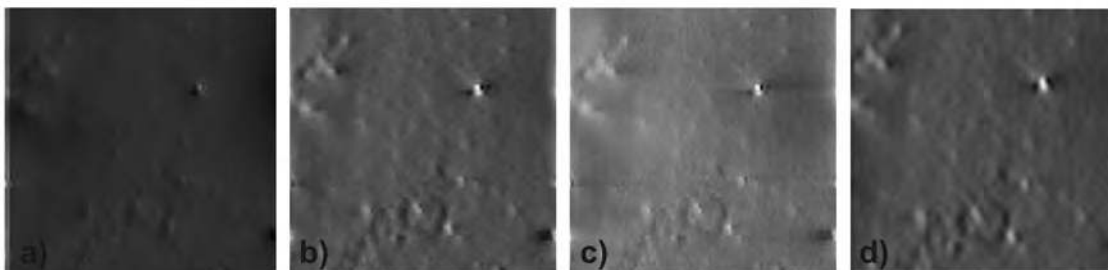


Figure 6.23: DPC image phase recovery: Comparison of different 1D reconstruction methods. a) DPC image with a shear in  $x$ -direction, b) phase reconstruction by exponential line-integration ( $\gamma_A = 0.9$ ), c) phase reconstruction by Hilbert transform method, d) phase reconstruction by Landweber iteration method.

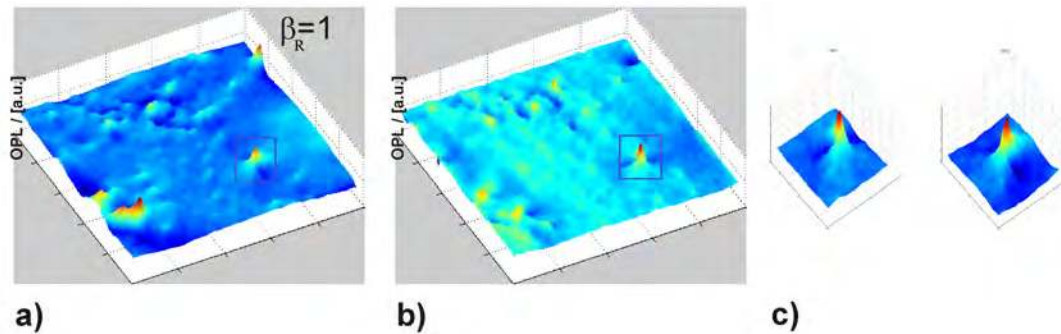


Figure 6.24: OPL reconstruction for the oil layer/embedded particle sample (S2) applying a Wiener filter-based deconvolution,  $\beta_R = 1$ . a) Reconstruction performed on the basis of directional phase derivative  $\phi_x(x,y)$ , b) reconstruction performed on the basis of directional phase derivative  $\phi_y(x,y)$ , c) enlarged view of indicated region showing the asymmetry of the microparticle peak (expected to be almost conical shaped).

the accumulation of noise and due to imaging irregularities, which may be caused by specular reflexes, oversaturation of the detector or partial absorption in real samples. These occurring stripes can be reduced by using the exponential line-integration approach or the (half-plane) HT method as demonstrated in Figure 6.22 c) and d) in comparison to straight-forward line-integration, shown in Figure 6.22 b). But, especially exponential line-integration and the Hilbert transform methods are only qualitative approaches usually applied only for better visualization [160] and as preprocessing for intensity-based segmentation methods [162]. By performing the deconvolution and optimization approach, including additionally regularization terms in the iteration, the streaking artifacts can be reduced, as depicted in Figure 6.23. However, a higher regularization parameter may also cause a too extended smoothing and a height reduction of the phase map.

A further drawback of 1D methods consists in the asymmetry of the reconstructed phase objects, e.g. for microparticle sample being originally almost symmetric. Here in the 1D reconstruction, the peaks are shrunk in the shear direction and elongated in perpendicular direction, as can be seen in Figure 6.24 c). This disadvantage is inherent for all 1D reconstruction approaches, since the information about the derivative in the direction orthogonal to the beam shearing is lost. To a certain amount this effect can be reduced, taking additional constraints (and regularization terms) in the approach, as it can be seen in Figure 6.25 for the reconstruction based on the Landweber iteration method. (Compare also Figures 6.18 and 6.19.) But on the other hand, due to the positivity constraint and choosing an arbitrary threshold therefore, the full quantitative information is lost due to these constraints.

In our opinion and based on the experience on measured data, 1D reconstruction only delivers insufficient results: Especially they do not provide quantitative information, but they can be exploited for qualitative results and visualization tasks.

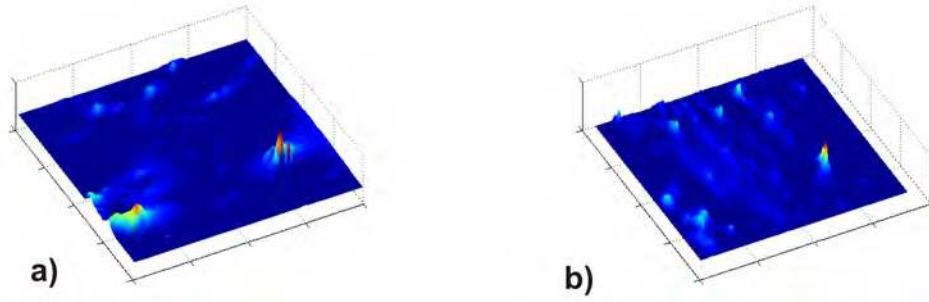


Figure 6.25: OPL reconstruction for the oil layer/embedded particle sample (S2) applying the constrained and regularized (P+) Landweber iteration method. a) Reconstruction performed on basis of directional phase derivative  $\phi_x(x,y)$ , b) reconstruction performed on basis of directional phase derivative  $\phi_y(x,y)$ .

### 6.4.2 Results: 2D reconstruction

The 2D reconstruction of the DPC-OCT images is performed on the set of test sample (S1)–(S3). In particular, we have regarded the Shape-from-Shading (SfS)-based reconstruction approach and its performance for phase reconstruction from two orthogonal DPC-OCT scans.

The validation of the performed imaging and reconstruction method with respect to its *quantitative character* is exemplified on a well-defined test sample. (Here represented by the microlens array test sample S1 with known dimensions, compare also Figure 6.5.) The procedure of complete 2D OPL reconstruction from the recorded en-face DPC-OCT scans is depicted in Figure 6.26. The reconstruction starts from the unwrapped data here, as already shown in Figure 6.15. We perform the SfS-based reconstruction individually for each interface. The representative layer for each interface is chosen according to the depth position of the maximum reflectivity signal at each interface. Finally a scaling of the numerical results with respect to the realized beam shear, the lateral resolution of the DPC-OCT scanning unit and the wavelength has to be performed. Afterwards the results can be interpreted in a quantitative way.

In case of the microlens array, the mathematical reconstruction of the OPL map at interface (2) yields – for a sample refractive index  $n = 1.449$  at  $\lambda = 1550$  nm – a total geometrical height of the individual lenslets of  $1.64 \mu\text{m}$ , closely matching the technically specified value of  $1.63 \mu\text{m}$ .

Under the assumption that the system is properly aligned and refraction at the interfaces can be neglected (i.e. approximately perpendicular incident waves are supposed) the ratio  $r_n$  of the optical path lengths  $\vartheta_i$  at different layers ( $i$ ) provides a measure for the refractive index of the material  $n_M$ . Especially for the microlens array we can derive for the ratio at interfaces (2) and (3)

$$r_n = \frac{\vartheta_2}{\vartheta_3} = \frac{n_M}{n_M - n_0} \quad \text{with } n_0 = 1 \quad \text{in air,} \quad (6.33)$$

according to the sketch in Figure 6.27 a) and b). This yields an estimation for the refractive index as

$$n_M = \frac{r_n}{r_n - 1}. \quad (6.34)$$

In Figure 6.28 both OPL profiles and the ratio between them are depicted, having an almost constant value  $r_n \sim 3$  (corresponding to  $n_M \sim 1.5$ ) in the central range of the microlens. In the outermost regions the ratio is slightly increasing. This weak increase can be explained by the influence of diffraction and reconstruction artifacts due to the non-smooth contour at the border line between microlens and bulk material.

To demonstrate the performance of the realized 2d-scanning setup and 2D reconstruction procedure, in comparison to 1d-scanning and 1D reconstruction methods, we have chosen a sample being imaged with a low SNR. (Here represented by the oil layer/microparticle test sample S2, compare also Figure 6.6.) The recorded, relatively noisy scans in Figure 6.29 a) and b) are visualizing the top reflection of the thin corrosion inhibiting oil layer with small embedded abrasion particles. Using both DPC scans (Figure 6.29 a) and b)), first we reconstructed the OPL map with a global Fast Fourier Transform (FFT)-based approach by solving the Laplace problem in the Fourier domain [170]. A slight blurring and haze is present in the reconstructed images, as shown in Figure 6.29 d), partly caused by the low pass characteristics of the inverse Laplace filtering. Furthermore, boundary artifacts, inherent to FFT-based methods, are recognizable. They can be reduced by image continuation and windowing.

The reconstruction by the SfS-method yields the best result, as shown in Figure 6.29 e) and f) with no streaking artifacts and less blurred features and areas, in comparison to Figure 6.29 c) and Figure 6.22. Furthermore, also the improved symmetry of the recovered objects against 1D approaches should be mentioned, as depicted in Figure 6.30 a) and b).

Finally, a specimen with steep phase derivatives has been investigated by us to show the potential of the procedure for imaging and reconstruction for samples with a *higher phase gradient*. (Here represented by the polymer film test sample S3, compare also Figure 6.7.) The difference to DIC imaging should be emphasized here again, where a weak phase gradient for the specimen has to be assumed for a quantitative phase imaging and reconstruction. Here, in DPC-OCT imaging, the measured phase differences, in case of exceeding the unambiguity range, are mapped into the interval  $[-\pi, \pi)$ , leading to wrapped regions in the DPC-OCT scans, as depicted in Figure 6.31 a) and b). Therefore, an additional phase unwrapping has been included in the reconstruction procedure. We assume again, a smooth continuous phase map for the investigated test sample, although being a simplification of real data. Likewise, a quality guided 2D unwrapping approach or a global FFT-based unwrapping approach [151] has been realized for this application to obtain the two orthogonal unwrapped DPC-OCT en-face scans as shown in Figure 6.31 c) and d). The further OPL reconstruction, as previously described for the other samples, is performed on both unwrapped phase derivative images. Finally, the 2D phase map at the chosen depth is computed and as 3D view depicted in Figure 6.31 e).

### 6.4.3 Discussion: DPC-OCT imaging and reconstruction

At the beginning, we have developed an optical DPC-OCT setup and demonstrated the feasibility of phase-sensitive imaging by this 2d-scanning modality for different specimens. Here, the potential for quantitative phase recovery by the performed mathematical reconstruction algorithms on the measured data could be shown. For different phase objects the performance of the whole procedure was tested by reconstructing the lateral phase map, extracted at different interfaces from the recorded DPC-OCT data. Quantitative results, which are spatially resolved in lateral and depth direction, can be obtained by the realized setup: for samples of larger elongated embedded phase



structures, for layered transparent materials (partially containing separated microstructures as particles or air bubbles) and for samples with steep phase gradients.

We have demonstrated, that the 2d-scanning DPC-OCT imaging technique, combined with 2D reconstruction approaches (especially SfS approaches) and -in case of high phase gradients- with phase unwrapping techniques, is a robust method coping with steep and extended phase structures, as well as handling low SNR images. Nevertheless, restrictions are given in case of observing rough surfaces or imaging through scattering interfaces.

Advantages and recognizable limitations of the performed DPC-OCT imaging and reconstruction system are summarized in the following:

#### **Advantages**

- *Quantitative measure:*

The whole phase information is contained in both directional phase derivative images. Hence, it is in principle possible to determine a quantitative OPL map from two orthogonal shear directions at different depth positions.

- *Linearity:*

The phase gradient is related in a linear dependence to the measured intensity gradient. Therefore, in DPC-OCT we are not restricted to a small phase gradient approximation for performing a quantitative reconstruction, as required for DIC imaging. Unwrapping approaches can be included in the analysis; however, they require a prior knowledge about interface smoothness.

- *Robustness:*

Reconstruction artifacts due to noise and phase discontinuities can be diminished in comparison to 1D approaches. Especially this robustness combined with a correct adjustment of the optical system finally allows that the quantitative phase map or optical path length can be properly reconstructed from two orthogonal shear directions.

#### **Limitations**

- *Scattering effects:*

Limitations of the realized DPC-OCT setup are given for highly scattering samples (e.g. microspheres) disturbing the fixed phase relationship between the adjacent probing waves by scattering.

- *Refraction effects:*

Investigating interfaces with very steep slopes can additionally result in refraction artifacts, which have to be compensated (e.g. by index matching) or have to be otherwise regarded as a restriction of the general measurement performance.

- *Phase stability:*

It has to be guaranteed that the intensity of the reflected signals is sufficiently high to obtain reliable phase information.

- *Birefringence:*

Since the measuring system is exploiting mutual phase information between the adjacent beams, resulting in an altered/rotated polarization of the back-reflected sample wave, birefringent specimen, introducing an additional rotation, can not be investigated by this optical setup.

- *Parametrization:*

For the mathematical reconstruction different parameters have to be adapted according to the SNR, (e.g. regularization parameter, discretization sizes). This requires an adaptation for different measurement situations.

Summarizing, we have demonstrated in this chapter a complete procedure for phase recovery in DPC-OCT imaging. We focused on both, the phase-based imaging and the reconstruction in a two-dimensional way. We could demonstrate by our developed DPC-OCT setup, containing a rotatable probing head, that phase-sensitive measurements and reconstruction of spatially resolved lateral phase maps can be performed at different depth positions. The performance could be improved by the chosen 2D shape-from-shading (or shape-from-gradient) method outperforming 1D integrational methods, as previously applied in the field of DPC-OCT imaging.

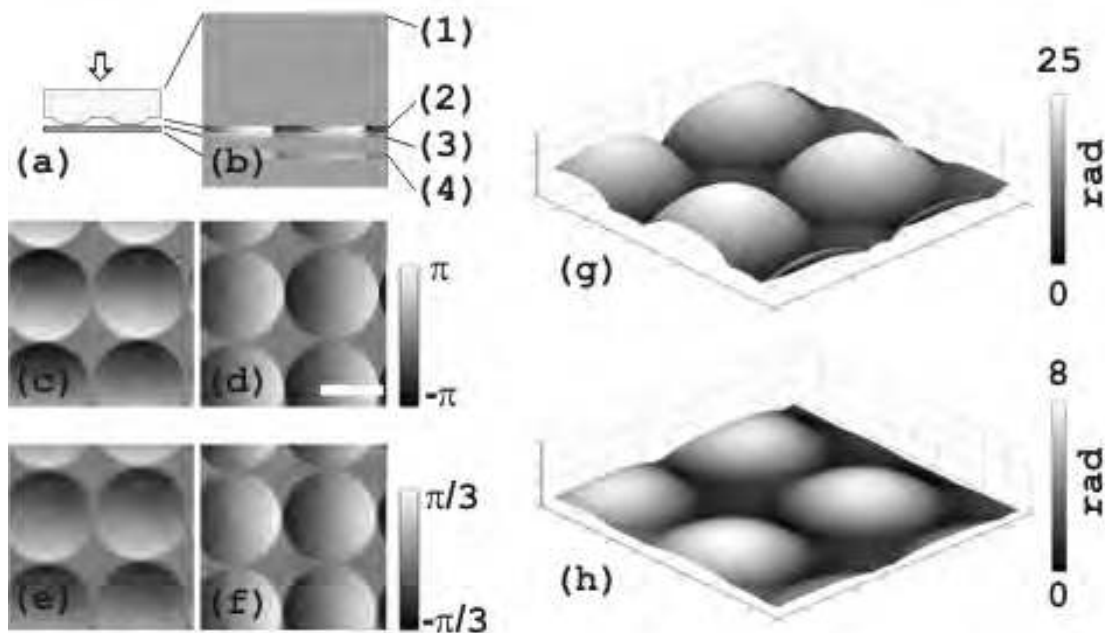


Figure 6.26: 2D phase map reconstruction for two different depth positions. The microlens array test structure, with a total of four imaged interfaces ((1)–(4)), is placed upside down on the microscope slide. a) Sketch of the sample, b) cross-sectional DPC-OCT image, c), d) en-face DPC-OCT images in  $x$ - and  $y$ -direction at interface (2), e), f) en-face DPC-OCT images at interface (4), g) reconstructed cumulative phase map at interface (2), h) cumulative phase map at interface (4). White scale bar:  $100 \mu\text{m}$

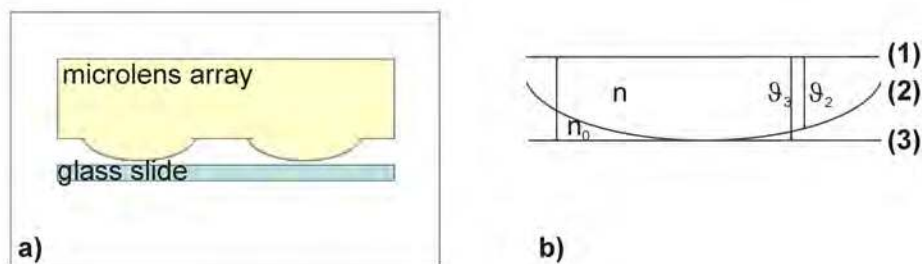


Figure 6.27: Scheme of microlens array reference test sample (S1) with indicated interfaces. a) Sketch of embedded microlens array, b) interface (1): air/quartz glass of the bulk material, interface (2): microlens front site quartz glass/air, interface (3): air/glass of plane microscope slide. The optical path lengths  $\vartheta_2$  and  $\vartheta_3$  are indicated and  $n_M$  is the refractive index of quartz glass substrate.

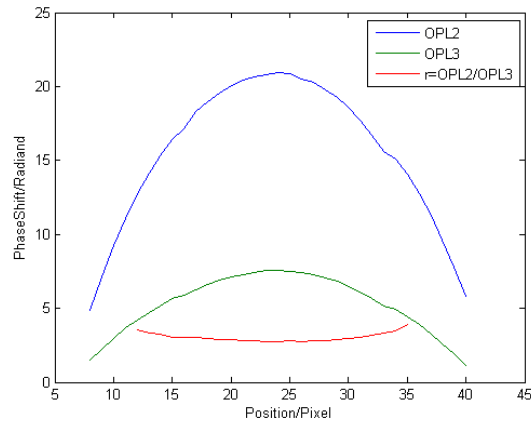


Figure 6.28: OPL profile of microlens reconstructed at interface (2) and (3) and the ratio of both (red line).

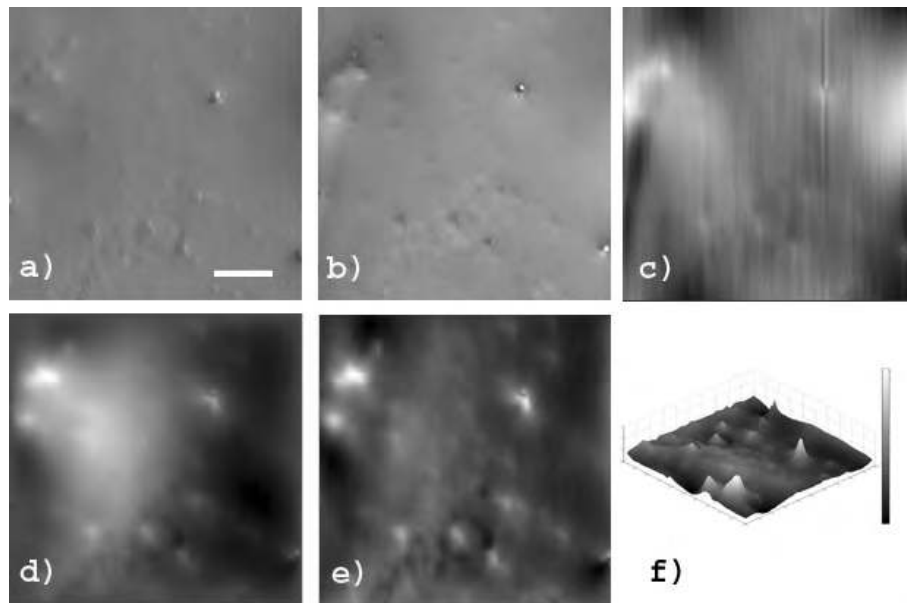


Figure 6.29: DPC-OCT image of an oil layer with embedded particles (S2). a), b) DPC images with shear in  $x$ - or  $y$ -direction, c) OPL reconstruction by numerical line-integration using the single scan displayed in (b), d) FFT-based OPL reconstruction from scans (a) and (b), e), f) OPL reconstruction with SFS method using scans (a) and (b). White scale bar:  $100 \mu\text{m}$

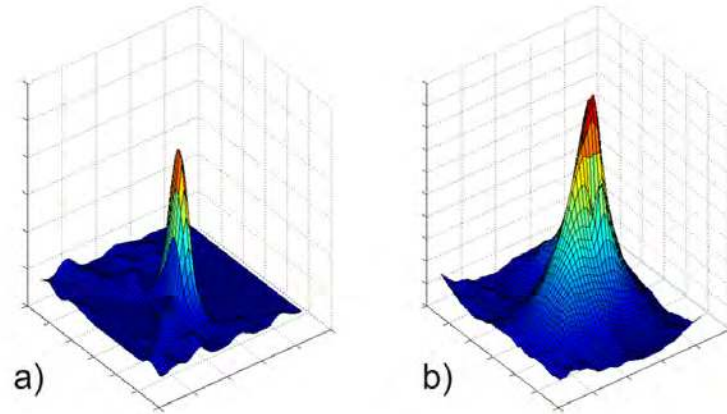


Figure 6.30: Detail of OPL reconstruction (resulting signal peak, expected to be conical, caused by a microparticle). a) OPL reconstruction performed by 1D Landweber iteration method, b) OPL reconstruction performed by 2D SfS-method.

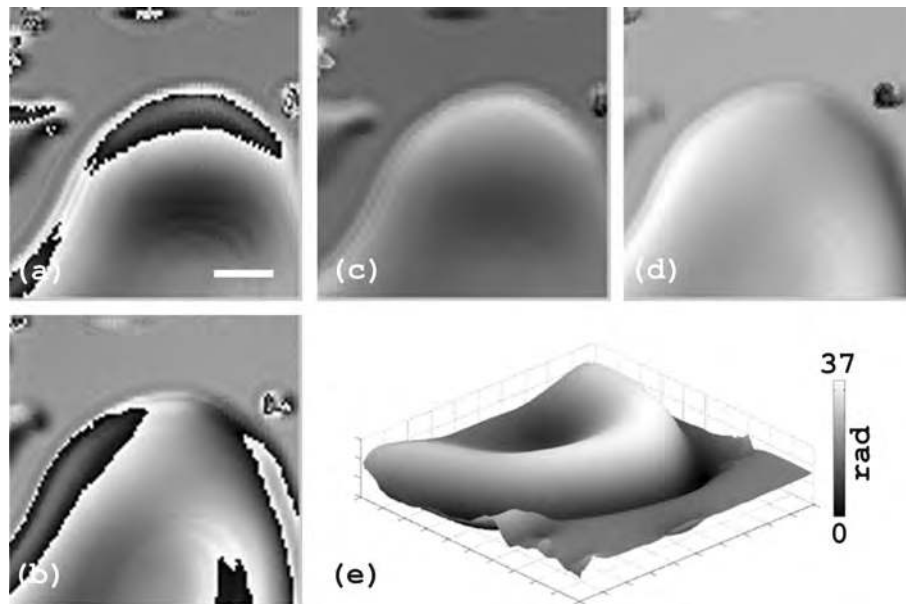


Figure 6.31: DPC-OCT image of a soft and uneven acrylic polymer film (S3) having a wrapped phase gradient map. a), b) Wrapped DPC images (shear in  $x$ - and  $y$ -direction), c), d) unwrapped phase of (a) and (b), e) total phase map reconstructed from (c) and (d). White scale bar:  $40 \mu\text{m}$



## Chapter 7

# Conclusions & Outlook

### 7.1 Conclusions

In this thesis we have considered different phase-sensitive imaging methods suitable for investigation and visualization of structures in the micrometer range. Questions and interesting aspects about qualitative and quantitative phase measurements and reconstruction approaches in the field of phase contrast microscopy and optical coherence tomography, about suitable approximations, similarities between phase-imaging techniques and about analogies between Fourier plane phase filtering techniques (especially spiral phase filter) in imaging and image processing have been discussed. We have incorporated components for differential phase imaging from PCM into the DPC-OCT imaging system, allowing the use of these elements in a two-dimensional way. Furthermore, interferometric fringe pattern analysis techniques have been successfully included for the two-dimensional analysis of PS-OCT applications.

In particular, the potential of OCT for obtaining detailed quantitative information with respect to phase-related quantities, arising from the combination of phase-sensitive OCT techniques with mathematical and signal processing approaches, has been demonstrated. We have developed and exemplified new approaches consisting of different steps for quantitative depth-resolved analysis both for PS-OCT and DPC-OCT. We have shown that improvements can be achieved by transposing the 1D phase-sensitive OCT technique to a 2D technique: On the one hand by modifying the imaging part (as realized in the developed 2d-scanning TD-DPC-OCT setup), and on the other hand by the mathematical reconstruction (as performed for PS-OCT retardation image analysis). The whole imaging and reconstruction tasks are discussed as a 2D problem taking into account the whole image content at once. This 2D consideration represents an improvement on the well-established 1D analysis approaches in the field of phase-sensitive OCT imaging. The developed setup and methods have been validated for different materials and test situations in real-world applications.

In our thesis we have presented how advanced methods of 2D signal analysis and image processing, originally developed in the field of interferometry, can be adapted and exploited for phase-based OCT imaging to extract inherent qualitative and quantitative information about internal anisotropic material states (in PS-OCT) or embedded phase structures (in DPC-OCT), to obtain interpretable and quantifiable results about specimens under investigation. The whole local information about spatially resolved stress states or birefringence distribution inside the material

can be used for a quantitative analysis, in extension and partially in contrast to previously applied 1D analysis techniques exploiting these features only in an one-dimensional or averaged way. Therefore, complicated and closed fringe patterns can now also be evaluated.

Finally, we could demonstrate that different limitations of previously applied 1D approaches (clipping and noise preventing automatized analysis) can be reduced or be removed by utilizing 2D techniques for image enhancement and demodulation.

In conclusion, the following results and improvements can be summarized for both realized and analyzed phase-sensitive OCT configurations:

### 7.1.1 PS-OCT imaging system

- The potential of the PS-OCT imaging system in combination with image processing for a 2D quantitative and depth-resolved stress/strain analysis could be demonstrated for the investigation of birefringent turbid materials. To the best of our knowledge, for the first time the 2D reconstruction approach in the field of PS-OCT retardation imaging has been performed.
- The exploitable depth and application range for analyzing PS-OCT retardation images could be extended by the suggested 2D reconstruction procedure. Hence, the information content of the PS-OCT images could be increased. We have verified our method on different technical samples and could demonstrate the feasibility of the proposed approach, including 2D demodulation schemes and image processing techniques, for the retardation and birefringence analysis in PS-OCT.

### 7.1.2 DPC-OCT imaging system

- A quantitative reconstruction of lateral OPL or phase maps at different depth positions from depth-resolved DPC-OCT signals is feasible and has been demonstrated by us.
- The recorded images contain the whole phase information, in contrast to DIC imaging. Furthermore, for suitable layered sample structures they may include additional approximative information about the refractive indices of the embedded structures.
- A reduction of reconstruction artifacts (in comparison with 1D approaches suffering from stripes, noise artifacts, etc.) could be achieved by the 2D approach which enables the reconstruction of meaningful lateral phase maps in 3D OCT imaging.
- Although the suggested method shows potential to be enhanced in its single components (e.g. with respect to the optical setup, with respect to mathematical performance), the working principle of the whole procedure – from measurement till phase map reconstruction – could be demonstrated. To the best of our knowledge, for the first time a 2D approach for orthogonal scanning DPC-OCT and phase reconstruction has been performed.
- The current DPC-OCT setup has been realized with conventional optical elements, e.g. a rotatable Wollaston prism for beam shearing. The incorporation of electro-optical beam shearing would further increase the performance of the DPC-OCT system. A more precise



positioning system and an increase of the A-scan rate of the measurement would enable an improved imaging modality.

## 7.2 Outlook

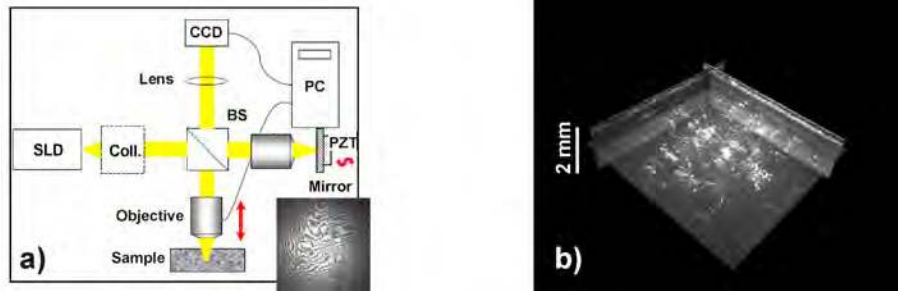


Figure 7.1: Illustration of FF-OCT imaging. a) Scheme of the optical setup for full-field OCT (FF-OCT) imaging. In contrast to conventional OCT the sample is moved over depth and the mirror is sinusoidally modulated by the piezo transducer (PZT), b) 3D visualization of a glass fiber-composite (GFC) structure embedded in epoxy resin imaged by FF-CPM techniques.

Upcoming full-field OCT (FF-OCT) techniques, depicted schematically in Figure 7.1 a), allow a further extension of the realized DPC-OCT and PS-OCT configurations [177]. Compared to the previously applied raster scanning OCT techniques FF-OCT will remarkably improve the speed of the measurement procedure also in time domain. As the sensitivity of the FF-imaging system will be limited, these techniques require either powerful broadband light sources or methods for additional contrast enhancement, which can be provided by mathematical image processing or programmable optics. Recent developments in Fourier plane filtering (FPF) techniques, nowadays often realized dynamically by addressable spatial light modulators [175, 176] enable a flexible or multiplexed realization of different phase filters by computational optics. Remembering the ideas, initially described in Chapter (2), where FPF is applied for influencing the image contrast in PCM, now we aim to combine FPF with OCT methods to modify the contrast similar to the application in PCM. We expect that the combination of electro-optical FPF, sophisticated modulation methods and FF-OCT techniques will provide further potential for the exploitation of phase information and contrast enhancement in coherent microscopic imaging.

Current experiments, utilizing FF-OCT techniques for imaging of technical materials, show the potential for extending these methods again in the field of 3D material investigation. Recently, we have demonstrated first results in coherent full-field imaging of technical micro-structures [178]. In Figure 7.1 b) a technical glass fiber-reinforced material imaged by our current FF-OCT setup is depicted. Thereby also the bridge to the field of coherent probe microscopy is opened by including microscopic components (microscope objectives) in the full-field OCT configuration. Full-field techniques are considered by us to become useful 3D imaging tools for advanced structural and functional material characterization, e.g. in the field of polymer or fiber-composites material research.

From the point of view in signal processing, FF-OCT will demand advanced fringe pattern analysis procedures in 3D to obtain both intensity and phase information encoded in the amplitude-

and phase-modulated 3D image stack. Conventional phase-stepping approaches in FF-OCT imaging, as realized in [179], may be replaced by single frame approaches.

Furthermore, with the new possibilities of computational optics, as realized by compressive sensing techniques in case of sparse data imaging [180] or by coded and sparse aperture techniques [182] for illumination, new perspectives for sampling and reconstruction open up. Phase shaping arrays [183] and the combination of OCT techniques with nonlinear optical microscopy could add new possibilities for a selective, enhanced visualization of microstructures in materials.

## Chapter 8

# Acknowledgments

The thesis, starting originally as hobby, and growing over weekends and some silent project periods, would not have been written without the help and support of various people at different places.

- Prof. Erich Peter Klement and PD Dr. David Stifter for their help, efforts, motivation and advice as supervisors,
- Prof. Monika Ritsch-Marte and her team (especially Dr. Christian Maurer) for discussions about SLMs, for providing spiral phase images and for opportunity of common experiments,
- Prof. Andreas Springer and Prof. Bernhard Zagar for their discussions in the field of signal processing,
- Prof. Dieter Petrak, head of my former department at the Academy of Science, for his advice in optics and long support,
- Prof. Gabriele Steidl and PD Dr. Ralf Wunderlich for their discussions about my questions in statistical modeling,
- PD Dr. Swanhild Bernstein for her support concerning my questions in the field of functional analysis,
- Dr. Bodo Heise, my husband, for his continuous advice and support in the field of mathematical theory and numerical implementation,
- Prof. Martin Burger for providing a helpful program for regularized differentiation,
- Prof. Joachim Weickert and DI Andreas Jablonski for their initial support in image denoising techniques,
- All my colleagues from FLLL, ZONA (especially Prof. Kurt Hingerl) and at Recendt GmbH (especially PD Dr. Peter Burgholzer) for the provided experimental possibilities,
- My former colleagues DI Elisabeth Leiss-Holzinger and Dr. Karin Wiesauer for delivering PS-OCT images and their support during my own OCT-measurement period,

- Dr. James Ong as native speaker and his wife Ellen for correcting my English style and structure,
- Prof. Günther Hecht, my first physics professor teaching not only physics but also civil courage in "old times", for organizing necessary subscription documents about 20 years later in changed "new times",
- My family and parents for their patience, help and encouraging over a long time period.

# Bibliography

- [1] B. Jähne, "*Digital Image Processing*", (Springer, Heidelberg, Berlin, 2002), 340-360.
- [2] P. C. Cheng, "*The contrast formation in optical microscopy*", in *Handbook of Biological Confocal Microscopy*, J. B. Pawley, ed., (Academic Press, New York, 2006), 162-204.
- [3] F. Zernike, "*Phase contrast, a new methods for observation of transparent objects*", *Physica* **9**, 686-698 (1942).
- [4] R. Hoffman, "*The modulation contrast microscope: principles and performance*", *J. Microsc.* **110**, 205-222 (1977).
- [5] P. J. Rodrigo, D. Palima, J. Glückstad, "*Accurate quantitative phase imaging using generalized phase contrast*", *Opt. Express* **16**, 2740-2751 (2008).
- [6] M. Pluta, "*Nomarski's DIC microscopy: a review*", *Proc. SPIE* **1846**, 10-25 (1994).
- [7] T. A. Pitts, J. F. Greenleaf, J. Lu, R. R. Kinnick, "*Tomographic Schlieren Imaging for Measurement of Beam Pressure and Intensity*", *Proc. IEEE Ultrasonics Symposium*, 1665-1668 (1994).
- [8] T. Neumann, H. Ermert, "*Schlieren visualization of ultrasonic wave fields with high spatial resolution*", *Ultrasonics* **44**, e1561-e1566 (2006).
- [9] D. Malacara, "*Optical Shop Testing*", 2nd ed., (Wiley, New York, 1992), 302-305.
- [10] U. Schnars, W. Jueptner, "*Digital Holography*", (Springer, Berlin, 2005).
- [11] E. Cucho, F. Bevilacqua, C. Depeursinge, "*Digital holography for quantitative phase-contrast imaging*", *Opt. Lett.* **24**, 291-3 (1999).
- [12] R. A. Patten, "*Michelson Interferometer as a remote gauge*", *Appl. Opt.* **10**, 2717-2721 (1971).
- [13] D. Huang, E. A. Swanson, C. P. Lin, J. S. Schuman, W. G. Stinson, W. Chang, M. R. Hee, T. Flotte, K. Gregory, C. A. Puliafito, J. G. Fujimoto, "*Optical Coherence Tomography*", *Science* **254**, 1178-1181 (1991).
- [14] J. G. Fujimoto, M. E. Brezinski, G. J. Tearney, S. A. Boppart, B. Bouma, M. R. Hee, J. F. Southern, E. A. Swanson, "*Optical biopsy and imaging using optical coherence tomography*", *Nature Med.* **1**, 970-972 (1995).
- [15] D. Stifter, "*Beyond biomedicine: a review of alternative applications and developments for optical coherence tomography*", *Appl. Phys. B* **88**, 337-357 (2007).
- [16] B. F. Kennedy, T. R. Hillman, R. A. McLaughlin, B. C. Quirk, D. D. Sampson, "*In vivo dynamic optical coherence elastography using a ring actuator*", *Opt. Express* **17**, 21762-21772 (2009).
- [17] M. R. Hee, D. Huang, E. A. Swanson, J. G. Fujimoto, "*Polarization-sensitive low-coherence reflectometer for birefringence characterization and ranging*", *J. Opt. Soc. Am. B* **9**, 903-908 (1992).
- [18] C. K. Hitzenberger, A. F. Fercher, "*Differential phase contrast in optical coherence tomography*", *Opt. Lett.* **24**, 622-624 (1999).
- [19] J. W. Hettinger, M. Mattozzi, W. R. Myers, M. E. Williams, A. Reeves, R. L. Parsons, R. C. Haskell, D. C. Petersen, R. Wang, J. I. Medford, "*Optical Coherence Microscopy. A Technology for Rapid, in Vivo, Non-Destructive Visualization of Plants and Plant Cells*", *Plant Physiology* **123**, 3Ü15 (2000).
- [20] C. Vinegoni, J. S. Bredfeldt, D. L. Marks, S. A. Boppart, "*Nonlinear optical contrast enhancement for optical coherence tomography*", *Opt. Express* **12**, 331-341 (2004).

- [21] A. L. Oldenburg, B. E. Applegate, J. A. Izatt, S. A. Boppart, "Molecular OCT Contrast Enhancement and Imaging", in: *Optical Coherence Tomography*, (Springer Berlin Heidelberg, 2008), 713-756.
- [22] M. Servin, J. A. Quiroga, J. L. Marroquin, "General  $n$ -dimensional quadrature transform and its application to interferogram demodulation", *J. Opt. Soc. Am. A* **20**, 925-934 (2003).
- [23] A. Barty, K. A. Nugent, D. Paganin, A. Roberts, "Quantitative optical phase microscopy", *Opt. Lett.* **23**, 817-819 (1998).
- [24] F. Zernike, "How I discovered phase contrast", *Science* **121**, 345-349 (1955).
- [25] M. Teschke, S. Sinzinger, "Phase contrast imaging—a generalized perspective", *J. Opt. Soc. Am. A* **26**, 1015-1021 (2009).
- [26] J. Glückstad, P. C. Mogensén, "Optimal phase contrast in common-path interferometry", *Appl. Opt.* **40**, 268-282 (2001).
- [27] R. Liang, J. K. Erwin, M. Mansuripur, "Variation on Zernike's phase-contrast microscope", *Appl. Opt.* **39**, 2152-2158 (2000).
- [28] C. Maurer, A. Jesacher, S. Bernet, M. Ritsch-Marte, "Phase contrast microscopy with full numerical aperture illumination", *Opt. Express* **16**, 19821-19829 (2008).
- [29] J. Lobera, J. M. Coupland, "Contrast enhancing techniques in digital holographic microscopy", *Meas. Sci. Technol.* **19**, 1-15 (2008).
- [30] W. Stoessel, "Fourieroptik", (Springer, Berlin, 1993), 174-177.
- [31] E. K. Reichel, B. G. Zagar, "Phase Contrast Method for Measuring Ultrasonic Fields", *IEEE Trans. Instr. Meas.* **55**, 1356-1361 (2006).
- [32] D. Murphy, "Differential interference contrast (DIC) microscopy and modulation contrast microscopy. Fundamentals of Light Microscopy and Digital Imaging", (Wiley-Liss, New York 2001) 153-168.
- [33] C. Preza, J. A. O'Sullivan, "Quantitative determination of specimen properties using computational DIC microscopy", *Proc. SPIE* **6630**, 66300E-1-66300E-11 (2007).
- [34] C. Preza, D. L. Snyder, J. A. Conchello, "Theoretical development and experimental evaluation for DIC microscopy", *J. Opt. Soc. Am. A* **16**, 2185-2199 (1999).
- [35] C. Preza, "Rotational-diversity phase estimation from DIC microscopy images", *J. Opt. Soc. Am. A* **17**, 415-424 (2000).
- [36] S. V. King, A. Libertun, R. Piestun, C. J. Cogswell, C. Preza, "Quantitative phase imaging through differential interference imaging", *J. Biomed. Opt.* **13**, 024020-0 – 1024020-10 (2008).
- [37] Q. Xie, D. Zhao, "Generation of dark hollow beams by using a fractional radial Hilbert transform system", *Optics Commun.* **275**, 394-398 (2007).
- [38] N. Bokor, Y. Iketaki, "Laguerre-Gaussian radial Hilbert transform for edge-enhancement Fourier transform x-ray microscopy", *Opt. Express* **17**, 5533-5539 (2009).
- [39] S. Fürhapter, A. Jesacher, S. Bernet, M. Ritsch-Marte, "Spiral phase contrast imaging in microscopy", *Opt. Express* **13**, 689-694 (2005).
- [40] A. Jesacher, S. Fürhapter, S. Bernet, M. Ritsch-Marte, "Shadow effects in spiral phase contrast microscopy", *Phys. Rev. Lett.* **94**, 233902:1-4 (2005).
- [41] Guohai Situ, Giancarlo Pedrini, Wolfgang Osten, "Spiral phase filtering and orientation-selective edge detection/enhancement", *J. Opt. Soc. Am. A* **26**, 1788-1796 (2009).
- [42] S. Bernet, A. Jesacher, S. Fürhapter, C. Maurer, M. Ritsch-Marte, "Quantitative imaging of complex samples by spiral phase contrast microscopy", *Opt. Express* **14**, 3792-3805 (2006).
- [43] K. G. Larkin, D. J. Bone, M. A. Oldfield, "Natural demodulation of two-dimensional fringe patterns. I. General background of the spiral phase quadrature transform", *J. Opt. Soc. Am. A* **18**, 1862-1870 (2001).
- [44] R. Müller, J. Marquard, "Die Hilberttransformation und ihre Verallgemeinerung in Optik und Bildverarbeitung", *Optik* **110**, 99-109 (1999).

- [45] M. Felsberg, G. Sommer, "The monogenic signal", IEEE Transactions on signal processing **49**, 3136-3144 (2001).
- [46] J. A. Davis, D. E. McNamara, D. M. Cottrell, J. Campos, "Image processing with the radial Hilbert transform: theory and experiments", Opt. Lett. **25**, 99-101 (2000).
- [47] M. Felsberg, G. Sommer, "Image features based on a new approach to 2D rotation invariant quadrature filters", ed. A. Heyden et. al., Computer Vision-ECCV **2350**, 369-383 (2002).
- [48] G. Popescu, L. P. Deflores, J. C. Vaughan, K. Badizadegan, H. Iwai, R. R. Dasari, M. S. Feld, "Fourier phase microscopy for investigation of biological structures and dynamics", Opt. Lett. **29**, 2503-2505 (2004).
- [49] T. Ikeda, G. Popescu, R. R. Dasari, M. S. Feld, "Hilbert phase microscopy for investigating fast dynamics in transparent systems", Opt. Lett. **30**, 1165-1168 (2005).
- [50] B. G. Zagar, B. Armingier, B. Heise, "Comparison of Various Algorithms for Phase Unwrapping in Optical Phase Microscopy", IEEE Proc. IMTC Warsaw, Poland, (2007).
- [51] C.J. R. Sheppard, "Three-dimensional phase imaging with the intensity transport equation", Appl. Opt. **41**, 5951-5955 (2002).
- [52] A. Grasnjow, A. Wuttig, R. Riesenberger, "Phase resolving microscopy by multi-plane diffraction detection", J. Microsc. **231**, 115-23 (2008).
- [53] S. S. Kou, L. Waller, G. Barbastathis, C. J. R. Sheppard, "Transport-of-intensity approach to differential interference contrast (TI-DIC) microscopy for quantitative phase imaging", Opt. Lett. **23**, 447-449 (2010).
- [54] J. J. Koenderink, "The structure of images", Biological Cybernetics **50**, 363-370, (1984).
- [55] L. Wietzke, G. Sommer, O. Fleischmann, "The geometry of the 2D image signal", IEEE Proc. CVPR, Miami, 1690-1697 (2009).
- [56] M. Felsberg, S. Kalkan, N. Krüger, "Continuous dimensionality characterization of image structures", Image and Vision Computing **27**, 628-636 (2009).
- [57] P. Kovési, "Invariant measures of image features from phase information", Thesis, University of Western Australia, 363-370 (1996).
- [58] J. P. Havlicek, A. C. Bovik, "Multi-component AM-FM image models and wavelet-based demodulation with component tracking", Proc. IEEE **41-45** (1994).
- [59] W. L. Chan, H. Choi, R. G. Baraniuk, "Coherent Multiscale Image Processing Using Dual-Tree Quaternion Wavelets", IEEE Trans. on Img. Proc., **17**, 1069-1081 (2008).
- [60] B. Boashash, "Estimating and Interpreting The Instantaneous Frequency of a Signal-Part 1: Fundamentals", Proc. IEEE **80**, (1992).
- [61] N. E. Huang, Z. Shen, S. R. Long, M. C. Wu, H. H. Shih, Q. Zheng, N-C. Yen, C. C. Tung, H. H. Liu, "The empirical mode decomposition and Hilbert spectrum for nonlinear and non-stationary time series analysis", Proc. R. Soc. Lond. **A454**, 903-995 (1998).
- [62] N. E. Huang, S. S. Shen, "Hilbert-Huang Transform and its applications", Interdisciplinary mathematical sciences **5**, (World Scientific Publishing Co, Singapore, 2005).
- [63] B. Shen, "Estimating the instantaneous frequencies of a multicomponent AM-FM image by bidimensional empirical mode decomposition", Proc. IEEE **283-287**(2005)
- [64] C. Damerval, S. Mignen, V. Perrier, "A Fast Algorithm for Bidimensional EMD", IEEE Sign. Proc. Lett. **12**, 701-704 (2005).
- [65] D. Gabor, "Theory of communications", Proc. Inst. Electr. Eng. Part III **93**, 29-457 (1946).
- [66] A. A. Oswald, "Early history of single-sideband transmission", Proc. IRE **44**, 1676-1679 (1956).
- [67] S. A. Cohen, "Spectrum Conservation and characteristics of single-sideband phase modulation", IEEE Trans. Electromagnetic Compatibility, **EMC-212**, 69-77 (1970).
- [68] J. Czarske, F. Hock, H. Müller, "Quadrature demodulation: a new LDV burst-signal frequency estimator", Proc. SPIE **2052**, 79-86 (1993).

- [69] D. Evans, W. McDicken, R. Skidmore, J. Woodcock, "*Doppler Ultrasound: Physics, Instrumentation and Clinical Applications*", (Chichester, UK: Wiley, 1989).
- [70] G. H. Granlund, H. Knutsson, "*Signal processing for computer vision*", (Kluwer Academic Publisher, Dordrecht, 1995) 165-167.
- [71] S. L. Hahn, "*Hilbert transforms in signal processing*", (Artech House, Inc., Norwood, MA, 1996).
- [72] K. G. Larkin, P. A. Fletcher, "A coherent framework for fingerprint analysis", *Optics Express* **15**, 8667-8677 (2007).
- [73] L. Qiao, W. Guo, W. Yuan, K. Niu, L. Peng, "Texture analysis on bidimensional empirical mode decompositions and quaternions", Proc. of the 2009 International Conference on Wavelet Analysis and Pattern Recognition, (2009).
- [74] J. P. Havlicek, J. W. Havlicek, A. C. Bovik, "The Analytic Image", IEEE Proc. ICIP, Santa Barbara, CA, Oct. 26-29, 446-449 (1997).
- [75] T. Bülow, D. Pallek, G. Sommer, "Riesz Transforms for the Isotropic Estimation of the Local Phase of Moiré Interferograms", Mustererkennung 2000, ed. G. Sommer et al., Springer Verlag, Berlin, DAGM 2000, 333-340 (2000).
- [76] M. Felsberg, G. Sommer, "Structure multivector for local analysis of images", Techn. Report **2001**, University Kiel, (2000).
- [77] M. Felsberg, G. Sommer, "The monogenic scale space: A Unifying Approach to Phase-Based Image Processing in Scale-Space", *J. Mathematical Imaging and Vision* **21**, 5-26 (2003).
- [78] G. Metikas, S. C. Olhede, "Multiple Multidimensional Morse Wavelets", *IEEE Trans. Signal Processing* **55**, 921-936 (2007).
- [79] L. Wietzke, O. Fleischmann, G. Sommer, "The Solution of the Interference-problem of 2D Waves by Means of Clifford Structures", Proc. ICNAAM **1168**, 817-820 (2009).
- [80] D. Zang, G. Sommer, "Signal modeling for two-dimensional image structures", *J. Vis. Commun. Image R.* **18**, 81-99 (2007).
- [81] L. Wietzke, G. Sommer, C. Schmaltz, J. Weickert, "Differential geometry of monogenic signal representations", Proc. 2nd Workshop "Robot Vision", Auckland, New Zealand, Gerald Sommer and Reinhard Klette (Eds.), LNCS, **4931**, Springer-Verlag Berlin, Heidelberg New York, 454-465 (2008).
- [82] E. Bedrosian, "A product theorem for Hilbert transforms", *Proc. IEEE* **51**, 868-869 (1963).
- [83] A. H. Nutall, "On the Quadrature Approximation to the Hilbert Transform of Modulated Signals", *Proc. IEEE* **54**, 1458-1459 (1966).
- [84] L. Mandel, "Complex representation of optical fields in coherence theory", *J. Opt. Soc. Am* **57**, 613-617 (1967).
- [85] L. Mandel, E. Wolf, "*Optical Coherence and Quantum Optics*", (Cambridge University Press, 1995).
- [86] M. Venouzio, H. Zhang, "Characterizing the Hilbert transform by the Bedrosian theorem", *J. Math. Anal. Appl.* **338**, 1477-1481 (2008).
- [87] T. Bülow, G. Sommer, "A Novel Approach to the 2D Analytic Signal", Proc. CAIP, (1999).
- [88] K. Khare, "Complex signal representation, Mandel's theorem, and spiral phase quadrature transform", *Appl. Opt.* **47**, E8-E12 (2008).
- [89] D. G. Fulton, G. Y. Rainich, "Generalizations to higher dimensions of the Cauchy integral formula", *Am. J. Math.* **54**, 235-241 (1932).
- [90] J. Ojeda-Castaneda, E. Jara, "Isotropic Hilbert transform by anisotropic spatial filtering", *Appl. Opt.* **25**, 4035-4038 (1986).
- [91] S. Equis, P. Jacquot, "Phase Extraction in Dynamic Speckle Interferometry with Empirical Mode Decomposition and Hilbert Transform", *J. Strain* 1-9 (online 2008).
- [92] A. F. Fercher, "Optical coherence tomography-developments, principles, applications", *Zeitschrift für Medizinische Physik*, in print, online Dec.2009.



- [93] J. F. de Boer, B. Cense, B. H. Park, M. C. Pierce, G. J. Tearney, B. E. Bouma, "Improved signal-to-noise ratio in spectral-domain compared with time-domain optical coherence tomography", *Opt. Lett.* **28**, 2067-2069 (2003).
- [94] R. Leitgeb, C. Hitzenberger, A. Fercher, "Performance of Fourier domain vs. time domain optical coherence tomography", *Opt. Express* **11**, 889-894 (2003).
- [95] A. F. Fercher, "Inverse scattering, dispersion and speckle in optical coherence tomography", in "Optical coherence tomography", W. Drexler, J. G. Fujimoto, ed., (Springer, Berlin, Heidelberg, 2008), 119-146.
- [96] J. A. Izatt, M. A. Choma, "Theory of Optical Coherence Tomography", in "Optical coherence tomography", W. Drexler, J. G. Fujimoto, ed., (Springer, Berlin, Heidelberg, 2008), 47-72.
- [97] Xueding Wang, Gang Yao, and Lihong V. Wang "Monte Carlo Model and Single-Scattering Approximation of the Propagation of Polarized Light in Turbid Media Containing Glucose", *Applied Opt.* **41**, 792-801 (2002).
- [98] J. M. Schmitt, A. Knüttel, M. Yadlowsky, R. F. Bonner, "Optical coherence tomography of a dense tissue: statistics of attenuation and backscattering", *Phys. Med. Biol.*, **42**, 1427-1439 (1994).
- [99] Y. Cheng, K. V. Larin, "Artificial fingerprint recognition by using optical coherence tomography with autocorrelation analysis", *Appl. Opt.* **45**, 9238-9245 (2006).
- [100] J. M. Schmitt, S. H. Xiang, K. M. Yung, "Speckle in optical coherence tomography", *J. Biomed. Optics* **4**, 95-105 (1999).
- [101] J. W. Goodman, "Random phasor sums", in "Speckle phenomena in optics", (Roberts and Comp., Englewood, 2007), 7-25.
- [102] G. Steidl, T. Teuber, "Removing multiplicative noise by Douglas-Rachford splitting methods", Preprint, University of Mannheim, (2009).
- [103] H. M. Salinas, D. C. Fernandez, "Comparison of PDE-Based Nonlinear Diffusion Approaches for Image Enhancement and Denoising in Optical Coherence Tomography", *IEEE Trans. Medical Imaging* **26**, 761-771 (2007).
- [104] J. F. de Boer, T. E. Milner, M. J. C. v. Gemert, J. S. Nelson, "Two-dimensional birefringence imaging in biological tissue by polarization-sensitive optical coherence tomography", *Opt. Lett.* **22**, 934-936 (1997).
- [105] J. M. Huntley, "Random Phase Measurement Errors in Digital Speckle Pattern Interferometry", *Optics and Lasers in Engineering* **26**, 131-150 (1997).
- [106] Z. Chen, T. E. Milner, S. Srinivas, X. Wang, A. Malekafzali, M. J. C. van Gemert, J. S. Nelson, "Noninvasive imaging of in vivo blood flow velocity using optical Doppler tomography", *Opt. Lett.* **22**, 1119-1121 (1997).
- [107] Z. Xu, L. Carrion, R. Maciejko, "A zero-crossing detection method applied to Doppler OCT", *Opt. Express* **16**, 4394-4412 (2008).
- [108] M. Bonesi, D. Y. Churmakov, L. J. Ritchie, I. V. Meglinski, "Turbulence monitoring with Doppler Optical Coherence Tomography", *Laser Physics Letters* **4**, 304-307 (2007).
- [109] Y. C. Ahn, W. Jung, J. Zhang, Z. Chen, "Investigation of laminar dispersion with optical coherence tomography and optical Doppler tomography", *Opt. Express* **13**, 8164-8171 (2005).
- [110] D. C. Adler, R. Huber, J. G. Fujimoto, "Phase-sensitive optical coherence tomography at up to 370,000 lines per second using buffered Fourier domain mode-locked lasers", *Opt. Lett.* **32**, 626-628 (2007).
- [111] J. A. Izatt, A. M. Rollins, R. Ung-Arunyawee, S. Yazdanfar, "System Integration and Signal/Image Processing", "Handbook of optical coherence tomography", ed. B. E. Bouma, G. J. Tearney, (Marcel Dekker AG, New York, 2002), 143-174.
- [112] R. K. Wang, S. Kirkpatrick, M. Hinds, "Phase-sensitive optical coherence elastography for mapping tissue microstrains in real time", *Appl. Phys. Lett.* **90**, 164105-164107 (2007).
- [113] M. Miura, M. Yamanari, T. Iwasaki, A. E. Elsner, S. Makita, T. Yatagai, Y. Yasuno, "Imaging Polarimetry in Age-Related Macular Degeneration", *Investigative Ophthalmology & Visual Science* **49**, 2661-2667, (2008).
- [114] M. Sticker, M. Pircher, E. Götzinger, H. Sattmann, A. F. Fercher, C. K. Hitzenberger, "En face imaging of single cell layers by differential phase-contrast optical coherence microscopy", *Opt. Lett.* **27**, 1126-1128 (2002).
- [115] C. Joo, T. Akkin, B. Cense, B. H. Park, J. F. de Boer, "Spectral domain optical coherence phase microscopy for quantitative-phase contrast imaging", *Opt. Lett.* **30**, 2131-2133 (2005).

- [116] D. Stifter, A. D. Sanchis Dufau, E. Breuer, K. Wiesauer, P. Burgholzer, O. Höglinger, M. Pircher, C. K. Hitzenberger, "Polarisation-sensitive optical coherence tomography for material characterisation and testing", *Insight* 47(4), 209-212 (2005).
- [117] D. Stifter, P. Burgholzer, O. Höglinger, E. Götzinger, C. K. Hitzenberger, "Polarisation-sensitive optical coherence tomography for material characterisation and strain-field mapping", *Appl. Phys. A* **76**, 1-5 (2003).
- [118] J. F. de Boer, S. M. Srinivas, A. Malekafzali, Z. Chen, J. S. Nelson, "Imaging thermally damaged tissue by polarization-sensitive optical coherence tomography", *Opt. Express* **3**, 212-218 (1998).
- [119] J. Young, G. Vargas, M. Ducros, S. A. Telenkov, B. J. F. Wong, T. E. Milner, "Thermally induced birefringence changes in cartilage using polarization-sensitive optical coherence tomography", *Proc. SPIE* **4257**, 213-220 (2001).
- [120] J. F. de Boer, T. E. Milner, "Review of polarization-sensitive optical coherence tomography and Stokes vector determination", *J. Biomed. Opt.* **7**, 359 (2002).
- [121] K. Wiesauer, A. D. Sanchis Dufau, E. Götzinger, M. Pircher, C. K. Hitzenberger, D. Stifter, "Non-destructive quantification of internal stress in polymer materials by polarisation-sensitive optical coherence tomography", *Acta Materialia* **53**, 2785-2791 (2005).
- [122] C. K. Hitzenberger, E. Götzinger, M. Sicker, M. Pircher, A. F. Fercher, "Measurement and imaging of birefringence and optic axis orientation by phase resolved polarization sensitive optical coherence tomography", *Opt. Express* **9**, 780-790, (2001).
- [123] O. C. Zienkiwicz, R. L. Taylor, "Finite element method for solid and structural mechanics", Elsevier (2005).
- [124] C. A. Brebbia, J. Dominguez, "Boundary element techniques: Theory and applications", (Springer-Verlag, Berlin, 1984).
- [125] G. Shyu, A. I. Isayev, H. Li, "Numerical simulation of flow-induced birefringence in injection molded disk", *Korea-Australia Rheology Journal*, **15**, 159-166 (2003).
- [126] C. M. OBraidaigh, G. B. McGuinness, R. B. Pipes, "Numerical analysis of stresses and deformations in composite materials sheet forming: central indentation of a circular sheet", *Composites Manufacturing*, **4**, 67-83(1993).
- [127] H. T. Jessop, F. C. Harris, "Photoelasticity: Principles and Methods", Dover Publications Inc., New York (1950).
- [128] K. Ramesh, "Digital photoelasticity: Advanced techniques and applications", (Springer-Verlag, Berlin, 2000).
- [129] Q. D. Liu, N. A. Fleck, J. E. Huber, D. P. Chu, "Birefringence measurements of creep near an electrode tip in transparent PLZT", *J. Eur. Ceram. Soc.* **29**, 2289-2296 (2009).
- [130] P. A. Williams, N. J. Kemp, D. Ives, J. Park, J. C. Dwelle, H. G. Rylander, T. E. Milner, "Noise model for polarization-sensitive optical coherence tomography", *Proc. SPIE* **6079**, 607929-1-607929-7 (2009).
- [131] M. Servin, J. C. Estrada, J. A. Quiroga, J. F. Mosiño, M. Cywiak, "Noise in phase shifting interferometry", *Opt. Exp.* **17**, 8789-8794 (2009).
- [132] B. Karamata, M. Laubscher, M. Leutenegger, S. Bourquin, T. Lasser, P. Lambelet, "Multiple scattering in optical coherence tomography. I. Investigation and modeling", *J. Opt. Soc. Am. A* **22**, 1369-1379.
- [133] J. M. Schmitt, S. H. Xiang, K. M. Yung, "Handbook of optical coherence tomography", ed. B. E. Bouma, G. J. Tearney, (Marcel Dekker AG, New York, 2002), 175-181.
- [134] B. Lehmann, H. Nobach, C. Tropea, "Measurement of acceleration using the laser Doppler technique", *Measurement Science and Technology* **13**, 1367-1381, (2002).
- [135] A. Stelzer, M. Pichler, "Resolution Enhancement with Model-Based Frequency estimation", *Subsurface Sens. Techn. Appl.* **4**, 241-261 (2003).
- [136] A. Björnham, L. Georg, "Frequency estimation from crossings of an observed mean level", *Biometrika* **63**, 507-512 (1976).
- [137] M. Takeda, H. Ina, S. Kobayashi, "Fouriertransform method of fringe-pattern analysis for computerbased topography and interferometry", *J. Opt. Soc. Am.* **72**, 156-160 (1982).
- [138] F. T. Wang, S. H. Chang, J. C. Lee, "Hybrid wavelet-Hilbert-Huang Spectrum Analysis", *Proc. Oceans-Europe* (2005).

- [139] F. A. M. Rodriguez, A. Federico, G. H. Kaufmann, "Hilbert transform analysis of a time series of speckle interferograms with a temporal carrier", *Appl. Opt.* **47**, 1310-1316 (2008).
- [140] C. Sciammarella, T. Kim, "Determination of strains from fringe patterns using space-frequency representations", *Opt. Eng.* **42**, 3182-3193 (2003).
- [141] J. T. Oh, S. W. Kim, "Polarization-sensitive optical coherence tomography for photoelasticity testing of glass/epoxy composites", *Opt. Express* **11**, 1669-1676 (2003).
- [142] B. H. Park, M. C. Pierce, B. Cense, S. Yun, M. Mujat, G. J. Tearney, B. E. Bouma, J. de Boer, "Real-time fiber-based multi-functional spectral domain coherence tomography at  $1.3\mu m$ ", *Opt. Express* **13**, 3931-3944 (2005).
- [143] D. Crespo, J. A. Quiroga, J. A. Gomez-Pedero, "Fast algorithm for estimation of the orientation term of a general quadrature transform with application to demodulation of an n-dimensional fringe pattern" *Appl. Opt.* **43**, 6139-6146 (2004).
- [144] N. C. Gallagher, G. L. Wise, "Median filters: a tutorial", *Proc. IEEE ISCAS* **88**, 1737-1744 (1988).
- [145] D. L. Donoho, I. M. Johnstone, "Ideal spatial adaptation by wavelet shrinkage", *Biometrika* **81**, 425-455 (1994).
- [146] A. Federico, G. Kaufmann, "Denoising in digital speckle pattern interferometry using wave atoms", *Opt. Lett.* **32**, 1232-1234 (2007).
- [147] J. Weickert, "Anisotropic Diffusion in Image Processing", *ECMI Series*, (Teubner, Stuttgart, 1998) 127-129.
- [148] J. Weickert, "Coherence-enhancing diffusion filtering", *Int. J. Comput. Vision* **31**, 111-127 (1999).
- [149] K. G. Larkin, "Uniform estimation of orientation using local and nonlocal 2-D energy operators", *Opt. Express* **13**, 8097-8121 (2005).
- [150] H.-E. Albrecht, M. Borys, N. Damaschke, C. Tropea, "Laser Doppler and Phase Doppler Measurement Techniques", (Springer, Berlin, Heidelberg, 2003).
- [151] D. C. Ghiglia, M. D. Pritt, "Two-dimensional Phase Unwrapping", (Wiley, New York, 1998).
- [152] J. A. Quiroga, M. Servin, F. Cuevas, "Modulo  $2\pi$  fringe orientation angle estimation by phase unwrapping with a regularized phase tracking algorithm", *J. Opt. Soc. Am. A* **19**, 1524-1531 (2002).
- [153] B. Stroebel, "Processing of interferometric phase maps as complex-valued phasor images", *Appl. Opt.* **35**, 2192-2198 (1996).
- [154] J. Villa, I. De la Rosa, G. Miramontes, J. A. Quiroga, "Phase recovery from a single fringe pattern using an orientational vector-field-regularized estimator", *J. Opt. Soc. Am. A* **22**, 2766-2773 (2005).
- [155] M. Nordström, D. A. Zauner, A. Boisen, J. Hübner, "Single-mode waveguides with SU-8 polymer core and cladding for MOEMS applications", *J. Lightwave Technol.* **25**, 1284-1289 (2007).
- [156] B. Heise, E. Leiss-Holzinger, M. Pircher, E. Götzinger, B. Baumann, C. K. Hitzenberger, D. Stifter, "Advanced Image Processing of Retardation Scans for PS-OCT", *Proc. SPIE* **7372**, 73720S-73720S-7 (2009).
- [157] A. Buades, B. Coll, J. M. Morel, "On image denoising methods", *CMLA, Tech. Rep.* **2004-15**, 2004.
- [158] B. Heise, K. Wiesauer, E. Götzinger, M. Pircher, C. K. Hitzenberger, R. Engelke, G. Ahrens, G. Grützner, D. Stifter, "Spatially Resolved Stress Measurements in Materials with Polarisation-Sensitive Optical Coherence Tomography: Image Acquisition and Processing Aspects", *J. Strain* **46**, 61-68 (2010).
- [159] Z. Kam, "Microscopic differential interference contrast image processing by line-integration (LID) and deconvolution", *Bioimaging* **6**, 166-176 (1998).
- [160] M. R. Arnison, C. J. Cogswell, N. I. Smith, P. W. Fekete, K. G. Larkin, "Using the Hilbert transform for 3D visualization of differential interference contrast microscope images", *J. Microsc.* **199**, 79-84 (2000).
- [161] B. Heise, A. Sonnleitner, E. P. Klement, "DIC-Image reconstruction in large cell scans", *J. Microscopy Research and Technique* **66**, 312-320 (2005).
- [162] B. Heise, H. Wolinski, L. Muresan, S. D. Kohlwein, E. P. Klement, "DIC-Image Reconstruction with Integrational Methods and Phase Filtering for Automated Analysis of Yeast Cell Scans", *Proc. OEAGM/AAPR, Obergurgl*, **209**, 169-178 (2006).

- [163] E. B. van Munster, L. J. van Vliet, J. A. Aten "Reconstruction of optical path length distributions from images obtained by a wide-field differential interference contrast microscope", *J. Microsc.* **188**, 149-157 (1997).
- [164] A. Murli, L. D'Amore, V. De Simone, "The Wiener Filter and Regularization Methods for Image Restoration Problems", *Proc. ICIAP* 394-399 (1999).
- [165] B. Heise, B. Armingner, "Some Aspects about Quantitative Reconstruction for Differential Interference Contrast (DIC) Microscopy", *Proc. Appl. Math. Mech.* **7**, 2150031-2150032 (2007).
- [166] F. Lenzen, O. Scherzer, S. Schindler, "Robust reconstruction of chopped and nodded images", *J. Astronomy and Astrophysics* **443**, 1087-1093 (2005).
- [167] P. A. Feinagle, A. P. Witkin, V. L. Stonick, "Processing of 3D DIC microscopy images for data visualization", *Proc. ICASSP*, 2160-2163 (1996).
- [168] B. Hofmann, "Mathematik inverser Probleme", (Teubner, Stuttgart-Leipzig, 1999).
- [169] M. J. Brooks, B. K. P. Horn, "Shape and source from shading", *Proc. Intern. Joint Conference on Artificial Intelligence*, 932-936 (1985).
- [170] R. T. Frankot, R. Chellappa, "A method for enforcing integrability in shape from shading algorithms", *IEEE Trans. Pattern Anal. and Mach. Intell.* **10**, 439-451 (1998).
- [171] A. Agrawal, R. Raskar, R. Chellappa, "What is the range for surface reconstructions from a gradient field?", *Proc. ECCV* (2006).
- [172] O. Vogel, A. Bruhn, J. Weickert, S. Didas, "Direct Shape-from-Shading with adaptive higher order regularisation", *LNCS* **4485**, 871-882 (2007).
- [173] B. Heise, D. Stifter, "Quantitative phase reconstruction for orthogonal scanning differential phase contrast-OCT", *Opt. Lett.* **34**, 1306-1308 (2009).
- [174] R. J. Young, P. A. Lovell, "Introduction to Polymers", Chapman & Hall (1991).
- [175] S. Zwick, M. Warber, W. Gorski, T. Haist, W. Osten, "Flexible Adaptive Phase Contrast Methods Using a Spatial Light Modulator", *Proc. DGaO* (2009).
- [176] T. J. McIntyre, C. Maurer, S. Bernet, M. Ritsch-Marte, "Differential interference contrast imaging using a spatial light modulator", *Opt. Lett.* **34**, 2988-2990 (2009).
- [177] A. C. Boccara, R. De Paepe, A. Dubois, M. Boccara, "Full-field optical coherence tomography (OCT) and early alterations in chloroplast morphology", *Proc. SPIE* **6755**, 67550E-1-67550E-5 (2007).
- [178] B. Heise, D. Stifter, "Coherent Imaging Microscopy: Applications and Challenges", 3rd International Workshop 3D Imaging, (Fontainebleau, France, 2010).
- [179] A. Dubois, L. Vabre, A. C. Boccara, E. Beaufort, "High-resolution full-field optical coherence tomography with a Linnik microscope", *Appl. Opt.* **41**, 805-812 (2002).
- [180] R. Baraniuk, "Compressive sensing", *IEEE Signal Proc. Mag.* **24**, 118-121 (2007).
- [181] B. Das, J. Joseph, K. Singh, "Phase-image-based sparse-gray-level data pages for holographic data storage", *Appl. Opt.* **48**, 5240-5249 (2009).
- [182] C. A. Fernandez, A. Wagadarikar, D. J. Brady, S. C. McCain, T. Oliver, "Fluorescence microscopy with a coded aperture snapshot spectral imager", *Proc. SPIE* **7184**, 71840Z-1-71840Z-11 (2009).
- [183] E. Potma, "Focus engineering of coherent anti-Stokes Raman-scattering microscopy enhances biomedical imaging capabilities", *Proc. SPIE* (2008).
- [184] The numerical implementation of CED algorithm has been implemented according to the Nonlinear Diffusion toolbox by Frederico D'Almeida, and was additionally kindly supported by Joachim Weickert. The numerical implementation of NLM algorithm has been implemented according to Non-local Mean toolbox by Gabriel Peyre. The numerical implementation of the SfS method was performed according to [172], kindly advised by Bodo Heise. The numerical differentiation software including Tikhonov regularization was kindly provided by Martin Burger.

- 
- [185] Different microscopic and interferometric images were kindly provided or the imaging of them was kindly supported by:  
DIC: Alois Sonnleitner, CBL Linz,  
PCM and SPM: Christian Maurer, Medical University Innsbruck,  
PCM: Frank Holtmann, University Muenster,  
PE: Martin Stockmann, TU Chemnitz,  
Conventional Interferometry: Bernd Armingier, JKU Linz,  
PS-OCT: Elisabeth Leiss, Karin Wiesauer, David Stifter, RECENDT GmbH and JKU Linz.



## **Publications related to the topic of this thesis:**

### **Journal papers**

Heise, B., Sonnleitner, A., Klement, E.P.: *DIC-Image reconstruction in large cell scans*.

J. Microscopy Research and Technique, 66(2005), pp. 312-320.

Heise, B., Stifter, D.: *Quantitative phase reconstruction for orthogonal scanning differential phase contrast-OCT*.

Opt. Letters, 34(2009), pp. 1306-1308.

Heise, B., Wiesauer, K., Goetzinger, E., Pircher, M., Hitzenberger, C.K., Engelke, R., Ahrens, G., Gruetzner, G., Stifter, D.: *Spatially Resolved Stress Measurements in Materials with Polarisation-Sensitive Optical Coherence Tomography: Image Acquisition and Processing Aspects*.

J. Strain, 46(2010), pp. 61-68.

Stifter, D., Leiss-Holzinger, E., Major, Z., Baumann, B., Pircher, M., Götzinger, E., Hitzenberger, C. K., Heise, B.: *Spectral-domain polarization-sensitive optical coherence tomography at 1550 nm for dynamic testing of polymers and composites*. Opt. Express, submitted.

### **Proceedings and Talks:**

Heise, B., Wolinski, H., Muresan, L., Kohlwein, S. D., Klement, E. P.: *DIC-Image Reconstruction with Integrational Methods and Phase Filtering for Automated Analysis of Yeast Cell Scans*.

Proc. OEAGM/AAPR, Obergurgl, **209**, 169-178 (2006).

Armingier, B.R., Zagar, B.G., Heise, B.: *Comparison of Various Algorithms for Phase Unwrapping in Optical Phase Microscopy*.

Proc. Instrumentation and Measurement Technology Conference, (IEEE IMTC, Warsaw, Poland, 2007).

Heise, B., Armingier, B.R.: *Phase-contrast measurement techniques: some aspects about phase microscopy and Schlieren imaging*.

PAMM, Proc. Appl. Math. Mech. 7 (2007), pp. 2150031-2150032, (ICIAM, Zurich, Switzerland, 2007).

Kuijper, A., Heise, B.: *An Automatic Cell Segmentation Method for Differential Interference Contrast Microscopy*.

In: Proc. International Conference on Pattern Recognition, (ICPR, Tampa, Florida, USA, 2008).

Heise, B., Leiss-Holzinger, E., Pircher, M., Goetzinger, E., Baumann, B., Hitzemberger, Ch.K., Stifter, D.: *Advanced Image Processing of Retardation Scans for PS-OCT*. European Conferences on Biomedical Optics (ECBO, Munich, Germany, 2009).

Proc. SPIE, vol. 7372 (2009) pp. 73720S-73720S-7.

Heise, B., Wurm, M., Wiesauer, K., Stifter, D.: *Spectral Domain-OCT: Application Fields in Material Research*.

Fraunhofer Institute of Photonic Technology Jena, (IPHT Jena, Germany, 2008, invited talk) .

Heise, B., Leiss, E., Stifter, D.: *Optical Coherence Tomography: Imaging and Image Processing aspects for Material Inspection Applications*.

Fraunhofer-Institut für Techno- und Wirtschaftsmathematik, (BAMEK, ITWM Kaiserslautern, Germany, 2008, invited talk).

Heise, B., Schausberger, S., Leiss-Holzinger E., Stifter, D.: *Polarization-Sensitive Optical Coherence Tomography*.

3rd Winterschool Ellipsometry, (Bad Hallein, Austria, March 2010, invited talk).

Heise, B., Schausberger, S., Stifter, D.: *Fringe analysis for low-coherence interferometric imaging methods*.

Photon 10, (Southampton, UK, August 2010), accepted.



# Lebenslauf Bettina Heise

Name:	Bettina Heise, geb. Klyne
Titel, akad. Grad:	Diplomphysikerin
geboren:	11. Februar 1964 in Zwickau, Sachsen
Staatsbürgerschaft:	deutsch
Familienstand:	verheiratet, 2 Kinder
Anschrift:	Golfplatzstrasse 4, A- 4040 Linz-Puchenu

## Schule

1970 - 1980	Polytechnische Oberschule
1980 - 1982	Spezialklasse für Mathematik, Physik und Technik an der TU Karl-Marx-Stadt (Chemnitz, Deutschland)
Juni 1982	erweiterte Matura auf mathematisch- naturwissenschaftlichem Gebiet an der TU Karl-Marx-Stadt (Chemnitz)

## Studium

September 1982 - Juli 1987	5- jähriges Studium an der TU Karl-Marx-Stadt (Chemnitz) Fachrichtung: Technische Physik, Vertiefungsrichtung: Festkörperphysik, (Prof. Hecht).
Mai 1985 - Juli 1985	Praktikum in der radiologischen Abteilung des Bezirkskrankenhauses Chemnitz.
September 1986 - Juli 1987	Diplomarbeit am Institut für Mechanik der Akademie der Wissenschaften, Chemnitz.
Juli 1987	Abschluss des Studiums als Diplomphysikerin.

## Berufliche Entwicklung

September 1987 - Mai 1989	Wissenschaftliche Mitarbeiterin am Institut für Mechanik (IMech) der Akademie der Wissenschaften (AdW), Karl-Marx-Stadt (Chemnitz), Sachsen. Fachbereich: Rheologie und Mehrphasenströmungen. <ul style="list-style-type: none"><li>• Arbeitsgebiet: optische Strömungsmesstechnik für Partikelströmungen, (Prof. Petrak).</li></ul>
------------------------------	---

Mai 1989 - Mai 1990	Karenzurlaub für das erste Kind.
Mai 1990 - Dezember 1991	Fortsetzung der Tätigkeit am Institut für Mechanik.
Jänner 1992 - August 1992	Karenzurlaub für das zweite Kind.
August 1992 - Jänner 1994	Fortsetzung der Tätigkeit als wissenschaftliche Mitarbeiterin in der Projektgruppe Mehrphasenströmung (hervorgegangen aus dem Institut für Mechanik) an der TU Chemnitz.
Februar 1994	Übersiedlung aus familiären Gründen nach Linz, Österreich.
September 1996 - Dezember 1998	4 –semestriges Zusatzstudium Lasertechnik und Lasertechnologie an der Friedrich - Schiller - Universität Jena, Deutschland
Seit 2001	Wissenschaftliche Mitarbeiterin und Projektleitung am Institut für wissenschaftliche mathematische Systeme (FLLL) der Johannes Kepler Universität Linz, (Prof. Klement).
November 2007- Dezember 2009	Zusätzlich teilbeschäftigt als wissenschaftliche Mitarbeiterin in der Upper Austrian Research GmbH (UAR bzw. RECENDT) <ul style="list-style-type: none"> <li>• Arbeitsgebiet: Optische Kohärenz Tomografie</li> </ul>
Seit Januar 2010-	Wissenschaftliche Mitarbeiterin am Christian Doppler Labor <ul style="list-style-type: none"> <li>• CDL MS-MACH, Johannes Kepler Universität Linz</li> </ul>



